Interplay of geometry and dynamics in mesoscopic model systems

Der Fakultät für Mathematik und Naturwissenschaften der
Technischen Universität Ilmenau vorgelegte

Dissertation

zur Erlangung des akademischen Grades eines

Doctor rerum naturalium (Dr. rer. nat.)

vorgelegt von
Frau Dipl.-Phys. Pia Stockschläder
geboren am 16.05.1988 in Mainz

Gutachten erstattet von:
Prof. Dr. Martina Hentschel
Prof. Dr. Klaus Richter
Prof. Dr. Erich Runge

Datum der Einreichung: 04.10.2016
Datum der wissenschaftlichen Aussprache: 01.02.2017

urn:nbn:de:gbv:ilm1-2017000059

Abstract

In this work, we study the interplay of the system geometry and the boundary shape with the properties and dynamics of different mesoscopic model systems.

In the first part, we investigate extended ray-optical models for dielectric optical microcavities. Ray optics is an efficient tool to predict the far-field emission of these systems. When considering systems on lengths scales on the order of few light wavelengths, however, corrections to geometrical optics can be necessary to account for wave effects. These corrections to ray optics are the Goos-Hänchen shift, a lateral shift along the interface, and the Fresnel filtering effect, an angular shift, which violates the ray-optical laws of reflection and refraction and the principle of ray-path reversibility. We discuss these beam shift effects at planar and curved boundaries and study the influence of different parameters on the correction terms. An important finding is that the boundary curvature enhances the Fresnel filtering effect, whereas, it reduces the Goos-Hänchen shift. We apply the ray-optical model to deformed microdisks, systems with curved boundaries, and to triangular cavities, systems with only planar boundaries. Correctly including finite-wavelength effects can be important to establish good agreement between the ray description and results of experiments or wave simulations for both, systems with curved and with planar boundaries. The systems can not only be classified by their boundary shape but also by their classical ray dynamics, whether it is chaotic or non-chaotic. For systems with chaotic dynamics it is well known that the unstable manifold of the chaotic saddle determines the far-field emission. For non-chaotic systems – we consider deformed disks with small deformations and triangles – we discuss that the trajectories with the smallest nonzero decay rates determine the emission pattern. Further, we include intensity amplification in the ray-optical model and find it necessary to obtain reliable results in highly lossy lasing systems.

In the second part, we discuss graphene-like systems. For these systems, we study the influence of uniaxial strain in a tight-binding model on the honeycomb lattice. Uniaxial compression leads to a phase transition and to the formation of edge states perpendicular to the strain direction independent of the edge termination. Further, we introduce a ray model as a possibility to describe graphene devices as efficiently as the ray-optical model allows for dielectric optical microcavities.

Zusammenfassung

Diese Arbeit behandelt anhand verschiedenener mesoskopischer Modellsysteme das Zusammenspiel von Geometrie und Form eines Systems mit seinen Eigenschaften und seiner Dynamik.

Im ersten Teil wird ein erweitertes strahlenoptisches Modell für dielektrische optische Mikrokavitäten untersucht. Strahlenoptik ist eine effiziente Methode, um die Fernfeldabstrahlung dieser Systeme vorherzusagen. Werden allerdings Systeme betrachtet, deren Abmessungen nur wenige Lichtwellenlängen betragen, können Korrekturen der geometrischen Optik notwendig werden, um Welleneffekte zu berücksichtigen. Diese Korrekturen sind die Goos-Hänchen-Verschiebung, eine seitliche Verschiebung des Strahls entlang der Grenzfläche, und der Effekt des Fresnel-Filterns, eine Korrektur des Winkels, die das Reflexions- und das Brechungsgesetz der Strahlenoptik und das Prinzip der Umkehrbarkeit des Strahlengangs bricht. Diese Strahlverschiebungen werden für ebene und gekrümmte Grenzflächen diskutiert, außerdem werden die Einflüsse verschiedener Parameter auf die Korrekturterme untersucht. Ein wichtiges Resultat ist, dass die Krümmung der Grenzfläche den Effekt des Fresnel-Filterns verstärkt, wohingegen sie die Goos-Hänchen-Verschiebung abschwächt. Anschließend wird das strahlenoptische Modell auf verschiedene Beispiele angewendet, nämlich Mikrokavitäten in der Form von deformierten Kreisscheiben, also Systeme mit gekrümmten Grenzflächen, und dreieckige Kavitäten, also Systeme mit ausschließlich ebenen Grenzflächen. Sowohl für Systeme mit gekrümmten als auch mit ebenen Grenzflächen kann es wichtig sein, die auf endlichen Wellenlängen beruhenden Korrekturen miteinzubeziehen, um eine gute Übereinstimmung zwischen der Strahlenbeschreibung und Ergebnissen aus Experimenten oder Wellensimulationen zu erhalten. Die Systeme können aber nicht nur durch ihre Grenzfläche charakterisiert werden, sondern auch dadurch, ob ihre klassische Dynamik chaotisch oder nicht-chaotisch ist. Für Systeme mit chaotischer Dynamik ist bekannt, dass die Fernfeldabstrahlung durch die instabile Mannigfaltigkeit des chaotischen Sattels bestimmt wird. Als Beispiele für nicht-chaotische Systeme werden deformierte Kreisscheiben mit kleinen Verformungen und Dreiecke betrachtet. Für diese Systeme wird erörtert, dass die Abstrahlung durch die Trajektorien mit den kleinsten, nicht-verschwindenden Zerfallsraten bestimmt wird. Darüber hinaus kann es notwendig sein, Intensitätsverstärkung im Strahlenbild zu berücksichtigen, um verlässliche Ergebnisse für stark verlustbehaftete Lasersysteme zu erhalten.

Im zweiten Teil werden graphenartige Systeme diskutiert. An diesen wird zuerst der Einfluss von einachsigen Verformungen in einem tight-binding-Modell des hexagonalen Gitters untersucht. Einachsige Stauchung des Gitters führt zu einem Phasenübergang und zur Ausbildung von Randzuständen senkrecht zur Verzerrungsrichtung. Diese Randzustände sind unabhängig von der genauen Terminierung des Gitters. Als zweites wird ein Strahlenmodell eingeführt, das eine Beschreibung von Graphen-Bauelementen ermöglichen könnte, die genauso effizient ist wie die Strahlenbeschreibung von optischen Systemen.

Contents

Chapter 1

Introduction

The term mesoscopic designates the transition regime between the microscopic and the macroscopic scale. It describes systems or devices with typical dimensions approximately on the same order of magnitude as the length scale responsible for its dynamics – the wavelength, the phase coherence length or the mean free path.

Optical microcavities are mesoscopic systems for light [1–3]. In these systems, the light is confined in regions with typical dimensions on the order of magnitude of several to several hundreds of the light's wavelength. There are two basic methods how this confinement can be achieved. On the one hand, distributed Bragg reflectors in vertical-cavity surface-emitting lasers [4] and photonic crystal defect cavities [5] use the interference of multiply reflected or scattered light. On the other hand, light can be confined by total internal reflection at a dielectric interface between an optically dense material with a higher refractive index and a material with a lower refractive index. This method can be applied to three-dimensional structures, like microspheres [6, 7] or microtoroids [8], and to quasi two-dimensional structures, like microdisks [9] or other flat shapes with a large width to height ratio (see, *e.g.*, [10, 11]).

These optical microcavities offer many possibilities for applications. For example, they can be used as the resonant cavities of microlasers that promise to be the ideal miniaturized light source. As they can be fabricated by standard techniques they can be easily integrated in opto-electronic devices [12, 13]. The high confinement of the light which is possible leads to efficient low-threshold lasing [14] and the emission direction can be chosen to suit the application by choosing the right shape of the cavity [15, 16]. Besides this and many other practical applications, like filters or sensors [3, 17], optical microcavities are also interesting to study more fundamental questions. One example is provided by the equivalence between the Helmholtz equation describing the electromagnetic modes and the Schrödinger equation determining the quantum mechanical wave function (see, *e.g.*, [18]). Thus, optical systems provide analogous models in which predictions from quantum mechanics can be tested which are otherwise not easily accessible. Therefore, optical (or more general electromagnetic) cavities are often used in the field of quantum chaos [19]. The same analogy can also be used to mimic the properties of solid state systems in optical systems, the so-called photonic crystals [5].

Since optical microcavities are interesting for many different applications, efficient methods for their theoretical description are needed. Like for most problems in electromagnetism, a direct analytical solution of Maxwell's equations with the appropriate boundary conditions is usually not possible [20]. Different numerical methods are successfully applied to study the properties of optical microcavities, like the finite-difference time-domain method [21, 22], the finite elements method [23, 24] or the boundary element method [25]. However, much can be learned about microcavities already by applying the simple methods of geometrical optics which is the short-wavelength limit of electromagnetism to these systems [10, 26–29]. A more detailed introduction to the ray-optics description of two-dimensional dielectric optical microcavities will be given in the following chapters.

Mesoscopic systems for electrons are solid state devices where the system size is on the order of or smaller than the phase coherence length of the charge carriers [30]. Typical systems that are often studied are two-dimensional electron gases [31], quantum wires [32, 33] or quantum dots [34, 35] which are often implemented in semiconductor heterostructures [36]. Quantum dots can also be interpreted as microcavities for electrons. The two-dimensional material graphene [37] and related carbon-based nanostructures [38] are also a suitable basis to study mesoscopic effects. In quasi one-dimensional graphene nanoribbons [39] one can study the influence of interference effects on the conductance through the sample [40, 41]. Quantum dots can be realized in graphene [42] by confining the electrons by external potentials [43, 44] or in finite-sized graphene flakes [45, 46]. A strong analogy between the electronic states in a graphene quantum dot and the modes in an optical microcavity can be found [44, 47].

1.1 Scope of the work

This work has two main topics. On the one hand, we discuss an effective ray description of different systems, dielectric optical microcavities as well as electronic cavities in graphene, in the framework of ray-wave-correspondence. On the other hand, we examine symmetries and symmetry breaking in these systems, especially, their connection to and interplay with the dynamics of the considered system.

The first part of the work, chapters 2-4, deals with the ray description of dielectric optical microcavities. Dielectric optical microcavities and microlasers are interesting both as mesoscopic model systems and as devices in micro-optics applications. The ray optics model has proven to be an efficient and useful way to describe the properties of these systems, especially, their far-field emission characteristics.

In chapter 2, we discuss wave-inspired corrections to the ray optics description of optical microcavities. These corrections, known as Goos-Hänchen shift and Fresnel filtering, stem from the wave-nature of light and have to be included in a ray optics description to obtain reliable results if the system size is reduced to several wavelengths. We calculate these beam shift effects from an expectation value approach at planar and curved interfaces and discuss in detail the influence of all relevant parameters, the beam width, the refractive index and, especially, the boundary curvature, on the correction terms [48, 49].

When the beam shifts are included in a ray-optical description the trajectory of a light ray is no longer reversible as the reversed trajectory can suffer different corrections than the original trajectory. We examine this breaking of the time reversal symmetry from the point of view of a light beam of finite width reflected at a dielectric interface. We introduce the overlap of the original beam and the time-reversed reflected beam as a combined measure of the beam shift effects.

In the following chapter, chapter 3, we apply the wave-inspired corrections to microcavities with curved boundaries. In this context, we compare several methods to include the influence of the boundary curvature in an amended ray optics description. By using different boundary shapes, we can also study the effect of the symmetry of the cavity on the far-field emission and the effect of the beam shifts on the symmetry-induced properties of the trajectories.

Further, we discuss the differences in the description of systems with chaotic and non-chaotic classical dynamics. For optical microcavities with chaotic classical dynamics it is known that the unstable manifold of the chaotic saddle determines the far-field emission. In the case of systems with non-chaotic dynamics, we argue that the trajectories with the smallest nonzero decay rates will determine the emission characteristics instead.

In chapter 4, we use the ray optics model to describe dielectric optical microcavities in the shape of triangles with low refractive index [50]. Although triangles are the simplest polygons, triangular microcavities show an intriguing interplay between geometry, ray dynamics and optical properties. Here, we include amplification in the ray model to obtain a reliable description of the highly lossy systems. As the ray dynamics in polygonal systems is non-chaotic we can use the decay rates to identify the trajectories which determine the far-field emission. The trajectories with the smallest decay rates depend strongly on the geometry and the optical properties of the system and, in general, need not be periodic. Therefore, we suggest that they provide a more general explanation for the emission patterns than short periodic orbits which are frequently employed to explain the far-field of polygonal microcavities. To account for finite wavelength effects we study the influence of the beam shift effects on the trajectories and the far-field emission of two highly symmetrical triangles, the equilateral and the right isosceles triangle.

The last part of this work, chapter 5, deals with a different model system, graphene-like hexagonal lattice systems. First, we discuss the influence of uniaxial strain in a tight-binding model on the hexagonal lattice. Uniaxial strain breaks the discrete rotational symmetry of the undistorted honeycomb lattice. It leads to a phase transition and to the appearance of edge states. Whereas the existence of edge states in unperturbed graphene-like systems depends sensitively on the precise termination of the boundary, the edge states that appear under strain are predicted to be robust and independent of the edge termination.

Further, we apply the concept of ray-wave-correspondence to the electrons in graphene. In the same spirit as the ray description of optical microcavities, we discuss an effective ray description of graphene devices as a possibility to model the electronic properties of these systems efficiently.

Chapter 2

Wave-inspired corrections to ray optics at planar and curved interfaces

In this chapter, we discuss corrections to geometrical optics which stem from the wave nature of light and are important for an efficient ray-optical description of dielectric optical microcavities. First, we give a short introduction to the ray optics description of microcavities and the concept of ray-wave correspondence. Then, we study the wave corrections occurring for the reflection of a light beam at a planar dielectric interface. A consequence of the finite width of any light beam is that the reflection of the beam at a dielectric interface is not reversible. This breaking of the ray-path reversibility is examined in the third section. In the fourth section, the beam shift effects for the reflection of a light beam at a curved dielectric interface are studied in detail, paying special attention to the influence of the boundary curvature.

2.1 Ray optics description of microcavities

Large optical systems like microscopes or telescopes are well described by geometrical optics. Geometrical optics, also called ray optics, is the zero-wavelength limit of electromagnetism. Thus, it is well suited to describe systems that are large compared to the wavelength of the light. Nevertheless, it has proven useful to apply ray-optical methods also to smaller systems.

In the following, we introduce the basic concepts of the ray-optical approach to the description of dielectric optical microcavities.

2.1.1 Microcavities as optical billiards

Billiards is a popular and well-studied subject in mathematics and mathematical physics, see [51] and references therein for an introduction and further reading. A simplified mathematical billiard is a bounded region in the plane with a point mass that moves freely inside the region and is reflected elastically at the boundary. That means that the particle moves with constant velocity along a straight line until it hits the boundary where it is specularly reflected.

A light ray, in the sense of the geometrical optics limit of electromagnetism, propagating in a homogeneous and isotropic medium bounded by perfectly reflecting walls behaves like the particle in the mathematical billiard. According to Fermat's principle, the light ray follows a straight path inside the medium and is specularly reflected at the boundaries. Hence, the name optical billiards is often used. This can be realized for microwaves in a superconductive, thus, perfectly reflective cavity [52, 53].

If the region is not bounded by perfectly reflecting walls but by the interface between two different dielectric media the ray is not completely reflected but can be partly transmitted. The direction of the transmitted ray is given by Snell's Law which also follows from Fermat's principle. Thus, dielectric optical microcavities can be interpreted as partially open billiards [54]. The amount of openness is given by the ratio of the refractive indices $n = n_1/n_2$ of the two media. Without loss of generality, the refractive index of the medium inside the cavity can be set to $n_1 = n$ and outside to $n_2 = 1$. Then, Snell's Law reads

$$\sin(\chi_{\text{trans}}) = n \sin(\chi_{\text{in}}) \tag{2.1}$$

where the angles of incidence and transmission, χ_{in} and χ_{trans}, are measured with respect to the local normal to the boundary. For $n > 1$ transmission can only occur if $\sin(\chi_{\text{in}}) < 1/n$. For incident angles larger than the critical angle χ_c defined by $\sin(\chi_c) = 1/n$ the light ray is confined inside the cavity by total internal reflection. The limit $n \to \infty$ corresponds to the usual closed billiards.

The main difference between the mathematical billiards and the optical system in the ray limit is the possibility of ray-splitting as a light ray has the intensity as an additional property. The point particle considered in mathematical billiards can be lost, if an opening is introduced in the boundary, but it cannot be split in a transmitted and a reflected part. At each reflection of a light ray at a dielectric interface, however, a part or all of the incident intensity is reflected and a part can be transmitted.

The dynamics of the billiards system is fully described in the phase space. The full four-dimensional phase space of a particle in a two-dimensional planar billiards considered here can be reduced to a suitable two dimensional Poincaré surface of section using the fact that the particle moves freely between two reflections. The appropriate coordinates are the so-called Birkhoff coordinates (s, p) where s is the position on the appropriately parameterized boundary and $p = \sin(\chi_{\text{in}})$ is the transverse momentum component. Thus, the billiards dynamics can be seen as a mapping between one reflection with (s, p) and the next reflection with (s', p'). In the optical case, one additionally has to keep track of the intensity.

We restrict our discussion in this work to two-dimensional geometries. A two-dimensional microcavity can be interpreted as the cross section (here chosen to be in the y-z-plane) of an infinitely long dielectric cylinder (along the x-direction) [20]. In this case, Maxwell's equations can be decoupled by the two linear polarizations of the electromagnetic wave, transverse magnetic (TM) and transverse electric (TE) polarization. In the case of TM polarization, the magnetic field $\vec{H}$ oscillates in the cavity plane and the component perpendicular to the plane, parallel to the cylinder axis vanishes $H_x = 0$; Maxwell's equations reduce to the scalar Helmholtz equation for the electric field component E_x perpendicular to the plane. Analogously, for TE polarization, the electric field $\vec{E}$ oscillates in the cavity plane and the perpendicular component vanishes, $E_x = 0$ and Maxwell's equations are reduced to the scalar Helmholtz equation for the magnetic field component E_x parallel to the cylinder axis. In the following we will always characterize the polarization state of the light by TE or TM.

2.1.2 Wave corrections to ray optics

The treatment of dielectric optical microcavities as optical billiards, thus, treating the electromagnetic waves in the zero-wavelength limit of geometrical optics, is based on the concept of ray-wave correspondence [26]. Based on this concept, the modes and the far-field emission patterns of microcavities in various shapes have been successfully predicted from ray optics calculations [10, 27–29].

Although ray-wave correspondence is a very robust concept, deviations from ray-optics occur when the system sizes are no longer large compared to the wavelength [55–57], especially, when the system dimensions are of the order of the light wavelength [58, 59]. These deviations are caused by the wave nature of light. For the theoretical description of optical systems that are not large compared to the wavelength full electromagnetic simulations should be used. However, these simulations are computationally expensive.

In order to, still, use the simple and efficient ray-optical description, the deviations have to be taken into account to obtain accurate results [57]. This can be done by including correction terms to the laws of geometrical optics. These are known as the Goos-Hänchen shift [60–62] and the Fresnel filtering effect [56, 63]. They act in the two different directions in phase space spanned by the Birkhoff coordinates (s, p) [64]. The Goos-Hänchen shift is a lateral shift of the reflected light ray along the interface, *i.e.*, is a correction to the position coordinate s. The Fresnel filtering effect describes corrections to the angles of reflection and transmission, *i.e.*, acts on the momentum $p = \sin(\chi)$. There are several conventions in the literature on how to define and call the angular shifts. Often, the term angular Goos-Hänchen shift is also used [65–68]. Here, we do not want to discuss the subtle differences between the different definitions and we use the term Fresnel filtering for all angular correction terms (see Ref. [68] for a discussion).

The two effects can be included into the ray-optical description in an effective manner, their physical origin will be discussed below. The classical billiards mapping $(s,p) \to (s'(s,p),p'(s,p))$ is replaced by a new map including corrections to the position on the boundary arising from the Goos-Hänchen shift and to the momentum, or angle of incidence, stemming from the Fresnel filtering effect.

The wave corrections are not restricted to electromagnetic waves, rather, they occur always when the system size is of the order of the wavelength. It has been observed, *e.g.*, for ultrasound waves [69], for electron waves in semiconductor nanostructures [70] or in graphene [71], or for quantum mechanical wave packets [72]. The Goos-Hänchen shift in graphene will be discussed briefly in section 5.4.

2.2 Beam shifts at planar interfaces

In this section, the wave corrections, Goos-Hänchen shift and Fresnel filtering, will be calculated for a light beam reflected at a planar dielectric interface. The beam shifts at planar interfaces are well established and exhaustively studied in literature, see, *e.g.*, [73] for an early review of the Goos-Hänchen effect and [67] for a recent overview that considers the full three dimensional problem. Nevertheless, the planar case is studied in detail here. On the one hand, it is important to introduce the methods, on the other hand, the results derived here will be used in an extended ray description of triangular microcavities in chapter 4.

2.2.1 Goos-Hänchen shift

Figure 2.1 shows a schematic picture of a light ray reflected at a planar interface between two different dielectric materials including the beam shift effects. The lateral shift along the interface D_{GH} due to the Goos-Hänchen effect and the angular deflection $\Delta\chi_{\mathrm{FF}}$ due to the Fresnel filtering effect are marked.

The lateral shift of a light beam under total reflection was already predicted by Newton. It is named Goos-Hänchen shift after F. Goos and H. Hänchen who first measured it in the 1940s [60, 74]. An early quantitative explanation has been given by K. Artmann [61]. The simplest version of Artmann's argumentation is the following. Consider a superposition of two plane waves with the same wavenumber k, but slightly different directions, $p = \sin(\chi_{\mathrm{in}})$ and $p' = p + \Delta p$, incident on a dielectric interface with relative refractive index n (see Fig. 2.2(a)). The incident wave at the interface defined by $(y = 0, z)$ reads

$$\begin{aligned} E_{\mathrm{in}}(z) &= E_0 \left(\mathrm{e}^{inkpz} + \mathrm{e}^{inkp'z} \right) \\ &= E_0 \mathrm{e}^{inkpz} \left(1 + \mathrm{e}^{ink\Delta pz} \right) . \end{aligned}$$

We assume that both plane wave components are totally internally reflected, *i.e.*, $p, p' > 1/n$. In this case, the reflection coefficient reads $\rho(p) = \mathrm{e}^{\mathrm{i}\varphi(p)}$.

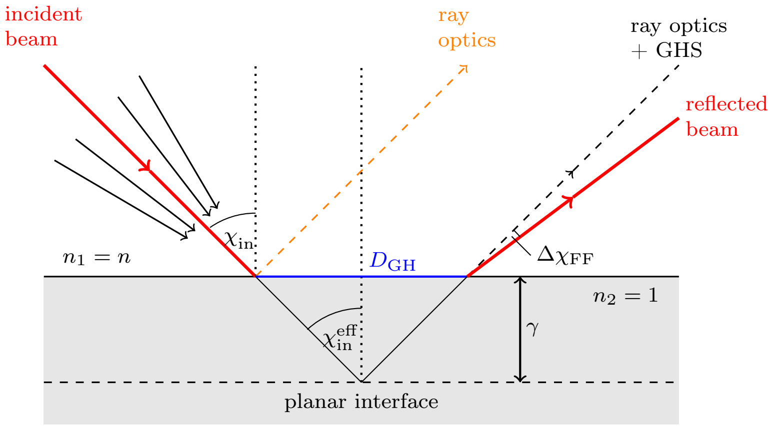

Figure 2.1: Schematic picture of the beam shifts at planar interfaces. Incident and reflected rays are shown in red. The relative refractive index is $n = n_1/n_2$. The effective interface is depicted as dashed line, γ is the penetration depth. The normals to the interface and the effective interface (dotted lines) define the angle of incidence $\chi_{\rm in}$ and the effective angle of incidence $\chi_{\rm in}^{\rm eff}$. The reflected ray predicted from ray optics (dashed orange), the lateral shift along the interface $D_{\rm GH}$ due to the Goos-Hänchen effect (blue), and the angular deflection $\Delta\chi_{\rm FF}$ due to the Fresnel filtering effect are marked.

Thus, the reflected wave reads

$$\begin{aligned}
E_{\rm ref}(z) &= E_0\left(\mathrm{e}^{\mathrm{i}nkpz+\mathrm{i}\varphi(p)} + \mathrm{e}^{\mathrm{i}nkp'z+\mathrm{i}\varphi(p')}\right) \\
&= E_0 \exp(\mathrm{i}(nkpz+\varphi(p)))\left(1+\exp\left(\mathrm{i}nk\Delta p\left(z+\frac{1}{nk}\frac{\Delta\varphi}{\Delta p}\right)\right)\right) \\
&= E_0 \exp\left(\mathrm{i}\varphi - \mathrm{i}\Delta\varphi\frac{p}{\Delta p}\right)\exp(\mathrm{i}nkp(z+\Delta z))\,(1+\exp(\mathrm{i}nk\Delta p(z+\Delta z))) \\
&= \exp\left(\mathrm{i}\varphi - \mathrm{i}\Delta\varphi\frac{p}{\Delta p}\right) E_{\rm in}(z+\Delta z)
\end{aligned}$$

with $\Delta\varphi = \varphi(p') - \varphi(p)$ and

$$\Delta z = \frac{1}{nk}\frac{\Delta\varphi}{\Delta p}.$$

Thus, the absolute value of the reflected wave corresponds to the incident wave shifted by Δz along the boundary. If the difference Δp in the directions is small the difference quotient is approximately the derivative and the shift in terms of the wavelength reads

$$\frac{\Delta z}{\lambda} \approx \frac{1}{2\pi n}\frac{\mathrm{d}\varphi(p)}{\mathrm{d}p}. \tag{2.2}$$

This is the Artmann formula for the Goos-Hänchen shift. It is shown in Fig. 2.2(b) for the relative refractive index $n = 1.5$ (the relevant phase of the reflection coefficient is shown in Fig. 2.3(b)).

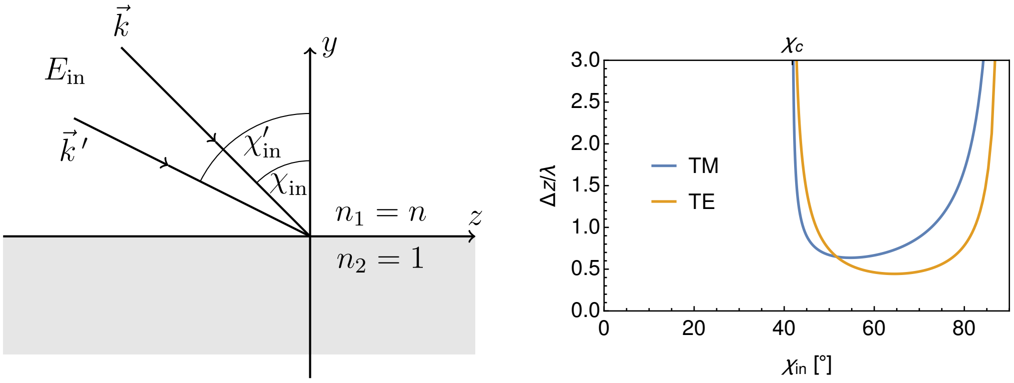

(a) Schematics of the incoming beam.

(b) Goos-Hänchen shift according to the Artmann formula Eq. 2.2 for $n = 1.5$.

Figure 2.2: Artmann result for the Goos-Hänchen shift derived from an incoming beam consisting of two plane wave components. The different plane waves gain different phase shifts under reflection which leads to a lateral shift.

This very simple analytic approach has two major shortcomings. It is applicable only for total internal reflection and it diverges for grazing incidence ($\chi_{\mathrm{in}} \to 90°$) as well as directly at the critical angle as the phase of the reflection coefficient has a sharp kink there. Thus, we have to employ a different approach to obtain meaningful values for the Goos-Hänchen shift also at and below the critical angle. Before we introduce the expectation value approach that we will use to calculate the beam shifts in the next section, we look at Goos-Hänchen shift from a different perspective and discuss the second shift, the Fresnel filtering effect.

A light wave that is incident on a dielectric interface from an optically denser to an optically thinner medium with an angle of incidence larger than the critical angle of total internal reflection will be continued as an evanescent wave inside the optically thinner medium. Taking into account these exponentially decaying contribution at the boundary leads to a shift of the order of the vacuum light wavelength λ of the reflected beam [61, 62, 75]. Intuitively, one can imagine that the light is not reflected directly at the interface but at an effective interface under an effective angle of incidence $\chi_{\mathrm{in}}^{\mathrm{eff}}$, as depicted in Fig. 2.1. The effective interface is parallel to the real boundary and situated at a distance γ inside the optically thinner medium where γ is the penetration depth of the evanescent wave. Then, the lateral shift D_{GH} along the boundary can be approximated as $D_{\mathrm{GH}} \approx 2\gamma \tan(\chi_{\mathrm{in}}^{\mathrm{eff}})$. At a planar interface, the effective angle of incidence equals the incident angle at the real interface, $\chi_{\mathrm{in}}^{\mathrm{eff}} = \chi_{\mathrm{in}}$. The penetration depth, however, is not constant but depends on the angle of incidence and the polarization of the incident light.

2.2.2 Fresnel filtering effect

The origin of the second beam shift effect, the Fresnel filtering effect, is the finite spatial extent of a real light beam, a solution of Maxwell's equations, as opposed to the idealized light rays of geometrical optics [63, 66]. The finite width induces a distribution of angles of incidence around the central incident angle χ_{in} of the beam. A beam of finite width is composed of plane waves whose wave vectors point in directions distributed in an interval around the central direction of the beam. This angular spread is indicated in Fig. 2.1 by the thin black arrows near the red arrow for the incident ray.

To understand the Fresnel filtering effect, consider a beam whose central angle of incidence is the critical angle, $\chi_{\text{in}} = \chi_c$. Upon reflection, all smaller angles in the distribution will be partially transmitted, whereas all angles larger than the critical angle will be totally reflected. Thus, the mean angle of the reflected light beam will deviate from χ_{in}. This leads to a violation of the standard law of reflection, the angle of reflection χ_{ref} no longer equals the angle of incidence χ_{in}, rather, it is $\chi_{\text{ref}} = \chi_{\text{in}} + \Delta\chi_{\text{FF}}$, with the correction term $\Delta\chi_{\text{FF}}$ due to the Fresnel filtering effect. From this argumentation, it is seen that the Fresnel filtering effect is most important around χ_c and for beams narrow in space, *i.e.*, with a broad angular distribution.

2.2.3 Beam shifts as expectation values

In this work, we use an expectation value approach to the beam shifts [76]. This approach is more widely applicable than many approximative formulas discussed in literature [61, 62, 67, 75]. Especially, it is not limited to angles of incidence above or near the critical angle but yields meaningful results for a wide range of incident angles.

In the planar case, the beam is expanded in plane waves. The calculations are restricted to the interface, denoted by the z-axis. The angles of incidence χ are related to the direction of the incident plane wave via $k_z^{\text{in}} = nk\sin(\chi) = nkp$ with the wavenumber $k = 2\pi/\lambda$ where λ is the vacuum wavelength of the light beam and $p = \sin(\chi)$. The incident beam is given by

$$E_I(z) = \int_0^1 \mathrm{d}p\, e_I(p)\mathrm{e}^{\mathrm{i}nkpz}, \tag{2.3}$$

where the transverse beam profile $e_I(p)$ is supposed to be a narrow distribution in momentum p with expectation value $p = p_0$ corresponding to the central angle of incidence χ_{in} with $p_0 = \sin(\chi_{\text{in}})$.

The reflected beam is obtained by applying the Fresnel reflection coefficients [20] to the incident beam profile, $e_R(p) = \rho(p)e_I(p)$. The Fresnel equations [20] expressed in $p = \sin(\chi)$ read for both, TM and TE, polarizations

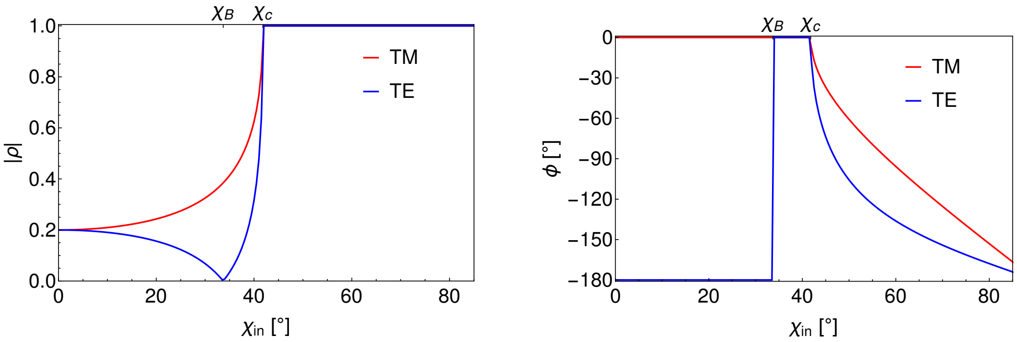

(a) Absolute value $|\rho|$ of the reflection coefficients $\rho = |\rho|\mathrm{e}^{\mathrm{i}\varphi}$.

(b) Phase φ of the reflection coefficients $\rho = |\rho|\mathrm{e}^{\mathrm{i}\varphi}$.

Figure 2.3: Reflection coefficients at a planar interface with relative refractive index $n = 1.5$ for both polarizations, TM (red) and TE (blue).

$$\begin{aligned} \rho_{\mathrm{TM}}(p) &= \frac{n\sqrt{1-p^2} - \sqrt{1-n^2p^2}}{n\sqrt{1-p^2} + \sqrt{1-n^2p^2}} \\ \rho_{\mathrm{TE}}(p) &= \frac{\sqrt{1-p^2} - n\sqrt{1-n^2p^2}}{\sqrt{1-p^2} + n\sqrt{1-n^2p^2}} \end{aligned} \tag{2.4}$$

where TE polarization shows the Brewster angle χ_B, given by $\tan(\chi_B) = 1/n$ with $\rho_{\mathrm{TE}}(\sin(\chi_B)) = 0$. In general, the reflection coefficients are complex numbers. Their absolute value and phase as a function of the incident angle are shown in Fig. 2.3 for the reflection at a dielectric interface with relative refractive index $n = 1.5$. With that, the reflected beam in real space is

$$E_R(z) = \int_0^1 \mathrm{d}p \, e_R(p) \mathrm{e}^{\mathrm{i}nkpz}. \tag{2.5}$$

We define the position of incidence of the beam on the interface as the expectation value of z of the incident beam profile

$$\langle z \rangle_{\mathrm{in}} = \frac{\int_{-\infty}^{\infty} \mathrm{d}z \, E_I^*(z) \, z \, E_I(z)}{\int_{-\infty}^{\infty} \mathrm{d}z \, |E_I(z)|^2}. \tag{2.6}$$

The position of reflection is analogously given by the z-expectation value of the reflected beam profile

$$\langle z \rangle_{\mathrm{ref}} = \frac{\int_{-\infty}^{\infty} \mathrm{d}z \, E_R^*(z) \, z \, E_R(z)}{\int_{-\infty}^{\infty} \mathrm{d}z \, |E_R(z)|^2}. \tag{2.7}$$

The difference between these two positions is the Goos-Hänchen shift along the boundary

$$D_{\mathrm{GH}} = \langle z \rangle_{\mathrm{ref}} - \langle z \rangle_{\mathrm{in}}. \tag{2.8}$$

If the incident beam profile in angular momentum space is symmetric with respect to the central momentum component p_0, Eq. (2.6) yields $\langle z \rangle_{\text{in}} = 0$ and the position of incidence marks the origin of the chosen coordinate system. Hence, the Goos-Hänchen shift becomes $D_{\text{GH}} = \langle z \rangle_{\text{ref}}$ which is the case in all the examples that we consider here.

The expectation values of the momentum p calculated with the angular profiles give the directions of the beams. The mean angle of incidence χ_{in} corresponds to

$$\langle p \rangle_{\text{in}} = \frac{\int_0^1 \mathrm{d}p\, e_I^*(p)\, p\, e_I(p)}{\int_0^1 \mathrm{d}p\, |e_I(p)|^2}. \tag{2.9}$$

By the choice of the incident angular profile it is $\langle p \rangle_{\text{in}} = p_0 = \sin(\chi_{\text{in}})$. The mean angle of reflection χ_{ref} can be calculated from the p-expectation value of the reflected angular profile

$$\langle p \rangle_{\text{ref}} = \frac{\int_0^1 \mathrm{d}p\, e_R^*(p)\, p\, e_R(p)}{\int_0^1 \mathrm{d}p\, |e_R(p)|^2} = \frac{\int_0^1 \mathrm{d}p\, p\, R(p)\, |e_I(p)|^2}{\int_0^1 \mathrm{d}p\, R(p)\, |e_I(p)|^2} \tag{2.10}$$

with $\langle p \rangle_{\text{ref}} = \sin(\chi_{\text{ref}})$. Here, we have introduced the intensity reflection coefficient $R(p) = |\rho(p)|^2$. The difference between the mean angle of incidence and of reflection is the angular shift constituting the Fresnel filtering effect, $\Delta\chi_{\text{FF}} = \chi_{\text{ref}} - \chi_{\text{in}}$.

For an evaluation of these formulas, we chose a Gaussian with mean value p_0 and standard deviation ϵ as the transverse beam profile in momentum space,

$$e_I(p) = \frac{1}{\sqrt{2\pi}\epsilon} \mathrm{e}^{-\frac{(p-p_0)^2}{2\epsilon^2}}, \tag{2.11}$$

since Gaussian beams are often realized in experiment. However, the beam shifts can be easily evaluated for other transverse beam profiles with the expectation value formulas.

2.2.4 Discussion of the results and comparison to wave simulations

Full electromagnetic wave simulations have been performed by Jakob Kreismann (now a PhD student in the group of Prof. M. Hentschel, TU Ilmenau, group for Theoretical Physics II and Computational Physics) using the finite-difference time-domain method (FDTD) [48, 49, 77]. A Gaussian beam impinging on a dielectric interface is used to obtain the beam shifts as shown in Fig. 2.4. For more details concerning the simulations and their evaluation refer to [77].

The beam waist w of the Gaussian beam in real space used in the simulation and the angular spread ϵ of the beam profile, defined in Eq. (2.11), used in the analytical expectation value approach are connected by

$$\frac{w}{\lambda} = \frac{\sqrt{2}}{\pi\epsilon}. \tag{2.12}$$

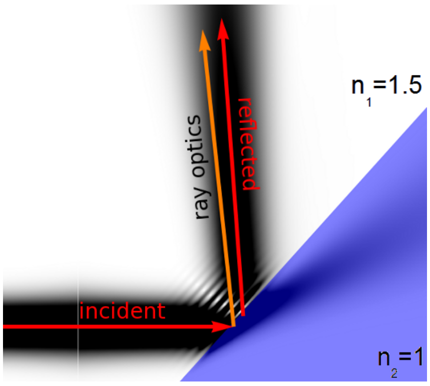

Figure 2.4: Real space picture of a TM polarized Gaussian beam with width $w/\lambda = 5$ reflected at a planar dielectric interface with relative refractive index $n = 1.5$ near critical incidence. The direction of incident and reflected beams are given by red arrows, the direction of the reflected beam expected from ray optics is given by the orange arrow. Courtesy of J. Kreismann.

A comparison between the results of the FDTD simulations and the evaluation of the expectation value approach is presented in Fig. 2.5, where Goos-Hänchen shift and Fresnel filtering are shown for both polarizations (TE in blue, TM in red) as function of χ_{in}. Taking into account that there is no free fitting parameter the agreement between the two methods is reasonable even well below the critical angle; and the curves almost coincide for larger angles of incidence.

The FDTD simulation yields smaller values than the analytical approach for subcritical angles of incidence due to two effects. First, incident and reflected beams overlap in practice, and this overlap is larger when the two beams are closer together, *i.e.* for smaller angles of incidence. This can lead to difficulties with correctly determining the direction of the reflected beam because, on the one hand, the two beams are not clearly separated and, on the other hand, they might interfere. Both influences are not captured in the analytical formulas. Second, the necessary discretization of the boundary in the simulation induces wave scattering since the interface acts like a reflection grating. These two effects, the overlap of the beams and the scattered waves, affect the inferred beam propagation direction resulting in the underestimation of the beam shifts.

Taking a general look on the results, the following is seen. Both effects are strongest around the critical angle. In the example here, the Goos-Hänchen shift reaches the maximum values $D_{\text{GH}} \approx 3\lambda$ for TE polarization and $D_{\text{GH}} \approx 1.5\lambda$ for TM polarization. The expectation value approach predicts maximum angular shifts $\Delta\chi_{\text{FF}} \approx 8.5^\circ$ for TE polarization and $\Delta\chi_{\text{FF}} \approx 3.5^\circ$ for TM polarization, whereas, in the simulation maximum values $\Delta\chi_{\text{FF}} \approx 6.5^\circ$ and $\Delta\chi_{\text{FF}} \approx 2^\circ$ are found for the two polarizations, respectively. The Goos-

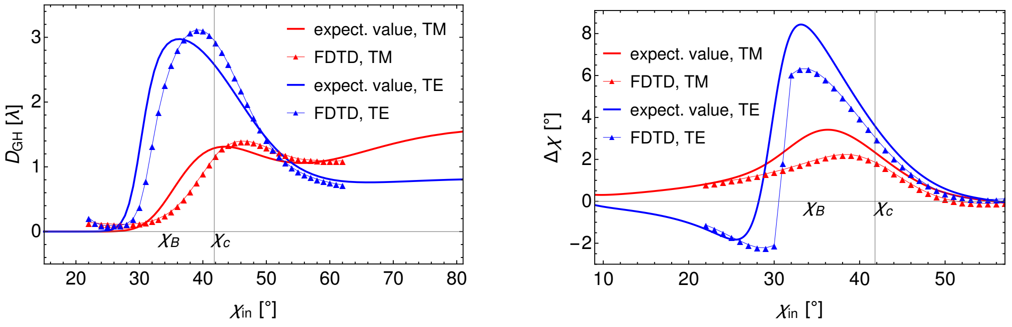

(a) Goos-Hänchen shift (b) Fresnel filtering

Figure 2.5: Comparison between evaluation of the beam shift formulas (solid) and FDTD results (triangles, courtesy of J. Kreismann) for the beam shifts of a Gaussian beam reflected at a planar interface for TM and TE polarization (red and blue, respectively); $n = 1.5$, $w/\lambda = 5$.

Hänchen shift is zero for small angles and takes on finite values for supercritical incidence.

The Fresnel filtering effect leads to a small but finite angular shift for small angles and drops to zero in the regime of total internal reflection. For TE polarization, the angular shift is negative for small angles, reaches a minimum and changes sign for angles smaller than the Brewster angle before it reaches its maximum for angles smaller than the critical angle. To understand this behavior, we look at the incident and reflected angular profiles, $|e_I(\chi)|^2$ and $|e_R(\chi)|^2$, respectively, for different central angles of incidence, as shown in Fig. 2.6. In panel (a) the central angle of incidence is chosen to be the critical angle. In the reflected angular distribution it is clearly seen, that the angle components larger than the critical angle are totally reflected, whereas, the smaller angle components are almost completely missing because the reflection coefficient quickly drops to small values below the critical angle. Consequently, the expectation value of the reflected angular profile is shifted to larger angles than the central angle of incidence, leading to a positive value for the Fresnel filtering effect. This argument is true for a range of incident angles around the critical angle for both polarizations. For TM polarization this is the only effect, resulting in a positive Fresnel filtering effect for all incident angles. For TE polarization, the Brewster angle introduces an additional effect. In Fig. 2.6(b) the incident and reflected angular distributions are shown for a central angle of incidence close to, but smaller than the Brewster angle. It can be seen that no light is reflected directly at the Brewster angle and the whole reflected profile is influenced in such a way that the expectation value of this distribution is found at smaller angles than the central angle of incidence. This explains the observation that the Fresnel filtering effect for TE polarization is negative for small angles of incidence and changes sign near the Brewster angle.

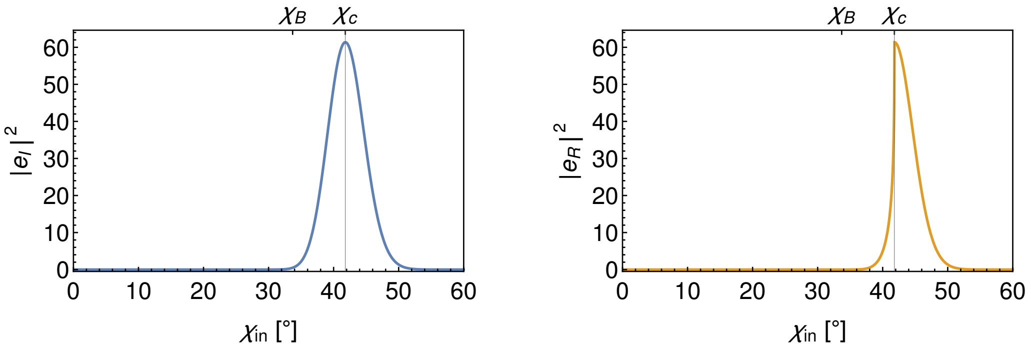

(a) Central angle of incidence $\chi_{\text{in}} = \chi_c \approx 41.8°$.

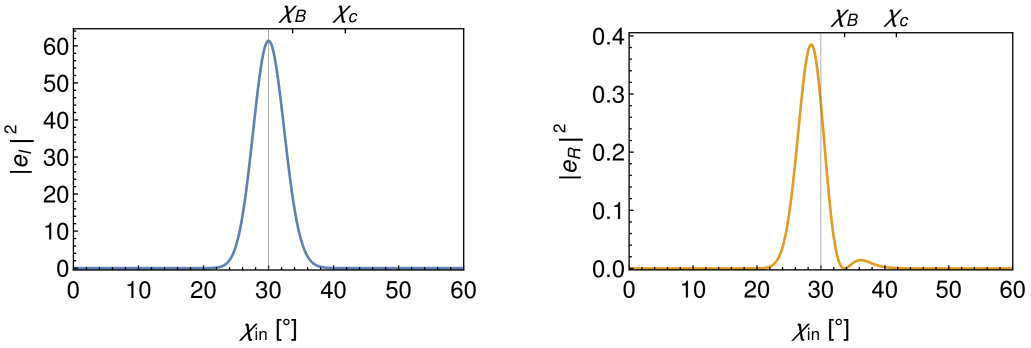

(b) Central angle of incidence $\chi_{\text{in}} = 30°$.

Figure 2.6: Incident (blue, left) and reflected (orange, right) angular profiles, $|e_I(\chi)|^2$ and $|e_R(\chi)|^2$, respectively, for two different central angles of incidence for TE polarization. The incident profile e_I is given by a normal distribution in the transverse momentum component $p = \sin(\chi)$ defined in Eq. (2.11) with standard deviation $\epsilon \approx 0.05$. The relative refractive index is $n = 1.5$ with $\chi_c \approx 41.8°$, $\chi_B \approx 33.7°$.

In general, both effects, the Goos-Hänchen shift and Fresnel filtering, are more pronounced for TE polarization. For the lateral shift, this has already been predicted by the early explanation by Artmann [61] and measured by Goos and Hänchen [74]. Due to the Brewster angle feature, the reflected beams are more strongly distorted for TE polarization than for TM polarization if the angular profile encounters the region around the Brewster angle. Thus, the beam shifts are strongly enhanced in the vicinity of the Brewster angle.

2.2.5 Influence of the beam width

Here, we discuss the influence of the beam width w/λ of the incident beam in real space on the beam shifts at a planar interface [49]. The results for the Goos-Hänchen shift and the Fresnel filtering effect from the expectation value approach using Gaussian beam profiles with varying width are shown in Fig. 2.7 (an alternative presentation can be found in the appendix, Fig. B.1).

In the figure, two effects can be clearly seen. Firstly, both effects are broadened with reduced beam width, thus, giving a contribution for a larger range of incident angles. Secondly, the maximum of the lateral shift D_{GH} increases while the maximal values of the angular deflection $\Delta\chi_{\text{FF}}$ decrease with increasing beam width. This is understood in the intuitive picture discussed in sections 2.2.1 and 2.2.2. The Goos-Hänchen shift depends on the spatial extent of the beam, whereas, the Fresnel filtering depends on the width of the

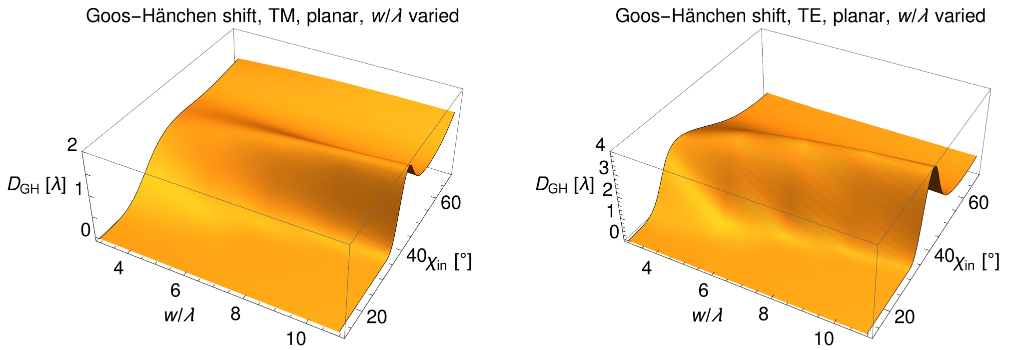

(a) Goos-Hänchen shift, TM polarization.
(b) Goos-Hänchen shift, TE polarization.

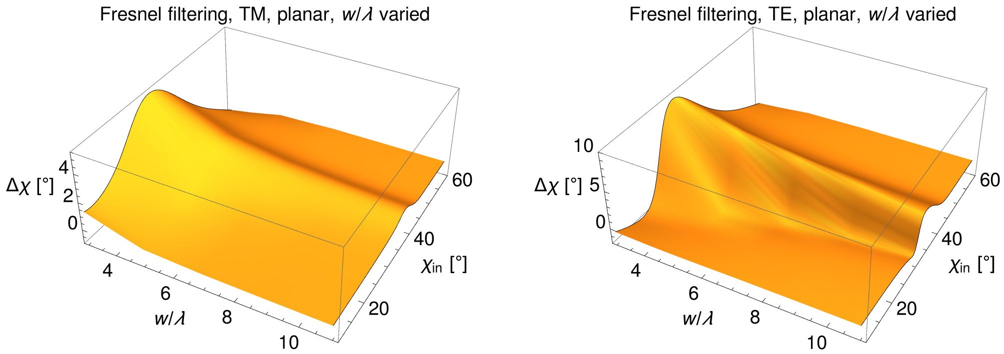

(c) Fresnel filtering, TM polarization.
(d) Fresnel filtering, TE polarization.

Figure 2.7: Influence of the beam width on the Goos-Hänchen shift D_{GH} and on the Fresnel filtering effect $\Delta\chi_{\text{FF}}$ at a planar interface according to Eq. (2.8) and Eq. (2.10), respectively. The wavenumber k is fixed while the beam waist w/λ is varied. The relative refractive index is $n = 1.5$, $\chi_c \approx 41.8°$, $\chi_B \approx 33.7°$. An alternative presentation of this data can be found in Fig. B.1.

angular distribution. As the spatial and the angular profiles are the Fourier transform of each other, a broader beam in space corresponds to a narrower angular spectrum. Hence, the change of the real space beam width leads to the opposing trends for the two beam shift effects.

Increasing the spatial width of the beam corresponds to decreasing the angular spread: a broad beam is composed of only few plane wave components. In the limit $w/\lambda \to \infty$, the Fresnel filtering effect vanishes and the Goos-Hänchen shift resembles more closely the Artmann result, see Eq. (2.2) and Fig. 2.2, which has been derived for only two plane wave components. This can be seen already in the results shown in Fig. 2.7 for increasing w/λ. The Goos-Hänchen shift becomes more strongly peaked at the critical angle which is reminiscent of the singularity in the Artmann result, for subcritical incidence the shift vanishes quickly and for supercritical incidence the shift is larger for TM polarization than for for TE polarization.

2.2.6 Influence of the relative refractive index

In most examples in this chapter, we use the relative refractive index $n = 1.5$ which is typical for glass or transparent polymers in air. This rather low index of refraction is well suited for illustrating the beam shift. First, the penetration depth into the optically thinner medium is larger if the refractive index contrast is lower, thus, the beam shifts are supposed to be larger. Second, the critical angle $\chi_c \approx 42°$ is approximately in the center of the possible angles of incidence, therefore, the beam shift effects are important for a larger range of incident angles. Further, the Brewster angle for TE polarization is well separated from the critical angle.

In many practical applications, however, higher relative refractive indices are relevant. On the one hand, typical semiconductor material have high refractive indices for the relevant wavelengths (for example in the infrared: AlN $n \approx 2$, GaAs $n \approx 3.3$, Ge $n \approx 4$ [78]). On the other hand, only a high refractive index contrast allows for good confinement of light by total internal reflection. Therefore, we study here the influence of the relative refractive index on the beam shifts.

If we want to compare the results for different refractive indices we have two possibilities: We can calculate the beam shifts either for constant beam width with respect to the vacuum wavelength or for constant beam width inside the medium. We show the results for fixed beam width in vacuum in Fig. 2.8 and the results for fixed beam width in the medium in Fig. 2.9 for different relative refractive indices up to $n = 3.5$. Note that the parameters are chosen to coincide for $n = 2$.

The Goos-Hänchen shift for TM polarized light and the Fresnel filtering effect for both polarizations behave as expected: The beam shifts decrease for increasing relative refractive index. As the widths of the incident beams are different in the two scenarios (except for $n = 2$) the absolute sizes of the beam

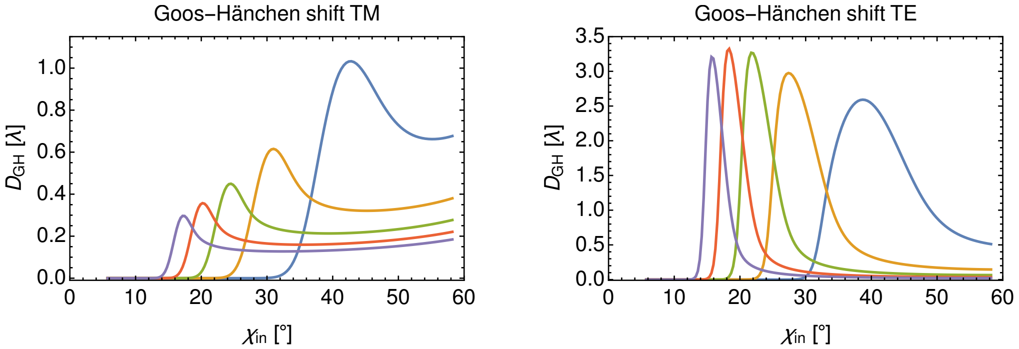

(a) GHS, TM polarization.

(b) GHS, TE polarization.

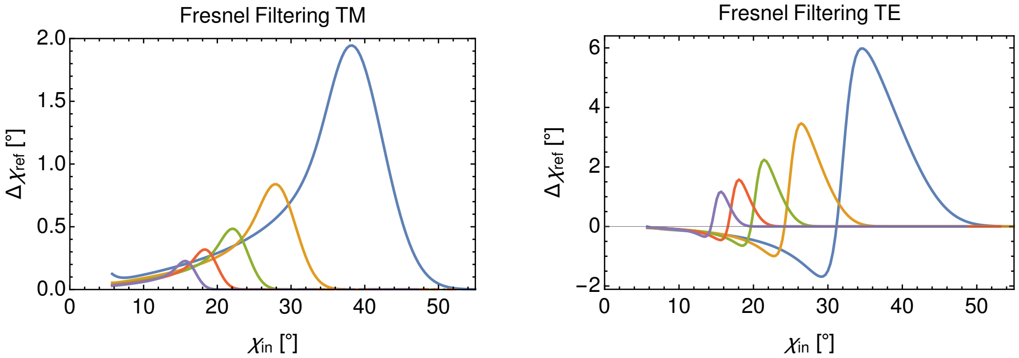

(c) FF, TM polarization.

(d) FF, TE polarization.

Figure 2.8: Influence of the relative refractive index on the Goos-Hänchen shift D_{GH} and on the Fresnel filtering effect $\Delta\chi_{\mathrm{FF}}$ at a planar interface according to Eq. (2.8) and Eq. (2.10), respectively. Beam width with respect to vacuum wavenumber fixed, $\epsilon = 0.09$.

shifts differ but the trend is the same.

The Goos-Hänchen shift for TE polarization does not follow this trend. We have already seen that the Brewster angle enhances the lateral shift in its vicinity. For higher refractive index, the Brewster angles is closer to the critical angle: for $n = 1.5$ the distance between the two angles is $\chi_c - \chi_B \approx 8.1°$, whereas, it reduces to only $\chi_c - \chi_B \approx 0.66°$ for $n = 3.5$. Therefore, the high values expected for the critical angle and for the Brewster angle add up in a small interval of incident angles. This effect partially counteracts the decreasing trend.

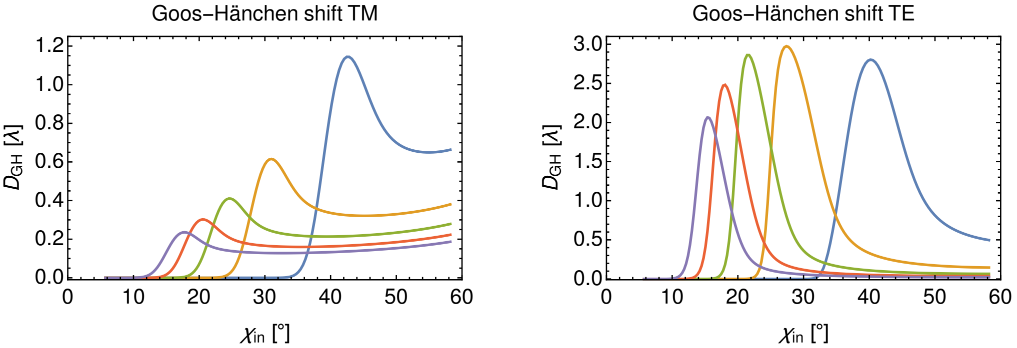

(a) GHS, TM polarization.

(b) GHS, TE polarization.

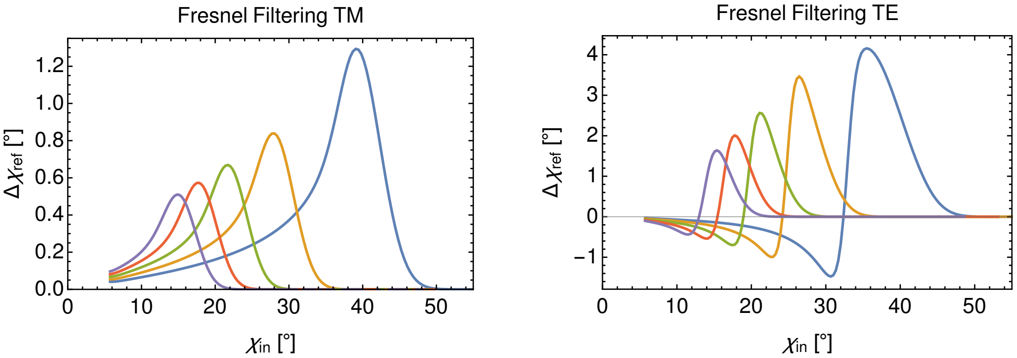

(c) FF, TM polarization.

(d) FF, TE polarization.

Figure 2.9: Influence of the relative refractive index on the Goos-Hänchen shift D_{GH} and on the Fresnel filtering effect $\Delta\chi_{\mathrm{FF}}$ at a planar interface according to Eq. (2.8) and Eq. (2.10), respectively. Beam width in the medium fixed, $\epsilon/n = 0.045$.

2.2.7 Beam shifts in transmission

Analogous to the definition of the mean direction of the reflected beam in Eq. (2.10) we can define the mean direction of the transmitted beam as the p-expectation value of the transmitted angular profile

$$\langle p \rangle_{\text{trans}} = \frac{\int_0^{1/n} \mathrm{d}p \, p \, T(p) \, |e_I(p)|^2}{\int_0^{1/n} \mathrm{d}p \, T(p) \, |e_I(p)|^2} \tag{2.13}$$

with the intensity transmission coefficient $T(p) = 1 - R(p)$. Here, the integration runs only over those momenta $p \leq 1/n$ for which partial transmission is possible. The mean angle of transmission χ_{trans} is given by $n \langle p \rangle_{\text{trans}} = \sin(\chi_{\text{trans}})$ where the change in direction between the incident and the transmitted ray due to the refractive index contrast is taken into account. The difference between the mean angle of transmission calculated from the transmitted beam and the angle of transmission expected from Snell's law is the Fresnel filtering effect in transmission

$$\Delta\chi_{\text{FF}}^{\text{trans}} = \chi_{\text{trans}} - \arcsin(n \sin(\chi_{\text{in}})). \tag{2.14}$$

The resulting Fresnel filtering in transmission evaluated for a Gaussian angular profile according to Eq. (2.11) with varying angular spread ϵ is shown in Fig. 2.10. For all incident angles and both polarizations, the angular shift is negative, *i.e.*, the corrected angle of transmission is smaller than classically expected from Snell's law. This is easily understood in the intuitive picture. If the mean angle of incidence is the critical angle the corresponding transmitted ray is parallel to the interface. However, there are still components in the beam with smaller angles of incidence which are transmitted to smaller angles, thus, the expectation value of the transmitted beam is shifted to smaller angles.

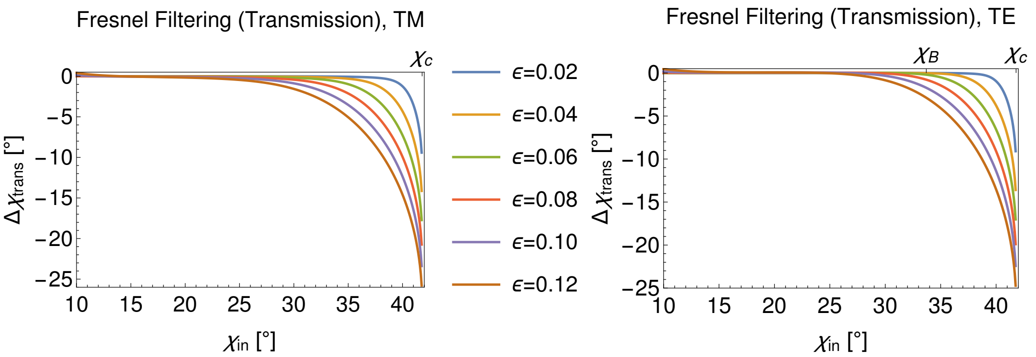

(a) TM polarization.

(b) TE polarization.

Figure 2.10: Fresnel filtering effect in transmission according to Eq. (2.14) at a planar interface with relative refractive index $n = 1.5$, angular spread ϵ varied.

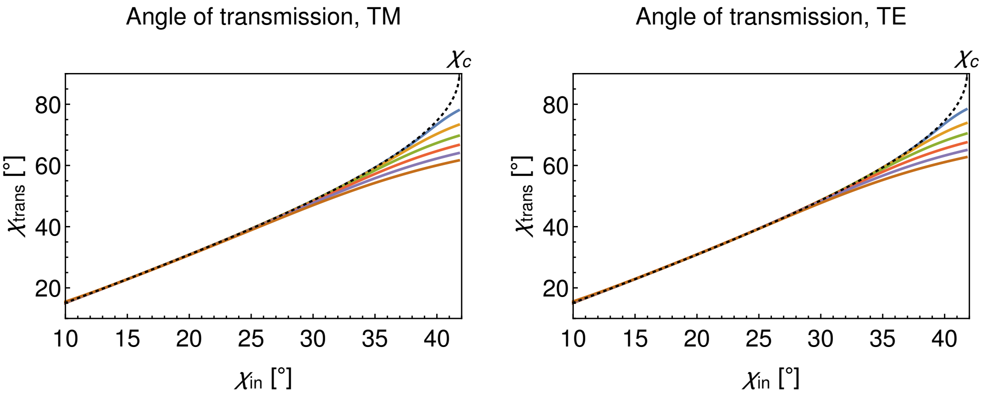

(a) TM polarization.

(b) TE polarization.

Figure 2.11: Angle of transmission as a function of the incident angle calculated from the expectation value Eq. (2.13) for different ϵ (colored lines, same colors as Fig. 2.10) in comparison to Snell's law (black dotted line) at a planar interface with relative refractive index $n = 1.5$.

With increasing angular spread of the incident beam the absolute value of the angular shift in transmission increases, just as the Fresnel filtering effect in reflection. Not only the absolute value of the shift becomes larger but also the range of incident angles, where the shift has a relevant contribution, increases. The correction terms are found to be rather large near critical incidence, $\Delta\chi_{\rm FF}^{\rm trans}(\chi_c) \approx 10°$ for the smallest angular spread up to $\Delta\chi_{\rm FF}^{\rm trans}(\chi_c) \approx 25°$ for the largest angular spread considered here. However, also the angle of transmission expected from Snell's law increases quickly when the incident angle approaches the critical angle. To make this point clearer we show the transmitted angle calculated from the expectation value approach in comparison with the angle of transmission expected from Snell's law in Fig. 2.11. Just as argued above, the transmitted beam of finite width never reaches transmission parallel to the interface ($\chi_{\rm trans} = 90°$) as there are always components transmitted to smaller angles

The Goos-Hänchen shift does not play a role in transmission. As there is no phase shift between the incident and the transmitted waves, *cf.* Fig. 2.3, there is no spatial shift of the transmitted beam. The importance of the phase shift can be seen already in the simple derivation of the Artmann result, see. Eq. (2.2), which is based solely on the phase difference under total internal reflection. This follows also from the definitions of the expectation values in Eq. (2.6) and Eq. (2.7) which give a nonzero value only if there is an additional phase introduced in the definition of the spatial beam profiles Eq. (2.3) and Eq. (2.5).

2.3 Breaking of ray-path reversibility

In geometrical optics the path of a light ray propagating in dielectric media is perfectly reversible. The law of reflection and Snell's law do not distinguish between the directions in which the path is traversed. In reality, however, every light beam has a finite width and, thus, experiences the beam shifts discussed above.

Imagine an incident beam with central angle of incidence at the critical angle. Under reflection, this beam suffers relatively large beam shifts, especially, the angle of reflection becomes larger than the critical angle due to the Fresnel filtering effect. Inverting now the direction and taking the reflected part of the beam as new incident beam, this beam will experience only small beam shifts under reflection as its incident angle is now above critical incidence. In consequence, the new reflected beam, called back-reflected beam in the following, does not coincide with the original incident beam. This effect can be interpreted as non-Hamiltonian, *i.e.*, not time-symmetric dynamics [57].

2.3.1 Profiles of the incident, reflected and back-reflected beams

This behavior will be studied in more detail here for the reflection at a planar interface. The coordinate system used to this end is given by the z-direction along the boundary and the y-direction perpendicular to the boundary with the origin set to the point where the center of the incident beam hits the interface as shown in Fig. 2.12. All lengths will be given in units of the wavelength in the following.

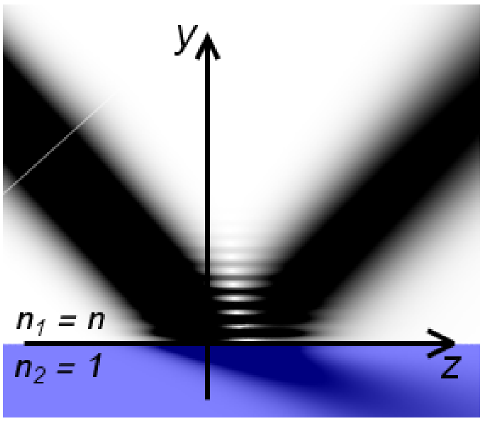

Figure 2.12: Definition of the coordinate system used in this section. The z-direction points along the boundary and the y-direction perpendicular to the boundary with the origin set to the point where the center of the incident beam hits the interface. Gaussian beam figure courtesy of J. Kreismann.

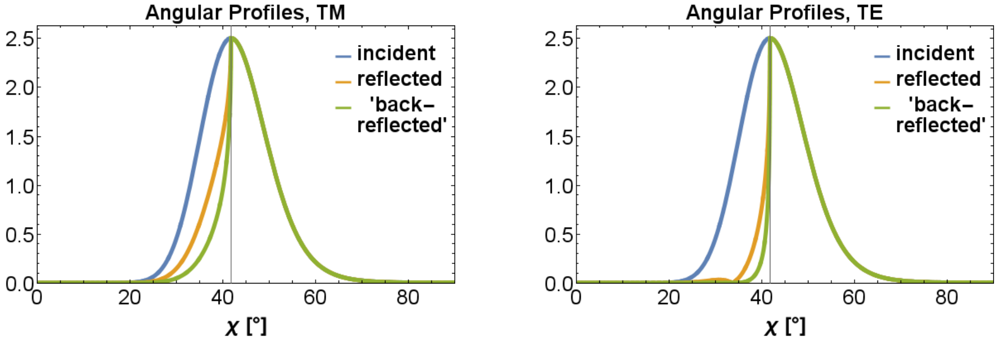

(a) TM polarization.

(b) TE polarization.

Figure 2.13: Angular beam profiles of incident (blue), reflected (orange) and back-reflected (green) beam as defined in the text for reflection at a planar interface with relative refractive index $n = 1.5$. The incident profile is a Gaussian defined in Eq. (2.11) with central k_z-component corresponding to angle of incidence $\chi_{\mathrm{in}} = \chi_c \approx 41.8°$ and angular spread ϵ corresponding to the real space width $w_0 = 5\lambda$ according to Eq. (2.12).

The incident beam profile in momentum space is $e_I(k_z)$ and the reflected profile $e_R(k_z)$ is obtained by applying the Fresnel reflection coefficients given in Eq. (2.4), $e_R(k_z) = \rho(k_z)e_I(k_z)$. Now, the direction of time is supposed to be reversed and the reflected beam is taken to be the new incident beam. This implies that the angular beam profile of the new incident beam is the same as the reflected profile, $e_{I2}(k_z) = e_R(k_z)$. The angular profile of the back-reflected beam, the reflection of the new incident beam, is obtained by applying the Fresnel coefficients again, $e_B(k_z) = \rho(k_z)e_{I2}(k_z) = \rho(k_z)^2 e_I(k_z)$.

For an illustration, the incident angular beam profile is chosen to be the Gaussian profile given in Eq. (2.11). The incident profile and the real parts of the resulting reflected and back-reflected profiles at the boundary are shown in Fig. 2.13 for both polarizations, TM and TE. Here, the central angle of incidence is chosen to be the critical angle of incidence. For all illustrations throughout this section, the relative refractive index is $n = 1.5$ and the width of the profile is $w_0 = 5\lambda$.

The corresponding spatial beam profiles at the interface are given by the Fourier transform of the angular profiles as explained in section 2.2. Analogously to Eq. (2.3) and (2.5), the spatial beam profiles of the incident and reflected beams are

$$\begin{aligned} E_I(z) &= \int \mathrm{d}k_z\, e_I(k_z)\mathrm{e}^{\mathrm{i}k_z z} \\ E_R(z) &= \int \mathrm{d}k_z\, e_R(k_z)\mathrm{e}^{\mathrm{i}k_z z} = \int \mathrm{d}k_z\, \rho(k_z)e_I(k_z)\mathrm{e}^{\mathrm{i}k_z z}. \end{aligned} \tag{2.15}$$

In the definition of the coordinate system, the origin of the z-axis has been

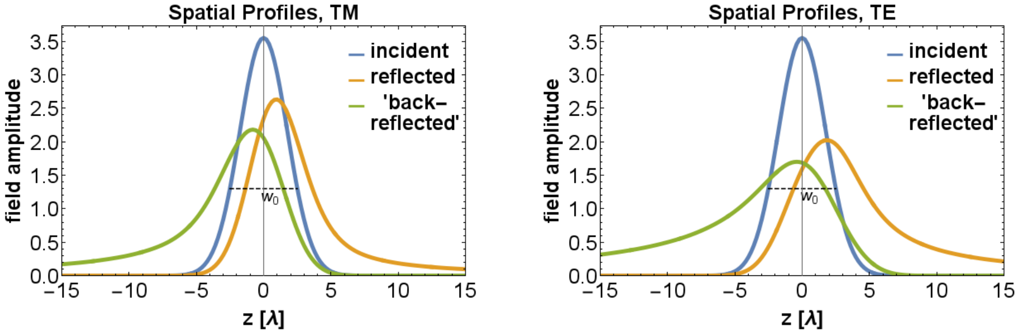

(a) TM polarization.

(b) TE polarization.

Figure 2.14: Spatial beam profiles at the boundary of incident (blue), reflected (orange) and back-reflected (green) beam as defined in Eq. (2.15) and (2.16), respectively, with the angular profiles shown in Fig. 2.13. The width $w_0 = 5\lambda$, corresponding to the standard deviation, of the original beam is marked with a dashed line.

chosen to coincide with the expectation value of the incident beam. This has to be taken into account in the definition of the new incident beam as the z-expectation value of the reflected beam might be shifted with respect to the original incident beam. This shift is just the Goos-Hänchen shift D_{GH} defined in Eq. (2.8). Thus, the spatial beam profiles of the new incident beam and the back-reflected beam are given by the Fourier transform with a shift from $z = 0$ to $z = D_{\mathrm{GH}}$

$$\begin{aligned} E_{I2}(z) &= \int \mathrm{d}k_z \, e_{I2}(k_z) \mathrm{e}^{-\mathrm{i}k_z(z-D_{\mathrm{GH}})} = \int \mathrm{d}k_z \, \rho(k_z) e_I(k_z) \mathrm{e}^{-\mathrm{i}k_z(z-D_{\mathrm{GH}})} \\ E_B(z) &= \int \mathrm{d}k_z \, e_B(k_z) \mathrm{e}^{-\mathrm{i}k_z(z-D_{\mathrm{GH}})} = \int \mathrm{d}k_z \, \rho(k_z)^2 e_I(k_z) \mathrm{e}^{-\mathrm{i}k_z(z-D_{\mathrm{GH}})} \end{aligned} \tag{2.16}$$

where the change in sign in the exponent accounts for the change in direction compared to the original incident and reflected beams in Eq. (2.15). The spatial beam profiles resulting from the exemplary angular profiles are shown in Fig. 2.14.

From these examples, it can be seen that the beam profiles of the incident and the back-reflected beam no longer coincide. Hence, the rays corresponding to these beams differ in their direction as well as in their central position at the boundary. Due to the Brewster angle feature in the reflection coefficient for TE-polarized light, which can be clearly seen in the reflected and back-reflected angular profiles shown in Fig. 2.13(b), the deviations are larger for TE-polarized beams than for TM-polarized ones.

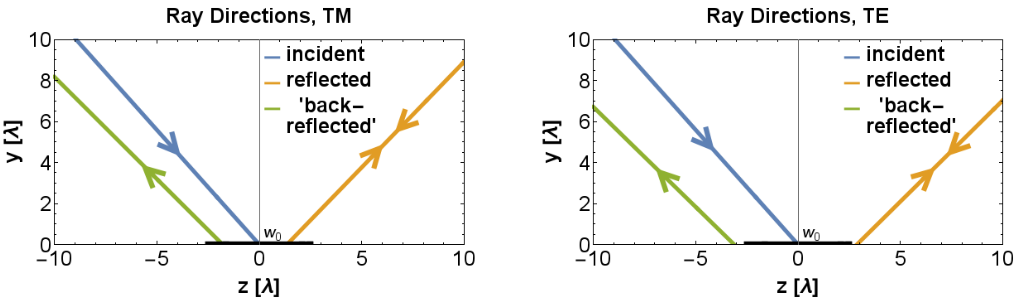

(a) TM polarization.

(b) TE polarization.

Figure 2.15: Incident (blue), reflected (orange) and back-reflected (green) rays inferred with Eq. (2.17) from the angular and spatial beam profiles shown in Fig. 2.13 and 2.14, respectively. For comparison of the shifts, the width w_0 of the original beam is marked with a black bar along the z-axis.

2.3.2 Directions of incident, reflected and back-reflected rays

The rays corresponding to the beam profiles can be inferred from the expectation values, in the same sense as the beam shifts have been defined previously. The direction of the ray can be obtained from the expectation value of k_z of the angular profile where the incident profile has been chosen initially such that its angular expectation value corresponds to the central angle of incidence. The central point at the boundary is given by the expectation value of z of the spatial profile where the origin of the z-axis is chosen to coincide with the expectation value of the incident spatial profile. Hence, the rays defined by their (y, z)-coordinates are

$$\begin{aligned} y_I(z) &= -z\cot(\chi_{\text{in}}) \\ y_R(z) &= (z - z_R)\cot(\chi_{\text{ref}}) \\ y_B(z) &= -(z - z_B)\cot(\chi_{\text{back}}). \end{aligned} \tag{2.17}$$

With the definitions of the Goos-Hänchen shift and the Fresnel filtering, one immediately obtains $z_R = D_{\text{GH}}$ and $\chi_{\text{ref}} = \chi_{\text{in}} + \Delta\chi_{\text{FF}}$. The parameter $z_B = \langle z \rangle_{\text{back}}$ is the spatial expectation value of the back-reflected beam analogous to Eq. (2.6) or Eq. (2.7), χ_{back} is obtained from the corresponding momentum expectation $\langle p \rangle_{\text{back}}$ value analogous to Eq. (2.9) or Eq. (2.10).

The ray directions resulting from the exemplary beam profiles discussed above are shown in Fig. 2.15. The deviation of the back-reflected ray from the incident ray is clearly seen. As expected from the distortions of the beam profiles, the ray directions for the TE case are subject to larger shifts than those for the TM case.

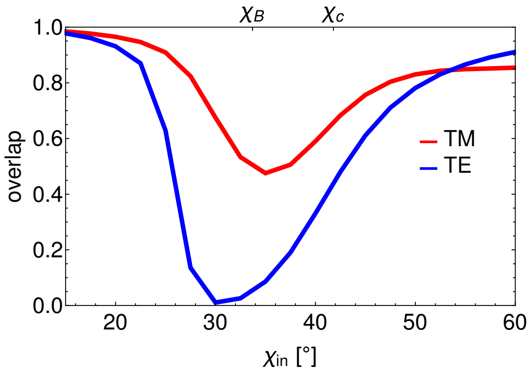

Figure 2.16: Spatial overlap $\mathcal{I}$ of incident and back-reflected beam at the boundary as a function of the angle of incidence χ_{in}. The overlap is calculated according to Eq. (2.18) for both polarizations, TM (red) and TE (blue), with the same incident profile as in the previous figures of this section, however, now with varying angle of incidence.

2.3.3 Measuring the irreversibility

As a measure of the irreversibility of the reflection of a light beam at a dielectric interface one can look at the overlap between the incident and the back-reflected beam. First, the overlap is examined directly at the interface $(y = 0, z)$. It is given by

$$\mathcal{I} = \frac{\left|\int \mathrm{d}z \, E_I^*(z) E_B(z)\right|^2}{\int \mathrm{d}z \, |E_I(z)|^2 \int \mathrm{d}z \, |E_B(z)|^2}. \tag{2.18}$$

The normalization assures that $\mathcal{I} = 1$ if the shapes of the incident and back-reflected beam profiles are identical. Hence, the intensity loss due to refraction is not taken into account here. The light-path is assumed to be perfectly reversible, expressed as $\mathcal{I} = 1$, if the rays calculated from the incident and back-reflected beam profiles are equal although the intensity of the back-reflected light might be lower than the incident intensity.

The overlap at the interface as a function of the incident angle is shown in Fig. 2.16. In this example the same incident profile is used as in the examples above, however, now with varying angle of incidence. It can be seen that the overlap reflects the angular dependence of the beam shifts. It is close to 1 where both beam shift effects are small and decreases for angles where the beam shifts are large. Consequently, the reversibility is most strongly violated for beams with originally critical incidence where both beam shift effects have the largest contribution.

So far, only the beam profiles directly at the interface have been defined, not the beams away from the boundary. To calculate the overlap of the beams also as a function of the distance from the boundary, an approximation to the real beams is used. It is assumed that the transverse profile does not change as

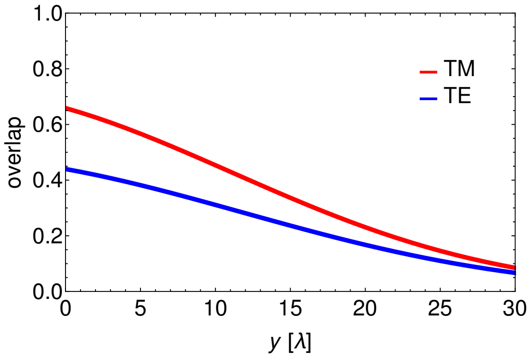

Figure 2.17: Spatial overlap $\mathcal{I}(y)$ of incident ($\chi_{\text{in}} = \chi_c$) and back-reflected beam as a function of the distance from the interface y. The overlap is calculated according to Eq. (2.19) for both polarizations, TM (red) and TE (blue), with the same original incident profile with critical incidence as in the previous figures.

the beam propagates towards or away from the boundary. Hence, the overlap as a function of the distance y from the boundary can be calculated as

$$\mathcal{I}(y) = \frac{\left|\int \mathrm{d}z\, E_I^*(z) E_B(z + \Delta z(y))\right|^2}{\int \mathrm{d}z\ |E_I(z)|^2 \int \mathrm{d}z\ |E_B(z + \Delta z(y))|^2} \tag{2.19}$$

where $\Delta z(y) = y(\tan(\chi_{\text{back}}) - \tan(\chi_{\text{in}}))$ is the change in distance between the incident and back-reflected ray according to Eq. (2.17). This approximation, of course, neglects the dispersion of the beams. Thus, it is applicable only for small distances from the interface where the dispersion can be assumed to be small.

The overlap $\mathcal{I}(y)$ as a function of the distance y from the interface is shown in Fig. 2.17 calculated for the same original incident profile with critical incidence as before. In the dependency of the overlap on the distance, the contributions of the two beam shift effects can be seen. If the Goos-Hänchen shift is large, which is the case in this example with critical incidence, the overlap is smaller than 1 already directly at the interface, *i.e.* for $y = 0$. The angular deflection due to the Fresnel filtering effect leads to decreasing overlap with increasing distance from the boundary.

Finally, in Fig. 2.18, the spatial overlap of incident and back-reflected beam is depicted with the combined dependencies on both, the initial angle of incidence χ_{in} and the distance from the boundary y. For small angles of incidence, the Goos-Hänchen shift vanishes but the Fresnel filtering has a finite, though small, contribution. This leads to the overlap being nearly unity for $y = 0$ and decreasing for $y > 0$. For incidence around the critical angle, both effects play a role and the overlap is small already directly at the boundary and decreases further with increasing distance. For even larger angles, in the regime of total internal reflection where the Fresnel filtering effect vanishes and only the

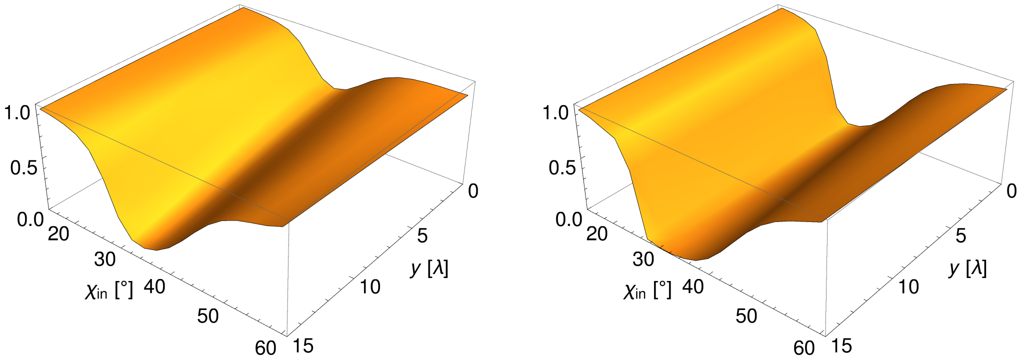

(a) TM polarization.

(b) TE polarization.

Figure 2.18: Spatial overlap $\mathcal{I}$ of incident and back-reflected beam as a function of the incident angle χ_{in} and of the distance from the interface y. The overlap is calculated according to Eq. (2.19). The incident profile is a Gaussian defined in Eq. (2.11) with varying central k_z-component corresponding to the angle of incidence.

Goos-Hänchen shift contributes, the overlap is smaller than 1 and stays nearly constant for all distances.

In conclusion, the spatial overlap of incident and back-reflected beam can be seen as a combined measure of the wave-corrections to ray optics. Both beam shift contributions, the lateral displacement due to the Goos-Hänchen shift and the angular deflection due to the Fresnel filtering effect, are represented in this single quantity.

2.4 Beam shifts at curved interfaces

An increasing number of computations [79, 80] and experiments [55, 56, 59, 81] find deviations from the naive ray model and emphasize the importance of wave corrections in small dielectric cavities with curved boundaries.

At a curved interface, the same beam shift effects as for a planar interface, the Goos-Hänchen shift and the Fresnel filtering effect, occur. However, the boundary curvature strongly influences both effects. Some aspects of the interplay between boundary curvature and beam shifts have been studied previously. A general phase-space analysis of this problem is given in Ref. [64]. The influence of boundary curvature and the beam shifts on the far-field emission of a quadrupolar microcavity is discussed in Ref. [82]. In Ref. [79] the phase space structure of a Limaçon-shaped microcavity is examined with respect to the effects of the beam shifts at the curved interface.

Here, we will discuss the beam shifts at curved interfaces more generally and thoroughly. The section starts with a qualitative discussion of the influence of curvature in an intuitive picture of the beam shifts. Then, quantitative expressions for the correction terms are derived using a similar expectation value approach as in the planar case. With these expressions at hand, we study the effect of curvature systematically.

2.4.1 Intuitive picture

A schematic picture of the beam shift effects at a convexly curved interface between two different dielectric materials is shown in Fig. 2.19. In our notation, a convex interface is defined by the interface seen by a ray that travels inside a circle. In principle, the beam shifts at the curved interface can be intuitively understood in the same way as explained for the planar case in sections 2.2.1 and 2.2.2. However, there are two major differences induced by the boundary curvature.

On the one hand, the effective angle of incidence no longer equals the incident angle at the real interface. Rather, one finds $\chi_{\text{in}}^{\text{eff}} < \chi_{\text{in}}$ for a convexly curved boundary. As the Goos-Hänchen shift can still be approximated as $D_{\text{GH}} \approx 2\gamma \tan(\chi_{\text{in}}^{\text{eff}})$ it is expected to decrease with increasing curvature. Especially, the lateral shift at a convexly curved interface will be smaller than in the planar case if all other parameters are fixed. In this approximation, we have implied that the penetration depth γ is the same as in the planar case, in contrast to Ref. [83] where the Goos-Hänchen shift was assumed to be independent of the curvature. We think that it is justified to assume that γ is completely determined by the relative refractive index, the wavelength, and the incident angle and it does not depend on the curvature of the interface.

On the other hand, the angular spread of the incident plane wave components is effectively enhanced due to the curvature. This will lead to an increased angular deflection due to the Fresnel filtering effect at curved interfaces compared to the result for planar interfaces. Further, the Fresnel filtering is

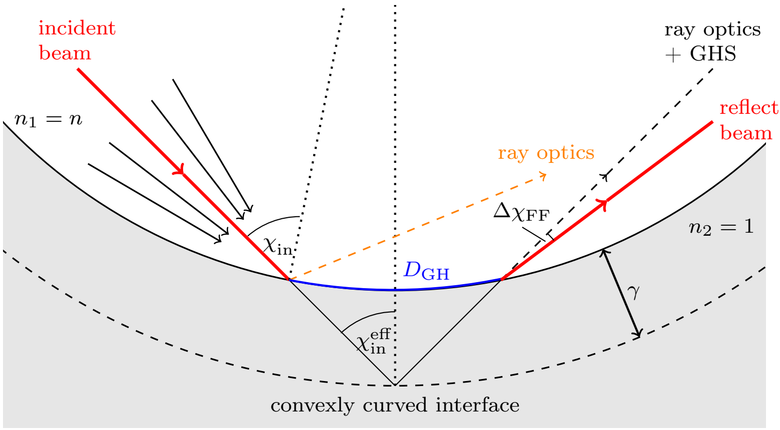

Figure 2.19: Schematic picture of the beam shifts at curved interfaces. Incident and reflected beam are shown in red. The relative refractive index is $n = n_1/n_2$. The effective interface is depicted as dashed line, γ is the penetration depth. The normals to the interface and the effective interface (dotted lines) define the angle of incidence χ_{in} and the effective angle of incidence $\chi_{\text{in}}^{\text{eff}}$. The reflected beam predicted from ray optics is shown as dashed orange arrow. The lateral shift along the interface D_{GH} due to the Goos-Hänchen effect (blue) and the angular deflection $\Delta\chi_{\text{FF}}$ due to the Fresnel filtering effect are marked.

expected to increase with increasing curvature. These qualitative predictions from the intuitive picture will be tested with a quantitative analysis in the following.

2.4.2 Corrected reflection coefficients for curved interfaces

For curved interfaces, we concentrate on circularly symmetric systems with radius R as any curved boundary can be locally approximated by a circle. Due to the radial symmetry, polar coordinates (r, α) are used and cylinder functions, Bessel and Hankel functions, are the appropriate basis functions. In this case, angular momentum conservation leads to a relation between the angular wavenumber m of the cylinder function J_m and the angle of incidence χ [15, 83]

$$\sin(\chi) = \frac{m}{nkR}. \tag{2.20}$$

According to Ref. [83], the reflection coefficients at a convexly curved interface read

$$\rho_c = \frac{\cos(\chi) + i\mathcal{F}}{\cos(\chi) - i\mathcal{F}} \tag{2.21}$$

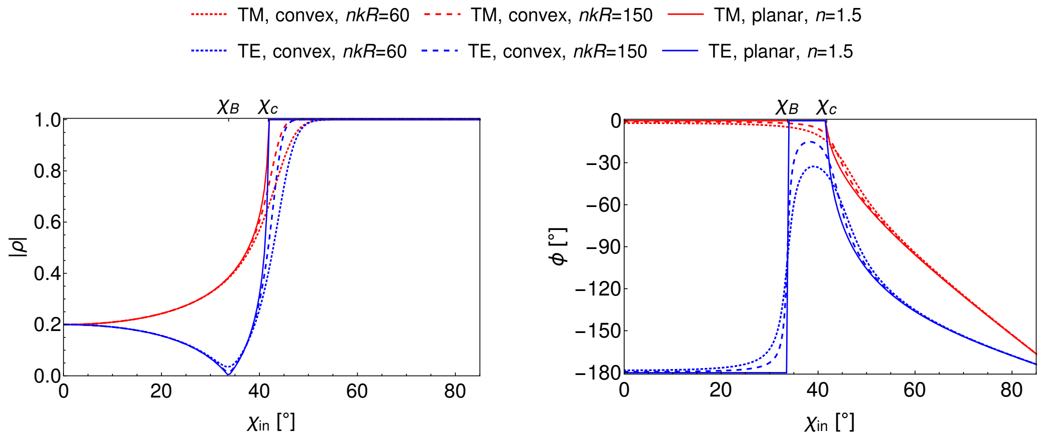

(b) Absolute value $|\rho|$ of the reflection coefficients $\rho = |\rho|e^{i\varphi}$.

(c) Phase φ of the reflection coefficients $\rho = |\rho|e^{i\varphi}$.

Figure 2.20: Reflection coefficients at curved (broken curves) and planar (solid curves) interfaces according to Eq. (2.21) and Eq. (2.4), respectively, for both polarizations, TM (red) and TE (blue). Relative refractive index $n = 1.5$ for the planar case, dimensionless size parameter $nkR = 150$ (dashed) and $nkR = 60$ (dotted) for the curved cases.

with

$$\mathcal{F}^{\mathrm{TE}} = n\frac{H_m^{(1)'}(kR)}{H_m^{(1)}(kR)} \quad \text{and} \quad \mathcal{F}^{\mathrm{TM}} = \frac{1}{n^2}\mathcal{F}^{\mathrm{TE}}$$

where $H_m^{(1)}$ is the Hankel function of the first kind and prime denotes the derivative with respect to the full argument. A comparison of the corrected reflection coefficients at curved interfaces with the usual Fresnel coefficients for planar interfaces according to Eq. (2.4) is shown in Fig. 2.20.

The most important difference between the reflection coefficients for planar and curved interfaces is the fact that the critical angle and, for TE polarization, also the Brewster angle are no longer sharp features in the curved case. Further, the onset of total internal reflection where $R = |\rho|^2 = 1$ is shifted to larger angles.

If we apply the Artmann formula for the Goos-Hänchen shift, Eq. (2.2), to the corrected reflection coefficients we obtain a first approximation for the lateral shift of the reflected beam at a curved boundary. We write the reflection coefficients $\rho_c(m) = |\rho(m)|e^{i\varphi(m)}$. Then, the equivalent of the Artmann formula Eq. (2.2) for the curved interface reads

$$\frac{\Delta s}{\lambda} = \frac{nkR}{2\pi}\frac{d\varphi(m)}{dm}. \tag{2.22}$$

The resulting shifts along the boundary are shown in Fig. 2.21 for two different size parameters, $nkR = 30$ and $nkR = 60$. In the regime of total internal

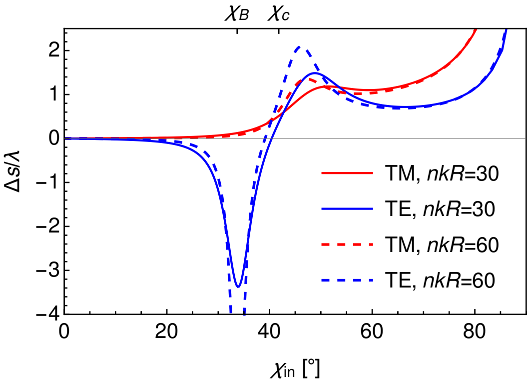

Figure 2.21: First order approximation of the Goos-Hänchen shift at curved interfaces according to Eq. (2.22) resulting from the corrected reflection coefficients for two different size parameters, $nkR = 30$ and $nkR = 60$, with relative refractive index $n = 1.5$.

reflection, the behavior of the original Artmann result at planar interfaces (see Eq. (2.2) and Fig. 2.2) and the analogous result at curved interfaces is very similar. At the critical angle and in the regime of partial transmission the results differ considerably. As the corrected reflection coefficients show no sharp kink at the critical angle the approximation for the Goos-Hänchen shift shows no singularity there, rather it exhibits a finite value at the critical angle. Further, the shift is nonzero also below the critical angle because the corrected reflection coefficients have a non-trivial phase even in the regime of partial transmission. Although the Artmann result for the lateral shift under reflection at curved interfaces does not show the unphysical divergence at the critical angle which is found for the planar case, *cf.* Eq. (2.2) and Fig. 2.2, it is still a first-order approximation. As such, it does not capture the influence of the beam width.

Most strikingly, the Goos-Hänchen shift becomes negative in the case of TE polarization near the Brewster angle which is easily explained by the behavior of the phase of the corrected reflection coefficient near the Brewster angle. For the reflection of a light beam at a planar interface between two normal dielectric materials, however, the lateral shift of the reflected beam cannot become negative because of energy conservation, see *e.g.* [84]. Negative Goos-Hänchen shift near the Brewster angle at curved interfaces has been reported previously for electromagnetic wave simulations [80], however, without any physical explanation.

2.4.3 Beam shifts as expectation values

Analogously to the expectation value approach for the beam shifts at planar interfaces, the beam shifts at convexly curved interfaces can be defined as expectation values [48]. Here, we make use of the circular symmetry and the

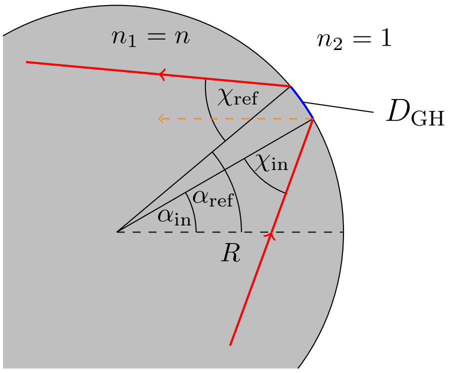

Figure 2.22: Schematics of a reflection at the inner boundary of a circle with radius R and relative refractive index $n = n_1/n_2$ defining the angles of incidence and reflection, $\chi_{\rm in}$ and $\chi_{\rm ref}$, respectively. The polar angles $\alpha_{\rm in}$ and $\alpha_{\rm ref}$ define the position of incidence and reflection at the boundary, their difference leads to the lateral shift $D_{\rm GH}$ along the boundary.

corrected Fresnel coefficients. The notation used here is clarified in Fig. 2.22.

The beams are conveniently expanded in polar coordinates (r, α) using Bessel functions. The incident light beam at the interface $r = R$, then, is

$$E_I(\alpha) = \sum_m e_I(m) \mathrm{e}^{\mathrm{i}m\alpha} J_m(nkR). \tag{2.23}$$

The transverse beam profile in angular momentum space $e_I(m)$ is chosen to be a narrow distribution in m with expectation value at the central angular wavenumber m_0 corresponding to $\chi_{\rm in}$ using Eq. (2.20), $\sin(\chi_{\rm in}) = m_0/(nkR)$. The reflected beam is obtained by applying the corrected Fresnel reflection coefficients for convexly curved interfaces given in Eq. (2.21) to the incident beam profile, $e_R(m) = \rho_c(m) e_I(m)$, giving

$$E_R(\alpha) = \sum_m e_R(m) \mathrm{e}^{\mathrm{i}m\alpha} J_m(nkR). \tag{2.24}$$

Here, the beam shifts are obtained from the expectation values of the polar angle and the angular wavenumber. The mean position of incidence on the boundary is given by the expectation value of the polar angle α with respect to the incident beam

$$\langle\alpha\rangle_{\rm in} = \frac{\int_{-\pi}^{\pi} \mathrm{d}\alpha\, E_I^*(\alpha)\, \alpha\, E_I(\alpha)}{\int_{-\pi}^{\pi} \mathrm{d}\alpha\, E_I^*(\alpha) E_I(\alpha)}. \tag{2.25}$$

Correspondingly, the mean position of reflection of the beam is given by the α-expectation value of the reflected beam profile

$$\langle\alpha\rangle_{\rm ref} = \frac{\int_{-\pi}^{\pi} \mathrm{d}\alpha\, E_R^*(\alpha)\, \alpha\, E_R(\alpha)}{\int_{-\pi}^{\pi} \mathrm{d}\alpha\, E_R^*(\alpha) E_R(\alpha)}. \tag{2.26}$$

The lateral shift D_{GH} along the interface, given in multiples of the vacuum wavelength λ, is obtained from the possible difference between the mean positions of reflection and incidence

$$\frac{D_{\mathrm{GH}}}{\lambda} = \frac{nkR}{2\pi}\left(\langle\alpha\rangle_{\mathrm{ref}} - \langle\alpha\rangle_{\mathrm{in}}\right). \tag{2.27}$$

If the incident beam profile is symmetric Eq. (2.25) yields $\langle\alpha\rangle_{\mathrm{in}} = 0$ and the position of incidence marks the origin of the polar angle. Hence, the expression for the Goos-Hänchen shift D_{GH} simplifies accordingly.

We can obtain the mean angles of incidence and reflection from the expectation values of the angular wavenumber. The expectation value of m with respect to the incident angular profile

$$\langle m\rangle_{\mathrm{in}} = \frac{\sum_m e_I^*(m)\, m\, e_I(m)}{\sum_m e_I^*(m) e_I(m)} \tag{2.28}$$

equals the mean angular wavenumber, $\langle m\rangle_{\mathrm{in}} = m_0$, corresponding to the chosen angle of incidence χ_{in} with $\chi_{\mathrm{in}} = m_0/(nkR)$. The angle of reflection χ_{ref} is obtained from the m-expectation value of the reflected angular profile

$$\langle m\rangle_{\mathrm{ref}} = \frac{\sum_m e_R^*(m)\, m\, e_R(m)}{\sum_m e_R^*(m) e_R(m)} = \frac{\sum_m m\, R(m)\, |e_I(m)|^2}{\sum_m R(m)\, |e_I(m)|^2} \tag{2.29}$$

with $\sin(\chi_{\mathrm{ref}}) = \langle m\rangle_{\mathrm{ref}}/(nkR)$. Equivalently to the planar case, the intensity transmission coefficient is $R(m) = |\rho_c(m)|^2$ The angular deflection due to the Fresnel filtering effect then is

$$\Delta\chi_{\mathrm{FF}} = \chi_{\mathrm{ref}} - \chi_{\mathrm{in}} = \arcsin\left(\frac{\langle m\rangle_{\mathrm{ref}}}{nkR}\right) - \arcsin\left(\frac{m_0}{nkR}\right). \tag{2.30}$$

Analogously to the beam shifts in transmission discussed for planar interfaces, the Fresnel filtering effect in transmission at a curved interface can be defined as

$$\langle m\rangle_{\mathrm{trans}} = \frac{\sum_m m\, T(m)\, |e_I(m)|^2}{\sum_m T(m)\, |e_I(m)|^2} \tag{2.31}$$

with the intensity transmission coefficient $T(m) = 1 - R(m)$. The angular shift $\Delta\chi_{\mathrm{FF}}^{\mathrm{trans}}$ is the difference between the mean angle of transmission calculated from the expectation value of the transmitted beam and the angle of transmission expected from Snell's law

$$\begin{aligned}\Delta\chi_{\mathrm{FF}}^{\mathrm{trans}} &= \chi_{\mathrm{trans}} - \arcsin(n\sin(\chi_{\mathrm{in}}))\\ &= \arcsin\left(\frac{\langle m\rangle_{\mathrm{trans}}}{kR}\right) - \arcsin\left(\frac{m_0}{kR}\right).\end{aligned} \tag{2.32}$$

For the evaluation of these formulas, as the transverse beam profile in angular momentum space we chose

$$e_I(m) = \frac{1}{\sqrt{2\pi}\sigma}\mathrm{e}^{-\frac{(m-m_0)^2}{2\sigma^2}} \tag{2.33}$$

which is a normal distribution in m with mean value m_0 and standard deviation σ similar to the Gaussian beam profile defined in Eq. (2.11) for planar interfaces.

2.4.4 Discussion of the results and comparison to wave simulations

As in the planar case (*cf.* section 2.2.4), the beam shifts calculated from the expectation value approach are compared to the beam shifts obtained from full electromagnetic wave simulations [48, 49, 77]. The beam waist w of the Gaussian beam in real space used in the simulation and the spread σ in terms of the angular wavenumber of the beam profile, defined in Eq. (2.33) and used in the analytical expectation value approach are connected by

$$\frac{w}{\lambda} = \frac{\sqrt{2}kR}{\pi\sigma}. \tag{2.34}$$

Note that σ is the width of the beam profile measured in the dimensionless angular wavenumber and not directly in the angular momentum. Therefore, the radius R has to appear explicitly in the conversion formula Eq. (2.34).

A comparison between the results of the FDTD simulations and the evaluation of the expectation value approach is presented in Fig. 2.23, where the Goos-Hänchen shift and the Fresnel filtering are shown for both polarizations (TE in blue, TM in red) as function of χ_{in}. For incident angles above the critical angle both approaches agree well. For smaller angles, the results of the simulations underestimate both effects, as in the planar case. Still, the agreement for the Fresnel filtering effect is reasonable. However, for the Goos-Hänchen shift the mismatch, here, is larger.

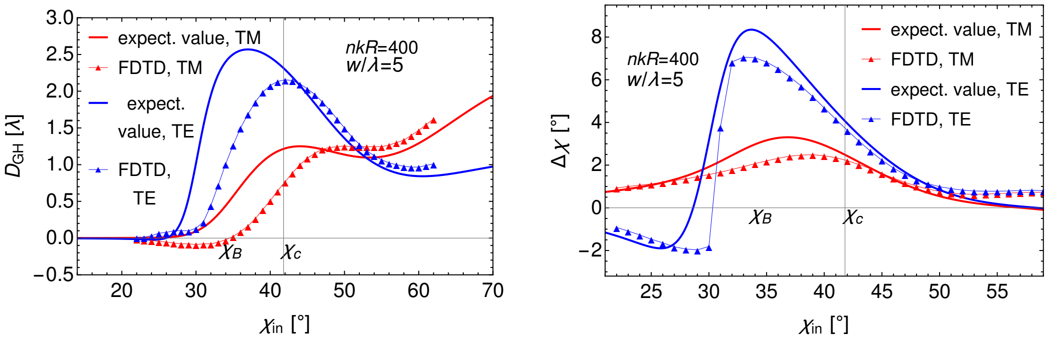

(a) Goos-Hänchen shift.

(b) Fresnel filtering.

Figure 2.23: Comparison between evaluation of the beam shift formulas (solid curve) and FDTD results (triangles, courtesy of J. Kreismann) for the beam shifts of a Gaussian beam reflected at a convexly curved interface for TM and TE polarization (red and blue, respectively); $nkR = 400$, $w/\lambda = 5$.

In addition to the problems that arise with the results of the simulations in the planar case (see the discussion in section 2.2.4), the boundary curvature introduces another difficulty. Consider two parallel rays intersecting a planar interface and a convexly curved interface, then, the distance of the two intersection points measured along the boundary is longer for the curved boundary. Thus, a slight error in the determination of the ray direction leads to a larger error in the inferred Goos-Hänchen shift at a curved interface than at a planar interface.

We find that both effects are on the same order of magnitude as in planar case. The Goos-Hänchen shift is slightly smaller than in the planar case, as expected from intuitive picture. It results in lateral shifts up to $D_{\mathrm{GH}} \approx 1.5\lambda$ for TM polarization and up to $D_{\mathrm{GH}} \approx 2.5\lambda$ for TE polarization. The Fresnel filtering effect is expected to be enhanced by the curvature but is found here to be almost identical compared to the planar case. Its values calculated from the expectation value approach lie between $\Delta\chi \approx -2^\circ$ and $\Delta\chi \approx 8.5^\circ$ for TE polarization and have a maximum at $\Delta\chi \approx 3.5^\circ$ for TM polarization. The influence of the curvature will be discussed in more detail in the next section, where we find that higher curvature does, indeed, enhance the angular shift.

2.4.5 Influence of curvature

To study the effect of curvature on the beam shifts at convexly curved interfaces we examine two different cases [48, 49]. Firstly, the radius of curvature R is changed while the angular spread σ is kept fixed, shown in Fig. 2.24. Secondly, in Fig. 2.25 the results are shown for the case when the curvature $\kappa = 1/R$ is changed while the beam width w/λ is fixed. An alternative presentation can be found in the appendix, Figs. B.2 and B.3.

The results confirm the predictions made in the intuitive picture. When the radius is decreased, the effective angle of incidence is lower, thus, the Goos-Hänchen shift decreases in both cases. For the Fresnel filtering effect, however, the situation is more involved. In the case of fixed angular spread in the beam, $\sigma =$ const. (Fig. 2.24), the effective angular spread with respect to the interface is increased at a more strongly curved interface. Hence, the angular shift $\Delta\chi_{\mathrm{FF}}$ increases with decreasing radius. In the case of fixed beam width,

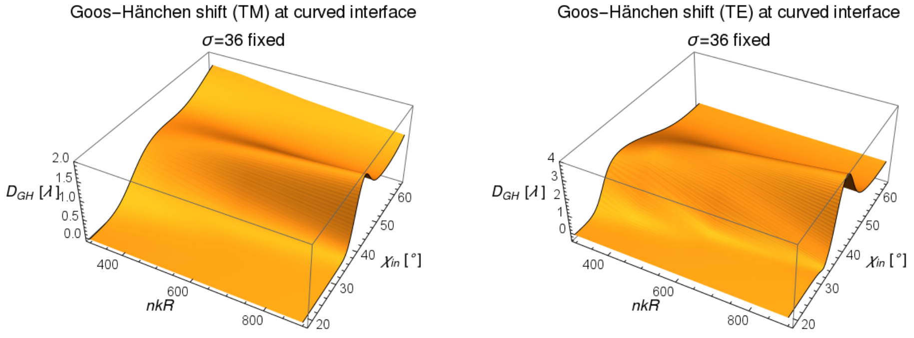

(a) TM polarization. (b) TE polarization.

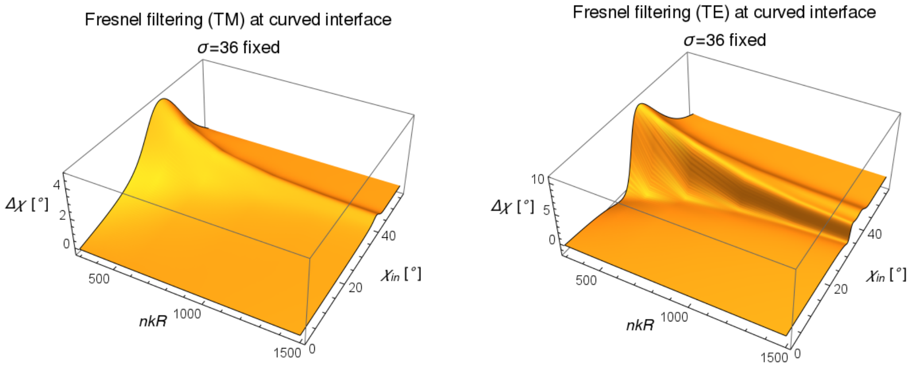

(c) TM polarization. (d) TE polarization.

Figure 2.24: Influence of angular spread on the Goos-Hänchen shift and the Fresnel filtering effect at convexly curved interfaces according to Eq. (2.27) and Eq. (2.30), respectively. Wavenumber k and angular spread $\sigma = 36$ are fixed while the curvature $\kappa = 1/R$ is varied. The relative refractive index is $n = 1.5$, $\chi_c \approx 41.8°$, $\chi_B \approx 33.7°$. An alternative presentation of this data can be found in Fig. B.2.

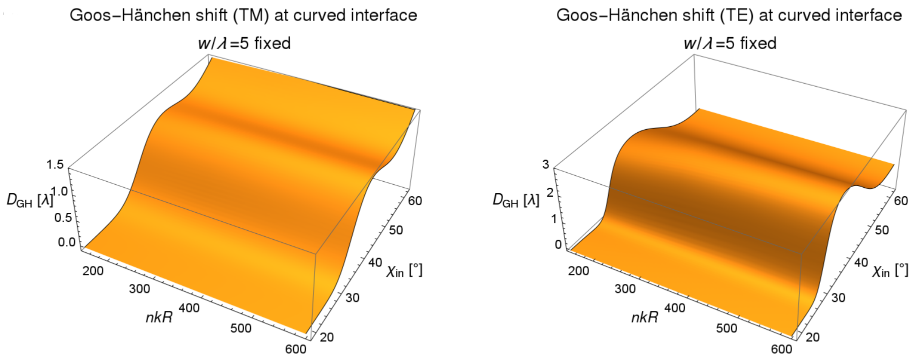

(a) TM polarization.

(b) TE polarization.

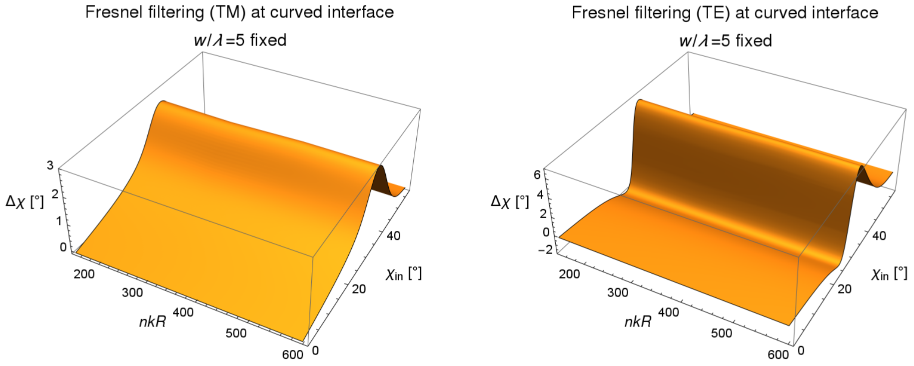

(c) TM polarization.

(d) TE polarization.

Figure 2.25: Influence of the beam width on the Goos-Hänchen shift and the Fresnel filtering effect at convexly curved interfaces according to Eq. (2.27) and Eq. (2.30), respectively. Wavenumber k and width $w/\lambda = 5$ are fixed while the curvature $\kappa = 1/R$ is varied. The relative refractive index is $n = 1.5$, $\chi_c \approx 41.8°$, $\chi_B \approx 33.7°$. An alternative presentation of this data can be found in Fig. B.3.

$w/\lambda =$ const. (Fig. 2.25), however, the angular spread σ changes, according to $w/\lambda = \sqrt{2}kR/(\pi\sigma)$, linearly with the radius of curvature when k and w/λ are fixed. Hence, the angular spread is increased by the same amount as the curvature is reduced. Consequently, the Fresnel filtering effect is unchanged in absolute size, only the position of the maximum is shifted and the features are broader for smaller R.

2.5 Conclusions

In this chapter, we have discussed the beam shift effects, Goos-Hänchen shift and Fresnel filtering, for planar and curved interfaces. If we want to include the correction terms in an amended ray-optical description of dielectric optical microcavities, it is important to know how the beam shifts affect the trajectories and the far-field emission.

One important consequence of including the beam shifts in the ray optics description is the loss of the reversibility of the ray trajectory due to the Fresnel filtering effect. The reflection of the time-reversed trajectory no longer coincides with the incident ray. We have studied this irreversibility using the beam profiles of a beam of finite width reflected at a dielectric interface. We suggest the overlap of the incident and the back-reflected beam profiles as a quantity to measure the amount of irreversibility. It is large if the reflection is reversible and vanishes if the back-reflected beam is completely different from the incident beam. This quantity can also be seen as a combined measure of the beam shift effects as its dependence on the incident angle and the distance from the boundary reflects both, the Goos-Hänchen shift and the Fresnel filtering effect.

In an amended ray-optics model of polygonal microcavities which have only planar boundaries, only the angular shift due to the Fresnel filtering effect plays a role as it affects the propagation direction of the trajectory and the emission direction. The Goos-Hänchen shift, on the contrary, leads only to a parallel shift of the trajectory but not to a change in direction, neither of the ray inside the cavity nor of the emission.

For systems with curved and mixed boundaries, both effects are important. The Fresnel filtering effect is of special importance here because it strongly increases with curvature. Hence, it can have a large impact on the trajectories and the prediction of the emission direction. We have found that the Goos-Hänchen shift is diminished at strongly curved interfaces, however, it still has to be taken into account in amended ray optics as the shift along a curved boundary also affects the direction of the resulting ray. Furthermore, with increasing boundary curvature, both effects are important in a larger range of incident angles and can play a role also far away from the critical angle.

We will apply the beam shifts, examined in detail here, to the two different cases, dielectric optical cavities with curved boundaries and polygonal cavities, in the following chapters. In the context of these examples, we will discuss the consequences of the beam shifts in more detail.

Chapter 3

Wave corrections applied to a ray optics description of deformed microdisks

In this chapter, we apply the ray-optical approach to deformed microdisks, *i.e.*, dielectric microcavities with a boundary defined by a curve that is a smooth deformation of a circle.

An important class of dielectric optical microcavities are quasi-two dimensional, convexly curved cavities, like circular disks [9], deformed disks as the Limaçon [27, 85, 86] or the quadrupole [82, 87], the spiral [55, 88], the stadium [89–91], and many other shapes [10, 15]. On the one hand, these systems are promising for applications as they can show important features, like directional emission and low-threshold lasing, on the other hand, they are interesting as model systems [1–3]. Smooth deformations of circular disks are especially important as they can be easily tuned from the circle with integrable classical dynamics to systems with partially or fully chaotic dynamics.

On the one hand, we apply the finite-wavelength corrections to ray optics at curved boundaries derived in the last chapter to different model systems and show their influence on the behavior of the systems. On the other hand, we discuss the differences that occur in the ray-optical description of chaotic and non-chaotic systems.

3.1 Amended ray-optics at curved interfaces

As an application of the beam shifts for curved interfaces we examine amended ray optics descriptions of dielectric microcavities with curved boundaries here. If one wants to include corrections to the classical ray optics in that case, there arises the question how to correctly include the effect of the boundary curvature.

Ray optics is the limit $\lambda \to 0$ of electromagnetism. In this limit, every boundary appears flat. To correct for finite wavelength effects, however, the boundary curvature has to be taken into account. Several possibilities can be thought of to accomplish this task:

1. Use the corrected reflection coefficients for curved interfaces instead of the usual Fresnel coefficients.

2. Use the normal Fresnel coefficients, but include the beam shifts.

3. Use the corrected reflection coefficients and include the beam shifts.

The corrected reflection coefficients for curved interfaces implicitly introduce wave and curvature effects to the ray-description. Therefore, it was argued in Ref. [82] that it is sufficient to use the corrected reflection coefficients and it is not necessary to include the beam shifts explicitly to account for the finite wavelength effects. In this approach, the calculation of the reflected and transmitted rays still follows the principle rules of geometric optics, only the critical angle is shifted and the reflected and transmitted intensities differ from the planar case.

The second possibility follows the complementary line of thought. Including the beam shifts, introduces the wave and curvature effects explicitly by making corrections to the laws of reflection and refraction. It can be argued that all wave and curvature effects are captured by the beam shifts and, consequently, it is not necessary to use the corrected reflection and transmission coefficients to calculate the intensities. This method has been applied in Ref. [92] to an elliptical cavity, in Ref. [79] to a Limaçon-shaped cavity, and in Ref. [57] to a spiral and an annular cavity. In all these cases, however, only the trajectories and the modes of the cavity have been studied, not the far-field.

Here, we claim that more satisfactory results are obtained only by combining the two approaches. The beam shifts are needed to correct the directions of the rays and the corrected reflection and transmission coefficients are necessary to calculate the intensities at a curved dielectric interface.

We study the different ray-optical approaches with several examples. A circular cavity is used to illustrate the influence of the beam shifts on the ray dynamics. The different approaches, classical geometrical optics and the three possibilities for amended ray optics, are discussed in detail for a Limaçon-shaped cavity. Comparing the results from the ray model to experimental results suggests that indeed both corrections, the corrected reflection coefficients and the beam shifts, are necessary to obtain detailed agreement between ray optics and experiment. For an asymmetrically deformed cavity, we examine the interplay of the wave corrections with the deformation strength where very small deformations result in non-chaotic classical dynamics and larger deformations in partially chaotic classical dynamics.

The details about the implementation and the evaluation of the ray description of optical microcavities can be found in appendix A.

3.2 The circular cavity: Illustrating the effects of the beam shifts

Circular cavities are usually not of practical interest as they exhibit an isotropic emission pattern in the plane because of their radial symmetry. As the angular momentum is conserved in a circular disk, due to the symmetry, the angle of incidence stays the same along each trajectory. Hence, the classical billiards mapping becomes particularly simple, only the position on the boundary s changes, whereas, the momentum p is constant along each trajectory. Due to its simplicity, the circular cavity is, however, ideal to illustrate the influence of the wave corrections discussed in the previous chapter.

Sample trajectories resulting from classical geometric optics in a circular dielectric cavity with relative refractive index $n = 3$ are shown in Fig. 3.1 in real space and in phase space. The spatial coordinate is not given in terms of the arc length s along the boundary, but as the polar angle ϕ that parameterizes the boundary, $s = R\phi$. As the angle of incidence χ stays fixed for each trajectory, the phase space projections lie on the horizontal line $\sin(\chi) = \text{const}$. A trajectory that starts with an angle larger than the critical angle, *i.e.* above the critical line with $|\sin(\chi)| = 1/n$, is confined inside the cavity by total internal reflection for all times. A trajectory that starts with an angle smaller than the critical angle, *i.e.* in the so-called leaky region, the phase space region with $|\sin(\chi)| < 1/n$, will suffer refractive losses at each reflection.

Here, we want to illustrate the effect of the beam shifts on the ray dynamics. Therefore, we study for the circular cavity only the second possibility of amended ray optics discussed in the previous section. At each reflection Goos-

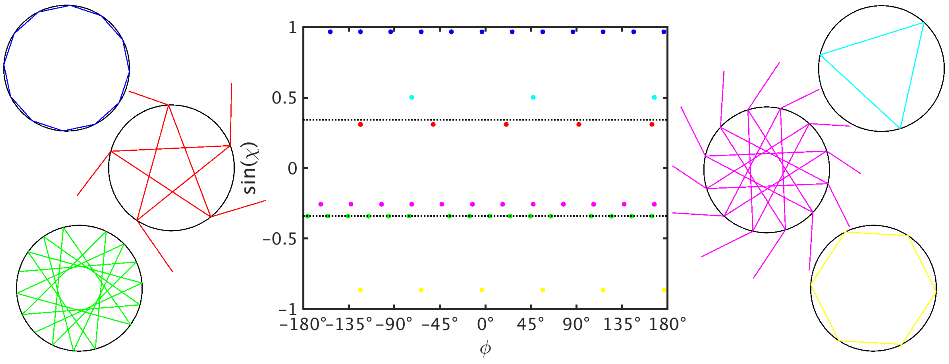

Figure 3.1: Trajectories and their phase space representation in a circular dielectric optical cavity with relative refractive index $n = 3$ resulting from classical ray optics (independent of polarization). The critical line $\sin(\chi_c) = 1/n$ is drawn as dashed line in the phase space plot. The colored dots in the phase space belong to the trajectory of the same color. Initial angles $\chi = 75°$ (blue), $30°$ (cyan), $18°$ (red), $-20°$ (green), $-15°$ (magenta), $-60°$ (yellow).

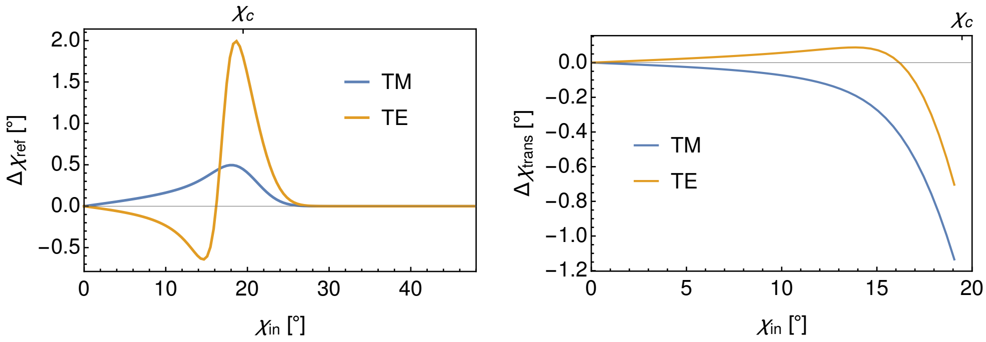

(a) Fresnel filtering in reflection according to Eq. (2.30).

(b) Fresnel filtering in transmission according to Eq. (2.32).

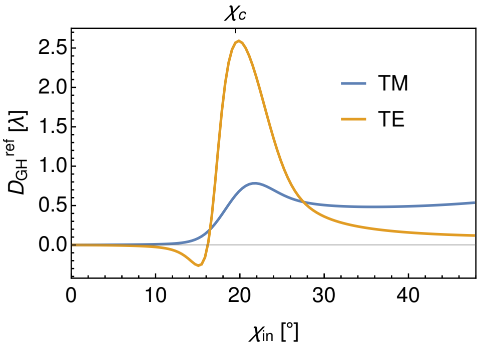

(c) Goos-Hänchen shift according to Eq. (2.27).

Figure 3.2: Beam shifts at a curved interface from the expectation value approach with dimensionless size parameter $kR = 50$, relative refractive index $n = 3$ ($\chi_c \approx 19.5°$, $\chi_B \approx 18.4°$), beam width $w/\lambda = 10$.

Hänchen shift and Fresnel filtering are included, the intensities are calculated with the normal Fresnel coefficients. The inclusion of the beam shifts, in particular the angular shift due to the Fresnel filtering effect, lifts the symmetry for a single ray trajectory. A ray model that includes the the correction terms does no longer conserve angular momentum.

The beam shifts that we use here for the amended ray optics description of the circular microcavity are shown in Fig. 3.2. They are calculated from the expectation value formulas Eq. (2.30) and (2.27) for the reflection of a Gaussian beam with width $w/\lambda = 10$ at a convexly curved interface with relative refractive index $n = 3$ and dimensionless size parameter $kR = 50$. For TE polarization, the Fresnel filtering in reflection ranges between $\Delta\chi_{\text{ref}} \approx -0.7°$ below the Brewster angle and $\Delta\chi_{\text{ref}} \approx 2°$ near the critical angle and in transmission between $\Delta\chi_{\text{trans}} \approx 0.1°$ and $\Delta\chi_{\text{trans}} \approx -0.6°$. The Goos-Hänchen shift amounts at most to $D_{\text{GH}} \approx 2.5\lambda$. For TM polarization, the maximum values of the Goos-Hänchen shift, $D_{\text{GH}} \approx 0.7\lambda$, and the Fresnel filtering in reflection, $\Delta\chi_{\text{ref}} \approx 0.5°$, are much smaller, whereas the Fresnel filtering effect in transmission is a bit stronger, $\Delta\chi_{\text{trans}} \approx -1.1°$ at most.

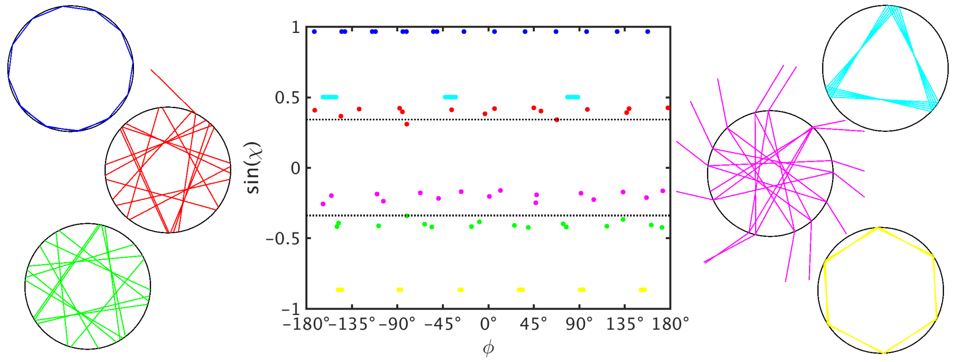

Figure 3.3: Trajectories and their phase space representation in a circular dielectric optical cavity with relative refractive index $n = 3$ and dimensionless size parameter $kR = 50$ resulting from amended ray optics for TE polarization including the beam shifts given in Fig. 3.2. The critical line $\sin(\chi_c) = 1/n$ is drawn as dashed line in the phase space plot. The colored dots in the phase space belong to the trajectory of the same color. Initial angles $\chi = 75°$ (blue), 30° (cyan), 18° (red), −20° (green), −15° (magenta), −60° (yellow) as in Fig. 3.1.

The rays with the same initial conditions as in Fig. 3.1 are now propagated through the circular cavity under the influence of the beam shifts for TE polarization. The resulting trajectories and their phase-space portraits are shown in Fig. 3.3. The perturbations due to the beam shift effects on the originally regular trajectories are clearly seen. In the phase space portrait, it is seen that the two effects act in the two distinct phase space directions [64]. The Goos-Hänchen shift yields a shift in the horizontal direction, only changing the position on the boundary, but not the angle. In contrast, the Fresnel filtering effect leads to a shift in the vertical direction, along the angular axis. Note that the conclusions are in principle the same for TM polarization, however, the effects are less pronounced.

To clarify the action of the beam shifts we, first, examine the trajectory with initial incident angle $\chi_{\text{in}} = 30°$ (cyan in Fig. 3.1 and 3.3). In the classical geometric optics, this is the periodic triangle orbit. Including the beam shifts breaks the periodicity. However, only the Goos-Hänchen shift has an influence on the trajectory as the Fresnel filtering effect has already dropped to zero for $\chi_{\text{in}} = 30°$. Thus, the angle of incidence is not changed and the phase-space projections of subsequent reflections are shifted only along the horizontal line $\sin(\chi_{\text{in}}) = \text{const}$. Second, we discuss the trajectory with initial incident angle $\chi_{\text{in}} = 18°$ (red in Fig. 3.1 and 3.3) which is close to the critical angle $\chi_c \approx 19.5°$. This trajectory suffers strong perturbations from both beam shift effects. It changes from the regular star-shaped orbit in the unperturbed case to a rather irregular, non-periodic trajectory. As the angular shift is positive in the relevant incident angle interval, the trajectory which started below the

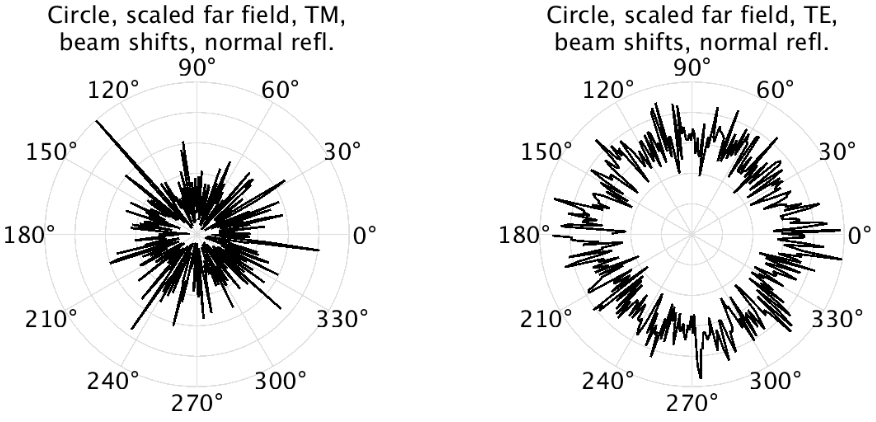

(a) TM polarization. (b) TE polarization.

Figure 3.4: Far-field emission of the circular cavity calculated from ray optics including the beam shifts of Fig. 3.2 for both polarizations.

critical line is shifted above the critical line after only one reflection. Hence, the inclusion of beam shifts leads to a better confinement of light in this case.

Now, we study the far-field emission. The emission of a circular cavity is expected to be isotropic in the plane due to the radial symmetry and the resulting conservation of angular momentum. Including the beam shifts in the ray description, however, lifts this symmetry for the single trajectory. Nevertheless, the far-field emission shown in Fig. 3.4 is still isotropic as it arises from many rays and the ensemble of rays still reflects the rotational symmetry.

3.3 The Limaçon cavity: Influence of the beam shifts on the far-field emission

We will discuss the different possibilities of including wave and curvature effects in a ray-optical description of dielectric optical microcavities using the example of a Limaçon-shaped cavity. Cavities with a boundary given by the Limaçon-curve are well studied both theoretically and experimentally [59, 85, 86, 93]. They are interesting because they combine modes with high quality factors, thus enabling low-threshold lasing, with directional emission [16, 27].

The Limaçon curve is a smooth deformation of a circle. It is given in polar coordinates

$$r(\phi) = R_0\,(1 + \epsilon\cos(\phi)) \tag{3.1}$$

with the mean radius R_0 and the deformation parameter $0 \leq \epsilon < 1$. The limiting cases are the circle of radius R_0 for $\epsilon = 0$ and the cardioid for $\epsilon = 1$ (blue and green curve in Fig. 3.5, respectively). The curve has the mirror symmetry $r(-\phi) = r(\phi)$.

The radius of curvature R_c is an important quantity when we want to consider curvature effects. For a curve $r(\phi)$ in polar coordinates it is given by (*cf.* Eq. (3.441) in [94])

$$R_\mathrm{c}(\phi) = \frac{(r^2 + r'^2)^{3/2}}{|r^2 + 2r'^2 - rr''|} \tag{3.2}$$

with $r'(\phi) = \frac{\mathrm{d}r}{\mathrm{d}\phi}$ and $r''(\phi) = \frac{\mathrm{d}^2 r}{\mathrm{d}\phi^2}$. The radius of curvature of exemplary Limaçon curves is shown in Fig. 3.5(b).

It has been shown that Limaçon-shaped cavities with deformations of approximately $0.4 < \epsilon < 0.5$ and relative refractive index $n \approx 3$ show unidi-

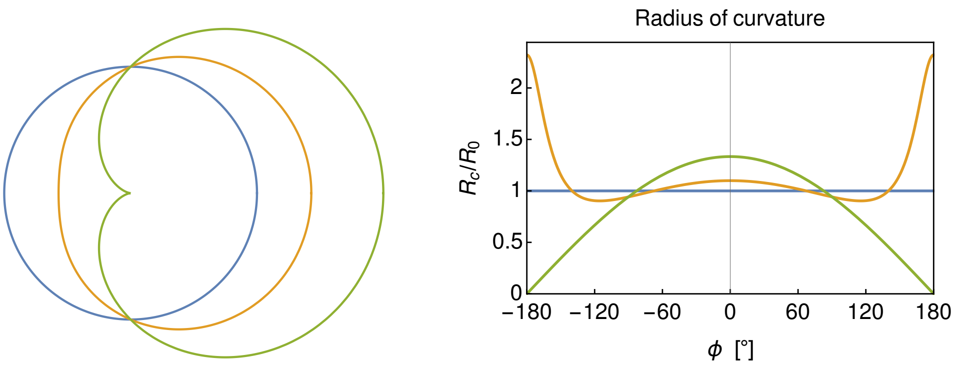

(a) Boundary curves $r(\phi)$.

(b) Radius of curvature $R_\mathrm{c}(\phi)$.

Figure 3.5: Limaçon curves according to Eq. (3.1) and their radii of curvature according to Eq. (3.2). The limiting cases with $\epsilon = 0$ (circle, blue) and $\epsilon = 1$ (cardioid, green) and a generic case with $\epsilon = 0.43$ (orange).

rectional emission [27]. Here, we will discuss a Limaçon-shaped cavity with $\epsilon = 0.43$ (shown in orange in Fig. 3.5) and relative refractive index $n = 3.3$ which is chosen to fit the study presented in [93]. The shape of this system is shown in orange in Fig. 3.5. Its radius of curvature is highest for $\phi = \pm 180°$ where it amounts to $R_{\text{max}} \approx 2.3 R_0$ and smallest, $R_{\text{min}} \approx 0.9 R_0$, for $\phi \approx \pm 115.5°$. For the chosen deformation parameter, the classical billiards dynamics of the Limaçon cavity is predominantly chaotic [27] in contrast to the integrable dynamics of the circle. Thus, almost every trajectory will at some point in time reach the leaky region where it is partly refracted out of the cavity. In particular, this is also true for trajectories started in the region of total internal reflection.

For dielectric optical microcavities with chaotic classical dynamics, it has been shown that the unstable manifold of the chaotic saddle determines the far-field emission pattern [10, 27, 89, 95, 96]. The chaotic saddle are those trajectories that never leave the cavity by refraction, neither in forward nor in backward time evolution, and its unstable manifold are the trajectories that converge to the chaotic saddle in backwards time evolution [97]. Therefore, the unstable manifold consists of trajectories which are confined inside the cavity by total internal reflection for a long time before they are eventually refracted out. The overlap of the unstable manifold with the leaky region, the region in phase space with $|\sin(\chi)| < 1/n$ where partial transmission is possible, determines the emission directions from the cavity.

In the following, the results from the different, classical and corrected, ray-optical approaches to the Limaçon-shaped cavity are presented, with special focus on the unstable manifold and the resulting far-field emission. As discussed in section 2.3, the inclusion of beam shifts to ray-optics breaks the principle of ray-path reversibility. To study this effect and its influence on the emission pattern, we evaluate the contributions of clockwise and counterclockwise propagating rays to the total far-field emission separately. Here, we use the convention that counterclockwise propagation corresponds to $\sin(\chi) > 0$.

3.3.1 Standard ray description: Fresnel reflection coefficients, no beam shifts

First, the standard geometrical optics description is applied to the Limaçon cavity, using the normal law of reflection, Snell's law for refraction and the standard Fresnel coefficients for the intensities. The intensity reflection coefficients for the relative refractive index $n = 3.3$ are given as solid curves in Fig. 3.6.

The resulting far-field emission pattern and the unstable manifold are shown in Fig. 3.7 and 3.8, respectively, for both polarizations, TM and TE. These results reproduce the findings of [27] which are also discussed in detail in [16]. For TE polarized light, emission with a strong directionality in the 0°-direction is found. Whereas, for TM polarized light, there are two additional,

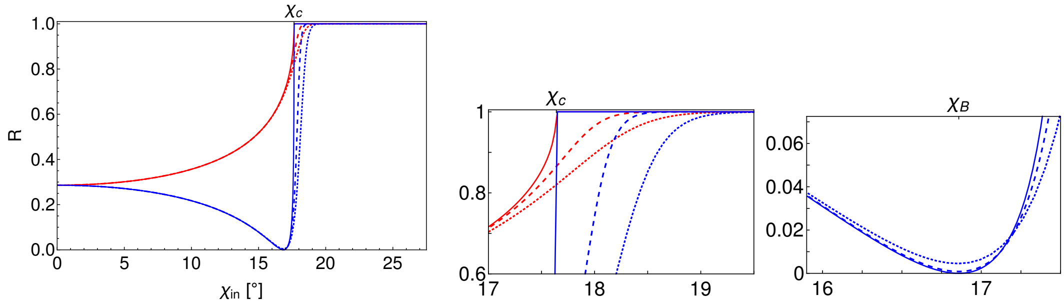

(a) Intensity reflection coefficients.

(b) Close-up around critical angle $\chi_c \approx 17.64°$ (left) and Brewster angle $\chi_B \approx 16.86°$ (right).

Figure 3.6: Intensity reflection coefficients at planar (solid) and curved (broken) interfaces according to Eq. (2.4) and Eq. (2.21), respectively, for TM (red) and TE (blue) polarization. Relative refractive index $n = 3.3$ for the planar case, dimensionless size parameter $nkR_{\text{max}} \approx 1126$ (dashed) and $nkR_{\text{min}} \approx 438$ (dotted) for the curved cases corresponding to the maximum and minimum radii of the Limaçon with $kR_0 = 147$ and $\epsilon = 0.43$.

symmetry related, emission peaks found at far-field angles of approximately 140° and 220° in addition to the emission peak in the 0°-direction.

The far-field emission is determined by the high intensity contributions of the unstable manifold in the leaky region. For TE polarization, only two significant contributions are found, one contribution around $\phi \approx -45°$ for $\sin(\chi) > 0$

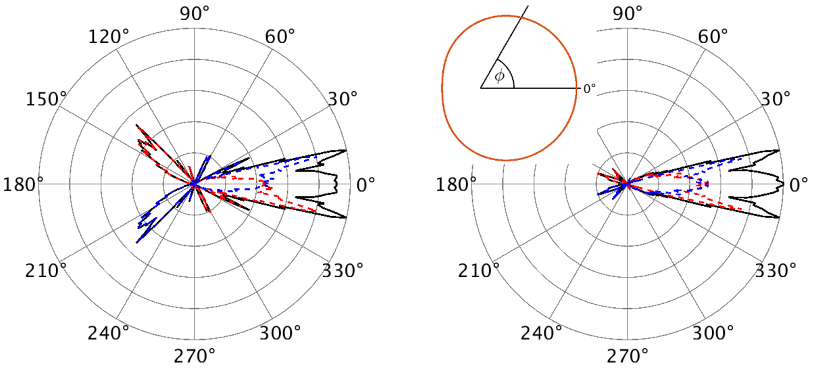

(a) TM polarization.

(b) TE polarization.

Figure 3.7: Far-field emission calculated from the classical ray optical description of a Limaçon cavity with $\epsilon = 0.43$, $n = 3.3$ for (a) TM and (b) TE polarization. The contributions of the clockwise (red, dashed) and counterclockwise (blue, dashed) propagating rays to the total far-field (black, solid) are indicated. The shape of the cavity and the definition of the far-field angle are shown as inset in the far-field plot for TE polarization.

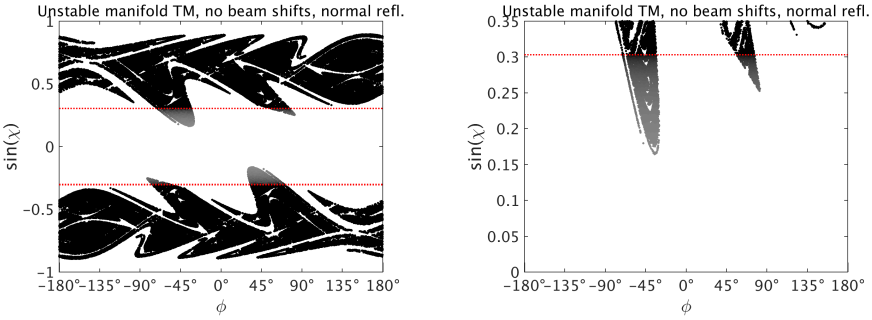

(a) TM polarization.

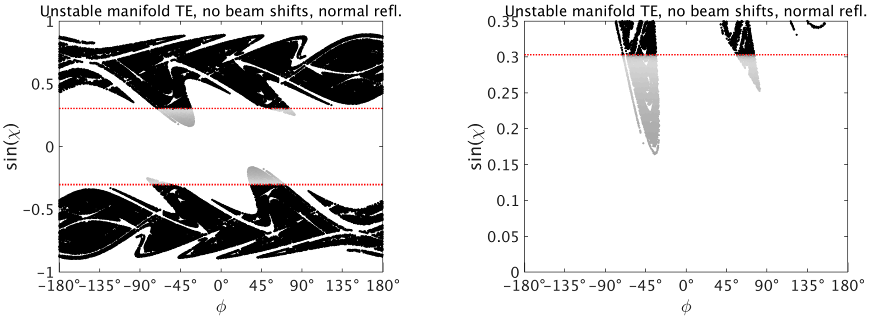

(b) TE polarization.

Figure 3.8: Fresnel weighted unstable manifold for (a) TM and (b) TE polarization resulting from the classical ray optical description of a Limaçon cavity with $\epsilon = 0.43$, $n = 3.3$. The critical line $\sin(\chi_c) = 1/n$ is marked as a red dotted line. *Left:* Full phase space. *Right:* Close-up for $0 \leq \sin(\chi) \leq 0.35$.

and the symmetry related counterpart around $\phi \approx 45°$ for $\sin(\chi) < 0$. These contributions lead to the emission in the 0°-direction. For TM polarization there are two additional significant contributions around $\phi \approx \pm 60°$ which are strongly suppressed in the TE case due to the Brewster angle [27]. They lead to the additional emission peaks in the directions $\phi \approx 140°$ and $\phi \approx 220°$.

Further, the contributions of clockwise (red, dashed) and counterclockwise (blue, dashed) rays are shown in the far-field plots, Fig. 3.7. As expected, the two contributions are related by the mirror symmetry of the system.

The predictions based on the ray-optical model have been impressively confirmed in experiments for both polarizations, TE [85, 93, 98] and TM [86]. However, especially in Ref. [93], the question was raised if the agreement between the ray optics predictions and the experimental results could be improved by including wave corrections in the ray-optical description.

3.3.2 Amended ray optics 1: Corrected reflection coefficients, no beam shifts

As the first correction to classical ray optics, the corrected reflection coefficients for curved interfaces according to Eq. (2.21) are used instead of the usual Fresnel coefficients. As the curvature is not constant along the Limaçon curve the reflection coefficients do not only depend on the angle of incidence but also on the position along the boundary. The resulting reflection coefficients for the maximum and minimum radius of curvature of the Limaçon, R_{max} and R_{min}, are given as broken curves in Fig. 3.6. Due to the large refractive index, $n = 3.3$, and the rather large size parameter, $kR_0 = 147$, of the cavity considered here, the deviations between the corrected and the standard reflection coefficients are not large but still noticeable, as seen in the close-ups around the Brewster angle and the critical angle Fig. 3.6(b).

The unstable manifold resulting from this amended ray optics description is shown in Fig. 3.9. The most important effect of the corrected reflection

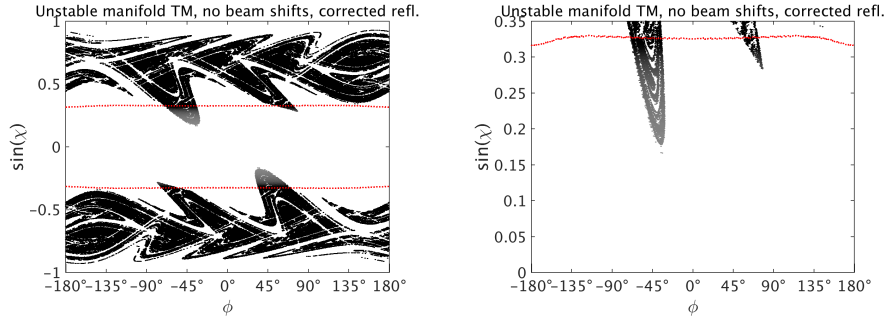

(a) TM polarization.

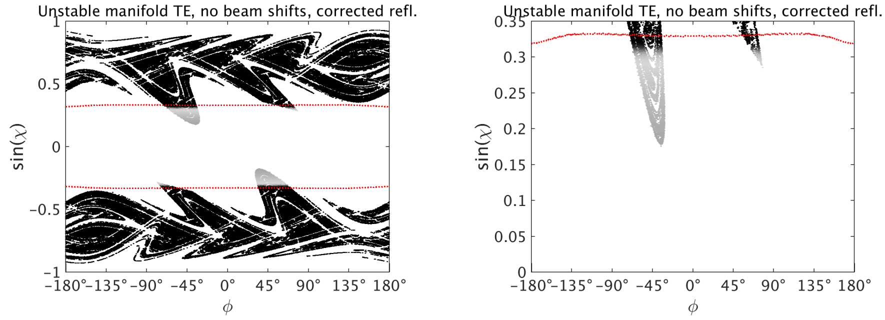

(b) TE polarization.

Figure 3.9: Fresnel weighted unstable manifold for (a) TM and (b) TE polarization resulting from the amended ray optical description of a Limaçon cavity with $\epsilon = 0.43$, $n = 3.3$, $kR_0 = 147$ using the corrected reflection coefficients for curved interfaces. The critical line resulting from the corrected reflection coefficients as a function of the position on the boundary is marked as a red dotted curve. *Left:* Full phase space. *Right:* Close-up for $0 \leq \sin(\chi) \leq 0.35$.

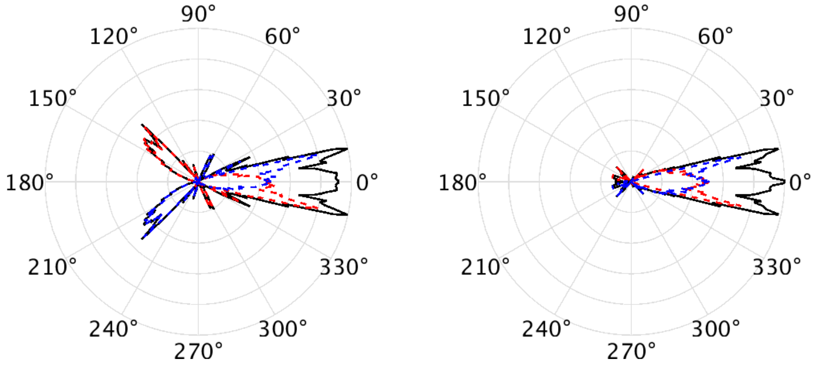

(a) TM polarization.

(b) TE polarization.

Figure 3.10: Far-field emission for (a) TM and (b) TE polarization calculated from the amended ray optical description of a Limaçon cavity with $\epsilon = 0.43$, $n = 3.3$, $kR_0 = 147$ using the corrected reflection coefficients for curved interfaces. The contributions of the clockwise (red, dashed) and counterclockwise (blue, dashed) propagating rays to the total far-field (black, solid) are indicated.

coefficients is the shift of the critical line denoting the onset of total internal reflection. Here, we define the regime of total internal reflection by $R > 0.999$. The critical line is shifted to higher absolute values of $|\sin(\chi)| > 1/n$. Further, the onset of total internal reflection depends on the local curvature. Thus, the critical angle is no longer constant for all polar angles ϕ and the critical line becomes curved. These corrections, however, do not strongly influence the overlap of the unstable manifold with the leaky region. Consequently, the far-field emission pattern, see Fig. 3.10, is not changed compared to the standard ray optics result.

Further, the reversibility of the rays is not affected by the reflection coefficients. Hence, we expect no change concerning the contributions of clockwise and counterclockwise propagating rays what is found in the results.

3.3.3 Amended ray optics 2: Fresnel reflection coefficients, beam shifts

In the second possibility to include wave corrections in the ray-optics description, usual Fresnel coefficients are used to calculate the intensities but Goos-Hänchen shift and Fresnel filtering are included at each reflection. The beam shifts from the expectation value approach suitable for the description of the chosen Limaçon cavity are shown in Fig. 3.11. They are calculated for a Gaussian transverse profile according to Eq. (2.33) with beam width $w/\lambda = 10$ and for the mean radius R_0 of the Limaçon curve. They would change only slightly between the minimum and the maximum radius, thus, the approximation with the mean radius is justified.

For TE polarization, the values of the Fresnel filtering in reflection range between $\Delta\chi_{\text{ref}} \approx -0.5°$ below the Brewster angle and $\Delta\chi_{\text{ref}} \approx 1.8°$ near the critical angle and in transmission between $\Delta\chi_{\text{trans}} \approx 0.1°$ and $\Delta\chi_{\text{trans}} \approx -1°$. The Goos-Hänchen shift amounts to $D_{\text{GH}} \approx 4\lambda$ at most. For TM polarization, the maximum values of the Goos-Hänchen shift, $D_{\text{GH}} \approx 0.8\lambda$, and the Fresnel

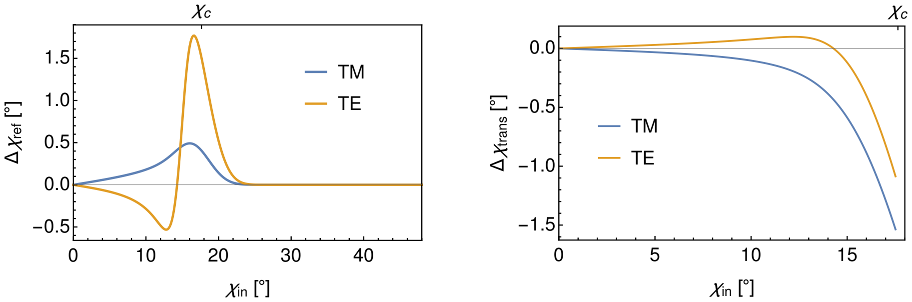

(a) Fresnel filtering in reflection according to Eq. (2.30).

(b) Fresnel filtering in transmission according to Eq. (2.32).

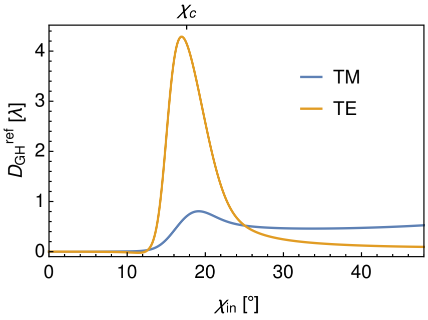

(c) Goos-Hänchen shift in reflection according to Eq. (2.27).

Figure 3.11: Beam shifts at a curved interface from the expectation value approach. Dimensionless size parameter $kR_0 = 147$ and relative refractive index $n = 3.3$ ($\chi_c \approx 17.6°$, $\chi_B \approx 16.9°$) are chosen to fit the experiment in [93], beam width $w/\lambda = 10$.

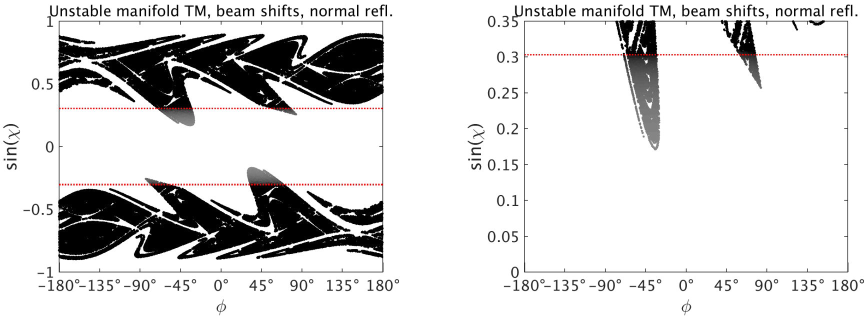

(a) TM polarization.

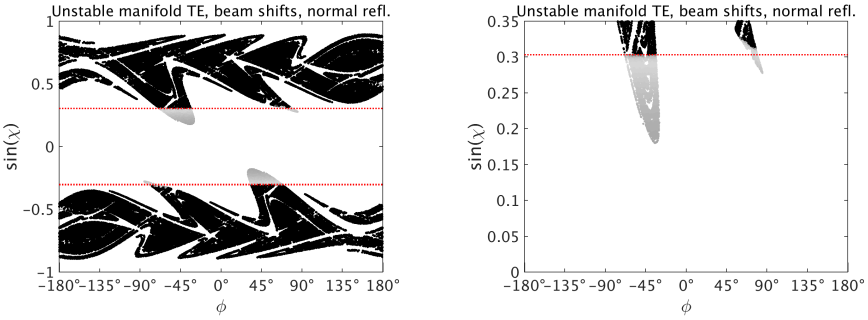

(b) TE polarization.

Figure 3.12: Fresnel weighted unstable manifold for (a) TM and (b) TE polarization resulting from the amended ray optical description of a Limaçon cavity with $\epsilon = 0.43$, $n = 3.3$, $kR_0 = 147$ including the beam shifts shown in Fig. 3.11. The critical lines $\sin(\chi) = \pm 1/n$ are marked as red dotted lines. *Left:* Full phase space. *Right:* Close-up for $0 \leq \sin(\chi) \leq 0.35$.

filtering in reflection, $\Delta\chi_{\mathrm{ref}} \approx 0.5°$, are much smaller, whereas the Fresnel filtering effect in transmission is a bit stronger, up to $\Delta\chi_{\mathrm{trans}} \approx -1.5°$.

The unstable manifold resulting from a ray optics model including these beam shifts is shown in 3.12. We observe small changes in the overlap of the unstable manifold with the leaky region. Especially, the minor contributions around $\phi \approx \pm 60°$ are even more strongly suppressed for TE polarization. This might be caused by the strong enhancement of the beam shifts due to the Brewster angle.

The most noticeable difference in the far-field emission, Fig. 3.13, compared to the far-field of the uncorrected description is the small dip occurring at 0° in the strong emission peak. This is not explained by the appearance of the unstable manifold alone. As the unstable manifold is not strongly influenced by the beam shifts, the rays that constitute the far-field still leave the cavity at the same positions in phase space. The transmitted rays, however, experience now a correction to their direction due to the Fresnel filtering effect. That means, that the phase space points map to slightly different far-field angles compared to the uncorrected ray optics. This effect can explain the changes

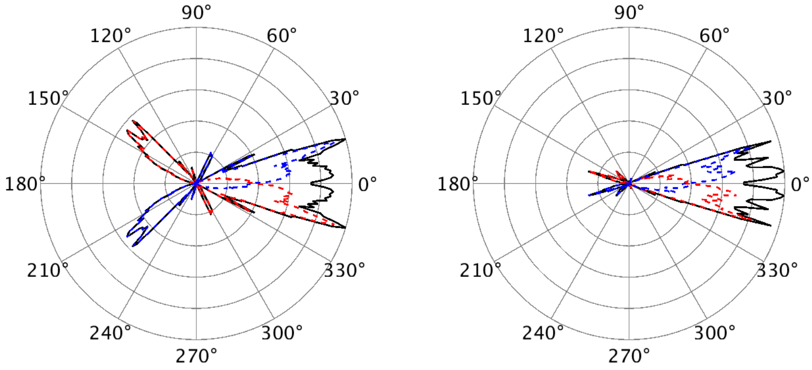

(a) TM polarization.

(b) TE polarization.

Figure 3.13: Far-field emission for (a) TM and (b) TE polarization calculated from the amended ray optical description of a Limaçon cavity with $\epsilon = 0.43$, $n = 3.3$, $kR_0 = 147$ including the beam shifts shown in Fig. 3.11. The contributions of the clockwise (red, dashed) and counterclockwise (blue, dashed) propagating rays to the total far-field (black, solid) are indicated.

observed in the far-field emission patterns without any significant changes to the appearance of the unstable manifold.

As discussed in section 2.3, the beam shift corrections break the reversibility of a single ray-trajectory. However, this irreversibility is not reflected in the far-field contributions of the clockwise and counterclockwise propagating rays. The two contributions are still perfect mirror images. Here, the same argument holds true as for the isotropic far-field of the circular cavity. Although a single trajectory does no longer coincide with its reversed partner the average over all possible ray trajectories, or, practically, a large ensemble of rays, still has to reflect the symmetry of the system.

3.3.4 Amended ray optics 3: Corrected reflection coefficients, beam shifts

Now, we combine the two previous approaches to an amended ray-optical description that includes all wave and curvature effects. We use the corrected reflection and transmission coefficients to calculate the intensities and include the beam shifts at each reflection.

The results of this approach are shown in Figs. 3.14 and 3.15. The observations and reasoning from the last two cases apply analogously to this case. There are no significant differences between the results of the ray-optics description including the beam shifts using uncorrected or corrected reflection coefficients. A more rigorous analysis is given in the next paragraph where we compare the different approaches in detail.

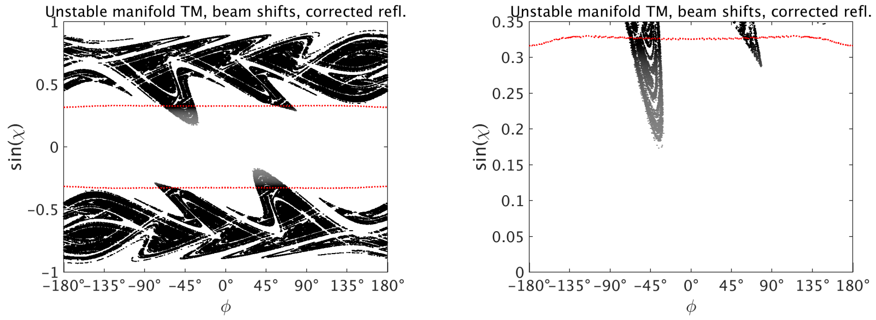

(a) TM polarization.

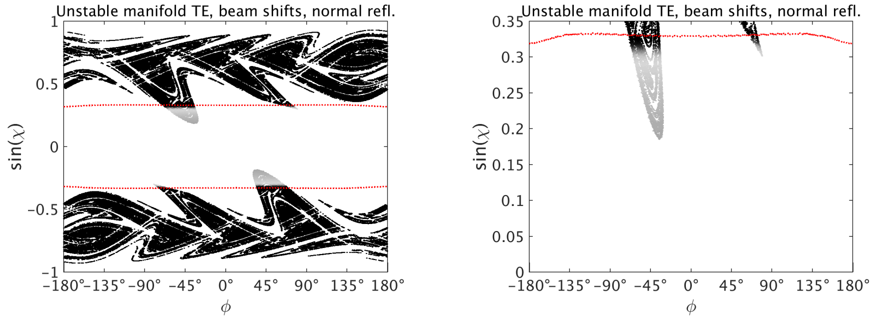

(b) TE polarization.

Figure 3.14: Fresnel weighted unstable manifold for (a) TM and (b) TE polarization resulting from the amended ray optical description of a Limaçon cavity with $\epsilon = 0.43$, $n = 3.3$, $kR_0 = 147$ using the corrected reflection coefficients for curved interfaces and including the beam shifts shown in Fig. 3.11. The critical lines resulting from the corrected reflection coefficients as a function of the position on the boundary are marked as red dotted curves. *Left:* Full phase space. *Right:* Close-up for $0 \leq \sin(\chi) \leq 0.35$.

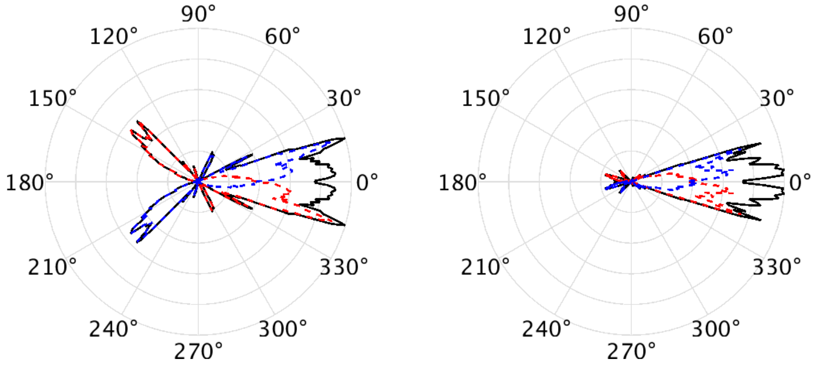

(a) TM polarization. (b) TE polarization.

Figure 3.15: Far-field emission for (a) TM and (b) TE polarization calculated from the amended ray optical description of a Limaçon cavity with $\epsilon = 0.43$, $n = 3.3$, $kR_0 = 147$ using the corrected reflection coefficients for curved interfaces and including the beam shifts shown in Fig. 3.11. The contributions of the clockwise (red, dashed) and counterclockwise (blue, dashed) propagating rays to the total far-field (black, solid) are indicated.

3.3.5 Comparison of the amended ray optics approaches

To conclude this section, the different methods are now directly compared. All resulting far-field emission patterns are shown in Fig. 3.16 on a logarithmic intensity scale showing only the upper half space to reveal more details. For TM polarization, there are no large deviations between the different methods seen besides the effects discussed already above. For TE polarization, there are some deviations which have not been seen in the presentation above.

We compare, now, the results of the corrected ray-optical approaches for TE polarization to the experimental findings presented in [93]. In the experiment, the cavity emitted TE polarized light. The figure showing the far-field from the experiment (green, solid) and from a classical ray description (red, broken) is reprinted here in Fig. 3.17. Although the overall agreement between the experimental and theoretical result is good there are some deviations. Most noticeably, the emission peak between $\phi = 150°$ and $\phi = 180°$ is found at a larger angle than expected from the ray calculation. Comparing this peak to the results of the corrected ray-optical approaches in Fig. 3.16, we see that this shift is corrected by the use of the reflection coefficients for curved interfaces (green, dashed and red, dotted curves). In both far-field patterns including the corrected reflection coefficients (red and green curves in Fig. 3.16), this peak is shifted with respect to the results of the standard Fresnel coefficients (black and blue curve in Fig. 3.16). Further, the shape and position of the dip around $\phi = 120°$ deviate between the experimental result and the classical ray calculation, seen in the inset of Fig. 3.17. This dip is better reproduced in the corrected results including the beam shift (blue and red curves in Fig. 3.16).

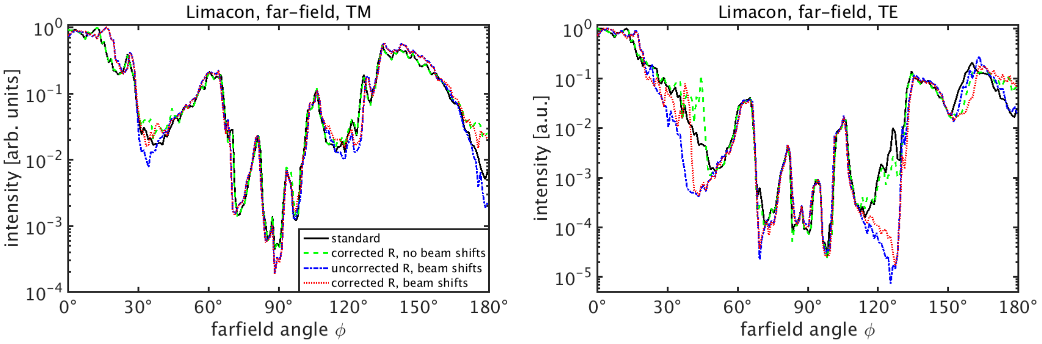

(a) TM polarization.

(b) TE polarization.

Figure 3.16: Far-field emission pattern in the upper half-plane on a logarithmic scale for (a) TM and (b) TE polarization. Results of the standard ray optics description (black, solid) and the different amended ray optics approaches, 1. using the corrected reflection coefficients for curved interfaces (green, dashed), 2. including the beam shifts (blue, dash-dotted), 3. using the corrected reflection coefficients and including the beam shifts (red, dotted).

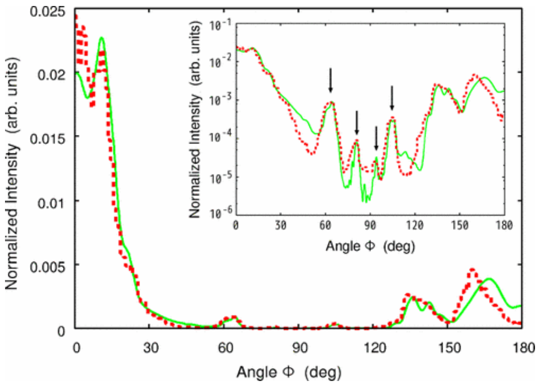

Figure 3.17: Comparison of far-field emission pattern of a Limaçon cavity measured in experiment and calculated from ray optics (green solid: experimental data averaged over several modes, red broken: far-field calculated from classical ray-optics), TE polarization in both cases. *Inset:* The same data on a logarithmic intensity scale. Reprinted figure with permission from S. Shinohara *et al.*, Phys. Rev. A **80**, 031801(R) [93]. Copyright (2009) by the American Physical Society.

These observations lead to the conclusion that the amended ray optics description using the corrected reflection coefficients for curved interfaces and including the beam shift effects, Goos-Hänchen shift and Fresnel filtering, is the appropriate approach to describe microcavities with curved boundaries in a ray picture. Both corrections, reflection coefficients and beam shifts, are needed to account for wave-induced deviations between experimental findings and a classical ray-optical description.

In general, good agreement is found between the prediction from ray optics and the far-field emission measured in experiment. Using the amended ray optics description we find even further improvement in the detailed structure of the emission pattern. One feature, however, agrees less well when comparing the experimental result (Fig. 3.17) and the amended ray-optics. The dip in the main emission peak at $\phi = 0$ predicted in the amended ray optics approach including the beam shifts (see Fig. 3.13 and 3.15) is not seen in the experiment [93]. In a different experiment with a cavity of the same shape, however, such a dip is observed [98].

3.4 A non-symmetric cavity: Influence of the wave corrections on the dynamics

To conclude this chapter, we apply the ray optics model to a cavity that lacks any symmetry. We consider the boundary curve

$$r(\phi) = R_0(1 + \epsilon_1 \cos(3\phi) + \epsilon_2 \sin(\phi)) \tag{3.3}$$

for two different sets of deformation parameters, $\epsilon_1 = 0.003$, $\epsilon_2 = 0.002$ and $\epsilon_1 = 0.03$, $\epsilon_2 = 0.02$. The two curves and their radii of curvature according to Eq. (3.2) are shown in Fig. 3.18.

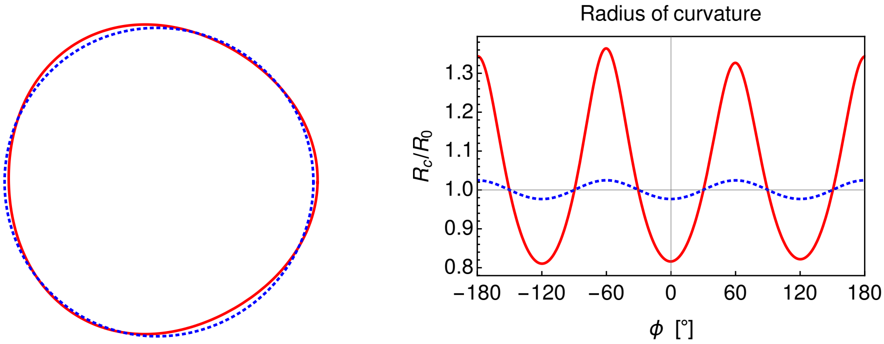

(a) Boundary curve $r(\phi)$. (b) Radius of curvature $R_c(\phi)/R_0$.

Figure 3.18: Curves according to Eq. (3.3) and their radii of curvature according to Eq. (3.2) for two different sets of deformation parameters, $\epsilon_1 = 0.003$, $\epsilon_2 = 0.002$ (blue, dotted) and $\epsilon_1 = 0.03$, $\epsilon_2 = 0.02$ (red).

For the ray-optical description of these cavities, we chose the main parameters as in the previous section for the Limaçon, $n = 3.3$ and $kR_0 = 147$. In the ray calculations we follow 60 000 rays started with random initial conditions on the boundary for 1 000 reflections.

3.4.1 Very small deformation: Non-chaotic dynamics

For the system with very small deformation parameters, $\epsilon_1 = 0.003$ and $\epsilon_2 = 0.002$, it follows from the KAM-theorem that the classical billiards dynamics is mainly non-chaotic [99]. Thus, the Poincaré surface of section of the classical phase space shown in Fig. 3.19 is very regular. For the optical system, this means that most rays that start above the critical line will stay above the critical line for all times. Therefore, they do not give any contribution to the far-field emission. Similarly, most trajectories that start below the critical line will stay in the leaky region for all times. These rays neither contribute significantly to the far-field as their intensity decreases very fast. Consequently,

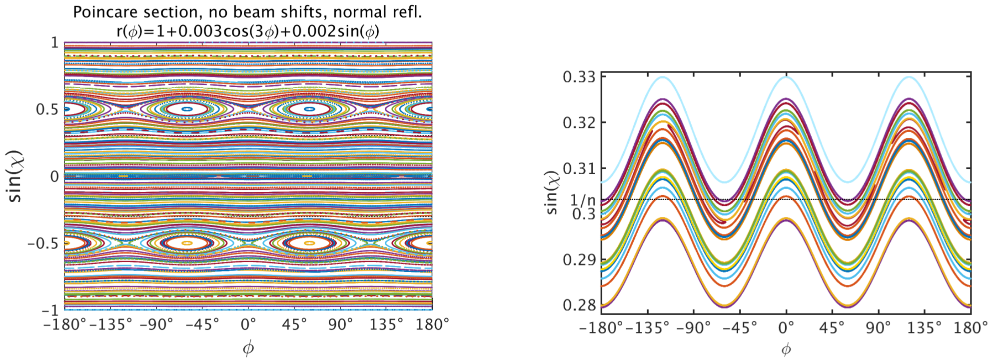

(a) Full Poincaré section.

(b) Close-up around the critical line.

Figure 3.19: Poincaré surface of section of the classical phase space of the billiard defined by the boundary curve Eq. (3.3) with $\epsilon_1 = 0.003$, $\epsilon_2 = 0.002$. The critical lines $\sin(\chi) = \pm 1/n$ for a dielectric cavity with relative refractive index $n = 3.3$ are drawn as dotted black lines.

we expect the far-field emission collected after some transition time to be dominated by trajectories that start in a small interval close to the critical line such that they are mostly but not completely confined by total internal reflection. The phase space portraits of some of these trajectories can be seen in Fig. 3.19(b) which shows a close-up of the Poincaré section around the critical line.

This qualitative reasoning can also be expressed in more quantitative terms. In the case of regular, non-chaotic dynamics, the time evolution of the intensity of a trajectory in an optical billiard is approximately given by

$$I(\ell_{\text{opt}}) \sim I_0 \mathrm{e}^{-\kappa \ell_{\text{opt}}} \tag{3.4}$$

where $\ell_{\text{opt}} = n\ell_{\text{geo}}$ is the optical pathlength that corresponds to the geometrical pathlength ℓ_{geo} that the trajectory has traveled inside the cavity with relative refractive index n The time is given by $t = \ell_{\text{opt}}/c$ with c the speed of light in vacuum and κ is the decay rate of the trajectory. If the trajectory is confined inside the cavity by total internal reflection for all times it is $\kappa = 0$, if the trajectory suffers refractive losses, $\kappa > 0$. We have to keep in mind that the intensity is not a continuous function of the time (or pathlength), rather, it changes only if the ray trajectory encounters the boundary, in between two reflections it stays unchanged.

To illustrate this behavior we show in Fig. 3.20(a) the evolution of the intensity of three different trajectories in the cavity considered here. We see that the dependence of the intensity on the pathlength can be well approximated by a straight line in the semilogarithmic plot, indicating exponential decay. The first trajectory starts well above the critical line and does not decay at all. The second trajectory starts near the critical line and exhibits a moderate

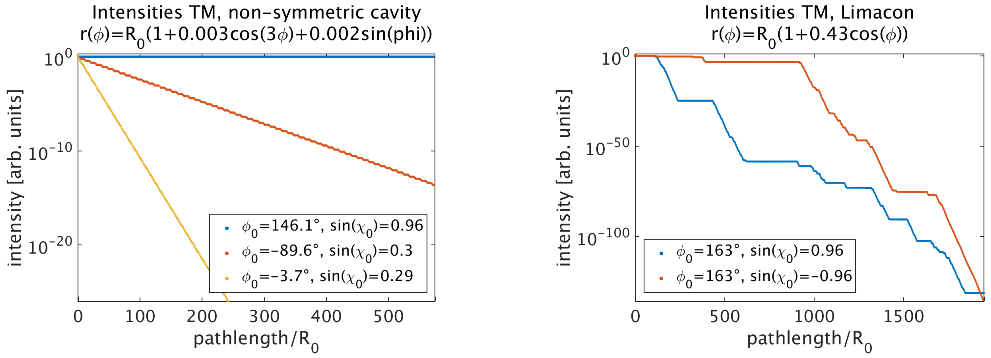

(a) Non-chaotic cavity.

(b) Chaotic cavity.

Figure 3.20: Time evolution of the reflected intensity of exemplary trajectories in two different cavities, (a) non-symmetric cavity with non-chaotic dynamics (boundary curve defined in Eq. (3.3) with $\epsilon_1 = 0.003$, $\epsilon_2 = 0.002$), (b) Limaçon cavity with predominantly chaotic classical dynamics (boundary curve defined in Eq. (3.1) with $\epsilon = 0.43$).

decay rate, while the third trajectory that starts below the critical line has a higher decay rate.

This concept is, however, not applicable to optical billiards with chaotic dynamics. In that case, the intensity evolves irregular with time, see, *e.g.*, the intensity evolution plotted in Fig. 3.20(b) for two exemplary trajectories in the Limaçon cavity discussed in the last section. Here, a trajectory which starts above the critical line can stay there for many bounces such that the intensity does not change for some time. Eventually the trajectory reaches the leaky region and the intensity decreases. Due to the chaoticity, the trajectory can stay in the leaky region for many bounces such that the intensity decays rapidly, or it reaches again the regime of total internal reflection after only few bounces such that the intensity is decreased only by a small amount before it stays constant again. Consequently, the intensity of a generic trajectory in a chaotic cavity cannot be approximated by an exponential decay, Eq. (3.4).

This argument, however, is applicable only to the evolution of the intensity of a single trajectories. The total intensity inside a cavity, *i.e.* the accumulated intensity of all trajectories, decays exponentially in both cases, chaotic and non-chaotic, after some transition time [100–102]. In this work, the term decay rate always refers to single trajectories.

In the previous section, we have discussed that the far-field emission of chaotic cavities is determined by the unstable manifold of the chaotic saddle. In the case of non-chaotic cavities, we argue here that the emission is dominated by the trajectories with the smallest nonzero decay rates. This concept is not only applied to the cavity studied here, it will be useful also for the triangular cavities studied in the next chapter.

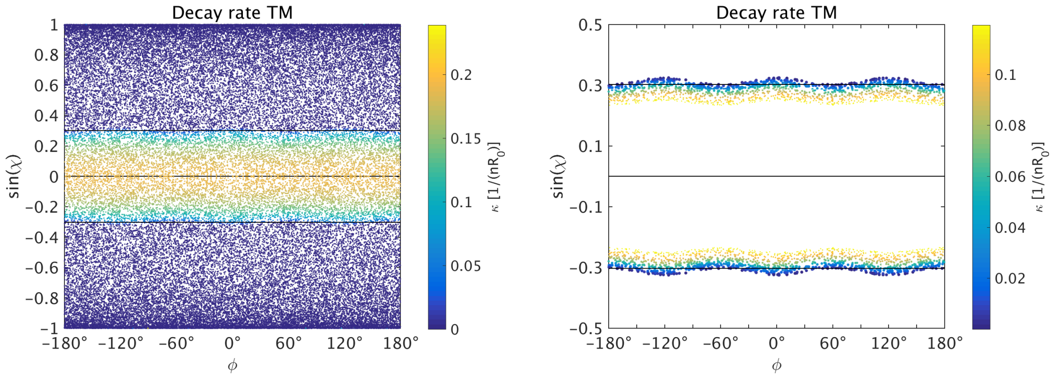

(a) TM polarization.

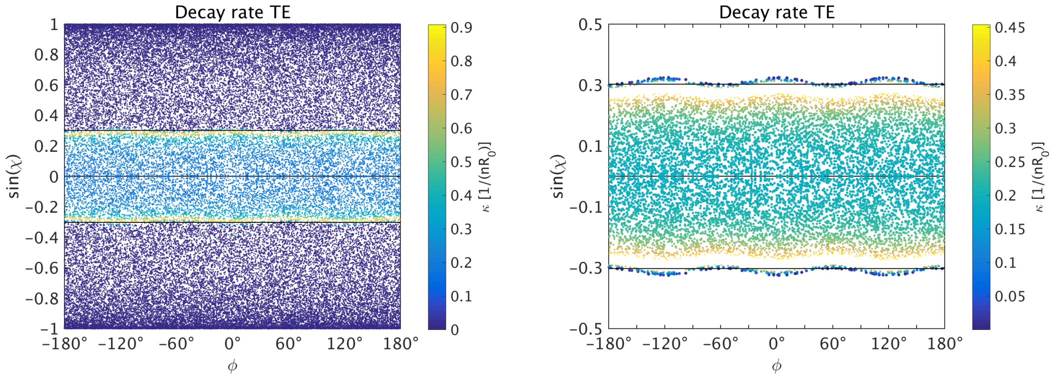

(b) TE polarization.

Figure 3.21: Decay rates κ of the trajectories in the optical billiard defined by the boundary curve Eq. (3.3) with $\epsilon_1 = 0.003$, $\epsilon_2 = 0.002$ with relative refractive index $n = 3.3$. The critical lines $\sin(\chi) = \pm 1/n$ are indicated. *Left:* Decay rates of all trajectories. *Right:* Close-up, $-0.5 \leq \sin(\chi) \leq 0.5$, on smallest nonzero decay rates, $0 < \kappa < \max(\kappa)/2$. Note the different color scales in all four panels.

The decay rates for the trajectories in the non-symmetric cavity with very small deformations with relative refractive index $n = 3.3$ are shown in Fig. 3.21. We calculate the decay rate for every trajectory started in the cavity. The initial conditions of the trajectories are approximately uniformly distributed with respect to the position on the boundary parameterized by the polar angle ϕ and the incident angle χ. As the initial condition uniquely determines the trajectory we show the decay rate at the phase space position of the initial condition of the corresponding trajectory. For both polarizations, we find that trajectories that start well above the critical line do not decay at all, their decay rate is $\kappa = 0$, as they never visit the leaky region. Trajectories starting in a small interval near the critical line have the smallest nonzero decay rates following the qualitative reasoning above. The precise distribution of the trajectories with small decay rates, however, differs for the two polarizations according to the differences between their reflection coefficients. Especially, the

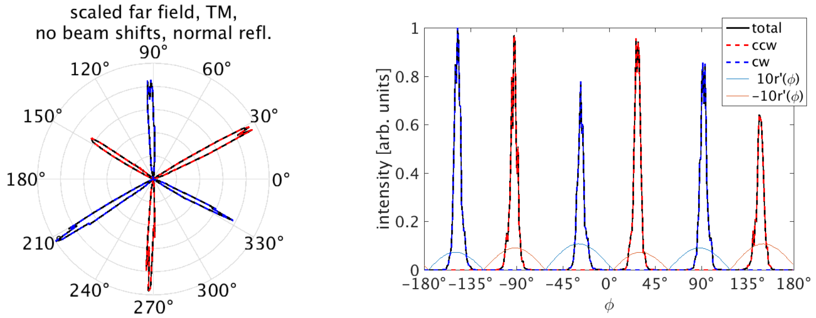

(a) TM polarization.

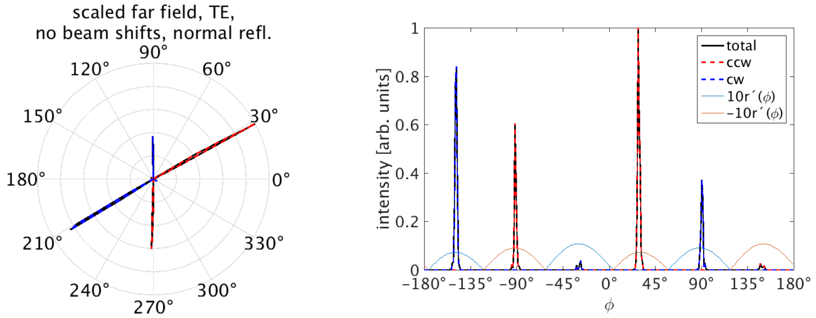

(b) TE polarization.

Figure 3.22: Far-field emission of the dielectric cavity with relative refractive index $n = 3.3$ defined by the boundary curve Eq. (3.3) with $\epsilon_1 = 0.003$, $\epsilon_2 = 0.002$, calculated from standard ray optics. The contributions of the clockwise (red, dashed) and counterclockwise (blue, dashed) propagating rays to the total far-field (black, solid) are indicated. The thin lines show the rescaled derivative of the boundary curve, $10r'(\phi)$ in blue, $-10r'(\phi)$ in red.

Brewster angle where no light is reflected for TE polarization leaves its trace in the decay rates with strongly enhanced decay (lighter colors in Fig. 3.21) for trajectories that encounter the Brewster angle.

We will discuss now the far-field of such a nearly circular cavity and how it is determined by the trajectories with the smallest decay rates. The far-field emission pattern calculated from standard ray optics is shown in Fig. 3.22 for both polarizations. As for the Limaçon cavity, the contributions of clockwise and counterclockwise propagating rays to the total far-field are evaluated separately and shown together with the total far-field emission. Since there is no mirror symmetry in the system the two contributions are not related by symmetry. However, they contribute approximately equally to the total far-field.

Although the deformation is very small and the deviation from the circle can be barely seen, the far-field emission pattern is not nearly isotropic but shows narrow peaks in six distinct directions. In Ref. [103], a similar situation, an almost circular cavity with very small deformations, have been studied with electromagnetic wave simulations. There, the authors found that the modes inside the cavity are not strongly influenced by the deformation and look almost like those for the circle, but the fields outside the cavity are extremely sensitive to the deformation. In general, the far-field is found to be strongly directional for optical cavities deviating only slightly from the perfect circular or spherical geometry [103]. Here, this directionality can be explained with the trajectories that have the smallest nonzero decay rates as discussed above. These trajectories have many incident angles above the critical line and only few incident angles slightly below the critical line. In general, the angles of incidence are larger in regions of smaller curvature and smaller where the curvature is high. Consequently, the emission occurs in approximately tangential direction at the points where the curvature of the boundary is highest [15]. These far-field directions are given by the angles where the derivative of the boundary curve $r'(\phi)$ exhibits extrema. Indeed, it is clearly seen in Fig. 3.22 that directions of the emission peaks coincide well with the extrema of $r'(\phi)$.

The differences between the far-field emission patterns for the two polarizations correspond to differences in the decay rates of the trajectories (*cf.* Fig. 3.21). For TE polarization, the emission peaks are narrower than for TM polarization and two emission directions, the peaks close to $\phi = -30°$ and $\phi = 150°$, respectively, are strongly suppressed. The reduced width of the peaks corresponds directly to the stronger contrast in decay rates. For TE polarization, there is a sharp step between the smallest decay rates and the slightly higher decay rates, whereas for TM polarization, there is a continuum of initial conditions which lead to trajectories with comparably low decay rates. Additionally, the Brewster angle feature leads to very high decay rates for trajectories in the case of TE polarization that have small decay rates in the case of TM polarization. This explains the two missing peaks in the far-field calculated for TE polarized light.

Now, we study the influence of wave corrections to the ray model of this cavity. We include Fresnel filtering and Goos-Hänchen shift at each reflection and apply the corrected reflection and transmission coefficients to calculate the intensities. For the correction terms, we use the same values as for the Limaçon which are given in Fig. 3.11.

The resulting Poincaré surface of section of the billiards dynamics in the cavity explicitly including the beam shift effects is shown in Fig. 3.23. The beam shifts introduce chaoticity and non-Hamiltonian behavior in the previously regular dynamics. The influence on the dynamics is strongest around the critical angle where both beam shift effects are largest. The angular shift due to the Fresnel filtering effect leads to a depletion of the phase-space area around the critical line. If a trajectory has an angle of incidence close to the critical angle it experiences a large angular correction and is shifted away from the critical line which has already been seen for the circular cavity above. In general, the influence is stronger for TE polarization. On the one hand, both correction terms, Fresnel filtering and Goos-Hänchen shift, are larger for TE polarization than for TM. On the other hand, the sign change of the Fresnel filtering correction near the Brewster angle enhances the depletion. Trajectories with incident angles above the Brewster angle are shifted above the critical line, whereas trajectories with incident angles below the Brewster angle are shifted towards the line $\sin(\chi) = 0$. Consequently, the depleted phase space area is enlarged. This formation of repellers and attractors in the phase space is a clear sign of non-Hamiltonian dynamics [57, 99].

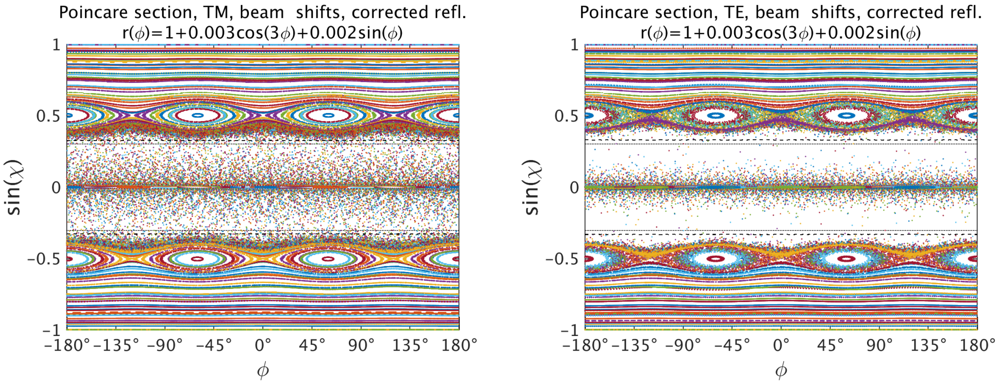

(a) TM polarization.

(b) TE polarization.

Figure 3.23: Poincaré surface of section of the dynamics in a billiard defined by the boundary curve Eq. (3.3) with $\epsilon_1 = 0.003$, $\epsilon_2 = 0.002$ including the beam shift corrections shown in Fig. 3.11 for both polarizations, TM and TE. The classical critical lines $\sin(\chi_c) = \pm 1/n$ for $n = 3.3$ are drawn as black dotted lines, the critical lines resulting from the corrected reflection coefficients as a function of the position on the boundary are marked as black dashed curves.

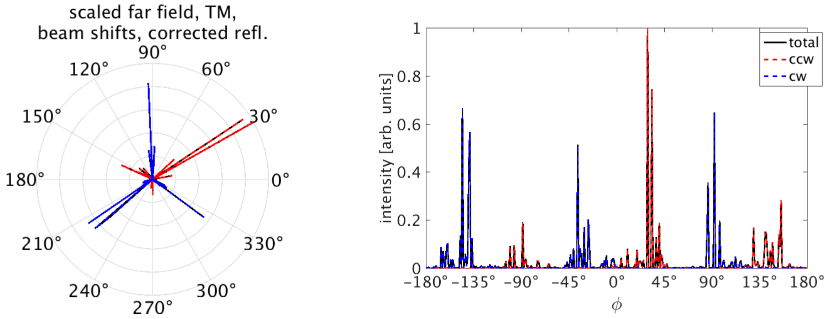

(a) TM polarization.

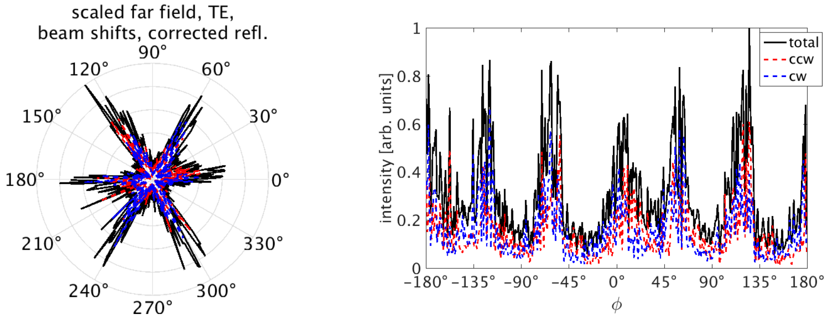

(b) TE polarization.

Figure 3.24: Far-field emission of the dielectric cavity with relative refractive index $n = 3.3$ defined by the boundary curve Eq. (3.3) with $\epsilon_1 = 0.003$, $\epsilon_2 = 0.002$, calculated from amended ray-optics including the corrected reflection coefficients for curved interfaces and the beam shift corrections shown in Fig. 3.11. The contributions of the clockwise (red, dashed) and counterclockwise (blue, dashed) propagating rays to the total far-field (black, solid) are indicated.

The resulting far-field calculated from ray optics including the beam shift effects and the corrected reflection and transmission coefficients is shown in Fig. 3.24 for both polarizations. The main emission directions obtained from the standard ray-optical model can still be recognized, but they are much less distinct. Especially for TE polarization where the wave corrections are large, the emission is strongly broadened. Due to the beam shifts, the far-field is no longer dominated by light transmitted in tangential direction at the points of highest curvature but the transmission occurs in less predictable directions.

In consequence, we find that the difference between the predicted far-field pattern of the weakly deformed cavity and the isotropic emission of the circular cavity becomes smaller if wave effects are included.

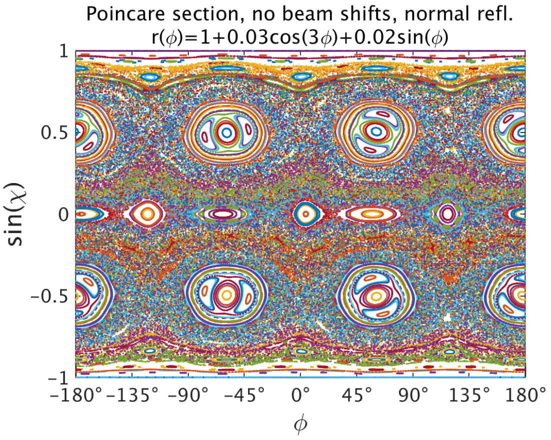

Figure 3.25: Poincaré surface of section of the classical phase space of the billiard defined by the boundary curve Eq. (3.3) with $\epsilon_1 = 0.03$, $\epsilon_2 = 0.02$.

3.4.2 Larger deformation: Partially chaotic dynamics

For the system with larger deformation parameters $\epsilon_1 = 0.03$ and $\epsilon_2 = 0.02$, the classical billiards dynamics exhibits a mixed phase-space. The Poincaré surface of section of the classical phase space given in Fig. 3.25 shows stable islands in a chaotic sea.

The unstable manifold can be used to determine the far-field not only for chaotic systems as discussed in the previous section but also for systems with a mixed phase-space [97]. The Fresnel-weighted unstable manifold resulting from standard ray-optics for this cavity, shown in Fig. 3.26, has two distinct contributions. One originates from the prominent stable islands around $\sin(\chi) = 0.5$

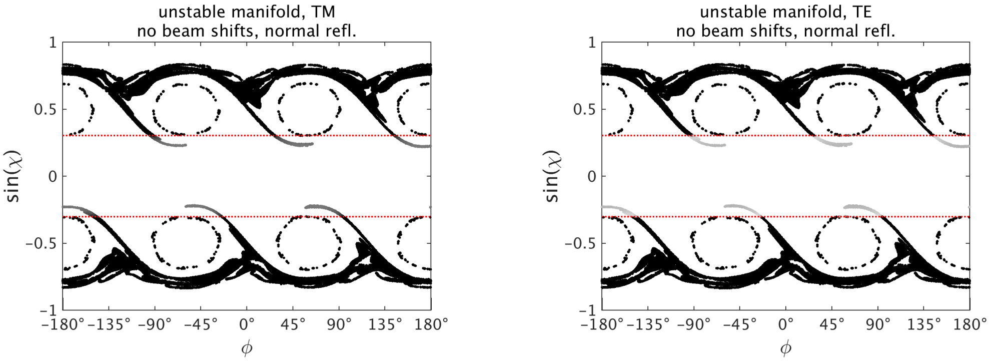

(a) TM polarization.

(b) TE polarization.

Figure 3.26: Fresnel weighted unstable manifold of the optical billiard defined by the boundary curve Eq. (3.3) with $\epsilon_1 = 0.03$, $\epsilon_2 = 0.02$, calculated from standard ray optics. The critical lines $\sin(\chi) = \pm 1/n$ for relative refractive index $n = 3.3$ are drawn as dotted red lines.

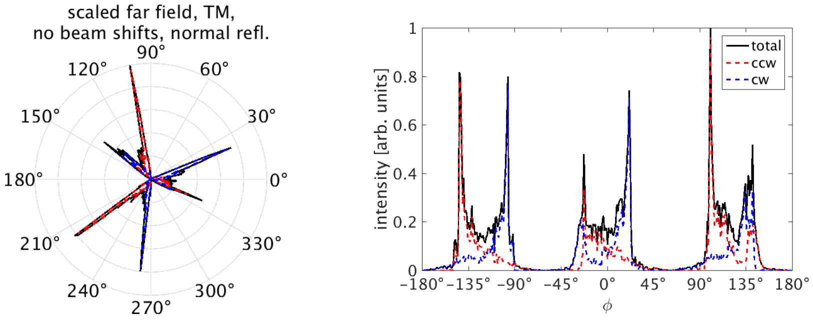

(a) TM polarization.

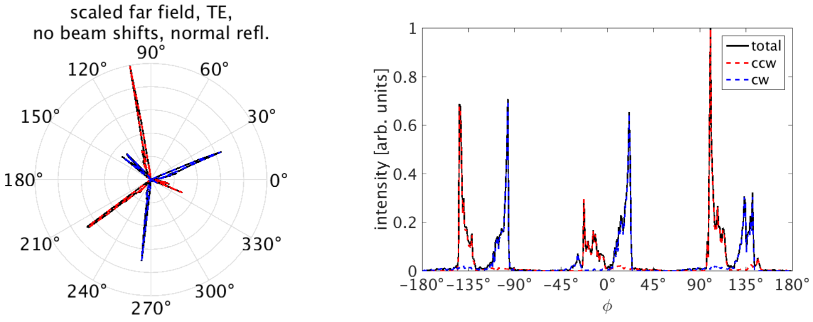

(b) TE polarization.

Figure 3.27: Far-field emission of the dielectric cavity with refractive index $n = 3.3$ defined by the boundary curve Eq. (3.3) with $\epsilon_1 = 0.03$, $\epsilon_2 = 0.02$, calculated from standard ray optics. The contributions of clockwise (red, dashed) and counterclockwise (blue, dashed) propagating rays to the total far-field (black, solid) are indicated.

and the other from the chaotic sea above these islands. The overlap of the unstable manifold with the leaky region is similar for both polarizations. Thus, we also expect the far-field patterns to be very similar for the two polarizations which is indeed found in the results, see Fig. 3.27. For TM polarization, the Fresnel-weighted unstable manifold in the leaky region is more intense. This is reflected in the broadened and less directional emission peaks.

Actually, the contributions from the stable islands do not belong to the unstable manifold of the chaotic saddle. However, as it determines the far-field in a similar way we treat it on an equal footing. These trajectories also stay confined inside the cavity for a long time before they eventually reach the leaky region and contribute to the far-field. They cross the critical line on a regular path, in contrast to the trajectories originating from the true unstable manifold which cross the critical line on a chaotic path.

To study these two influences, the chaotic and the regular, in more detail we have performed the ray simulation of this cavity also for different relative refractive indices. For higher (smaller) refractive indices the critical line is shifted to smaller (larger) values. In addition to $n = 3.3$ which is used throughout the rest of this chapter, we have chosen $n = 3$ and $n = 3.5$. The

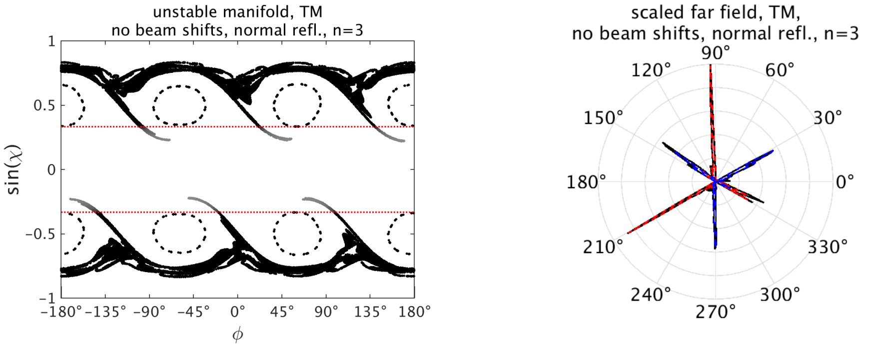

(a) $n = 3$, TM polarization.

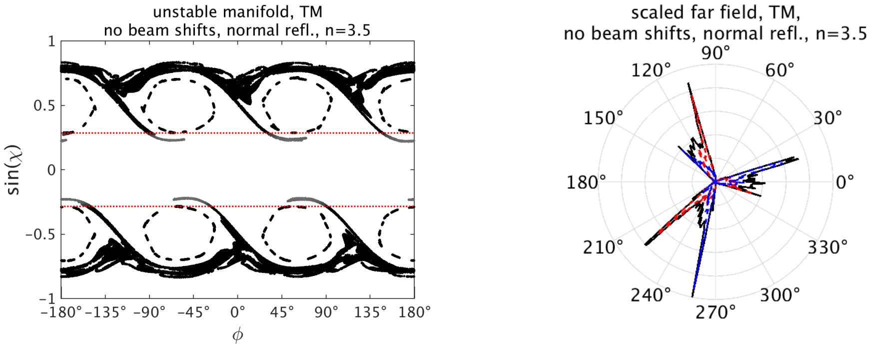

(b) $n = 3.5$, TM polarization.

Figure 3.28: Fresnel weighted unstable manifold and far-field emission of the dielectric cavity defined by the boundary curve Eq. (3.3) with $\epsilon_1 = 0.03$, $\epsilon_2 = 0.02$, calculated from standard ray optics for two different relative refractive indices. Compare to Figs. 3.26 and 3.27.

resulting unstable manifolds and far-field emission patterns for TM polarization are shown in Fig. 3.28. The critical line intersects the stable islands at different positions, therefore they have a different contribution, whereas the true unstable manifold part resulting from the chaotic saddle stays almost the same. The similarity between the unstable manifolds in all three cases, for $n = 3$, $n = 3.3$, and $n = 3.5$, explains why the far-field emission is also similar. The robustness of the far-field emission with respect to small changes in the parameters, the deformation or the refractive index, has been predicted also for the Limaçon cavity [27] and has been impressively confirmed in experiments [85, 86, 93, 104]

Now we study the influence of the wave corrections as for the weakly deformed cavity. In the Poincaré surface of section (see Fig. 3.29) we observe in principle the same effects as for the weakly deformed cavity. The beam shift effects introduce more chaoticity and non-Hamiltonian behavior, in particular, the islands around $\sin(\chi) = 0.5$ and $\sin(\chi) = 0$ are replaced by attractors and

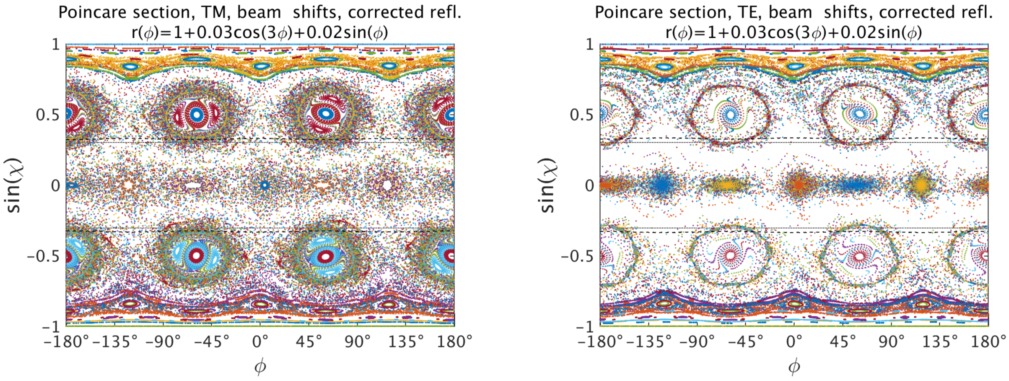

(a) TM polarization.

(b) TE polarization.

Figure 3.29: Poincaré surface of section of the dynamics in a billiard defined by the boundary curve Eq. (3.3) with $\epsilon_1 = 0.03$, $\epsilon_2 = 0.02$ including the beam shift corrections shown in Fig. 3.11 for both polarizations, TM and TE.

repellers [57]. Especially for TE polarization, the depletion of the phase-space area between the Brewster angle and the critical angle is again clearly seen.

The unstable manifold (see Fig. 3.30) is, however, not strongly influenced by the wave corrections. Consequently, the far-field emission resulting from the amended ray optics description, shown in Fig. 3.31, is also very similar to the uncorrected one. A similar result has been found already for the chaotic

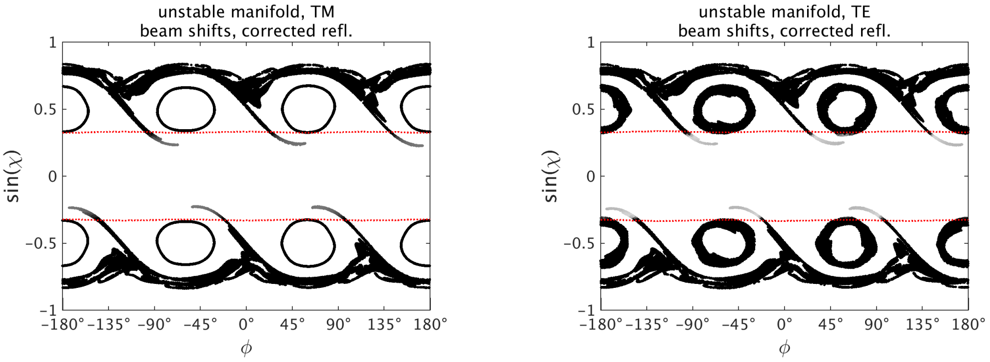

(a) TM polarization.

(b) TE polarization.

Figure 3.30: Fresnel weighted unstable manifold of the optical billiard defined by the boundary curve Eq. (3.3) with $\epsilon_1 = 0.03$, $\epsilon_2 = 0.02$, calculated from amended ray-optics including the corrected reflection coefficients for curved interfaces and the beam shift corrections shown in Fig. 3.11. The critical lines resulting from the corrected reflection coefficients as a function of the position on the boundary are marked as red dotted curves.

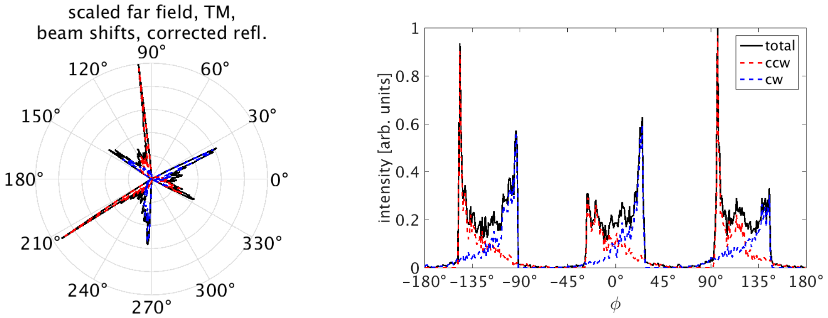

(a) TM polarization.

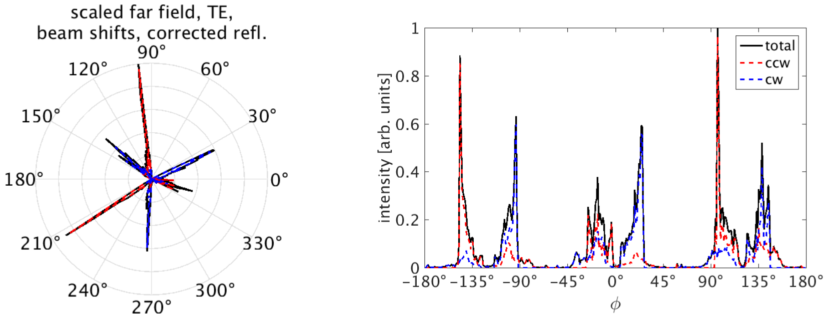

(b) TE polarization.

Figure 3.31: Far-field emission of the dielectric cavity with relative refractive index $n = 3.3$ defined by the boundary curve Eq. (3.3) with $\epsilon_1 = 0.03$, $\epsilon_2 = 0.02$, calculated from amended ray-optics including the corrected reflection coefficients for curved interfaces and the beam shift corrections shown in Fig. 3.11. The contributions of the clockwise (red, dashed) and counterclockwise (blue, dashed) propagating rays to the total far-field (black, solid) are indicated.

Limaçon cavity in the previous section. As long as the wave corrections have only a small influence the unstable manifold, the far-field is not strongly affected. The main difference between the unstable manifolds resulting from the standard and from the amended ray optics is observed in the parts that originate from the stable islands, whereas the true chaotic part is almost unaffected. On the one hand, the stable islands are strongly affected by the beam shifts. On the other hand, the critical line is shifted to higher angles due to the corrected reflection coefficients and intersects the islands now at a different position.

Although the wave corrections have only a small influence on the far-field emission they could lead to better agreement between the prediction from ray optics and experimental results as we have seen for the Limaçon cavity. However, we are not aware of experiments or wave simulations for the cavity shape discussed here.

3.5 Conlusions

In the first part of this chapter, we have discussed different possibilities to include finite-wavelength corrections in an amended ray optics description of dielectric optical microcavities with curved boundaries. To account for all wave and curvature effects, we suggest to use the corrected reflection coefficients for curved boundaries to calculate the intensities and, additionally, to include the beam shift effects, Goos-Hänchen shift and Fresnel filtering, in the ray dynamics.

The beam shifts have a strong influence on the evolution of the ray trajectories. The corrections to the position and angle at each reflection can destroy properties of the trajectories imposed by the symmetry of the system, like the conservation of angular momentum in a circular cavity. However, we find that the symmetry properties of the predicted far-field emission are not affected. As it results from a large ensemble of trajectories, it still reflects the symmetry of the cavity.

Further, we have discussed that the far-field pattern of non-chaotic systems is determined by the emission of the trajectories with the smallest nonzero decay rates. Whereas, for chaotic systems, it is well known that the overlap of the unstable manifold of the chaotic saddle with the leaky region determines the far-field emission. In a chaotic system, the definition of a decay rate for a single trajectory is not meaningful.

We find that the finite wavelength and curvature corrections have only small, though maybe important, effects on the emission of chaotic systems as long as they do not strongly affect the unstable manifold of the chaotic saddle which is a very robust and universal feature of the chaotic dynamics. For non-chaotic systems, the corrections, especially the explicit beam shift terms, can have a significant influence as they disturb the regular motion and introduce chaoticity and non-Hamiltonian behavior in the dynamics.

Chapter 4

Extended ray-optical description of triangular microlasers

In this chapter we present another application of ray-optics, the ray-optical description of triangular microlasers. In the first part, we discuss polygonal billiards and microcavities in general, and triangular systems in particular. Then we describe the extended ray-optical model which we apply to different triangles with varying symmetry, starting with the highly symmetric equilateral and right isosceles triangles, discussing other isosceles triangles and, lastly, triangles without any symmetry.

4.1 Polygonal (optical) billiards

In contrast to the systems with smooth boundaries considered in the previous chapter, polygons show sharp corners. The corner angles of a polygon take to some extent the role of the deformation parameters that were used to parameterize the deviations from the circle of the systems discussed in the last chapter. In this section, we discuss some of the most important properties of classical polygonal billiards and of polygonal optical microcavities.

4.1.1 Properties of polygonal billiards

Polygonal billiards have been exhaustively studied in the field of pure mathematics and mathematical physics, see, *e.g.*, [51, 105–107] and references therein. There is also a vast amount of literature dealing explicitly with billiard dynamics in triangles and the intriguing mathematical details that this, seemingly simple, problem poses, see, *e.g.*, [108, 109] and references therein. It has been shown that the properties of trajectories in generic triangular billiards display a rich behavior depending crucially on the realized geometry [108, 110–113].

A polygon is called rational if all its internal angles are rational multiples of π, *i.e.*, all angles can be written as $p\pi/q$ with p, q coprime integers. If one of its internal angles is not a rational multiple of π the polygon is called irrational. The billiard dynamics in a polygon crucially depends on the geometry, especially, on the fact if it is rational or not. Although most polygons are geometrically simple objects only few polygons exhibit integrable billiard dynamics. It can be shown that only those polygons are integrable whose internal angles are true fractions of π, *i.e.*, that can be written as π/q with integers q. This can be fulfilled only in rectangles and three kinds of triangles, the equilateral triangle, the right isosceles triangle and the equilateral triangle cut in half, *i.e.*, the triangle with internal angles $\pi/2$, $\pi/3$ and $\pi/6$ [109]. All other rational polygons have so-called pseudointegrable dynamics [114]. The term pseudointegrable was introduced by Berry and Richens and means that "trajectories in the classical phase space explore two-dimensional invariant surfaces which are generically not tori as in integrable systems but instead have the topology of multiply-handled spheres" [114]. The billiard dynamics in irrational polygons is supposed to be ergodic [115].

It is surprising that the dynamics of an irrational triangle and a generic rational triangle is supposed to be different as every irrational triangle can be approximated by a rational one to arbitrary precision (due to the fact that the rational numbers are dense in the space of real numbers).

We will discuss triangles belonging to the different symmetry classes, with integrable, pseudointegrable and ergodic classical dynamics.

4.1.2 Polygonal optical microcavities

As discussed in chapter 2, dielectric optical microcavities can be interpreted as open billiards. Due to the unusual pseudointegrable dynamics of a generic polygonal billiards the semiclassical treatment of polygons in the framework of ray-wave correspondence is difficult [116]. However, it has been shown that ray-wave correspondence is fulfilled if the system is "sufficiently open" [117]. That means, a ray optics description can be applied to polygonal optical microcavities with a rather low refractive index.

A semiclassical method that has been derived for polygonal billiards and can be used to study the optical modes of (pseudointegrable) polygonal microcavities is the so called superscar model [118]. It has been successfully applied to various systems, *e.g.*, to rectangles [118, 119], to squares and pentagons [11], to hexagons [120] or to triangles [118, 121]. However, we will not use this model in this work where the focus is on the prediction of the far-field emission and not on the optical modes.

Going from the closed, hard-walled systems to open systems, the optical microcavities considered here, poses another problem. Thinking in terms of wave dynamics, the two systems have different boundary conditions, Dirichlet and dielectric boundary conditions, respectively [20]. Whereas rectangles and the three special triangles with Dirichlet boundary conditions have integrable dynamics, their dynamics is no longer integrable when dielectric boundary conditions are applied [122]. Hence, the electromagnetic boundary value problem can no longer be easily solved even for the simplest dielectric polygons.

Dielectric optical microcavities and microlasers in the shape of triangles have been studied both experimentally and theoretically, see *e.g.*, [119, 123–125]. Our work is partly motivated by experiments performed in the group of M. Lebental and J. Zyss at ENS Cachan [126]. They studied microlasers in the shape of various triangles made from polymer thin-films doped with a laser dye. We will refer to the experimental results where appropriate.

4.2 Extended ray-optical model

The methods for a ray-optical description of dielectric microcavities have been discussed in detail in the last chapter for systems with curved boundaries. Here, we shortly give the details that are needed for the description of polygonal cavities with all planar boundaries. Further, we introduce the inclusion of intensity amplification in the ray model to achieve a better description of lasing cavities. The details about the implementation and the evaluation of the ray model can be found in appendix A.

4.2.1 Basic ray optics

The usual ray optics simulations follow the rules of classical geometrical optics using the laws of reflection and Snell's law as well as the Fresnel coefficients. The basic notation that we will use throughout this chapter is clarified in Fig. 4.1.

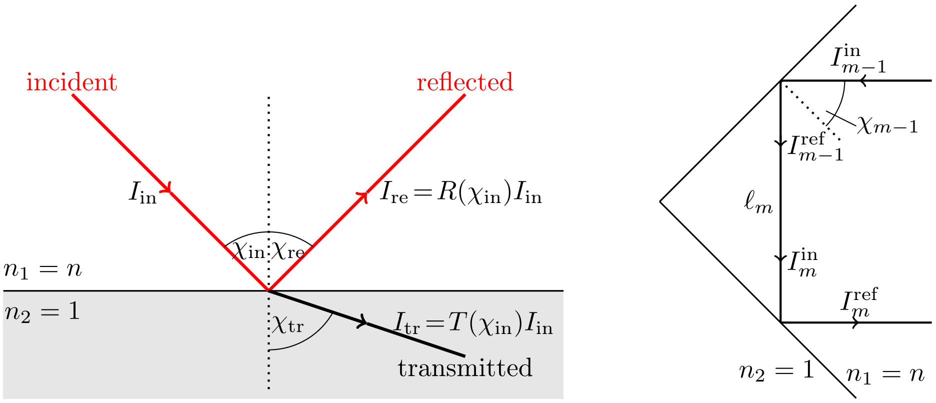

(a) Incident, reflected and transmitted rays.

(b) Trajectory between consecutive bounces.

Figure 4.1: Schematics of a light ray propagating inside a polygonal dielectric cavity. The cavity consists of an optically thicker material with relative refractive index $n = n_2/n_1 > 1$ surrounded by an optically thinner material with refractive index n_1.

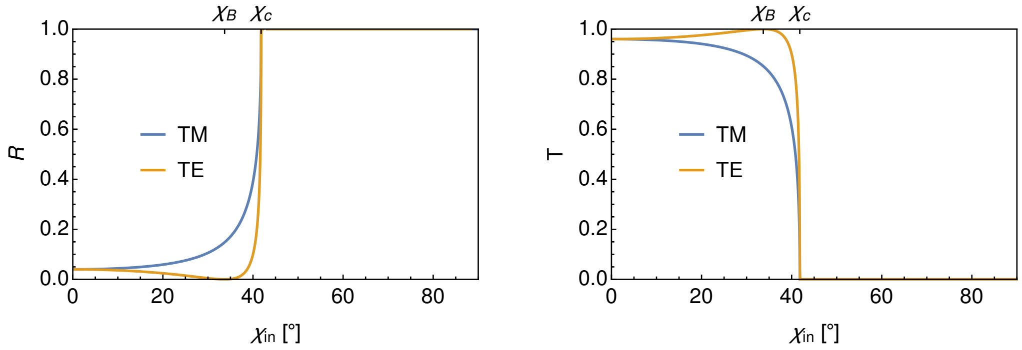

(a) Reflection coefficients.

(b) Transmission coefficients.

Figure 4.2: Intensity reflection and transmission coefficients at a planar interface with relative refractive index $n = 1.5$ for both polarizations, TE and TM. The critical angle $\chi_c \approx 41.8°$ and the Brewster angle (for TE polarization) $\chi_\text{B} = \arctan(1/n) \approx 33.7°$ are marked.

The reflected and transmitted intensities, I^ref and I^trans, are obtained from the incident intensity I^in using the Fresnel equations [20]. At the mth reflection point of the ray they are given by

$$I_m^\text{ref} = R(\chi_m) I_m^\text{in} \qquad \text{and} \qquad I_m^\text{trans} = T(\chi_m) I_m^\text{in} \tag{4.1}$$

with the corresponding angle of incidence, χ_m, and the Fresnel reflection and transmission coefficients, $R(\chi)$ and $T(\chi) = 1 - R(\chi)$, shown in Fig. 4.2 for TE and TM polarization. If not stated otherwise, we will use the relative refractive index $n = 1.5$ typical for several types of glass and transparent polymers throughout this chapter.

In the case of a passive cavity, the incident intensity is just the reflected intensity of the last bounce, $I_m^\text{in} = I_{m-1}^\text{ref}$. We assume no absorption or scattering losses inside the cavity, the only loss mechanism is transmission by refractive escape through the resonator boundary.

4.2.2 Amplification in the ray model

We include amplification along the light path in order to extend the ray model to active, lasing microcavities. To model gain in an active cavity, we assume uniform pumping and a uniform distribution of the active medium throughout the cavity. In previous works, this situation has been studied within a semiclassical laser theory [127] or using the Schrödinger-Bloch model [90, 128, 129]. A non-uniform gain distribution in chaotic cavities has been studied in the ray model in Ref. [101]. Generalizing the concept of Husimi functions [130] to active cavities illustrated the role of amplification along the light trajectory, and how transmission and reflection of light depend on the previously accumulated intensity [129]. These findings suggest that amplification can be taken into account in an effective manner.

Here, we use an effective exponential laser gain model [131]. The incident intensity in Eq. (4.1) is given by

$$I_m^{\mathrm{in}} = I_{m-1}^{\mathrm{ref}} \mathrm{e}^{\alpha \ell_m^{\mathrm{opt}}} \tag{4.2}$$

where $\alpha > 0$ is the gain coefficient of the active material and $\ell_m^{\mathrm{opt}} = n\ell_m$ is the optical path length between the $(m-1)$th and mth bounce. This means that the intensity gain is proportional to the intensity I_{m-1}^{ref} that enters the piece of trajectory under consideration.

This simple model serves as an efficient way to include amplification in the ray-optical description of microlasers although it neglects many effects that appear in real lasers. For example, it does not account for intensity saturation or for the lasing threshold of the active medium. In the ray model wave effects, like the frequency dependence of the amplification coefficient or the overlap of a mode with the gain profile, are naturally neglected.

In experiments with cavities made of a polymer doped with a laser dye, the above stated assumptions are usually fulfilled. Uniform pumping can be obtained when the cavities are optically pumped with a pump beam covering the whole cavity area. An approximately uniform distribution of the dye in the polymer matrix is ensured during the liquid phase processing of the material. Finally, lasing modes can be assumed to be fully developed even in the case of pulsed pumping as long as the photon round trip time is much shorter than the pump pulse. Typical gain coefficients for thin dye-doped polymer layers are of the order of magnitude of $\alpha \sim 10\,\mathrm{cm}^{-1}$-$100\,\mathrm{cm}^{-1}$ [132, 133].

Since the billiard dynamics in a triangle is not chaotic it does make sense to define decay rates for the intensities of the ray trajectories in triangular optical cavities as discussed in section 3.4. Combining the amplification, Eq. (4.2), and the intensity decay, Eq. (3.4), we obtain the approximate time evolution of each trajectory

$$I_j(\ell_{\mathrm{opt}}) \sim I_0 \mathrm{e}^{(\alpha - \kappa_j)\ell_{\mathrm{opt}}} \tag{4.3}$$

where the index j denotes the chosen trajectory. The decay rate κ_j depends on the precise trajectory, whereas, the amplification is the same for all trajectories in the model used here. If the gain exactly balances the averaged refractive losses of a given ray trajectory, $\alpha - \kappa_j = 0$, the intensity stays approximately the same for all times. The intensities of all other trajectories will either increase $(\alpha > \kappa_j)$ or decrease $(\alpha < \kappa_j)$ with time.

4.2.3 Wave corrections

To account for finite wavelength effects in the ray-optical model we also discuss the influence of the beam shifts. For polygonal billiards only the Fresnel filtering effect is of interest because the Goos-Hänchen shift leads simply to a parallel shift of the ray along the interface which does not affect the far-field emission direction. A ray trajectory including the corrections due to the

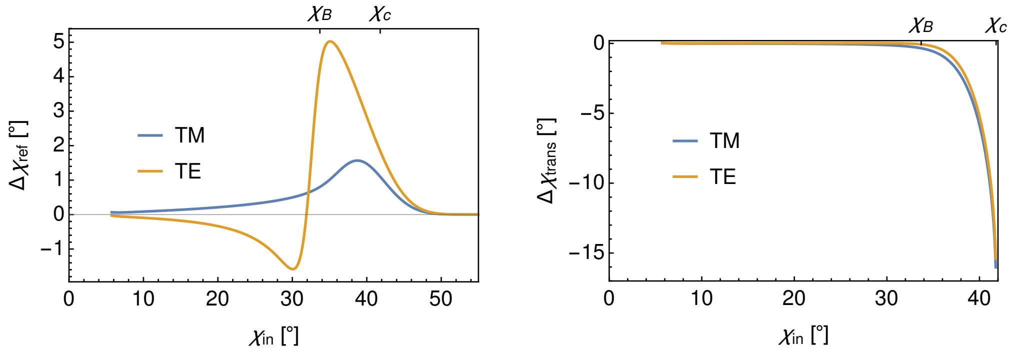

(a) Fresnel filtering in reflection, $\epsilon \approx 0.05$.

(b) Fresnel filtering in transmission, $\epsilon \approx 0.05$.

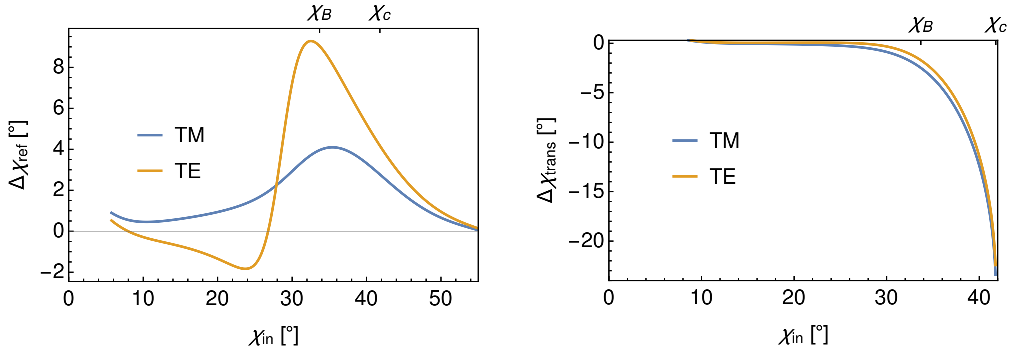

(c) Fresnel filtering in reflection, $\epsilon \approx 0.10$.

(d) Fresnel filtering in transmission, $\epsilon \approx 0.10$.

Figure 4.3: Fresnel-filtering correction $\Delta\chi$ at a planar interface calculated from the expectation value approach according to Eq. (2.10) and Eq. (2.14) discussed in section 2.2 for relative refractive index $n = 1.5$ and a Gaussian beam according to Eq. (2.11) with two different widths ϵ (first and second row, respectively).

Goos-Hänchen shift corresponds to the uncorrected trajectory in a larger but similar polygon. The angular shift induced by the Fresnel filtering, however, can have a strong effect on the trajectories in the cavity and the directions of the transmitted light.

The Fresnel filtering correction used here is calculated by the expectation value approach discussed in section 2.2 for the reflected and the transmitted beam. The transverse beam profile of the incident beam is a normal distribution in the momentum $p = \sin(\chi)$ according to Eq. (2.11). The resulting angular shifts in reflection and transmission for two different distributions of incident angles with a larger and a smaller standard deviation are shown in Fig. 4.3.

The two different beam widths correspond to different cavity sizes. There is no absolute length scale in the system, the cavity is described by the dimensionless size parameter nkL and the beam by the dimensionless beam parameter

ϵ. If the wavenumber k, or equivalently the wavelength $\lambda = 2\pi/k$, is kept fixed the cavity size can also be expressed by the effective size $\tilde{L} = \epsilon L$ measured in terms of the beam width. In this interpretation, a larger absolute cavity size L is needed to obtain the same effective size $\tilde{L}$ for a smaller beam parameter ϵ.

Including the Fresnel filtering effect in the ray model, the angles of reflection and transmission are no longer given purely by the law of reflection and Snell's law but are given as a function of the angle of incidence, $\chi^{\mathrm{ref}} = \chi^{\mathrm{in}} + \Delta\chi^{\mathrm{ref}}_{\mathrm{FF}}(\chi^{\mathrm{in}})$ and $\chi^{\mathrm{trans}} = \arcsin(n \sin(\chi^{\mathrm{in}})) + \Delta\chi^{\mathrm{trans}}_{\mathrm{FF}}(\chi^{\mathrm{in}})$.

4.2.4 Electromagnetic wave simulations

Full electromagnetic wave simulations of triangular optical microcavities have been performed by Jakob Kreismann using the finite-difference time-domain (FDTD) method [50]. In a first step, the resonant modes of the cavities are calculated. Then, the far-field emission is determined for the longest-lived modes where the life time is given in terms of the quality factor Q. As we discuss in this section mostly systems with low relative refractive index the light is poorly confined in the cavities. Thus, the modes decay very fast and the quality factors are low.

Throughout this chapter, we refer to these wave simulations and the resulting far-field emission or mode patterns are shown as a benchmark for the ray-optical calculations. We use the comparison to the wave results, especially, to test the finite size effects which are one of the main topics of this thesis.

4.3 Equilateral triangle

The equilateral triangle is the triangle with the highest symmetry and shows integrable billiards dynamics. Nevertheless, it is an interesting model system to study the interplay of the optical properties and the geometry [50].

4.3.1 Maximum intensity trajectories

All billiards-trajectories in an equilateral triangle can be easily constructed. Due to the symmetry, each trajectory is characterized by exactly three angles of incidence χ_1, χ_2, χ_3. Each trajectory is then given by a certain sequence of the χ_i that depends sensitively on the initial condition (the starting direction chosen at a certain point on one side of the triangle). Clearly, a generic trajectory will close only after infinite time and, therefore, is not periodic. Let $0^\circ \leq \chi_1 < 30^\circ$ be the initial angle of incidence, then $\chi_2 = 60^\circ - \chi_1$ and $\chi_3 = -(60^\circ + \chi_1)$ [110]. The sign of the angle χ specifies the directions of the incoming and outgoing rays at the corresponding reflection point, where the opposite sign changes the direction of the trajectory. The angle χ_3 with the largest absolute value always has the opposite sign in comparison to the two smaller angles, χ_1 and χ_2. Trajectories with reversed signs in all angles are equivalent except for their sense of rotation, we can thus restrict our considerations to the case $\chi_1 \geq 0^\circ$. An exemplary trajectory with starting angle $\chi_1 = 20^\circ$ and the resulting angles $\chi_2 = 40^\circ$ and $\chi_3 = -80^\circ$ is shown in Fig. 4.4(a). We note that the larger χ_1 is, the less frequent occurs χ_3 along the trajectory sequence. The two limiting cases are the quasi-Fabry-Perot orbit with $\chi_1 = 0^\circ$ and $\chi_{2/3} = \pm 60^\circ$ (sequence $\chi_1, \chi_2, \chi_1, \chi_3, \chi_1, \ldots$) and the inscribed triangle (and the corresponding family of period-doubled orbits) with

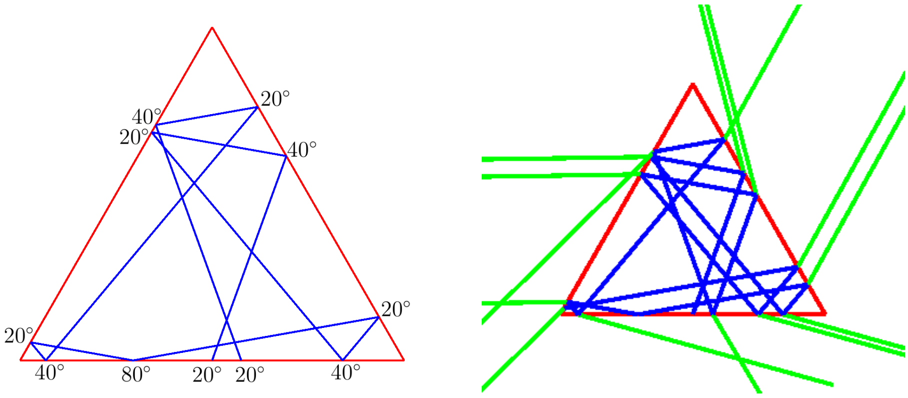

(a) Trajectory in the closed system.

(b) Trajectory in the open system with transmission for refractive index $n = 1.5$.

Figure 4.4: Exemplary trajectory in an equilateral triangle with starting angle $\chi_1 = 20^\circ$ and the resulting angles $\chi_2 = 40^\circ$ and $\chi_3 = -80^\circ$.

$\chi_1 = \chi_2 = 30^\circ$ where χ_3 does not occur any more.

So far, the intrinsic openness of the dielectric cavities has not been considered. As an example, we show the transmission due to refraction of the trajectory with starting angle $\chi_1 = 20^\circ$ in Fig. 4.4(b). Now, we discuss which of the possible trajectories are responsible for the emission characteristics of the dielectric triangular cavity. We find that trajectories, which maximize the reflected intensity inside the cavity, dominate the far-field emission. Although these trajectories are, in general, neither periodic nor simple, they determine the far-field emission for the following reason. For the equilateral triangle cavities with relatively low refractive index considered here, at least one of the angles of incidence lies below the critical angle since for $n < 2$ the critical angle of total internal reflection is $\chi_\mathrm{c} > 30^\circ$. Therefore every possible trajectory suffers refractive losses. In the long time limit, trajectories which retain the most reflected intensity inside the cavity will dominate the far-field emission. In other words, trajectories are favored that minimize their decay rate.

In Fig. 4.5 we show the decay rates of the trajectories in an equilateral triangle cavity with relative refractive index $n = 1.5$ with critical angle $\chi_c \approx 41.8^\circ$ and Brewster angle $\chi_B = \arctan(1/n) \approx 33.7^\circ$. Similar to Fig. 3.21 we show the decay rate for each trajectory in color code at the position of its initial condition given by the position s on the boundary and the incident angle χ. The boundary coordinate s is chosen to start in one of the three corners and $s = 1$ corresponds to the full perimeter of the cavity. As no trajectory is confined inside the cavity by total internal reflection, we find $\kappa > 0$ for all initial conditions. In general, the decay rates found here are much higher than the decay rates found for the deformed disk cavity discussed in the previous chapter (*cf.* Fig. 3.21) which is due to the lower refractive index considered here.

In the close-up on the initial conditions of the trajectories with small decay rates, right panels of Fig. 4.5, we can identify the trajectories which minimize the averaged refractive losses along their path. For TE polarization, we find the smallest decay rates for initial incident angles $\chi \approx 0^\circ$ and $\chi \approx \pm 60^\circ$ almost independent of the position on the boundary. These initial conditions belong to a family of simple periodic trajectories, the so-called quasi-Fabry-Perot trajectories shown in Fig. 4.6. For TM polarization, the smallest decay rates are found for trajectories with initial incident angles $\chi \approx \pm 18^\circ$, $\chi \approx \pm 42^\circ$, and $\chi \approx \pm 78^\circ$ for all initial positions on the boundary. These initial conditions also belong to only one family of trajectories, two representatives of this family are shown in Fig. 4.6.

In the case of the equilateral triangle where we can easily construct each trajectory we can also understand qualitatively which trajectories retain the highest intensity. We demand that the angle χ_1 with $0^\circ \leq \chi_1 < 30^\circ$ yields maximum reflectivity under the constraint that χ_2 and χ_3 remain above the critical angle contributing no refractive loss due to total internal reflection. The intensity reflection coefficients $R(\chi)$ and the resulting maximum intensity

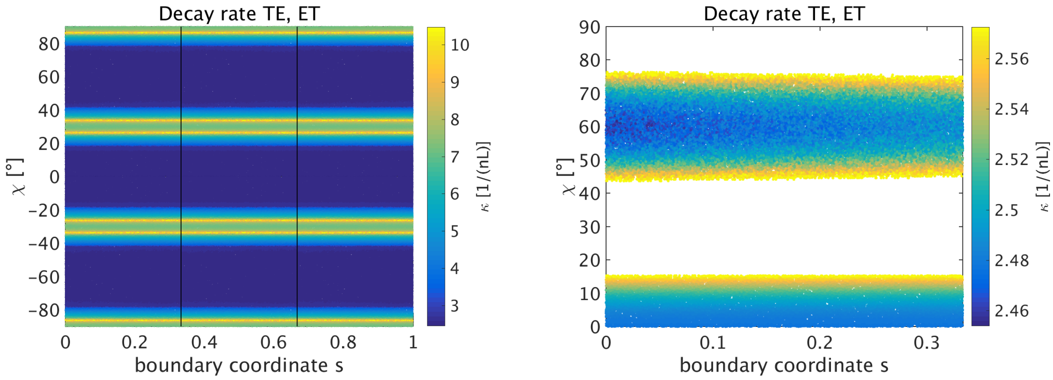

(a) TE polarization.

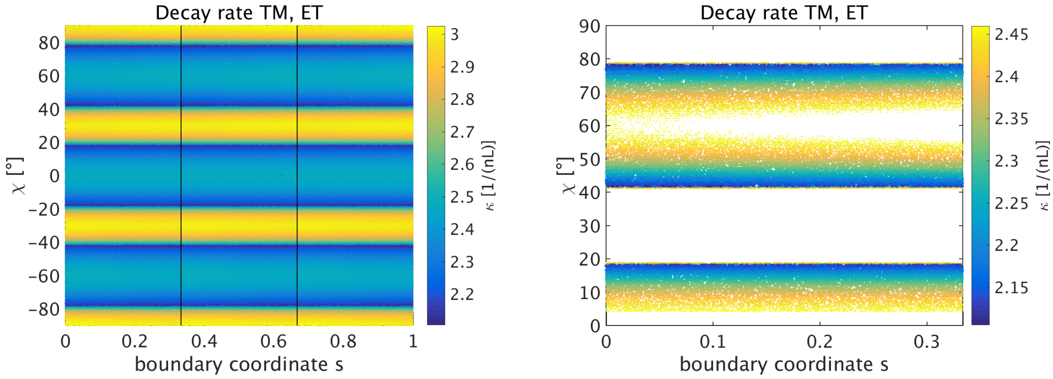

(b) TM polarization.

Figure 4.5: Decay rates of the trajectories in an equilateral triangle cavity with relative refractive index $n = 1.5$ ($\chi_c \approx 41.8°$, $\chi_B \approx 33.7°$). *Left:* Decay rates of all trajectories. The vertical lines denote the positions of the corners. *Right:* Close-up on smallest nonzero decay rates, only for rays starting on one of the three sides with positive angle of incidence (all remaining initial conditions are connected by symmetry). Note the different color scales in all four panels.

trajectories are depicted in Fig. 4.6 for both polarizations. For TE polarization, the highest reflectivity in the interval allowed for χ_1 is given for normal incidence, due to the vanishing reflectivity at the Brewster angle. This leads to the quasi-Fabry-Perot trajectories with $\chi_1 = 0°$, $\chi_2 = 60°$, $\chi_3 = -60°$. For TM polarization, however, the reflection coefficient increases monotonically. The angle $\chi_1 \approx 18°$ is the highest possible angle such that the next angle $\chi_2 = 60° - 18° = 42°$ is (just) above the critical angle. The corresponding maximum intensity trajectories with $\chi_1 = 18°$, $\chi_2 = 42°$, $\chi_3 = -78°$ are not simply periodic.

The emission of these maximum intensity trajectories is indeed found to dominate the far-field emission of the equilateral triangle which is discussed in detail in the following sections.

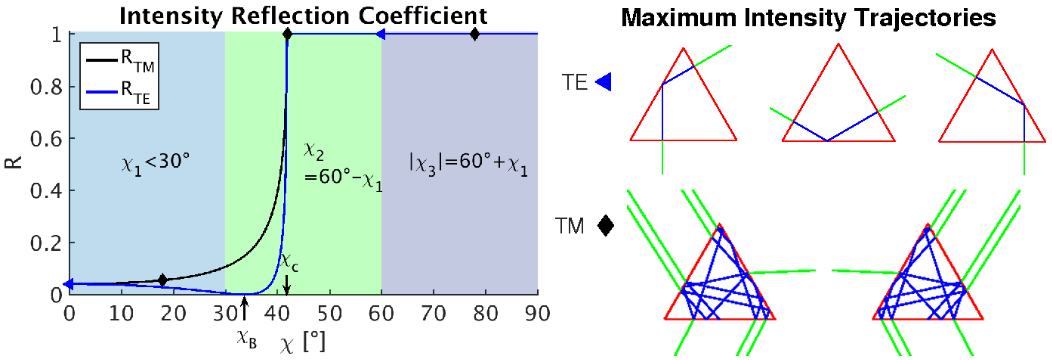

Figure 4.6: *Left:* The intensity reflection coefficient $R(\chi)$ for relative refractive index $n = 1.5$ for both polarizations, TE and TM. The intervals of possible incident angles in the equilateral triangle are marked by shading. The triangles and diamonds denote the incident angles of the maximum intensity trajectories for TE and TM polarization, respectively. *Right:* Examples of the families of maximum intensity trajectories for both polarizations. Quasi-Fabry-Perot orbits with $\chi_1 = 0°$, $\chi_2 = 60°$, $\chi_3 = -60°$ for TE polarization. Non-periodic trajectories with $\chi_1 = 18°$, $\chi_2 = 42°$, $\chi_3 = -78°$ for TM polarization.

4.3.2 Influence of amplification

In Fig. 4.7, we show the far-field emission of the equilateral triangle cavity calculated from usual, passive ray optics for both polarizations. The intensity is scaled such that the maximum equals 1 in each case. To obtain these results an ensemble of 600 000 rays (100 000 on each side in both directions) is propagated through the cavity for 200 reflections with the boundary. The initial conditions are uniformly distributed in angle and position on one of the three sides and symmetrized with respect to the symmetry of the cavity. The initial intensity of each ray is 1. We collect the transmitted intensities in some time interval $\tau_1 \leq t \leq \tau_2$ to calculate the far-field intensity distribution. The time is measured by the distance a light ray has traveled. We find the calculated far-field to be independent of the end time τ_2, however, it can be dependent of the starting time τ_1. Therefore, we show the far-field for different starting times in Fig. 4.7.

For TM polarization (see Fig. 4.7(b)), the calculated far-field is almost independent of the chosen time interval and can be nicely explained by the predicted family of maximum intensity trajectories. The angle of incidence $\chi_{\text{in}} = 18°$ leads to the angle of transmission $\chi_{\text{ref}} = \arcsin(n \sin(\chi_{\text{in}})) \approx 27.6°$. Taking into account the threefold symmetry of the cavity and the two possible traveling directions along the trajectory, gives the six observed far-field angles.

In the case of TE polarization (see Fig. 4.7(a)), however, the calculated far-field emission shows a strong sensitivity on the time interval used to collect the transmitted intensity. The main emission direction is perpendicular to

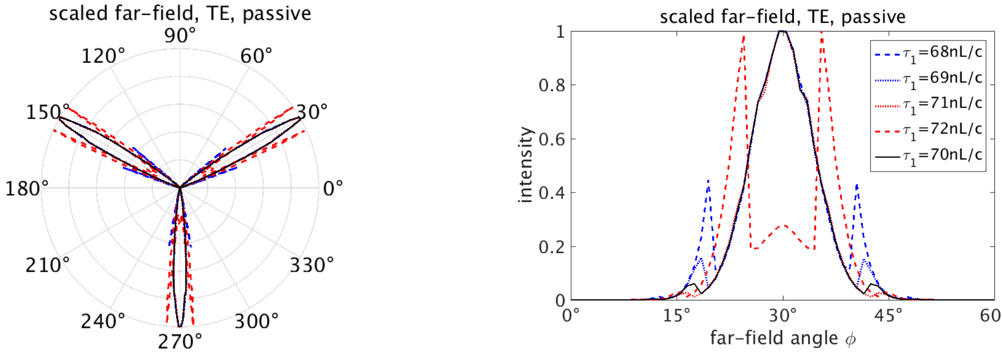

(a) TE polarization.

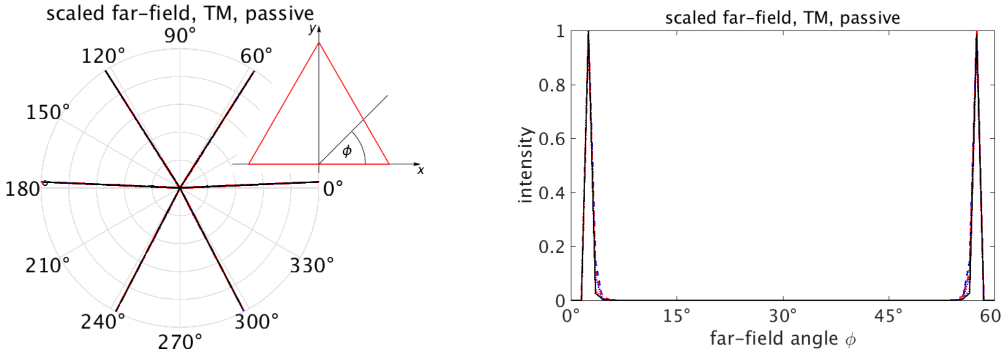

(b) TM polarization.

Figure 4.7: Far-field emission of the equilateral triangle from usual, passive ray optics. The far-field is collected in the time interval $\tau_1 \leq t \leq \tau_2$ with τ_1 varied and $\tau_2 = 86\,nL/c$ for all curves. Time is given in units of the optical path length, with the length L of one triangle side and c/n the speed of light in the medium. The inset in (b) defines the far-field angle ϕ and the orientation of the triangle with respect to the coordinate system.

the sides as expected for the quasi-Fabry-Perot trajectory. Depending on the chosen starting time, however, other directions have a significant contribution. Hence we cannot deduce a reliable prediction from the ray calculations.

To understand this behavior, we have to take a closer look at the possible trajectories in the triangular cavity. In contrast to the chaotic cavities discussed in the last chapter where a trajectory can be confined inside the cavity for a long time before it is eventually partially transmitted, every trajectory in the equilateral triangle with low refractive index transmits some intensity at least at every third reflection. That means that the intensity of every ray decreases rapidly. If several families of trajectories that lead to different far-field directions have comparable intensities but emit intensity at different times, the observed far-field emission depends very much on which of these trajectories transmits the highest intensity in the chosen time interval.

To make this point clearer we look at the quasi-Fabry-Perot trajectory

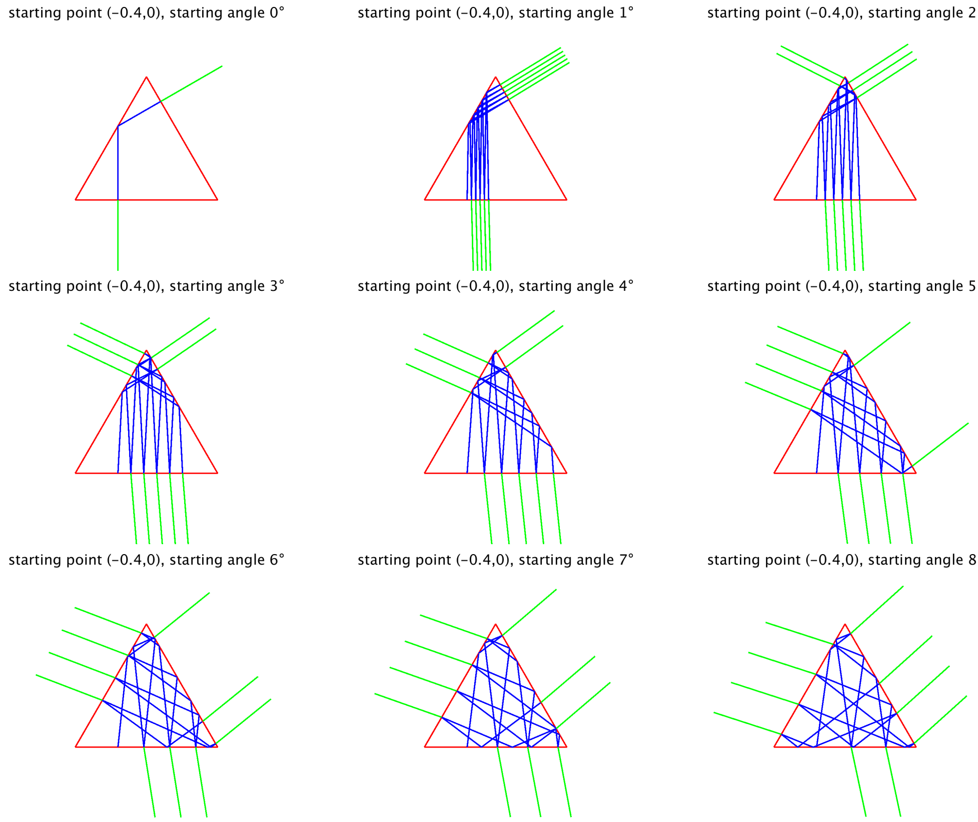

Figure 4.8: Sample trajectories that contribute to the far-field emission for TE polarization.

which is the maximum intensity trajectory for TE polarization and some other trajectories with angles $\chi_1 \leq 9^\circ$ which are expected to retain only slightly lower intensity. Examples of the families of these trajectories are depicted in Fig. 4.8 for a small number of reflections. The transmitted intensity of an ensemble of trajectories belonging to these families is plotted in Fig. 4.9 for a small interval of pathlengths corresponding to the starting times τ_1 used to calculate the far-field of Fig. 4.7. If we start to collect the transmitted intensities from this ensemble of trajectories in different intervals of time we see that the different families of trajectories contribute with varying weight to the accumulated intensity depending on the starting time.

We will look more closely at two examples. Firstly, we sum up the intensities that are transmitted for times $t \geq 68\,nL/c$. In this case, we find that the quasi-Fabry-Perot trajectories with $\chi_1 = 0^\circ$ give the highest contribution. However, trajectories with $\chi_1 > 0^\circ$ also have a non-negligible contribution. Thus we expect broad emission peaks with the maximum perpendicular to the sides of the triangle showing also contributions at angles tilted to the boundary normals. Secondly, we collect the intensities transmitted after $t = 72\,nL/c$. Then, the highest intensities come from trajectories with $\chi_1 \gtrsim 4^\circ$ and the contributions from the quasi-Fabry-Perot trajectories are approximately one order

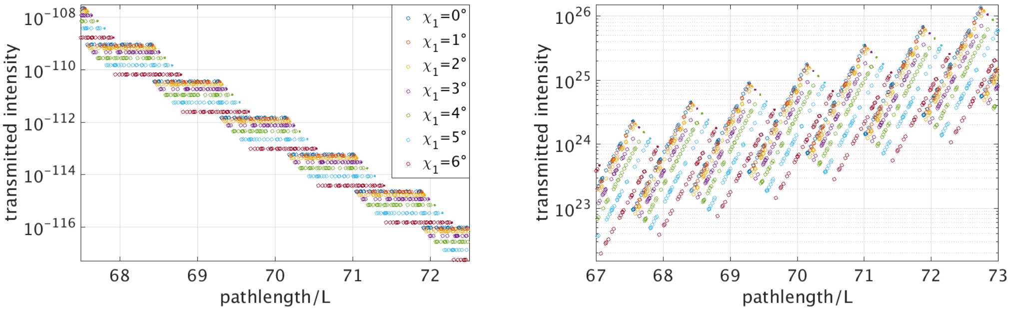

(a) Standard (passive) ray optics.

(b) Active ray optics.

Figure 4.9: Transmitted intensities in a small interval of time of trajectories that retain high intensity in the equilateral triangle for TE polarization.

of magnitude smaller than the maximum contribution. From this we expect the maximum far-field emission in directions tilted with small angles towards the boundary normals and suppressed emission directly perpendicular to the sides of the cavity. These two examples explain the far-field plotted as dashed lines in Fig. 4.7 (blue dashed: $\tau_1 = 68\, nL/c$, red dashed: $\tau_1 = 72\, nL/c$) and similar argumentation applies for other time intervals.

After a very long time, the family of maximum intensity trajectories will eventually outperform all other trajectories. For practical reasons, however, the calculations cannot be done for indefinitely long times. Especially the rapidly decreasing intensities limits the maximum number of reflections for which reasonable and numerically reliable results can be obtained.

We find that this problem can be solved if amplification in the active material is included in the ray simulation. The far-field pattern calculated from the ray model including amplification according to Eq. (4.2) is shown in Fig. 4.10. The gain coefficient is chosen to be $\alpha = 3L^{-1}$ where L is the length of one side of the triangle, all other parameters are the same as in the passive calculation. The far-field emission pattern for TM polarization does not change qualitatively compared to the passive case. For TE polarization, however, the emission is now independent of the interval used to calculate the far-field intensities. It shows emission lobes perpendicular to the triangle sides as expected from the maximum intensity trajectories.

In the active case, in contrast to the passive case, the quasi-Fabry-Perot trajectories contribute the highest intensity to the far-field in every (sufficiently long) interval of time. As the intensity amplification is proportional to the current intensity in the trajectory, the maximum intensity trajectories are amplified most strongly. This self-enhancing effect narrows the distribution of trajectories that contribute to the far-field. Consequently, the directionality is enhanced and the influence of the transition time, before the simulated measurement starts, is diminished. This can also be seen if we look at the

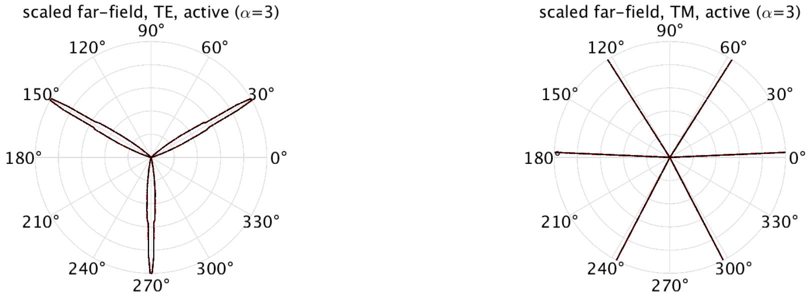

(a) TE polarization.

(b) TM polarization.

Figure 4.10: Far-field emission of the equilateral triangle from ray optics including intensity amplification according to Eq. (4.2) with $\alpha = 3L^{-1}$ where L is the length of one side of the triangle. The same time intervals for collecting the transmitted intensity as in Fig. 4.7.

transmitted intensities of the sample trajectories shown in Fig. 4.9(b).

For TM polarization the difference in intensity of the maximum intensity trajectory and slightly deviating ray trajectories is larger than for TE polarization, hence, the emission peaks are narrow even without amplification and the transition time does not play a role from the beginning. Consequently, the amplification has no qualitative effect on the far-field emission. However, it still has a quantitative effect leading to considerably higher total intensities. Thus, the active ray description introduced here yields more reliable results in the case of the highly lossy cavities made of low refractive index material (see also [50]).

From this argumentation we can also deduce the necessary gain coefficient α. It has to be chosen sufficiently large that at least the intensity of the maximum intensity trajectory increases in time.

4.3.3 Influence of beam shifts

In this section, the influence of the wave corrections, here only the Fresnel filtering effect, on the far-field emission of the equilateral triangle is discussed. For TE polarization, the correction terms shown in Fig. 4.3 included in an amended ray optics description do not have any influence on the far-field emission pattern. Therefore, it is not shown here. As discussed above, the far-field emission for TE polarization is dominated by the quasi-Fabry-Perot orbits which have incident angles far away from the critical angle where the wave corrections are small. Thus, the influence of the Fresnel filtering effect on these trajectories is small and other trajectories are not influenced strong enough to gain importance.

For TM polarization, however, the Fresnel filtering effect has a strong influ-

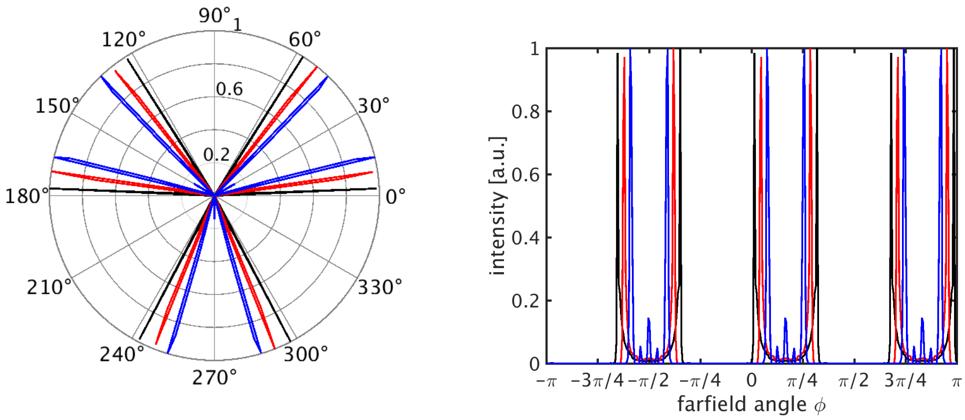

(a) Far-field in polar plot. (b) Far-field.

Figure 4.11: Influence of wave effects on the far-field emission of an equilateral triangle cavity for TM polarization. Far-field for TM polarization from pure ray optics (black) and from amended ray optics with moderate (red) and strong (blue) Fresnel filtering corrections included, see Sec. 4.2.3 for details concerning the correction terms. The far-field is calculated after a transition time of $\tau = 10\, nL/c$.

ence on the far-field emission characteristics. Figure 4.11 shows a comparison of the far-fields calculated from usual ray optics (black curves) and amended ray optics including both, the moderate (red curves) and the strong (blue curves), Fresnel filtering corrections given in Fig. 4.3. The maximum intensity trajectory that has been found to be mainly responsible for the far-field emission of TM polarized light has one incident angle close to the critical angle where the wave corrections are strong. This explains the deviations between the results of the usual and the amended ray optics. For large Fresnel filtering corrections, *i.e.* small cavities, the perturbation of the trajectories is so strong that the quasi-Fabry-Perot orbits give a small additional contribution to the far-field leading to small emission peaks perpendicular to the triangle sides.

This finding is interesting as the wave corrections are typically larger for TE polarized light. Hence, finite wavelength effects are observed more often for TE polarization than for TM polarization. The exceptional structure of the equilateral triangle leads to the opposite effect. Whereas the far-field emission of TE polarized light is not affected, we observe here a large influence of the Fresnel filtering effect for TM polarization.

4.3.4 Comparison to wave simulations and experiment

Now, we compare the predictions made from the ray-optical description of the equilateral triangle to results from experiment and wave simulations. In the experiment [126], the triangular microlasers only emit TE polarized light. For the equilateral triangle, they find narrow emission peaks perpendicular

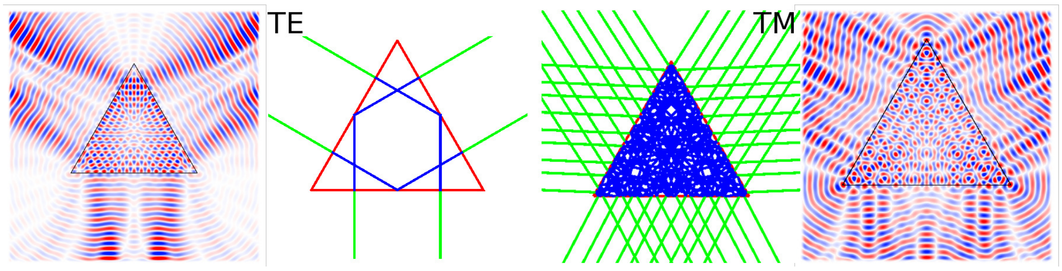

Figure 4.12: Mode patterns obtained from full electromagnetic wave simulations in the equilateral triangle cavity for both polarizations, TE and TM, in comparison with the predicted maximum intensity trajectories. The wave patterns show the modes used to calculate the far-fields in Fig. 4.13. Wave simulations courtesy of J. Kreismann.

to the triangle sides what is also found here with the ray model including amplification.

We can also estimate if the gain coefficient that we have chosen above is reasonable in comparison to the experiment. The equilateral triangle used in the experiment has a side length $L \approx 300\,\mu\text{m}$ [126]. Our gain coefficient then corresponds to $\alpha = 3L^{-1} \hat{=} 100\,\text{cm}^{-1}$. Although the gain coefficient is not reported in [126], the value is in line with values reported for similar dye doped polymer lasers [132, 133].

In Fig. 4.12, the mode patterns of the longest-lived modes of the wave simulations are shown together with examples of the predicted maximum intensity trajectories. The qualitative agreement between the wave and ray patterns further illustrates the correspondence of the two approaches. The low Q-factors of the modes, $Q = 85$ for the TE polarized mode and $Q = 230$ for the TM polarized mode, corresponding to low life times reflect the poor confinement of the light inside the cavity which is expected for the low relative refractive index.

Figure 4.13 shows a comparison of the far-field emission obtained from ray optics and from the longest-lived modes of the wave simulations. For TE polarization the two results agree well. The wave simulation also yields emission perpendicular to the triangle sides. For TM polarization, however, the result of the uncorrected ray-optics description, given by the black curve in the figure, does not agree well with the result of the simulation. The finite wavelength is not negligible in this case and the results of the amended ray optics including moderate wave corrections, given by the red curve, yields good agreement with the simulation. The need for wave-corrections is obvious as ray optics is strictly only valid in the limit $kL \to \infty$, whereas the wave simulations are performed in the regime $kL \approx 100$.

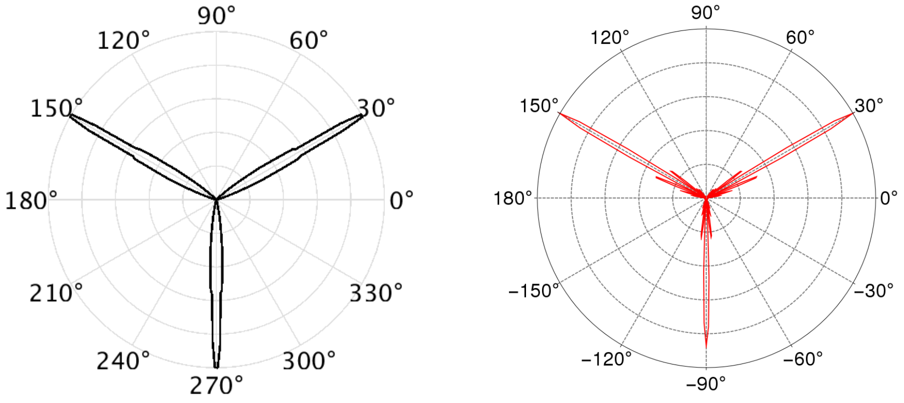

(a) TE polarization, ray (left) and wave (right) results.

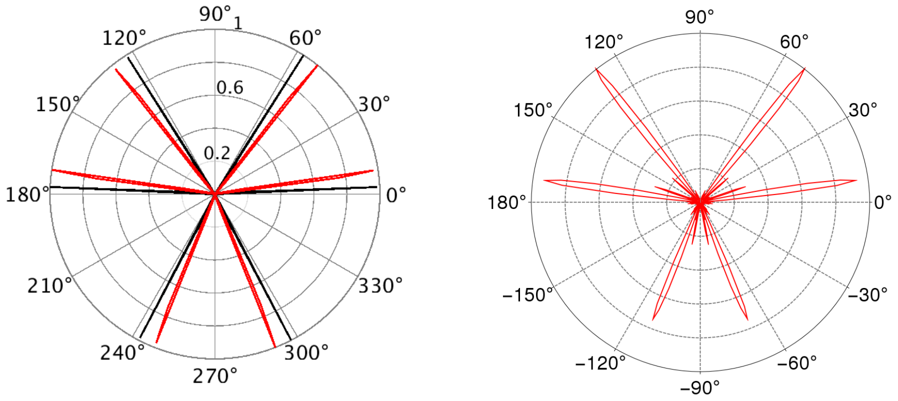

(b) TM polarization, ray (left) and wave (right) results.

Figure 4.13: Far-field emission patterns of the equilateral triangle cavity obtained from ray optics including amplification and from electromagnetic wave simulations for both polarizations, (a) TE and (b) TM. The wave results are calculated from the mode with the longest life-time in the cavity. The dimensionless wave numbers and quality factors of the corresponding modes are $\mathrm{Re}(kL) \approx 81$, $Q = 85$ for TE and $\mathrm{Re}(kL) \approx 96$, $Q = 230$ for TM where k is the wavenumber and L is the side length of the triangle. The additional red curve in the ray optics result for TM polarization shows the result of amended ray optics including moderate Fresnel filtering, see Sec. 4.2.3 for details concerning this correction. Wave simulations courtesy of J. Kreismann.

4.3.5 Influence of the refractive index

So far, we have discussed the equilateral triangle only for the relative refractive index $n = 1.5$. The construction of the maximum intensity trajectories relies strongly on the position of the critical angle with respect to the angles of the possible trajectories. Therefore it is interesting to study the equilateral triangle also for different refractive indices.

For small relative refractive indices $n < 2$ the argumentation leading to the maximum intensity trajectory is similar as in the discussion given above. This line of thought leads to the quasi-Fabry-Perot orbits as the maximum intensity trajectory for TE polarization. For TM polarization, the reflectivity is maximized for a trajectory with χ_2 just above the critical angle and the corresponding angle $\chi_1 = 60° - \chi_2$ determines the emission directions.

As another example for a small refractive index, we have chosen $n = 1.75$ with critical angle $\chi_c \approx 34.9°$. The calculated far-field emission for this system

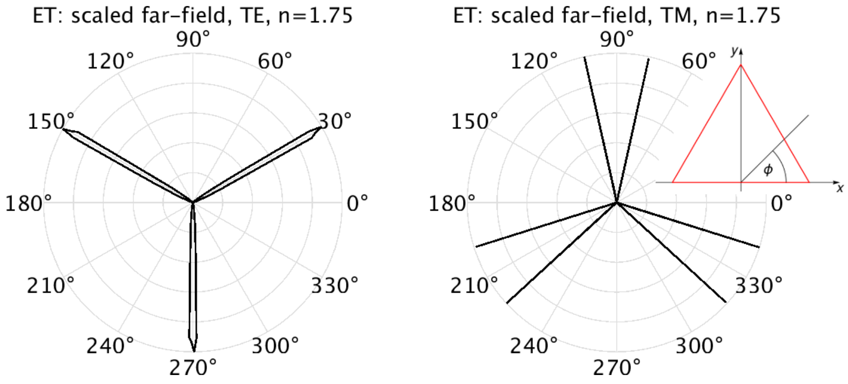

(a) $n = 1.75$, TE polarization.
(b) $n = 1.75$, TM polarization.

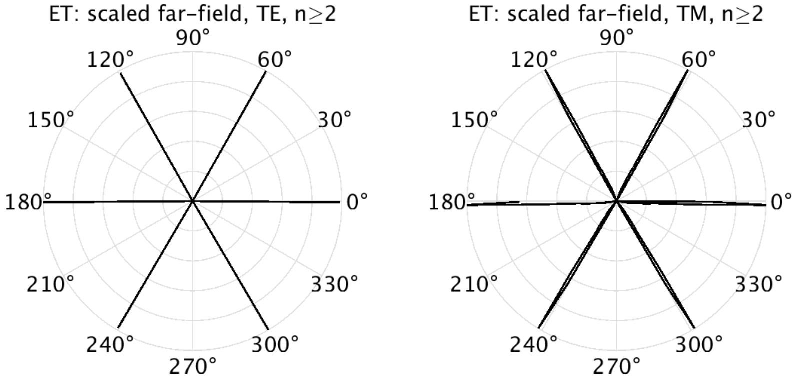

(c) $n = 3.3$, TE polarization.
(d) $n = 3.3$, TM polarization.

Figure 4.14: Far-field emission patterns of the equilateral triangle cavity with two different refractive indices obtained from ray optics including amplification for both polarizations, TE and TM. The inset in (b) defines the far-field angle ϕ and the orientation of the triangle with respect to the coordinate system.

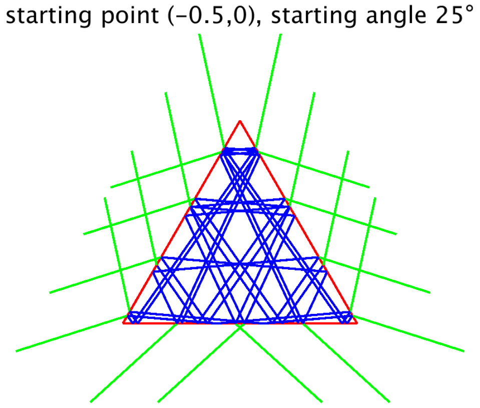

Figure 4.15: Maximum intensity trajectory in the equilateral triangle with relative refractive index $n = 1.75$ for TM polarization, angles of incidence $\chi_1 = 25°$, $\chi_2 = 35°$, $\chi_3 = -85°$.

is shown in Fig. 4.14(a) and (b). For TE polarization, we find again emission peaks perpendicular to the triangle sides which shows that the far-field emission is indeed dominated by the family of quasi-Fabry-Perot orbits. The predicted maximum intensity trajectory for TM polarization is the trajectory with $\chi_1 \approx 25°$, $\chi_2 \approx 35°$, $\chi_3 \approx -85°$ shown in Fig. 4.15. The resulting angle of refraction $\chi_{\text{out}} = \arcsin(n \sin(\chi_1)) \approx 47.7°$ together with the symmetry of the triangle explains nicely the observed intensity distribution in Fig. 4.14(b).

For larger refractive indices, $n \geq 2$, the critical angle is $\chi_c \leq 30°$. Thus, there exist trajectories in the equilateral triangle which are confined inside the cavity by total internal reflection for all times. The maximum intensity trajectories are now those trajectories that never leave the cavity which, however, do not contribute to the far-field. The emission is expected to be dominated by the trajectories with the smallest non-vanishing transmission. These are the trajectories with χ_1 just slightly below the critical angle leading to transmission parallel to the sides of the triangle independent of the precise position of the critical angle. In Fig. 4.14(c) and (d) we show the calculated far-field emission for an equilateral triangle with $n = 3.3$. The intensity distribution is indeed explained by emission parallel to the sides of the cavity. This is found true for all refractive indices $n \geq 2$.

4.4 Right isosceles triangle

The right isosceles triangle is the second example of a triangle with classical integrable dynamics. In contrast to the equilateral triangle, it shows only one symmetry, the mirror symmetry with respect to the height perpendicular to the hypotenuse. As it is a half of a square, known properties from square resonators can be translated to the right isosceles triangle.

4.4.1 Trajectories

For the construction of possible trajectories in the right isosceles triangle it is sufficient to restrict the initial conditions to points on one half of the hypotenuse and positive starting angles $\alpha < 45°$. Along the path, reflections occur at the legs with $\pm(45° \pm \alpha)$ and at the hypotenuse with $\pm\alpha$ and $\pm(90° - \alpha)$. All other trajectories are related by symmetry to such a trajectory. Some sample trajectories are shown in Fig. 4.16

From this construction of the possible trajectories it is seen that there is no trajectory that is completely trapped inside the cavity by total internal reflection. In the right isosceles triangle with relative refractive index $n = 1.5$ every trajectory suffers refractive losses. From the decay rates in Fig. 4.17 we

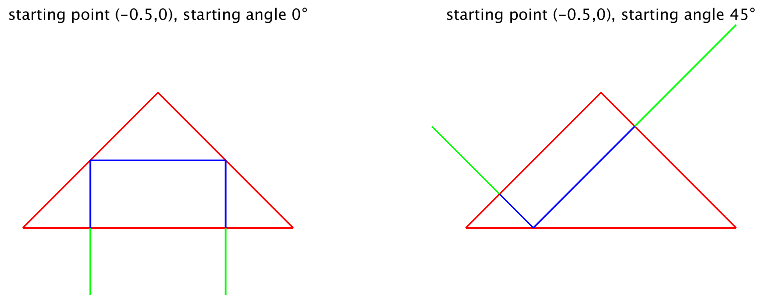
starting point (−0.5,0), starting angle 0°

starting point (−0.5,0), starting angle 45°

(a) Quasi-diamond trajectory.

(b) Quasi-Fabry-Perot trajectory.

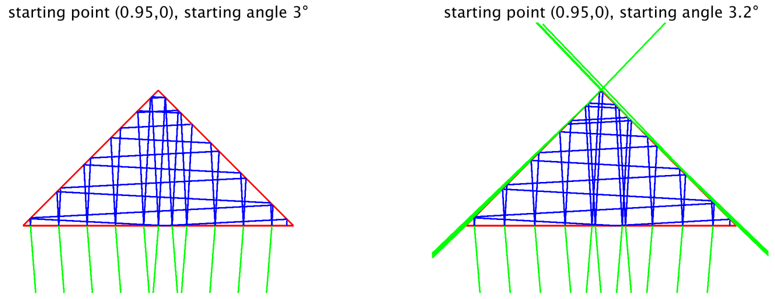
starting point (0.95,0), starting angle 3°

starting point (0.95,0), starting angle 3.2°

(c) High intensity trajectory for TM polarization.

(d) Trajectory exhibiting “grazing emission”.

Figure 4.16: Trajectories in the right isosceles triangle for relative refractive index $n = 1.5$, two simple periodic trajectories and two generic trajectories.

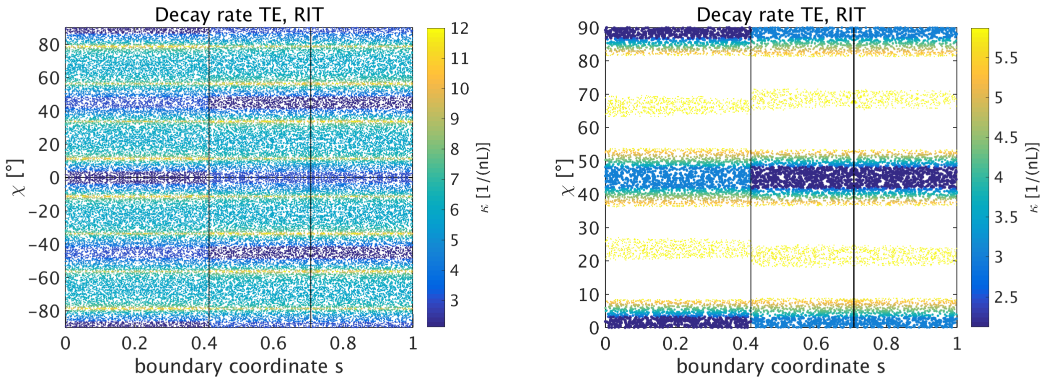

(a) TE polarization.

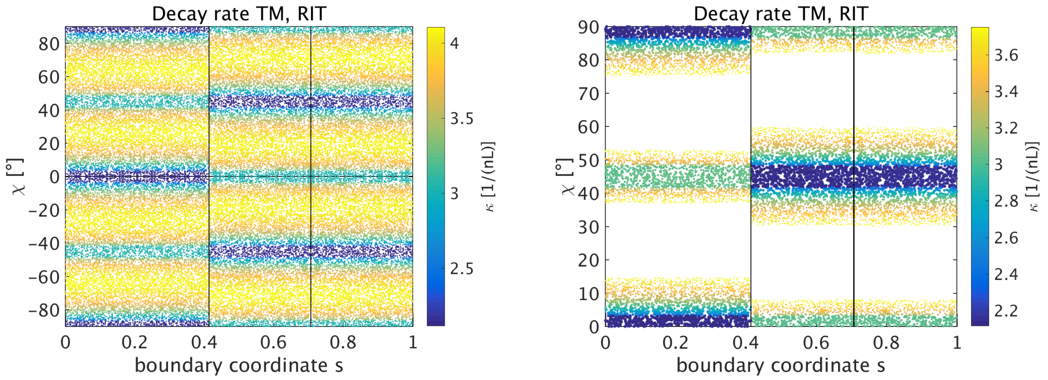

(b) TM polarization.

Figure 4.17: Decay rates κ of the trajectories in a right isosceles triangle cavity with relative refractive index $n = 1.5$ ($\chi_c \approx 41.8°$, $\chi_B \approx 33.7°$). The boundary coordinate s is scaled that the perimeter of the cavity equals 1, it runs first over the hypotenuse and then over the two legs. The vertical lines denote the positions of the corners. *Left:* Decay rates of all trajectories. *Right:* Close-up on smallest nonzero decay rates, only for rays starting with positive angle of incidence (the remaining initial conditions are connected by symmetry). Note the different color scales in all four panels.

infer the trajectories with the lowest averaged losses which are expected to dominate the far-field emission. For both polarizations, we find small decay rates for initial angles $\chi \approx 0°$ and $\chi \approx \pm 90°$ for starting positions on the hypotenuse and for initial angles $\chi \approx \pm 45°$ on the legs. The initial conditions $\chi = 0°$ on the hypotenuse and $\chi = 45°$ on the legs lead to the family of quasi-diamond trajectories as shown in Fig. 4.16(a). However, trajectories with slightly deviating initial conditions like the one shown in Fig. 4.16(c) have comparably low decay rates like the simple periodic quasi-diamond trajectory.

It is easily understood that slight deviations from the quasi-diamond trajectory starting from the hypotenuse with a small angle $\alpha \neq 0$ retain almost the same intensity as the original periodic trajectory, as long as the next angle of incidence at the leg ($45^\circ - \alpha$) stays above the critical angle $\chi_c \approx 41.8^\circ$ which is the case for $\alpha < 3.2^\circ$. For TM polarization, the reflected intensity that stays in the cavity is even a bit larger for these non-periodic trajectories, as the reflection coefficient is monotonically increasing. For TE polarization, however, the reflection coefficient decreases for small angles and the trajectories deviating slightly from the quasi-diamond trajectory are less confined in this case. Thus, the maximum intensity trajectories for the right isosceles cavity with relative refractive index $n = 1.5$ are the quasi-diamond trajectory for TE polarization and slight deviations thereof with $\alpha \approx 3.2^\circ$ for TM polarization. Further, we expect that the trajectories with starting angle $\alpha < 3.2^\circ$ will play an important role for both polarizations.

If the angle α is only slightly larger the refractive loss at the legs is still small and the transmitted light is almost parallel to the legs giving rise to emission in the far-field directions $\pm 45^\circ$ and $\pm 135^\circ$. An example of such a trajectory is shown in Fig. 4.16(d). Although these trajectories suffer stronger losses than the maximum intensity trajectories their decay rates are still small and they can have a non-negligible contribution to the far-field emission.

The second family of simple periodic trajectories, the quasi-Fabry-Perot trajectories (see Fig. 4.16(b)) with angles $\chi = \pm 45^\circ$ on the hypotenuse and $\chi = 0^\circ$ on the legs, have considerably higher decay rates. Thus, such trajectories are not expected to have significant contribution to the far-field.

A similar scenario has been studied in detail in experiments with square dielectric resonators made of a $n \approx 1.5$-material [134, 135]. There, the periodic diamond-orbit ($\chi_{\text{in}} = 45^\circ$ on all sides) is completely confined by total internal reflection. However, emission parallel to the sides of the square is found which can be explained by open trajectories that deviate slightly from the diamond-orbit such that the angle of incidence on two parallel sides $\chi_{\text{in1}} = 45^\circ - \epsilon$ is slightly below the critical angle and the incident angle on the remaining two sides $\chi_{\text{in2}} = 45^\circ + \epsilon$ is still well above the critical angle. As the right isosceles triangle is just a square cut in half, the effect that happens at the sides of the square happens here at the legs of the triangle. Only the boundary imposed by the hypotenuse no longer allows for complete confinement by total internal reflection.

4.4.2 Far-field emission

The far-field emission of the right isosceles triangle calculated from the ray model with and without amplification after different transition times is shown in Fig. 4.18 for both polarizations. The intensity is scaled such that the maximum intensity corresponds to 1. The far-field pattern is, indeed, dominated by the emission of the predicted maximum intensity trajectories. For TE polarization, the main emission peak is perpendicular to the hypotenuse (the -90°-direction) as expected from the quasi-diamond orbit shown in Fig. 4.16(a). For TM polarization, the emission is also mainly perpendicular to the hypotenuse

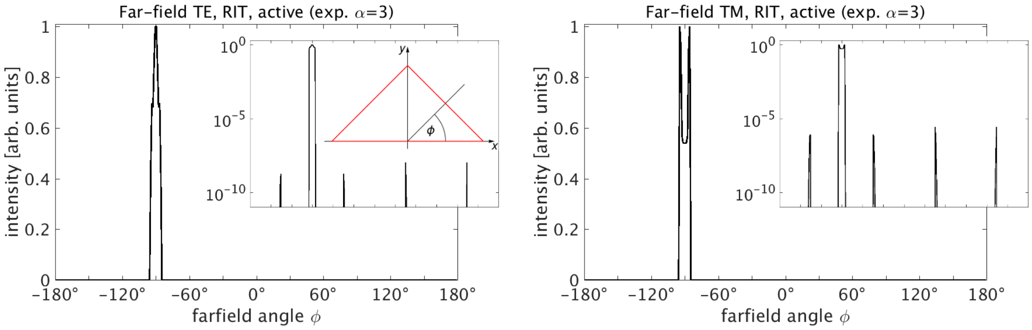

(a) TE polarization.

(b) TM polarization.

Figure 4.18: Far-field emission of the right isosceles triangle from ray optics with amplification (gain coefficient $\alpha = 3L^{-1}$ where L is the length of the hypotenuse) for both polarizations, TE and TM. *Insets:* Intensity on a logarithmic scale. The additional inset in (a) defines the far-field angle ϕ and the orientation of the triangle with respect to the coordinate system.

but with the highest emission in slightly tilted directions. In the close-up, small contributions in the directions ±45° and ±135° are seen additionally for both polarizations. For TE polarization, these additional peaks in the upper half-plane are higher than the peaks in the lower half-plane. This leads to the conclusion that both families of trajectories, the quasi-Fabry-Perot orbits shown in Fig. 4.16(b) and the small deviations from the quasi-diamond orbits with grazing emission shown in Fig. 4.16(c) make a small contribution here. For TM polarization, however, the peaks in the upper and the lower half-plane have almost the same height, thus, they are better explained by the grazing emission of the small deviations from the family of quasi-diamond orbits. This confirms the prediction of the maximum intensity trajectories discussed in the previous section.

Here, we show only the results of the active ray optics. In this example, the amplification in the ray description has only a small qualitative effect on the calculated far-field emission. However, the amplification has a considerable quantitative effect on the total intensity, leading to more reliable results, as already mentioned in the discussion of the influence of amplification in the last section.

4.4.3 Influence of beam shifts

Now, we examine the influence of wave corrections to the ray-optical description of the right isosceles triangle. The effect of the Fresnel filtering on the ray trajectories and on the far-field emission is discussed.

Figure 4.19 shows two sample trajectories resulting from Fresnel filtering corrected ray optics in the right isosceles triangle cavity. These ray trajectories are not exceptional but rather the rule for both polarizations and a broad range of initial conditions. The trajectories are pulled towards the quasi-diamond and the quasi-Fabry-Perot trajectories although their initial conditions are far from the initial conditions of the two periodic orbits. This effect is unique to the right isosceles triangle with relative refractive index around $n \approx 1.5$. There, the incident angle of 45° occurring in both simple periodic orbits is close to the critical angle. The Fresnel filtering effect is strongest around the critical angle and this large angular shift leads to a stabilization of the trajectories with on one of the two simple periodic trajectories. The fact that Fresnel filtering in reflection for TE polarization is negative below the critical angle due to the Brewster angle (*cf.* Fig. 4.3) accelerates this effect further for this polarization.

It has been proven that all periodic trajectories in right triangles are unstable [111, 112]. The inclusion of wave corrections into an amended ray optics model gives here, in the case of the right isosceles triangle, a mechanism to stabilize two short periodic trajectories, the quasi-diamond and the quasi-Fabry-Perot trajectory.

The stabilization of the trajectories on the two simple periodic trajectories is also reflected in the far-field emission shown in Fig. 4.20 calculated with the amended ray optics model. The emission is strongly suppressed in directions

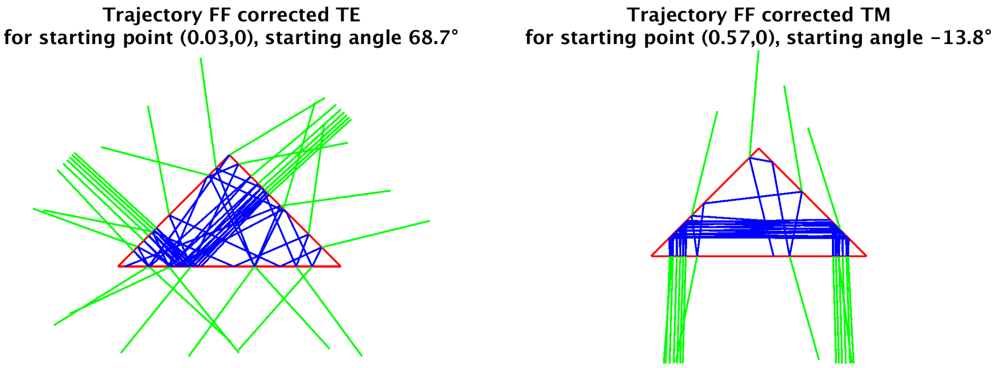

(a) Trajectory stabilized on a quasi-Fabry-Perot trajectory.

(b) Trajectory stabilized on a quasi-diamond trajectory.

Figure 4.19: Influence of the Fresnel filtering correction on the ray trajectories in the right isosceles triangle cavity with relative refractive index $n = 1.5$. Two ray trajectories subject to the strong Fresnel filtering correction shown in Fig. 4.3(c) and (d).

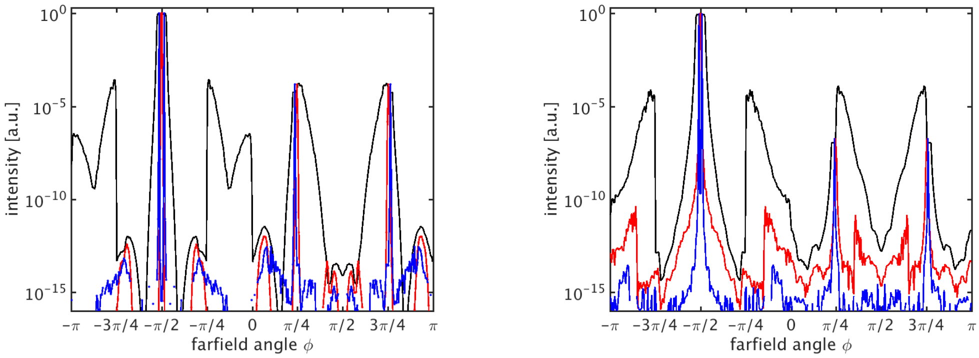

(a) TE polarization.

(b) TM polarization.

Figure 4.20: Influence of wave effects on the far-field emission of the right isosceles triangle cavity for both polarizations. Far-field calculated from pure ray optics (black) and from amended ray optics including the moderate (red) and strong (blue) Fresnel filtering corrections given in Fig. 4.3 (moderate: panels (a), (b); strong: panels (c), (d)), see Sec. 4.2.3 for details concerning the correction terms. The intensity is plotted on a logarithmic scale.

other than the directions perpendicular to the triangle sides expected from the quasi-diamond and the quasi-Fabry-Perot trajectories. This effect is enhanced for larger correction terms.

4.4.4 Comparison with wave simulations and experiment

Now, the results from the ray model are compared to the results from simulation and experiment. The longest-lived modes with dimensionless wavenumber $\mathrm{Re}(kL) \approx 100$ resulting from full electromagnetic wave simulations are shown in Fig. 4.21. A comparison with the ray trajectories shown in Fig. 4.16(a) and (c) which are predicted to dominate the far-field yields a good qualitative agreement. The mode patterns strongly resembles the quasi-diamond trajectory predicted to dominate the far-field. Further, a contribution that reminds of "grazing emission" can be seen. However, this contribution appears only in two directions, not in all four directions expected from a trajectory as the one shown in Fig. 4.16(c).

The far-field emission obtained from the wave simulations is shown in Fig. 4.22 for both polarizations. The main emission peak perpendicular to hypotenuse agrees well for both approaches, however, some discrepancies are seen for the minor emission directions. The grazing emission contribution in the lower half-plane at the far-field angles $-45°$ and $-135°$ are considerably higher in the wave simulations than expected from ray calculations for both polarizations. For TM polarization, the four small emission contributions at $\pm 45°$ and $\pm 135°$ are expected to be equally strong, whereas, the wave simulation yields higher peaks in the lower half-plane than in the upper half-plane. For TE polarization, the ray model predicts even the reverse trend for the heights of the four small emission contributions compared to the contributions found in the wave simulation. These discrepancies cannot be explained by finite wavelength effects as the inclusion of the Fresnel filtering corrections suppresses the peaks at $-45°$ and $-135°$. Additionally, we observe some small emission peaks in the wave result which are not seen in the ray optics result.

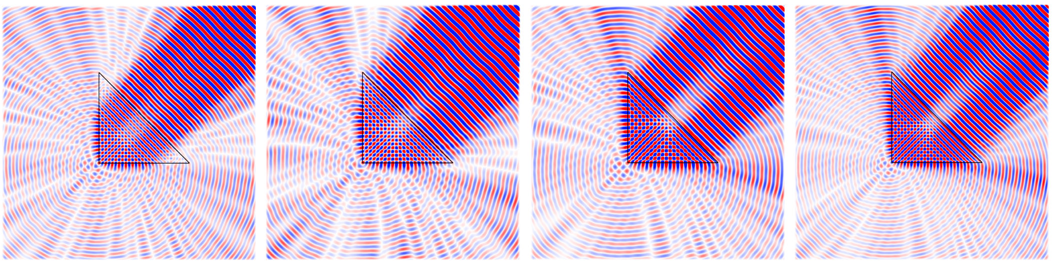

(a) TM polarization, $\mathrm{Re}(kL) \approx 113$, $Q \approx 201$. (b) TM polarization, $\mathrm{Re}(kL) \approx 101$, $Q \approx 116$. (c) TE polarization, $\mathrm{Re}(kL) \approx 101$, $Q \approx 69$. (d) TE polarization, $\mathrm{Re}(kL) \approx 116$, $Q \approx 58$.

Figure 4.21: Highest Q-modes with $kL \approx 100$ (L is the length of the hypotenuse) for the right isosceles triangle resulting from full electromagnetic wave simulations. Here, the triangle is differently oriented than in the rest of the section. Courtesy of J. Kreismann.

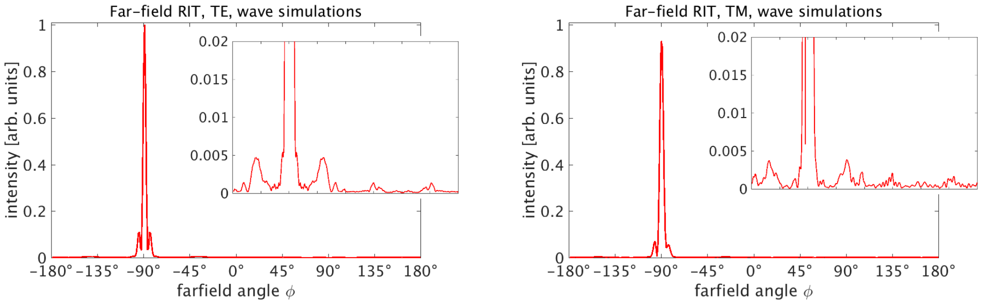

(a) TE polarization.

(b) TM polarization.

Figure 4.22: Far-field emission of the right isosceles triangle with relative refractive index $n = 1.5$ from wave simulations (courtesy of J. Kreismann). The plotted result is the average over the far-field of the two modes for each polarization shown in Fig. 4.21. *Inset:* Close-up for small intensities.

We also find good agreement with the experimental far-field [126] where only TE polarization is examined. There also a strong peak perpendicular to the hypotenuse and minor peaks in both directions parallel to the legs were observed. The small peaks in the upper half-plane were found to be larger than the contribution in the lower half-plane, what is also seen in our ray model for TE polarization.

In the experiment [126], photographs have been taken of the triangular cavities while they emit light. For the right isosceles triangle, the whole hypotenuse and the lower part of the legs close to the hypotenuse are found to glow brightly. The emission from the family of quasi-diamond trajectories explains the glowing of the whole hypotenuse in the photograph. The partial glowing of the legs can be explained in the following. A trajectory starts close to one end of the hypotenuse with a small angle towards the nearby leg. After being reflected from the leg it can reach the hypotenuse under a very large angle of incidence before going to the next leg. This feature is also seen in Fig. 4.16(c). This long optical path, significantly longer than going directly from one leg to the other, without losses leads to preferential amplification of such paths. However, only a very restricted interval of initial conditions leads to trajectories that have low refractive loss on the leg and an additional reflection on the hypotenuse with large angle of incidence. This might explain why the leg in the photograph only glows in the lower part close to the hypotenuse.

4.5 Other isosceles triangles

All isosceles triangles (other than the exceptional equilateral triangle) belong to the same symmetry class possessing one mirror axis. However, only the right isosceles triangle discussed in the previous section is integrable. All other isosceles triangles are pseudo-integrable or ergodic depending on whether the angles are rational or irrational. Several isosceles triangles shown in Fig. 4.23 will be discussed here, the two acute triangles with vertex angles $\gamma = 50°$ and $\gamma = 70°$ and the three obtuse triangles with $\gamma = 100°$, $\gamma = 110°$ and $\gamma = 120°$. The corner points, $P_1 = (-L\sqrt{\tan(\gamma/2)}, 0)$, $P_2 = (L\sqrt{\tan(\gamma/2)}, 0)$, and $P_3 = (0, L/\sqrt{\tan(\gamma/2)})$, are chosen such that the area of each triangle is $A = L^2$.

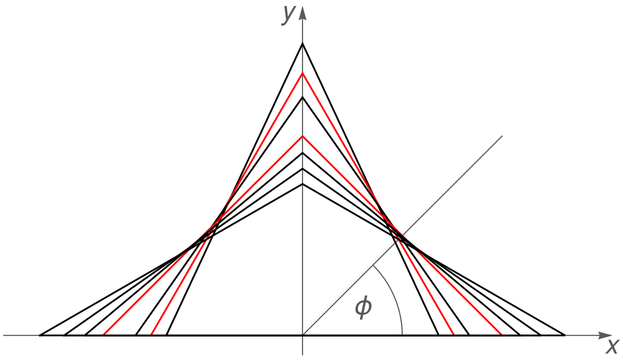

Figure 4.23: Isosceles triangles with vertex angles 50°, 70°, 100°, 110° and 120° (black, from top to bottom) and the special cases, equilateral and right isosceles triangle, with 60° and 90°, respectively (red). All triangles have equal area. *Gray:* Definition of the far-field angle ϕ and the orientation of the triangles with respect to the coordinate system.

For a generic isosceles triangle, we cannot construct the maximum intensity trajectories as easily as for the equilateral or the right isosceles triangle. However, they can be found by looking at the intensities of a large ensemble of trajectories after some time. To calculate the far-field of the isosceles triangles we use an ensemble of 60 000 rays that are propagated through the cavity for 300 reflections with $\alpha = 2L^{-1}$ as the gain coefficient. From this dataset we identify the trajectories that retain the highest intensities inside the cavity. We can infer the maximum intensity trajectories from the initial conditions of these trajectories. This method is used in the following for the different isosceles triangles shown in Fig. 4.23.

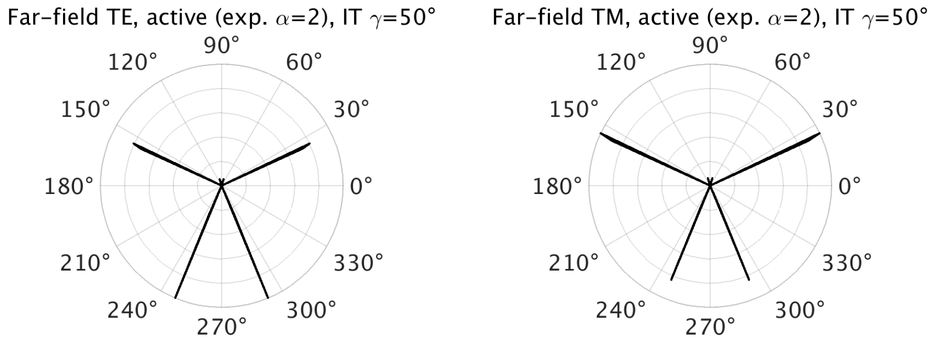

(a) TE polarization. (b) TM polarization.

Figure 4.24: Far-field emission of the isosceles triangle with $\gamma = 50^\circ$.

4.5.1 Isosceles triangle with vertex angle 50°

The calculated far-field emission patterns of the acute isosceles triangle with vertex angle $\gamma = 50^\circ$ are shown in Fig. 4.24 for both polarizations. The far-field characteristics are very similar for both polarizations showing two emission peaks in the upper half plane in the directions perpendicular to the legs (at 25° and $180^\circ - 25^\circ = 155^\circ$) and to peaks in the lower half plane at approximately $270^\circ \pm 23^\circ$.

From these emission directions we can already guess the responsible families of trajectories, the quasi-Fabry-Perot and the generalized quasi-Fabry-Perot trajectory shown in Fig. 4.25. Nevertheless, we want to deduce the maximum intensity trajectories from the data. To this end, we examine the decay rates of the trajectories shown in Fig. 4.26. The vertical lines in the figure correspond to the corners of the triangle such that it can be easily distinguished which

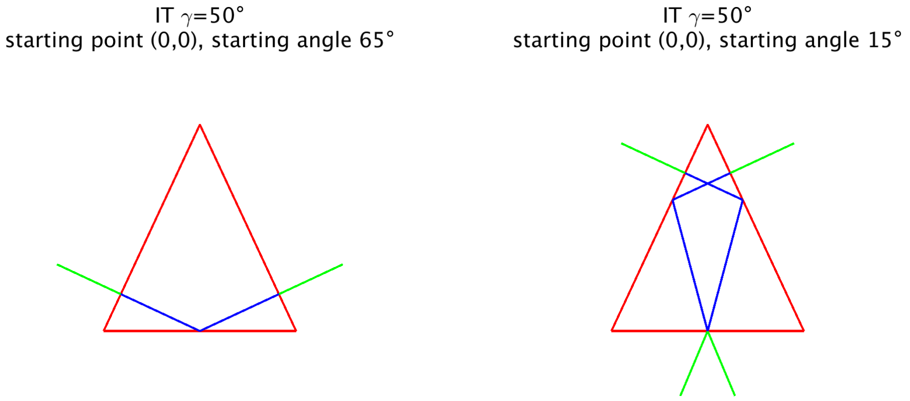

(a) Quasi-Fabry-Perot trajectory, starting with $\chi = \pm 65^\circ$ at point $(0,0)$ (center of the baseline).

(b) Generalized quasi-Fabry-Perot trajectory, starting with $\chi = \pm 15^\circ$ at point $(0,0)$ (center of the baseline).

Figure 4.25: High intensity trajectories in the isosceles triangle with $\gamma = 50^\circ$.

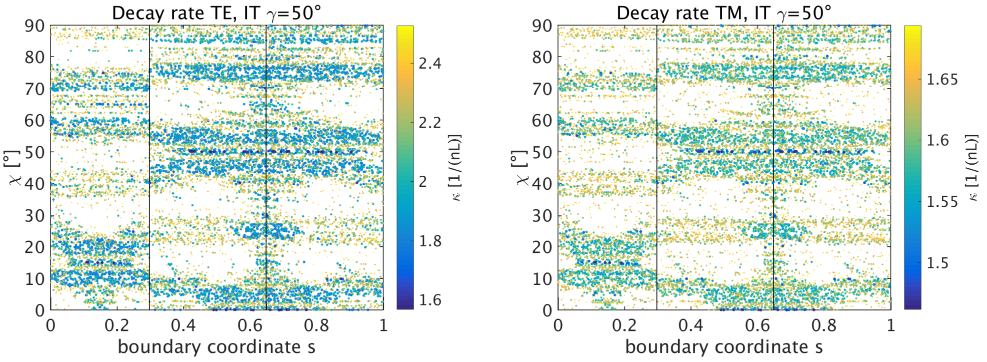

(a) TE polarization.

(b) TM polarization.

Figure 4.26: Decay rates κ of the trajectories in the isosceles triangle with $\gamma = 50°$ with relative refractive index $n = 1.5$ ($\chi_c \approx 41.8°$, $\chi_B \approx 33.7°$). The decay rates are plotted only for the 50% of the trajectories starting with positive angle of incidence that have the smallest decay rates. The boundary coordinate s is scaled that the perimeter of the cavity equals 1, it runs first over the baseline and then over the two legs. The vertical lines denote the positions of the corners.

intervals of the boundary coordinate belong to the baseline and the two legs, respectively. The start and the end of the boundary coordinate is chosen to be the lower left corner. Here and in the following, we no longer show the decay rates of all trajectories as in the previous cases but only those of the trajectories starting with positive initial angles, $\chi \geq 0$, and having low decay rates.

We find the smallest losses for trajectories that start with $\chi = 0°$ or $\chi = 50°$ on the legs or with $\chi = 15°$ on the baseline. These initial conditions, indeed, lead to the families of the quasi-Fabry-Perot and the generalized quasi-Fabry-Perot trajectories. One representative of each of the two families is shown in Fig. 4.25. The emission directions from these families of maximum intensity trajectories nicely explain the far-field emission.

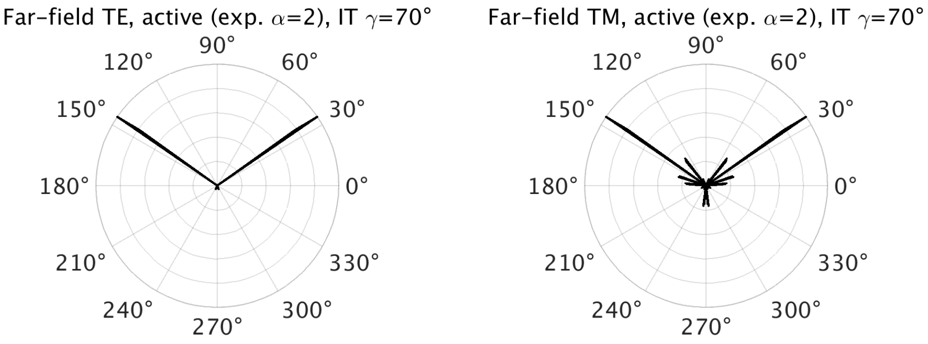

(a) TE polarization.

(b) TM polarization.

Figure 4.27: Far-field emission of the isosceles triangle with $\gamma = 70°$.

4.5.2 Isosceles triangle with vertex angle 70°

The same arguments are now applied to the isosceles triangle with vertex angle $\gamma = 70°$. The far-field emission is shown in Fig. 4.27. For both polarizations we find strong emission peaks in the directions perpendicular to the legs. Whereas this is the only contribution to the far-field for TE polarization, we find additional contributions for TM polarization.

From the decay rates in Fig. 4.28 we readily identify the family of quasi-Fabry-Perot trajectories (see Fig. 4.29(a)) with $\chi = \pm 55°$ on the baseline and $\chi = 0°$ on the legs as the maximum intensity trajectories for TE polarization and one possible family of maximum intensity trajectories for TM polarization. The initial conditions of the remaining high intensity trajectories for TM polarization lead to a second family of trajectories which is shown in Fig. 4.29(b). This family of trajectories has angles of incidence $\chi = \pm 5°$, $\pm 35°$, $\pm 45°$, $\pm 65°$ on the baseline and $\chi = \pm 10°$, $\pm 20°$, $\pm 50°$, $\pm 60°$ on the legs. The resulting emission directions also explain the additional contributions to the far-field.

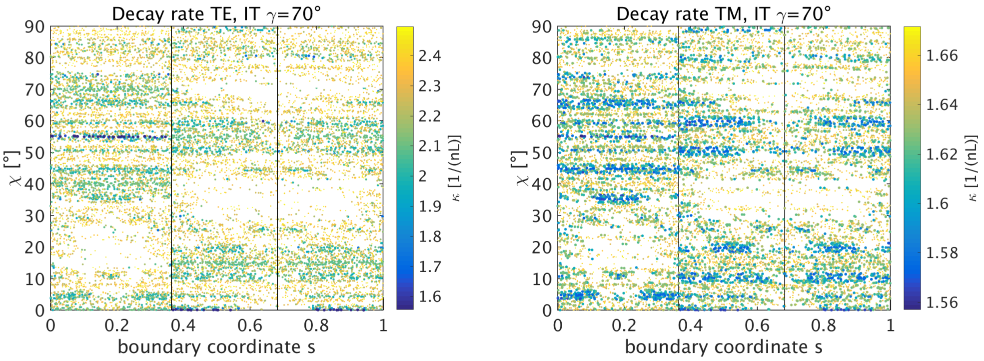

(a) TE polarization.

(b) TM polarization.

Figure 4.28: Decay rates in the isosceles triangle with $\gamma = 70°$. See caption of Fig. 4.26 for details.

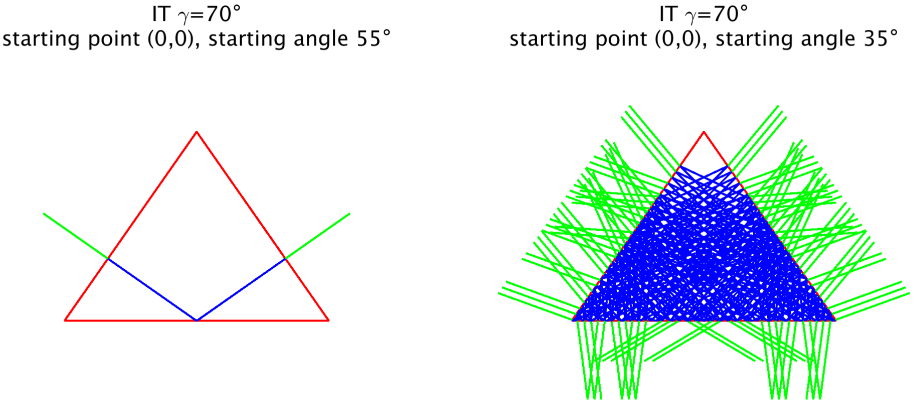

(a) Quasi-Fabry-Perot trajectory, starting with $\chi = \pm 55°$ at point $(0, 0)$ (center of the baseline).

(b) High intensity trajectory for TM polarization, starting with $\chi = \pm 35°$ at point $(0, 0)$ (center of the baseline).

Figure 4.29: High intensity trajectories in the isosceles triangle with $\gamma = 70°$.

4.5.3 Isosceles triangle with vertex angle 100°

The far-field emission of the isosceles triangle with vertex angle $\gamma = 100°$, shown in Fig. 4.30, is very different for the two polarizations. To understand the far-field emission pattern we identify the maximum intensity trajectories with the help of Fig. 4.31.

For TM polarization, the smallest decay rates are found for the family of periodic trajectories shown in Fig. 4.32(a) with angles of incidence $\chi = 0°, \pm 80°$ on the baseline and $\chi = \pm 40°$ on the legs. The long lossless part of this trajectory allows for strong amplification which makes this trajectory favorable. This explains also why the two emission peaks in the lower half space from the reflection points at the legs are much stronger than the corresponding emission peaks in the upper half space. A minor contribution to the far-field for TM polarization stems from a second periodic trajectory shown in Fig. 4.32(b)

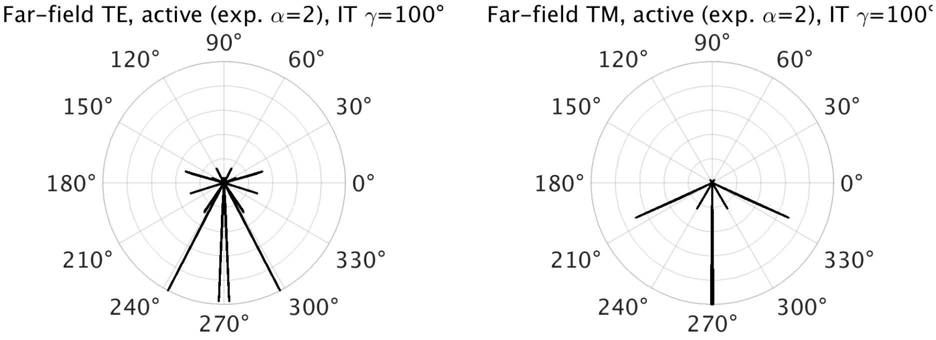

(a) TE polarization.

(b) TM polarization.

Figure 4.30: Far-field emission of the isosceles triangle with $\gamma = 100°$.

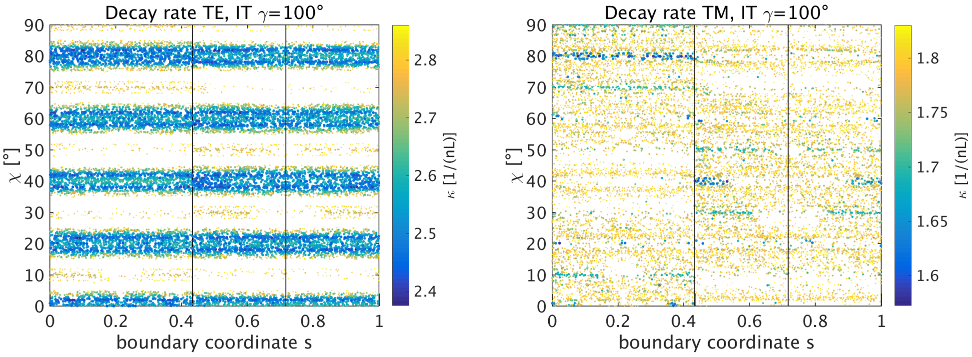

(a) TE polarization.

(b) TM polarization.

Figure 4.31: Decay rates in the isosceles triangle with $\gamma = 100°$. See caption of Fig. 4.26 for details.

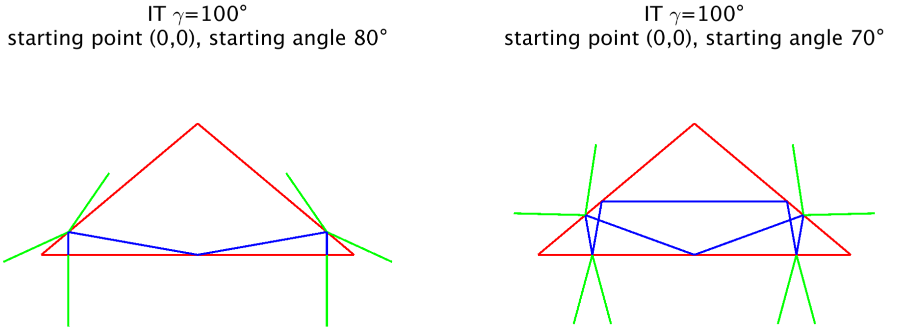

(a) Trajectory starting with $\chi = \pm 80°$ at point $(0, 0)$ (center of the baseline).

(b) Trajectory starting with $\chi = \pm 70°$ at point $(0, 0)$ (center of the baseline).

Figure 4.32: High intensity trajectories for TM polarization in the isosceles triangle with $\gamma = 100°$.

with angles of incidence $\chi = \pm 10°, \pm 70°$ on the baseline and $\chi = \pm 30°, \pm 50°$ on the legs that has a longer period and a more complicated structure.

For TE polarization, the initial conditions of the trajectories with the smallest decay rates, see Fig. 4.31(a), lead to a single family of trajectories. A representative of this family is shown in Fig. 4.33(a). Comparing the phase space portrait of this trajectory plotted in Fig. 4.33(b) with the initial conditions in Fig. 4.31(a) shows that all the initial conditions with very small losses correspond to this family of trajectories. The resulting emission directions explain the observed far-field directions.

In the experiment [126], the isosceles triangle with vertex angle 100° has been studied as well. However, there they observe a far-field emission pattern that can be explained by the emission directions of the family of quasi-Fabry-Perot trajectories with incident angles $\chi = \pm 40°$ on the baseline and $\chi = 0°$

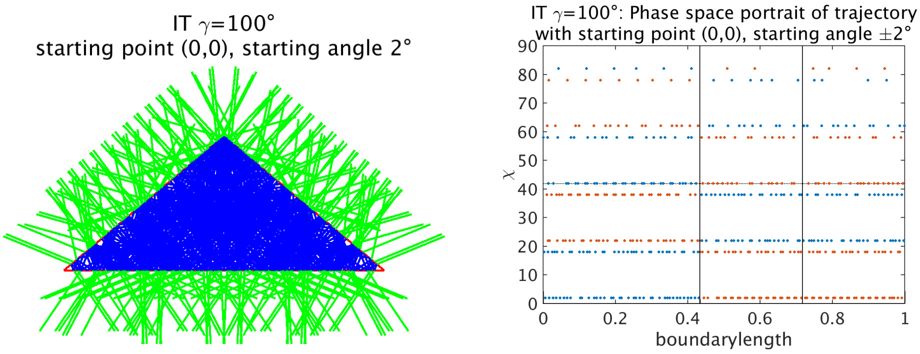

Figure 4.33: High intensity trajectory for TE polarization in the isosceles triangle with $\gamma = 100°$. Trajectory starting with $\chi = \pm 2°$ at point $(0, 0)$ (center of the baseline) and the corresponding phase space portrait of the trajectory with blue (red) dots for the positive (negative) starting angle. The vertical lines in the phase space plot denote the positions of the corners, the dotted horizontal line is the critical line.

on the legs, shown in Fig. 4.34, although these trajectories are highly lossy (high decay rates, *cf.* Fig. 4.31).

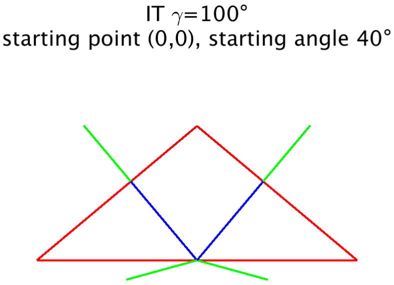

Figure 4.34: Representative of the family of quasi-Fabry-Perot trajectories ($\chi = \pm 40°$ on the baseline, $\chi = 0°$ on the legs) in the isosceles triangle with $\gamma = 100°$.

4.5.4 Isosceles triangle with vertex angle 110°

For the isosceles triangle with vertex angle $\gamma = 110°$ the far-field emission is shown in Fig. 4.35. It is again very different for the two polarizations. In the case of TE polarization, the far-field emission pattern can be nicely explained by the periodic trajectory shown in Fig. 4.37(a) with incident angles $\chi = \pm 20°, \pm 50°$ on the baseline and $\chi = \pm 15°, \pm 55°$ on the legs. These trajectories are also identified as the family of maximum intensity trajectories from the decay rates in Fig. 4.36(a). This finding agrees well with the experimental results reported in [126].

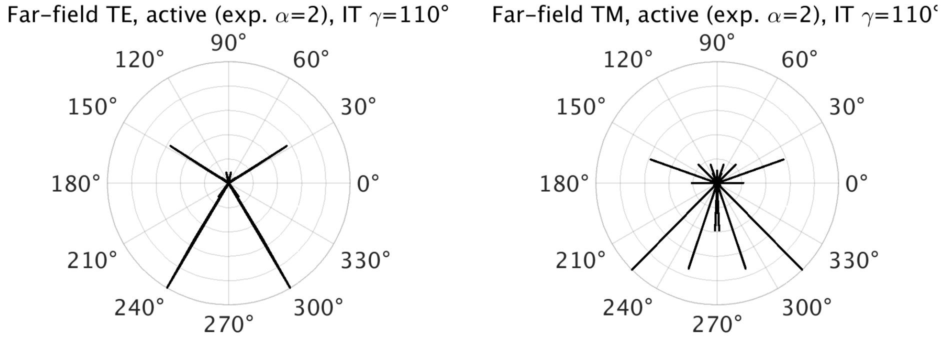

(a) TE polarization.

(b) TM polarization.

Figure 4.35: Far-field emission of the isosceles triangle with $\gamma = 110°$.

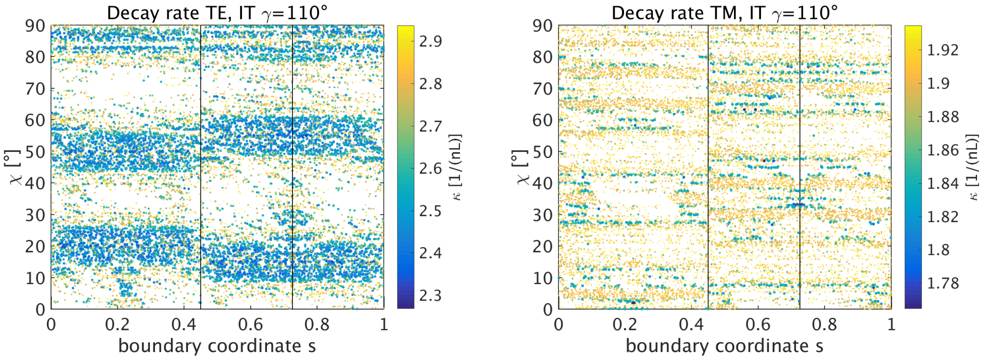

(a) TE polarization.

(b) TM polarization.

Figure 4.36: Decay rates in the isosceles triangle with $\gamma = 110°$. See caption of Fig. 4.26 for details.

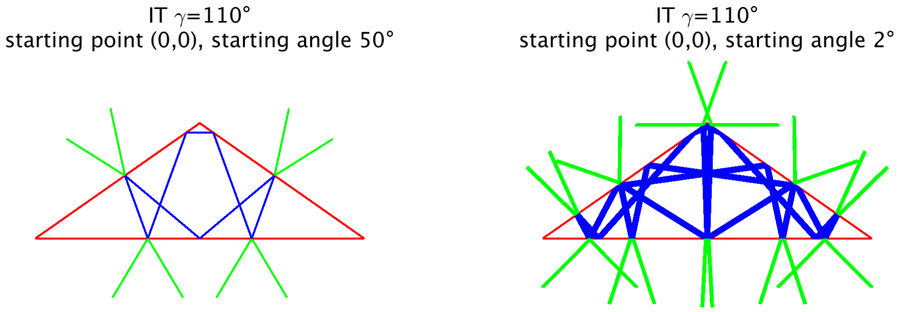

(a) "Double bow-tie" trajectory, starting with $\chi = \pm 50°$ at point $(0, 0)$ (center of the baseline).

(b) High intensity trajectory for TM polarization, starting with $\chi = \pm 2°$ at point $(0, 0)$ (center of the baseline).

Figure 4.37: High intensity trajectories in the isosceles triangle with $\gamma = 110°$.

For TM polarization, the far-field emission pattern has a more complicated structure. However, it can be explained by a single family of trajectories shown in Fig. 4.37(b). All initial conditions of the trajectories with the smallest decay rates plotted in Fig. 4.36(b) lead to this family.

4.5.5 Isosceles triangle with vertex angle 120°

The last isosceles triangle that we study here is the one with vertex angle $\gamma = 120°$. Its far-field emission shown in Fig. 4.38 exhibits a quite simple structure and shows the same emission directions for both polarizations. The structure of the far-field pattern is similar to the emission pattern for TE polarization of the isosceles triangle with vertex angle $\gamma = 110°$ which is found to be determined by a family of periodic trajectories. However, these trajectories no longer exist in the isosceles triangle with vertex angle $\gamma = 120°$.

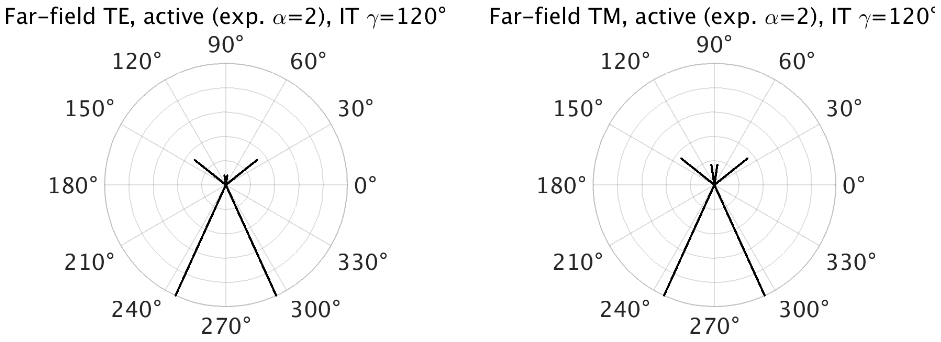

(a) TE polarization.

(b) TM polarization.

Figure 4.38: Far-field emission of the isosceles triangle with $\gamma = 120°$.

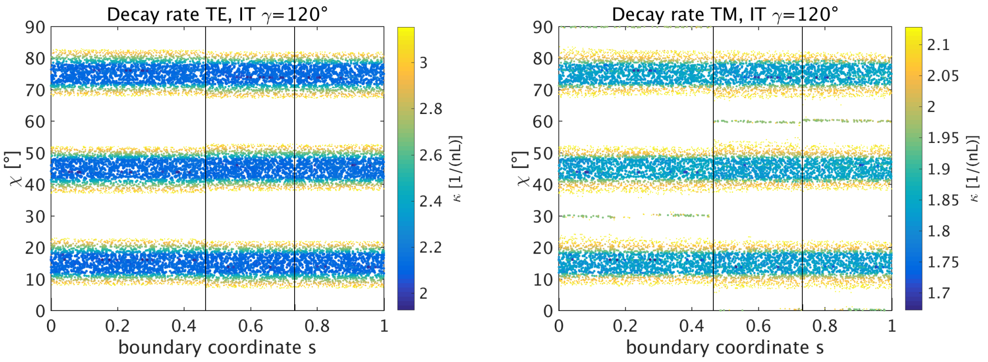

(a) TE polarization.

(b) TM polarization.

Figure 4.39: Decay rates in the isosceles triangle with $\gamma = 120°$. See caption of Fig. 4.26 for details.

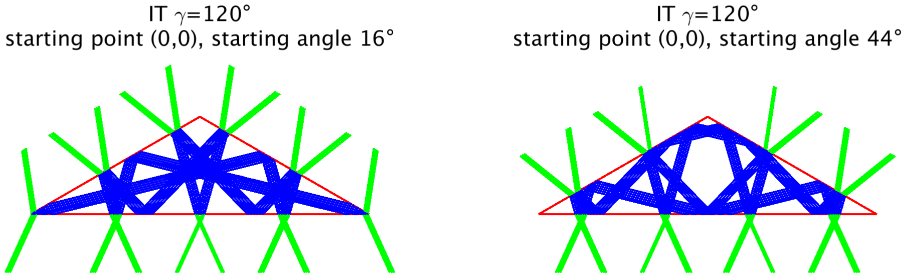

Figure 4.40: Two representatives of the family of high intensity trajectories in the isosceles triangle with $\gamma = 120°$.

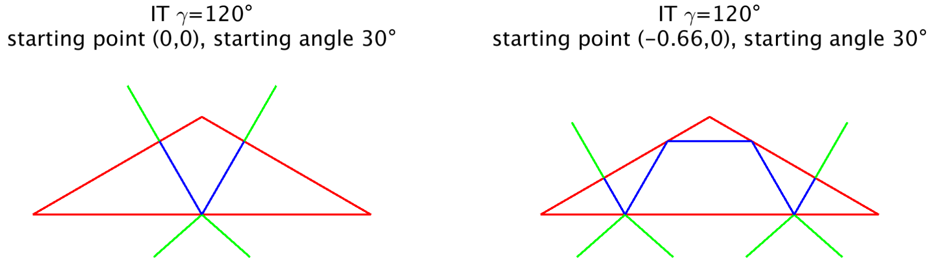

Figure 4.41: Two simple periodic trajectories in the isosceles triangle with $\gamma = 120°$ starting with $\chi = \pm 30°$ on the baseline.

The initial conditions of the trajectories with the smallest decay rates identified from Fig. 4.39 all lead to the same family of trajectories with incident angles $\chi = \pm 16°$, $\pm 44°$, $\pm 76°$ on the baseline and $\chi = \pm 14°$, $\pm 46°$, $\pm 74°$ on the legs. Two representatives of this family are shown in Fig. 4.40. The reflections with $\chi = \pm 16°$ on the baseline explain the two far-field peaks in the lower half-space, the reflections with $\chi = \pm 14°$ on the legs give the far-field directions in the upper half-space.

For TM polarization, additional trajectories with $\chi = \pm 30°$ on the baseline and $\chi = 0°$, $\chi = \pm 60°$ on the legs are found to have small decay rates (see Fig. 4.39(b)). These are the families of simple periodic trajectories shown in Fig. 4.41 where, however, the trajectory with the additional lossless bounces on the legs is favored over the simpler quasi-Fabry-Perot trajectory. As their decay rate is higher than that of the maximum intensity trajectories, they have no (visible) contribution to the far-field emission.

4.6 Pythagorean triangle

A Pythagorean triangle is a right triangle whose sides a_1, a_2, a_3 are integer numbers (in a suitably chosen length unit). Here, the smallest Pythagorean triangle is considered with $a_1 = 3$, $a_2 = 4$, $a_3 = 5$ which is shown in Fig. 4.42. Although it is a right angled triangle its other two angles (approximately 53.13° and 36.87°) are irrational multiples of π and, hence, its classical billiards dynamics is supposed to be ergodic.

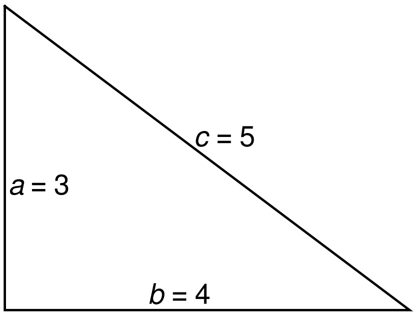

Figure 4.42: Pythagorean $(3, 4, 5)$ triangle.

4.6.1 Far-field emission and maximum intensity trajectories

The far-field emission of the Pythagorean triangle calculated from the ray model is shown in Fig. 4.43. The ray calculations have been done for an ensemble of 90 000 rays for 250 bounces. We have chosen the gain coefficient $\alpha = 6L^{-1}$ where L is the length of the hypotenuse. Here, we have to chose a higher gain coefficient compared to the previous sections to account for the higher decay rates (see Fig. 4.44) found for the Pythagorean triangle. The far-field emission is collected in the time interval $20\,nL/c < t \leq 70\,nL/c$.

To find the maximum intensity trajectories and understand the emission patterns, we apply the same method as used for the isosceles triangles in the previous section. For TM polarization, we identify two families of trajectories with very small decay rates from Fig. 4.44(b). The first is the family of the periodic orbits with normal incidence on the hypotenuse and incident angles $\chi = \arcsin(3/5) \approx \pm 36.87°$ on the longer leg and $\chi = \arcsin(4/5) \approx 53.13°$ on the shorter leg. An example of these trajectories is shown in Fig. 4.45. The second family can be deduced from the incident angles $\chi \approx 5°$ on the hypotenuse. Comparing the phase space portrait of one such trajectory shown in Fig. 4.46 with the initial conditions of the trajectories with smallest decay rates in Fig. 4.44(b) we see that the different initial conditions lead to the same family of trajectories.

In the same line of thought, we identify the maximum intensity trajectories for TE polarization from Fig. 4.44(a). Here, we find only one family of tra-

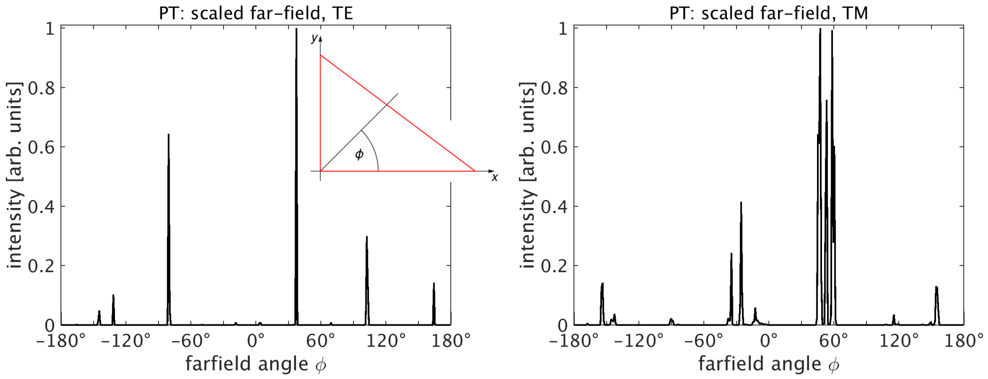

(a) TE polarization.

(b) TM polarization.

Figure 4.43: Far-field emission of the Pythagorean $(3, 4, 5)$ triangle with relative refractive index $n = 1.5$ obtained from the ray model including amplification according to Eq. (4.2) with $\alpha = 6L^{-1}$ where L is the length of the hypotenuse. The inset in (a) defines the far-field angle ϕ and the orientation of the triangle with respect to the coordinate system.

jectories. One example is the trajectory starting with $\chi = \pm 10°$ on the longer leg shown in Fig. 4.47. It is plausible that the periodic trajectories shown in Fig. 4.45 which contributed to the far-field for TM polarization is not favorable

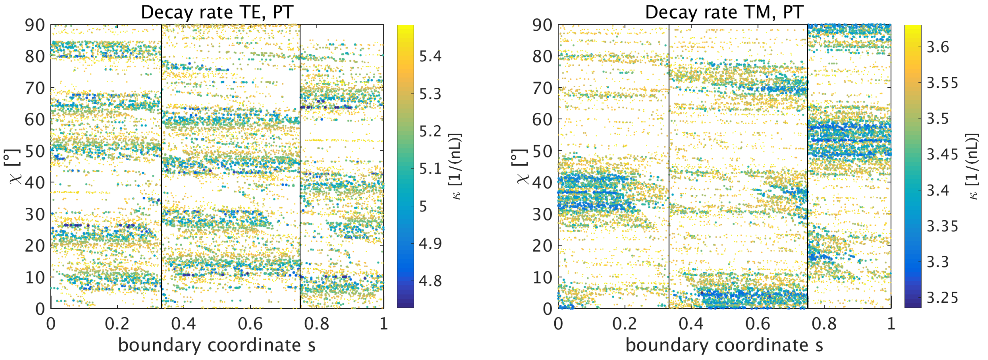

(a) TE polarization.

(b) TM polarization.

Figure 4.44: Decay rates κ of the trajectories in the Pythagorean $(3, 4, 5)$ triangle with relative refractive index $n = 1.5$ ($\chi_c \approx 41.8°$, $\chi_B \approx 33.7°$). The decay rates are plotted only for the trajectories starting with positive angle of incidence that have the small decay rates. The boundary coordinate s is scaled that the perimeter of the cavity equals 1, it runs first over the longer leg, then over the hypotenuse and over the short leg. The vertical lines denote the positions of the corners.

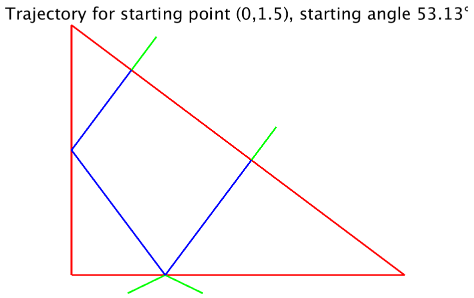

Figure 4.45: Periodic trajectory in the Pythagorean triangle.

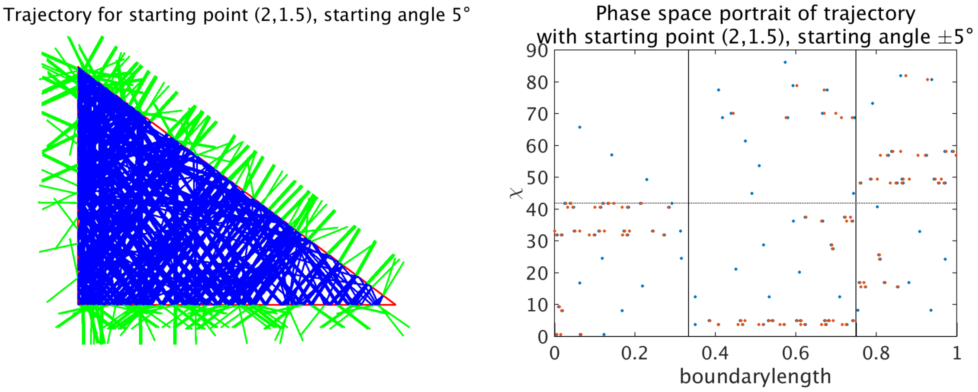

(a) Examplary trajectory.

(b) Phase-space portait.

Figure 4.46: High intensity trajectories for TM polarization in the Pythagorean triangle starting with $\chi = \pm 5°$ at point $(2, 1.5)$ (center of the hypotenuse) and the corresponding phase space portrait of the trajectory with blue (red) dots for the positive (negative) starting angle. The vertical lines in the phase space plot denote the positions of the corners, the dotted horizontal line is the critical line.

in the case of TE polarization as the incident angle $\chi = \arcsin(3/5) \approx \pm 36.87°$ is close to the Brewster angle $\chi_B \approx 33.7°$ where no light is reflected for TE polarization.

To verify that these trajectories explain the far-field patterns we compare them to the expected emission directions of the predicted maximum intensity trajectories in Fig. 4.48. For TM polarization, the emission directions of the periodic trajectories (red histogram), which is expected to be one family of maximum intensity trajectories, explain three of the major far-field peaks. All other major far-field peaks and almost all minor peaks coincide with emission directions of the non-periodic trajectories (green histogram) predicted to be the second family of maximum intensity trajectories. Due to the ergodicity of the classical billiards dynamics in the Pythagorean triangle, however, these trajectories produce many more emission directions which are not seen in the

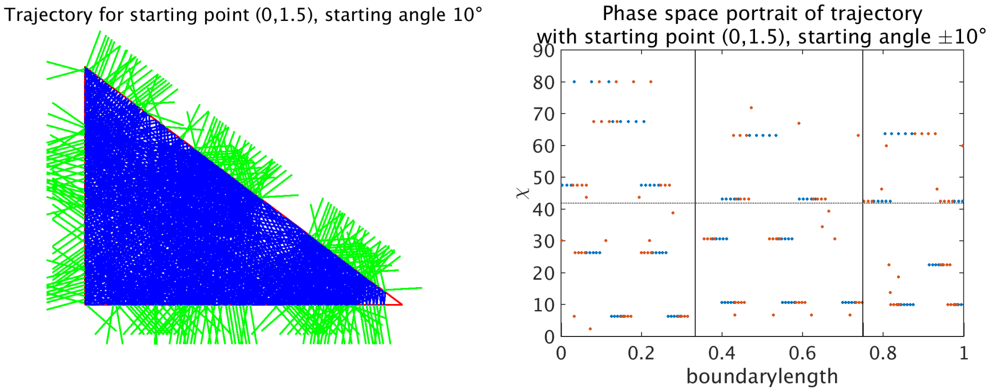

(a) Examplary trajectory.

(b) Phase-space portait.

Figure 4.47: High intensity trajectories for TE polarization in the Pythagorean triangle starting with $\chi = \pm 10°$ at point $(0, 1.5)$ (center of the short leg) and the corresponding phase space portrait of the trajectory with blue (red) dots for the positive (negative) starting angle. The vertical lines in the phase space plot denote the positions of the corners, the horizontal line is the critical line.

far-field. The same is true for TE polarization where all major and minor far-field peaks coincide with emission directions of the predicted maximum intensity trajectories.

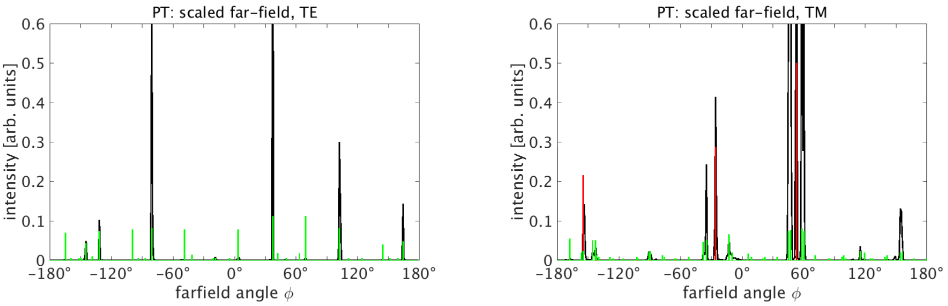

(a) TE polarization.

(b) TM polarization.

Figure 4.48: Far-field emission of the Pythagorean triangle calculated from ray optics (black curve, *cf.* Fig. 4.43) together with the emission directions from the maximum intensity trajectories (green histograms for the non-periodic trajectories shown in Fig. 4.46 and 4.47, red histogram for the periodic trajectory shown in Fig. 4.45).

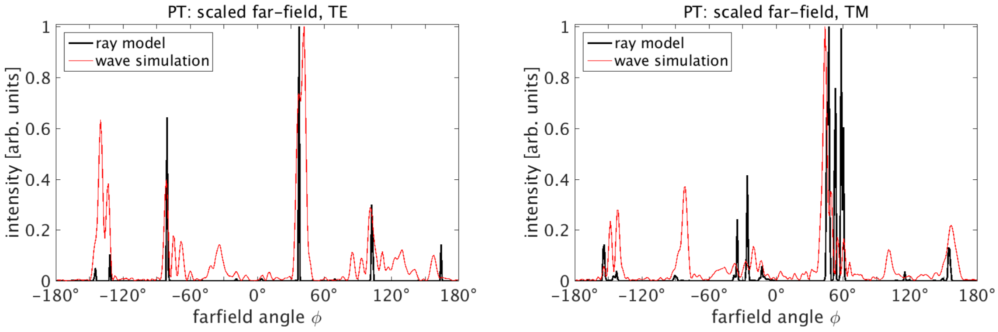

(a) TE polarization.

(b) TM polarization.

Figure 4.49: Far-field emission of the Pythagorean $(3,4,5)$ triangle with relative refractive index $n = 1.5$. The ray optics result (thick black) is obtained from the ray model including amplification according to Eq. (4.2) with $\alpha = 6L^{-1}$ where L is the length of the hypotenuse. The results from the wave simulations (thin red) are the far-fields of the highest Q-modes, for TE polarization a single mode with $Q = 300$ and $\mathrm{Re}(kL) \approx 103$, for TM polarization the average over two modes both with $Q = 54$ and $\mathrm{Re}(kL) \approx 117$, $\mathrm{Re}(kL) \approx 113$. Wave simulations courtesy of J. Kreismann.

4.6.2 Comparison with wave simulations and experiment

A comparison of the far-field emission of the Pythagorean triangle obtained from the ray model (black) and from wave simulations (red, courtesy of J. Kreismann) is shown in Fig. 4.49. The results from full electromagnetic wave simulations are calculated from the longest lived modes found in the cavity. For TM polarization, the far-field is averaged over two modes, both with quality factor $Q = 54$ and with $\mathrm{Re}(kL) \approx 117$, $\mathrm{Re}(kL) \approx 113$, respectively. For TE polarization, only a single mode with $Q = 300$ and $\mathrm{Re}(kL) \approx 103$ is used.

We find reasonable, though not perfect, agreement between the two approaches. Whereas the positions of the emission peaks agree to some extent, their relative heights and, especially, their widths do not. In the wave simulations the peaks are much broader than in the ray calculations where very narrow peaks are predicted. Furthermore, some more peaks occur in the wave results which are not found in the ray model.

In the experiment [126] the Pythagorean $(3,4,5)$ triangle has also been studied. There they observe a far-field pattern for TE polarization which can be explained by the emission from the periodic trajectory shown in Fig. 4.45. Our results from both, the ray and the wave approach, however, do not agree with the experimental finding. This difference remains an open question. We checked that including wave corrections does not compensate for the discrepancies.

4.7 Asymmetric triangles

To conclude this chapter, we study some asymmetric triangles. An important question that arises for possible applications of microcavity lasers is whether small deviations from the desired cavity geometry lead to large deviations in the emission pattern. In the last chapter, we have found a significant influence on the far-field emission of small deviations from a perfectly circular cavity.

To investigate this questions for triangular cavities we study triangles that interpolate between the equilateral triangle and the right isosceles triangle and exhibit the same area $A = L^2$. The triangles are parameterized as follows: The lower left corner point stays fixed at the origin $p_1 = (0, 0)$, the lower right corner point is chosen on the x-axis $p_2 = (2L/(\sqrt[4]{3} + t(\sqrt{2} - \sqrt[4]{3})), 0)$ and the upper corner point is parameterized by $p_3(t) = L(1/\sqrt[4]{3} - t/\sqrt[4]{3}, \sqrt[4]{3} + t(\sqrt{2} - \sqrt[4]{3}))$ with $t \in [0, 1]$ where $t = 0$ is the equilateral triangle and $t = 1$ is the right isosceles triangle. The resulting triangles for $t = 0, 0.02, 0.05, 0.1, 0.2, 0.4, 0.6, 0.8, 0.9, 0.95, 0.98, 1$ that we will study here are plotted in Fig. 4.50. The classical billiards dynamics is no longer integrable as soon as we introduce small deviations from the equilateral or the right isosceles geometry. However, that does not necessarily mean that the far-field emission is suddenly completely different.

The ray calculations are performed with 90 000 rays followed for 300 reflections with gain coefficient $\alpha = 2L^{-1}$. The far-field emission is collected in the time interval $30\,nL/c < \tau \leq \tau_{\max}$ where $\tau_{\max}$ corresponds to the length of the shortest trajectory in the ensemble, for all triangles $\tau_{\max} \approx 190\,nL/c$.

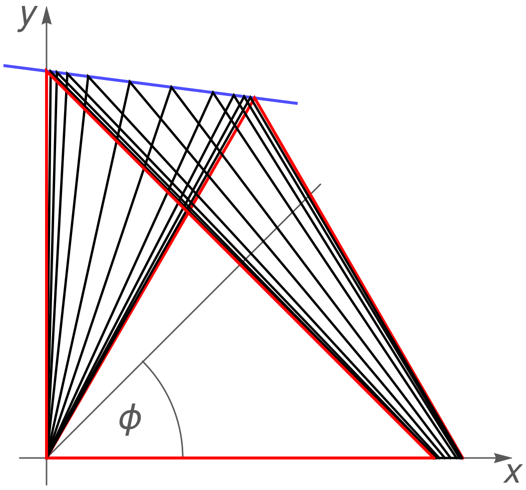

Figure 4.50: Asymmetric triangles (black) between the equilateral and right isosceles triangles (red) with equal area. The line on which all upper corner points lie is drawn in blue. *Gray:* Definition of the far-field angle ϕ and the orientation of the triangles with respect to the coordinate system.

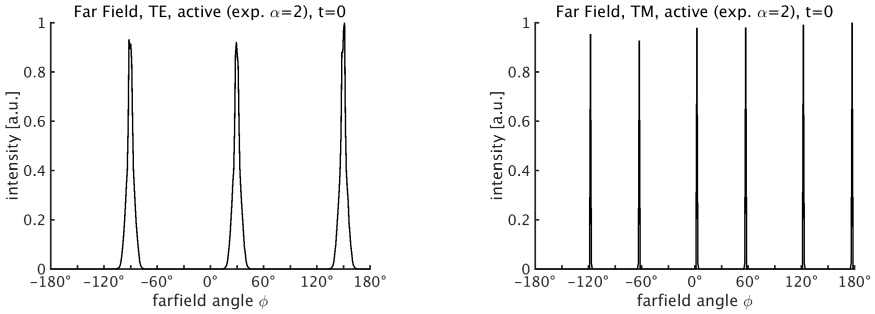

(a) $t = 0$ (equilateral triangle).

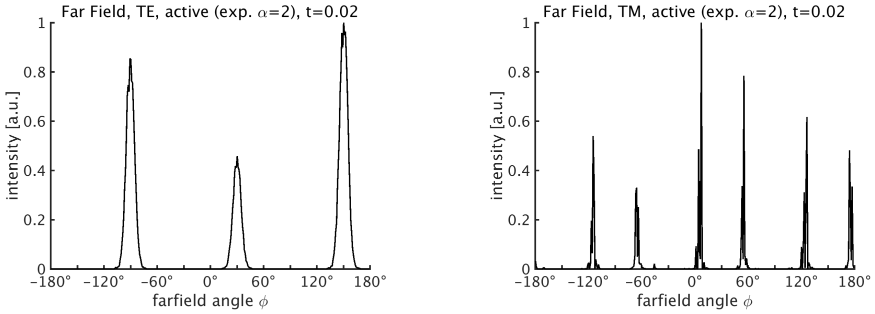

(b) $t = 0.02$.

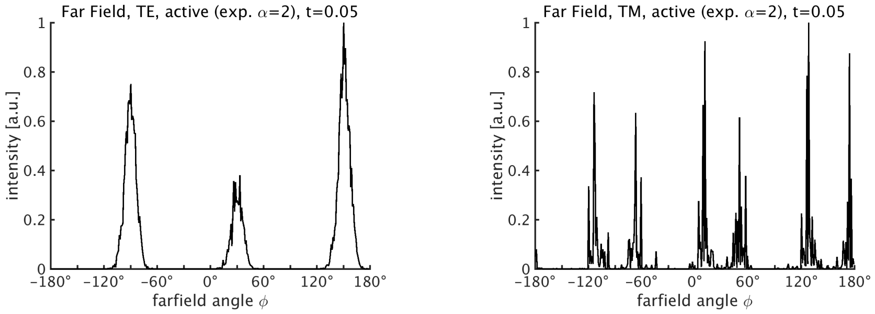

(c) $t = 0.05$.

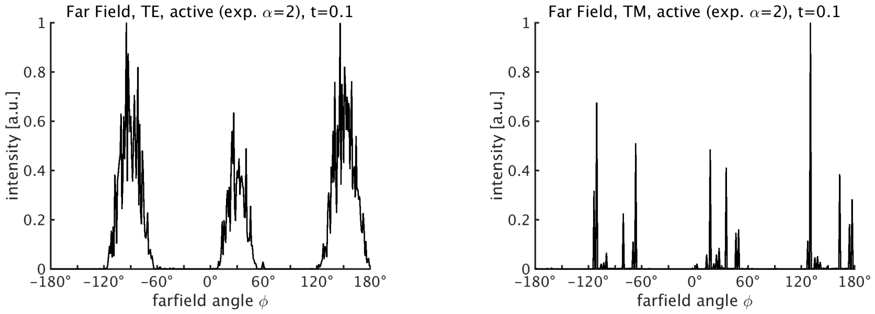

(d) $t = 0.1$.

Figure 4.51: Far-field emission of the triangles slightly deviating from the equilateral triangle shown in Fig. 4.50 with $t = 0$ (equilateral triangle) to $t = 0.1$, for TE (left) and TM (right) polarization.

The far-field emission patterns of the triangles slightly deviating from the equilateral triangle are shown in Fig. 4.51 with the equilateral triangle in the top row and deviations increasing from top to bottom. We observe that the far-field is not strongly influenced by small deviations from the symmetry and the main emission directions are preserved. The far-field for TE polarization is found to be more robust than for TM polarization although, for both polarizations, the maximum intensity trajectories of the equilateral triangle no longer exist in the asymmetric case. The very special family of trajectories found to explain the far-field of the equilateral triangle for TM polarization seems to be, not surprisingly, a bit more susceptible to perturbations than the periodic quasi-Fabry-Perot trajectory for TE polarization.

This is consistent with experimental results reported in [126] where they also studied a nearly equilateral triangle. The measured far-field emission is strongly broadened but still mainly perpendicular to the sides of the cavity.

The far-field emission patterns of the triangles slightly deviating from the right isosceles triangle are shown in Fig. 4.52 with the right isosceles triangle in the bottom row and the deviations decreasing from top to bottom. Note that the right isosceles triangle, here, is oriented differently than in section 4.4, the direction perpendicular to the hypotenuse is now at $\phi = 45°$. The far-field of the right isosceles triangle is found to be less robust to deviations from the symmetry than that of the equilateral triangle. Whereas for a very small deviation the emission directions are not strongly influenced, for larger (but still small) deviations the single peak with some finite width observed for the symmetrical cavity breaks up into narrow separated peaks. For TM polarization, these new peaks still correspond to the major emission directions of the right isosceles triangle. For TE polarization, however, the main emission direction perpendicular to the hypotenuse is lost.

For the strongly asymmetric triangles, the far-field emission patterns are shown in Fig. 4.53. As their shapes are no longer resemble one of the symmetrical triangles their far-fields do neither. The far-field of the triangle with parameter $t = 0.6$ for TE polarization shows strong dependence on the chosen starting time for collecting the transmitted intensities. Here, the chosen gain coefficient $\alpha = 2L^{-1}$ is not sufficiently large to yield overall intensity amplification in the ray dynamics. For all other triangles, independence of the starting and final time is ensured.

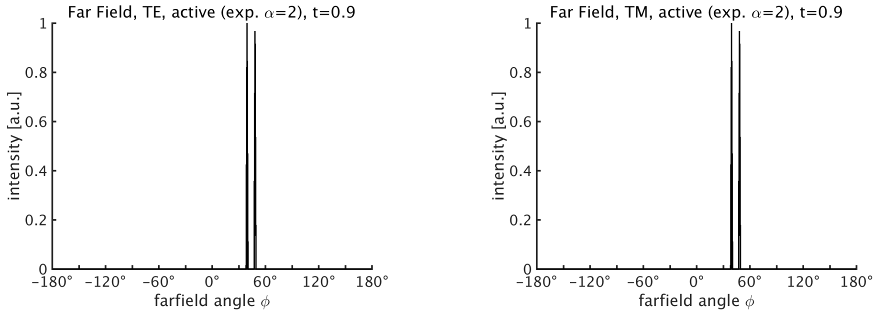

(a) $t = 0.9$.

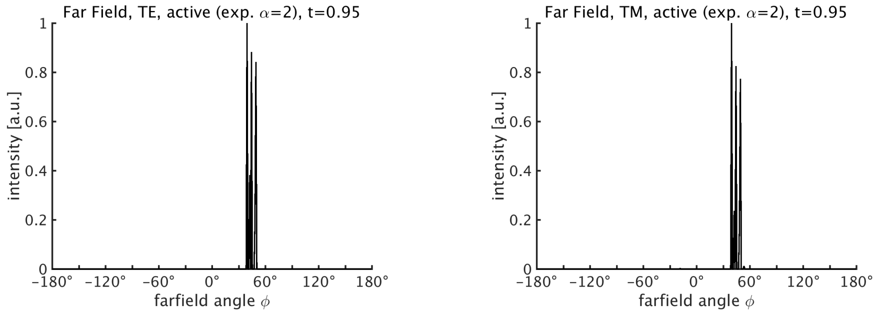

(b) $t = 0.95$.

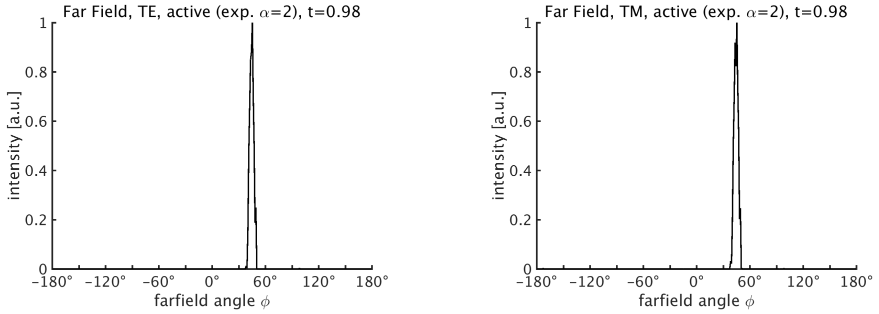

(c) $t = 0.98$.

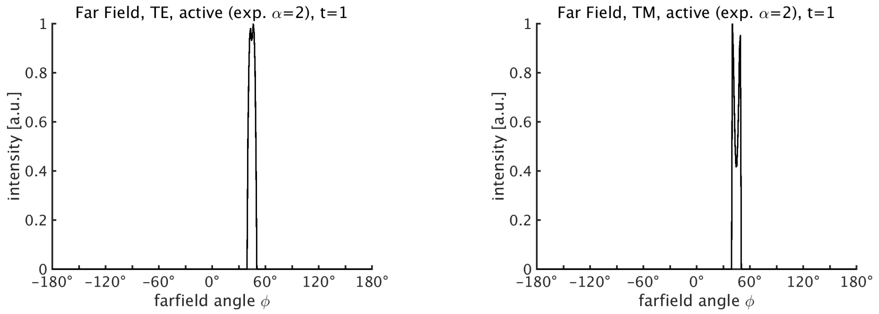

(d) $t = 1$ (right isosceles triangle).

Figure 4.52: Far-field emission of the triangles slightly deviating from the right isosceles triangle shown in Fig. 4.50, $t = 0.9$ to $t = 1$ (right isosceles triangle), for TE (left) and TM (right) polarization.

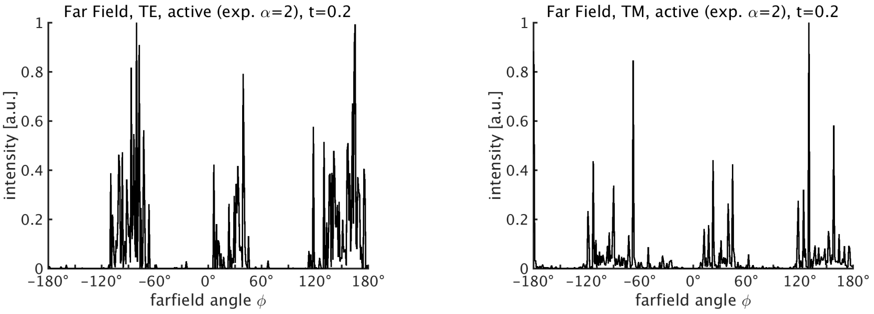

(a) $t = 0.2$.

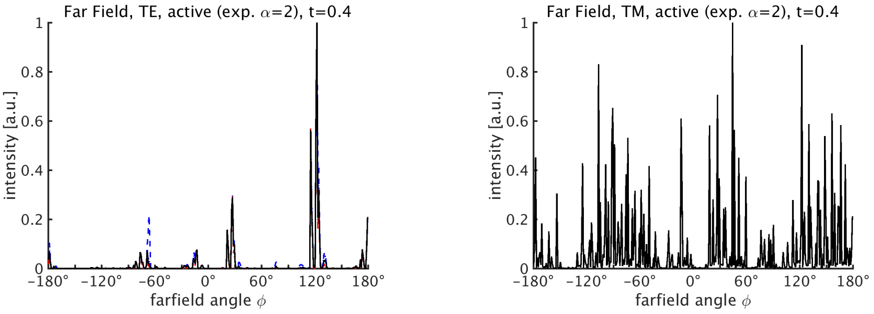

(b) $t = 0.4$.

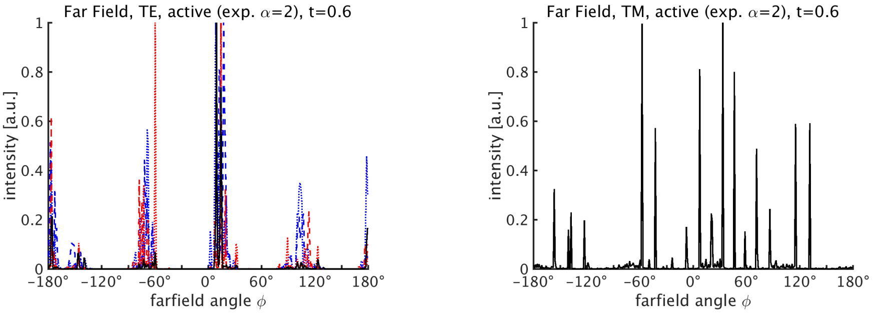

(c) $t = 0.6$.

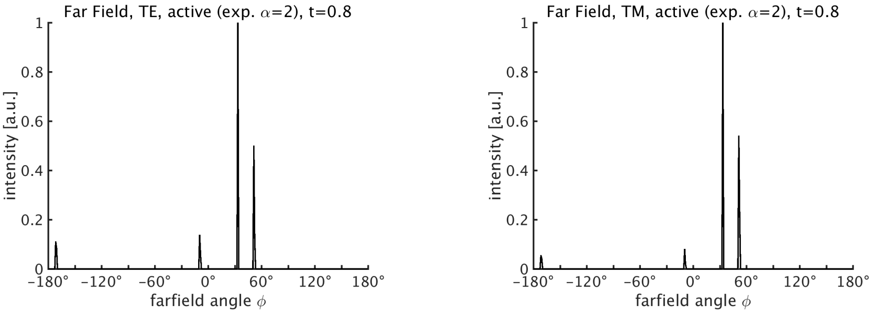

(d) $t = 0.8$.

Figure 4.53: Far-field emission of the strongly asymmetric triangles shown in Fig. 4.50, $t = 0.2$ to $t = 0.8$, for TE (left) and TM (right) polarization. The far-field calculated after the time of $\tau_1 = 30\,nL/c$ is drawn as full black curve, for slightly shorter (longer) transition times as broken blue (red) lines. The time difference is $3\,nL/c$ ($6\,nL/c$) for the dotted (dashed) lines.

4.8 Conclusions

In this chapter, we have studied triangular microlasers in the ray model. As polygonal systems, in general, have non-chaotic classical ray dynamics we have used the decay rates of the trajectories to predict which trajectories will determine the far-field emission, instead of the unstable manifold which is only applicable to chaotic systems as discussed in the previous chapter. Importantly, the trajectories with the smallest nonzero decay rates need not to be periodic.

Further, we have seen that it can be necessary to include amplification of the intensity in the ray model to make reliable predictions for the far-field emission of highly lossy systems. Amplification is especially important if there occur different families of trajectories with similarly small decay rates.

In two examples, the equilateral and the right isosceles triangle, we have studied the influence of finite-wavelength corrections. In the case of polygonal cavities only the angular shift due to the Fresnel filtering effect is relevant. As the correction terms are large near the critical angle, therefore, they have the strongest influence on trajectories with incident angles close to critical incidence. If the maximum intensity trajectories, the trajectories with the smallest decay rates which determine the far-field emission, have incident angles close to the critical angle, the far-field emission can be strongly affected by the wave corrections. We find this to be case for the equilateral triangle, where the beam shift effects explain differences seen between the far-field calculated from the ray optics description and from electromagnetic wave simulations. Only an amended ray-optics model including the Fresnel filtering effect could establish agreement with the result of the wave simulation. In the case of the right isosceles triangle, we find that the angular shift can stabilize trajectories on simple periodic orbits if the periodic trajectories have incident angles close to the critical angle.

Especially, in the case of the highly lossy systems with rather regular ray dynamics studied here, the interplay of the optical and the geometrical properties is very important. The precise position of the critical angle given by the material in relation to the possible angles of incidence for each trajectory given by the geometry of the system determines which trajectories decay fast and which retain higher intensity. Nevertheless, we find the far-field emission to be quite robust with respect to small deviations from highly symmetrical cavities. This finding is relevant for experiments and possible applications where uncertainties in the manufacturing process of the cavities can lead to slight deviations from the desired structure.

In many cases we find good agreement between the results of our ray-optical predictions and results from experiment and wave simulation. In some cases, however, the results agree only poorly or not at all. Especially, the results of the experiment reported in [126] suggest that periodic trajectories might be more important than predicted here.

Chapter 5

Manipulated graphene-like systems

In this chapter, we consider a different class of model systems: graphene-like hexagonal lattice systems.

Graphene is a two-dimensional allotrope of carbon where the carbon atoms are arranged on a hexagonal lattice. Since the first description of its successful isolation in 2004 [136], graphene has experienced a lot of attention and lead to research in many different directions because of its peculiar mechanical, electronic, transport, and optical properties [37, 41, 137].

First, we give a short introduction to the basic properties of graphene and related systems, so-called artificial graphene which mimics some properties of real graphene. Then, we discuss the effect of uniaxial strain in a tight-binding model on the honeycomb lattice and its effects on the properties of the system. We focus especially on finite hexagonal lattice systems and the appearance of edge states. Finally, we discuss an effective ray description for graphene devices which bridges between the solid state model used in this chapter and the optical models discussed in the previous chapters.

5.1 Introduction to real and artificial graphene

In this section, we introduce the basic electronic properties of graphene. The electrons on the hexagonal lattice can be easily described in a tight-binding model. The resulting dispersion shows one of the most intriguing features of graphene, the so-called Dirac point: The valence and the conduction band touch at the corners of the Brillouin zone and the dispersion is linear around these points. The low-energy excitations around these points can be described by a Dirac equation for massless relativistic particles. This very interesting feature can be realized not only in graphene but also in artificially created hexagonal lattice systems, so-called artificial graphene [138].

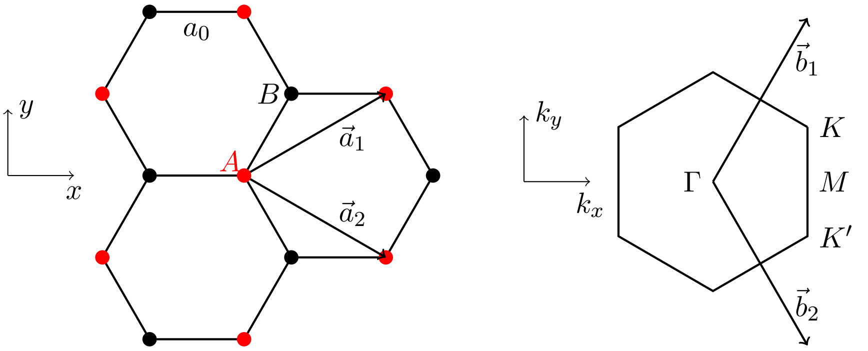

(a) Honeycomb lattice in real space.

(b) Brillouin zone of the honeycomb lattice

Figure 5.1: Honeycomb lattice and the corresponding Brillouin zone. $\vec{a}_1$, $\vec{a}_2$ are the lattice vectors, lattice sites A (black), B (red) define the two-atomic basis, a_0 is the nearest neighbor distance. $\vec{b}_1$, $\vec{b}_2$ are the reciprocal lattice vectors, Γ, M, K, K' are the high symmetry points of the Brillouin zone.

5.1.1 Tight-binding model

The carbon atoms in graphene are arranged on a two-dimensional hexagonal lattice, depicted in Fig. 5.1(a). The hexagonal lattice is not a basic lattice but a trigonal lattice with a two-atomic basis. The lattice vectors can be chosen as

$$\vec{a}_1 = \frac{a_0}{2}\begin{pmatrix}3\\ \sqrt{3}\end{pmatrix} \quad \text{and} \quad \vec{a}_2 = \frac{a_0}{2}\begin{pmatrix}3\\ -\sqrt{3}\end{pmatrix} \tag{5.1}$$

where a_0 is the nearest neighbor distance. The corresponding reciprocal lattice vectors are

$$\vec{b}_1 = \frac{2\pi}{3a_0}\begin{pmatrix}1\\ \sqrt{3}\end{pmatrix} \quad \text{and} \quad \vec{b}_2 = \frac{2\pi}{3a_0}\begin{pmatrix}1\\ -\sqrt{3}\end{pmatrix}. \tag{5.2}$$

The Brillouin zone is also hexagonal, as shown in in Fig. 5.1(b), with the high symmetry points Γ in the zone center, M in the middle of a zone edge, and the corner points K and K'.

The electronic structure of graphene can be easily described by a tight-binding model on the hexagonal lattice [37, 139]. Here, we apply a tight-binding model with up to third-nearest neighbor coupling similar to the models studied in Refs. [140–142], with the on-site energy ε_0, the nearest neighbor coupling t_1, the next-nearest neighbor coupling t_2, and the third-nearest neighbor coupling t_3. The model is schematically depicted in Fig. 5.2 where the couplings are illustrated.

This leads to the Hamiltonian in $\vec{k}$-space for a two-component wave function, $\psi = (\psi_A, \psi_B)$, in sublattice space

$$H_{\text{tb}} = \begin{pmatrix} \varepsilon_0 + f_2(\vec{k}) & f_1(\vec{k}) + f_3(\vec{k}) \\ f_1^*(\vec{k}) + f_3^*(\vec{k}) & \varepsilon_0 + f_2(\vec{k}) \end{pmatrix} \tag{5.3}$$

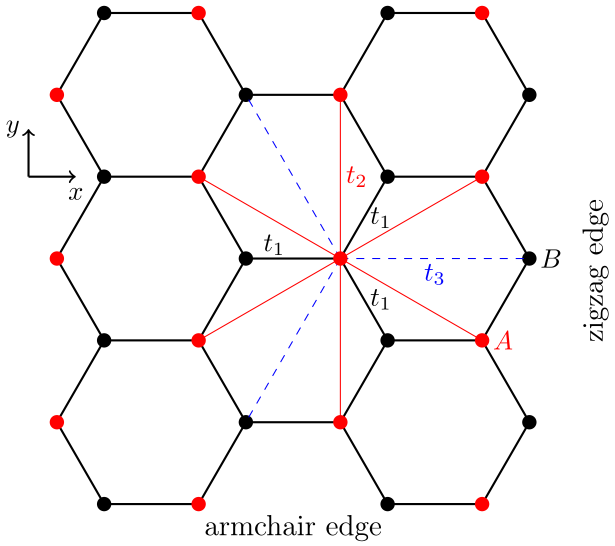

Figure 5.2: Schematics of the studied hexagonal lattice defining the sublattices A and B (red and black, respectively) and nearest neighbor, next-nearest neighbor, and third-nearest neighbor couplings, t_1 (black), t_2 (red), and t_3 (blue), respectively.

where

$$\begin{aligned} f_1(\vec{k}) &= -t_1\left(1+e^{i\vec{k}\cdot\vec{a_1}}+e^{i\vec{k}\cdot\vec{a_2}}\right) \\ f_2(\vec{k}) &= -2t_2\left[\cos\left(\vec{k}\cdot\vec{a_1}\right)+\cos\left(\vec{k}\cdot\vec{a_2}\right)+\cos\left(\vec{k}\cdot(\vec{a_1}-\vec{a_2})\right)\right] \\ f_3(\vec{k}) &= -t_3\left(e^{i\vec{k}\cdot(\vec{a_1}+\vec{a_2})}+2\cos\left(\vec{k}\cdot(\vec{a_1}-\vec{a_2})\right)\right) \end{aligned} \tag{5.4}$$

are the nearest neighbor, the next-nearest neighbor, and the third-nearest neighbor contributions, respectively. As the wave function in sublattice space looks like a spinor wave function the sublattice degree of freedom, A or B, is often called pseudospin.

The energy dispersion $\varepsilon(\vec{k})$ is obtained by diagonalizing the Hamiltonian, Eq. (5.3). Using the abbreviations defined in Eq. 5.4 it reads

$$\varepsilon_\pm(\vec{k}) = \varepsilon_0 + f_2(\vec{k}) \pm |f_1(\vec{k}) + f_3(\vec{k})|. \tag{5.5}$$

The parameters of the tight-binding model can be chosen to reproduce the dispersion of real or artificial graphene to high precision. Without loss of generality, the on-site energy can be set to zero, $\varepsilon_0 = 0$, as it gives only an overall offset in energy. The energy scale is set by the nearest neighbor interaction energy t_1, every energy will be given in multiples of t_1 in the following. Here, the remaining parameters, the next- and third-nearest neighbor coupling strength are chosen as $t_2 = -0.091t_1$ and $t_3 = 0.071t_1$ which are the values found to reproduce the experiments with a microwave analog of graphene [142, 143].

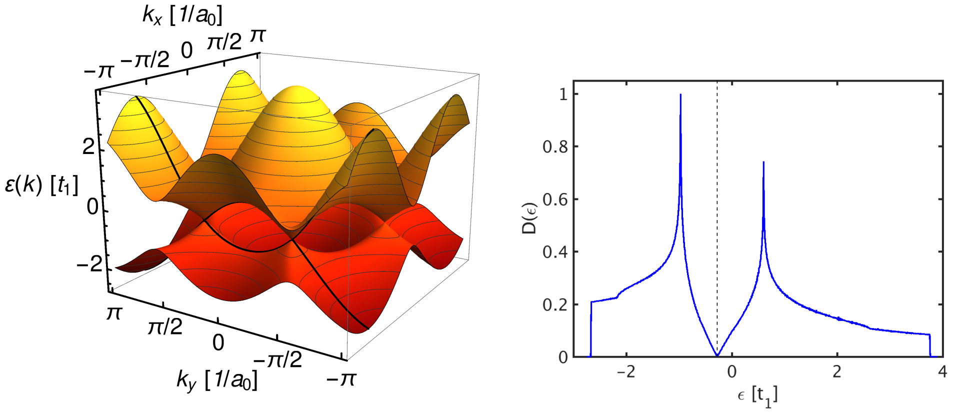

(a) Full dispersion.

(b) Density of states.

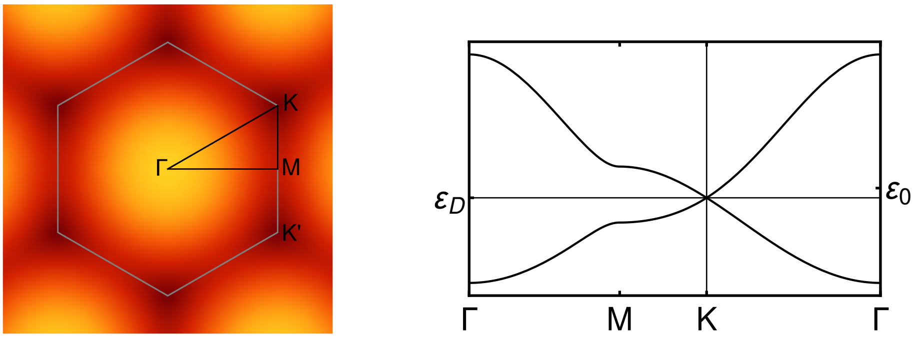

(c) Brillouin zone (gray) superimposed on the dispersion of the upper band in color scale.

(d) Dispersion of graphene along the high symmetry path in the Brillouin zone shown in (c).

Figure 5.3: Dispersion relation resulting from the tight-binding model on the hexagonal lattice defined in Eq. (5.3) with the parameters defined in the text.

They are also in the range expected for real graphene [139]. The resulting dispersion is shown in Fig. 5.3.

The two energy bands, $\varepsilon_+(\vec{k})$ and $\varepsilon_-(\vec{k})$, touch at the corner points of the Brillouin zone, K and K'. In the vicinity of these points the dispersion is conical. As this resembles the dispersion resulting from the Dirac equation for a massless particle, the two points are called Dirac points [37].

Due to charge neutrality, the bands have to be half filled in pristine graphene. The lower band $\varepsilon_-(\vec{k})$ is fully occupied and the upper band $\varepsilon_+(\vec{k})$ is empty. Thus, graphene is often classified as a semimetal or a gapless semiconductor [37]. The broken electron-hole-symmetry due to the next-nearest neighbor coupling is manifest in the asymmetry between the upper and the lower band and can be clearly seen in the dispersion as well as in the density of states.

The corresponding density of states is shown in Fig. 5.3(b). Right at the

Dirac point, the density of states vanishes. Following directly from the linear dispersion in the vicinity of the Dirac point, the density of states also increases linearly near the Dirac point. The local extrema of the dispersion at the M point in the Brillouin zone lead to the prominent van-Hove singularities in the density of states.

The conical dispersion around the K- and K'-point can already be obtained in a simpler version of the tight-binding model including only nearest neighbor interaction [37]. Including a finite value for the next-nearest neighbor interaction t_2 breaks the electron-hole symmetry and shifts the Dirac-energy ε_D, the energy at which the two bands touch, from the on-site energy ε_0 to the value $\varepsilon_D = \varepsilon_0 + 3t_2$. Both effects can be seen in Fig. 5.3. The third-nearest neighbor interaction t_3 does not have a strong effect on the dispersion as long as it is small compared to the nearest neighbor interaction, $|t_3| \ll t_1$. However, it should be included for completeness as the third-nearest neighbor distance in the hexagonal lattice is only slightly larger than the next-nearest neighbor distance [139]. If the third-nearest neighbor interaction is allowed to take on arbitrary values it leads to some interesting phenomena [144, 145].

The conical, “Dirac-like”, dispersion of the low-energy electronic excitations, one of graphene’s most intriguing features, has been described already in 1947 [146]. It is due to the symmetry of the lattice and the equivalence of the two sublattices in the two-dimensional hexagonal lattice formed by the carbon atoms of graphene. If the two sublattices are no longer equivalent a gap will open up and the dispersion becomes quadratic [147].

5.1.2 Dirac equation

Now, the dispersion around one of the two Dirac points, K or K', is examined in more detail. The Dirac points are

$$\vec{K} = \frac{2\pi}{3a_0}\begin{pmatrix} 1 \\ \frac{1}{\sqrt{3}} \end{pmatrix} \qquad \text{and} \qquad \vec{K}' = \frac{2\pi}{3a_0}\begin{pmatrix} 1 \\ -\frac{1}{\sqrt{3}} \end{pmatrix}. \tag{5.6}$$

Writing $\vec{k} = \vec{K} + \vec{q}$, the full dispersion Eq. (5.5) can be expanded for small $|\vec{q}|$ as

$$\varepsilon_\pm(\vec{q}) \approx \varepsilon_0 + 3t_2 \pm a_0\left(\frac{3}{2}t_1 - 3t_3\right)|\vec{q}|. \tag{5.7}$$

In the vicinity of the second Dirac point K' an analogous result is obtained.

A comparison between the full dispersion Eq. (5.5) and the linearized dispersion Eq. (5.7) is shown in Fig. 5.4 in the vicinity of one Dirac point. For small $|\vec{q}|$ the linearized dispersion agrees well with the full dispersion. For larger $|\vec{q}|$, however, the full dispersion deviates from the conical shape with a threefold symmetric direction dependence. This so-called trigonal warping [148] is captured only in the expansion to second order in $|\vec{q}|$ [37].

The linearized dispersion can be interpreted as the result from a two-dimensional Dirac equation for a massless particle. For the real-space wave

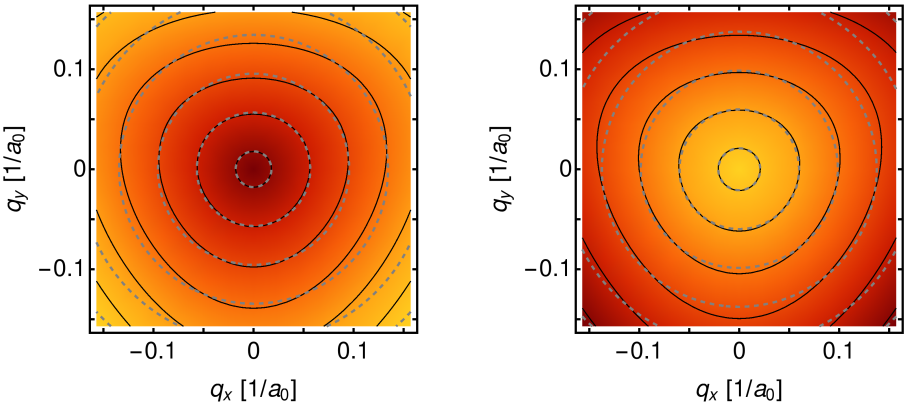

(a) The upper band ε_+.

(b) The lower band ε_-.

Figure 5.4: Comparison between the full dispersion Eq. (5.5) and the linearized dispersion Eq. (5.7) in the vicinity of the Dirac point K with $\vec{k} = \vec{K} + \vec{q}$. The full dispersion is shown in color scale with black contour lines, the contour lines (gray dashed) of the linearized dispersion are superimposed.

function $\psi(\vec{r}) = (\psi_A(\vec{r}), \psi_B(\vec{r}))$ in the vicinity of the Dirac points it can be written in the form

$$-\mathrm{i}\xi v_0 \vec{\sigma} \cdot \nabla \psi(\vec{r}) = (\varepsilon - \varepsilon_D)\psi(\vec{r}) \tag{5.8}$$

with the Pauli matrices $\vec{\sigma} = (\sigma_x, \sigma_y)$, the velocity $v_0 = a_0(3t_1/2 - 3t_3)$, the Dirac energy $\varepsilon_D = \varepsilon_0 + 3t_2$, and $\xi = \pm 1$ for the K- and K'-point, respectively. We use $\hbar \equiv 1$ throughout this chapter. The velocity v_0 takes the role of the speed of light and the sublattice degree of freedom, A or B, takes the role of the real spin in the usual Dirac equation. Therefore, the sublattice degree of freedom is called pseudospin as mentioned already earlier. In consequence, the low-energy excitations near the Dirac points in graphene behave like massless relativistic particles.

Another important feature of these Dirac-like excitations is their helicity or chirality [37]. The helicity operator is defined as

$$\hat{h} = \frac{1}{2}\vec{\sigma} \cdot \frac{\vec{p}}{|\vec{p}|} \tag{5.9}$$

where $\vec{p} = -\mathrm{i}\nabla$ is the momentum operator. It is directly seen from the Dirac equation Eq. (5.8) that its eigenfunctions are also eigenstates of the helicity operator. This means that the eigenstates of $\vec{\sigma}$ which acts on the sublattice degree of freedom is always aligned parallel or antiparallel to the direction of motion. Electron-like eigenstates of the Hamiltonian Eq. (5.8) have positive helicity, whereas, hole-like states have negative helicity [37].

Among other consequences, the chirality of the Dirac particles leads to the so-called Klein tunneling, perfect transmission through a potential barrier at normal incidence [149–151]. We will use this feature in section 5.4.

5.1.3 Photonic graphene

The existence of the Dirac cones in the dispersion of graphene relies only on the symmetry of the hexagonal lattice [146, 147]. Thus, this feature can be realized in many materials that have this symmetry [152]. Especially, the appearance of Dirac cones is not restricted to natural materials but can also be found in artificial structures. A review on different realizations, *e.g.*, in patterned two-dimensional electron gases, with molecules arranged on a surface, or ultracold atoms in an optical lattice, of this so called “artificial graphene” is given in [138].

The different realizations of artificial graphene are very versatile and can have advantages over real graphene. Often, they provide very good control over the configuration and geometry of the system. On the one hand, this allows for the study of defect-free samples with a well-defined geometry. On the other hand, this also enables the introduction of well-defined defects and impurities and the study of their influence. Further, the artificial graphene realizations are often easier to manipulate and allow for the study of wider parameter regimes that are not or not easily, accessible in real graphene.

In this work, the attention is drawn to photonic crystal analogs of graphene. In a photonic crystal [5], light takes the role of the electrons in a real crystal. Electromagnetism in a periodic dielectric governed by Maxwell’s equations is studied instead of quantum mechanics in a periodic potential based on the Schrödinger equation. The electronic band structure that classifies the energies $E_n(\vec{k})$ of the allowed eigenstates is replaced by the photonic band structure that gives the frequencies $\omega_n(\vec{k})$ of the allowed harmonic modes. On the basis of these ideas, “photonic graphene” has been realized in many experiments, see, *e.g.*, [153–155] for realizations at optical frequencies or [142, 143, 156] for realizations at microwave frequencies.

5.2 Band structure manipulations by uniaxial strain

In this section, we discuss the influence of uniaxial strain on the band structure of the hexagonal lattice systems. To this end, we use generalizations of the tight-binding model originally defined in Eq. (5.3) and (5.4) and in Fig. 5.2. The parameters of the tight-binding model can be tuned to reproduce the dispersion of real or artificial graphene to high precision. However, it also allows to study deviations from the pristine graphene lattice by simply changing the parameters. Though these manipulations, discussed in detail in the subsequent sections, cannot be easily implemented in real graphene, they might be experimentally accessed in artificial graphene.

5.2.1 Uniaxial strain in graphene-like systems

Uniaxial strain in the honeycomb lattice breaks the discrete rotational symmetry of the lattice. It can be modeled by varying the nearest neighbor coupling in one direction. In this model, a phase-transition from the gapless to a gapped phase is predicted [140, 141, 157, 158]. This phase transition has been observed in photonic [143, 159] and electronic [160] artificial graphene.

We chose the strain to act along one of the nearest neighbor directions defining the x-direction and the strain is modeled as $t_1' = \beta t_1$ as shown in Fig. 5.5. Then, the nearest neighbor contribution f_1 (see Eq. (5.4)) in the tight-binding Hamiltonian Eq. (5.3) becomes

$$f_1(\vec{k}) = -t_1' - t_1 \left(\mathrm{e}^{\mathrm{i}\vec{k}\cdot\vec{a_1}} + \mathrm{e}^{\mathrm{i}\vec{k}\cdot\vec{a_2}} \right). \tag{5.10}$$

Modifying also the next- and third-nearest neighbor contributions in the corresponding directions would be a more complete model of uniaxial strain. However, as the next- and third-nearest neighbor coupling parameters are more than an order of magnitude lower than the nearest neighbor coupling, it is a good approximation that they stay the same in all directions.

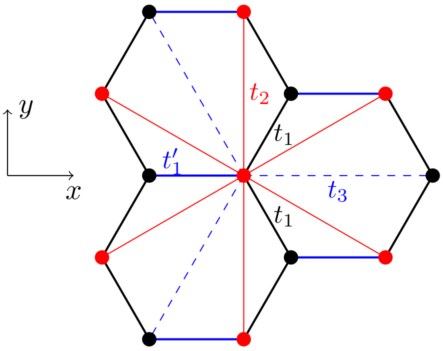

Figure 5.5: Schematics of the coupling parameters used in the tight-binding Hamiltonian to model uniaxial strain in x-direction.

By applying strain $\beta \neq 1$ in the x-direction, the two neighboring Dirac points K and K' move along the k_y-direction. If the coupling becomes weaker, $\beta < 1$, which can be translated to a stretching of the lattice, the two points move further apart (see Fig. 5.6(b)). When the coupling becomes stronger, $\beta > 1$, corresponding to a compression of the lattice, the two Dirac points move closer together until they touch for the critical value $\beta_c = 2 - 3t_3/t_1$, see Fig. 5.6(c) and (d). For even stronger strain, a gap opens up in the spectrum, see Fig. 5.6(d). Hence, β_c marks a phase transition from the gapless phase to the gapped phase which is well studied in the literature, *cf.* [140, 141, 157, 158].

At the critical strain where the two Dirac points merge, the low energy expansion of the dispersion also changes its shape. Whereas it is linear in all directions as long as the two Dirac points are separated, it becomes quadratic in the k_y-direction when the Dirac points have merged. In the perpendicular direction, the k_x-direction, the dispersion stays linear.

In photonic graphene, the coupling constants are mainly determined by the lattice constant, *i.e.* by the nearest neighbor distance [142]. Thus, uniaxial strain is realized in the experiments with photonic graphene by reducing the nearest neighbor distance along one of the three lattice directions [143, 159]. Although these experiments are a good realization of the model they introduce an effect that is not captured in the model. They change the size and the shape of the unit cell.

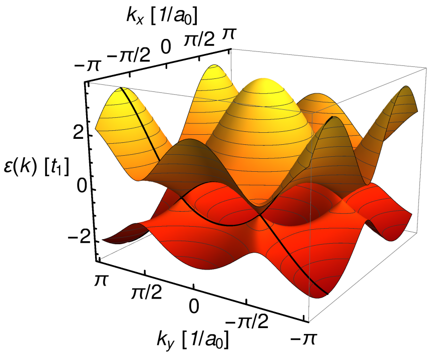

(a) Unstrained $\beta = 1$.

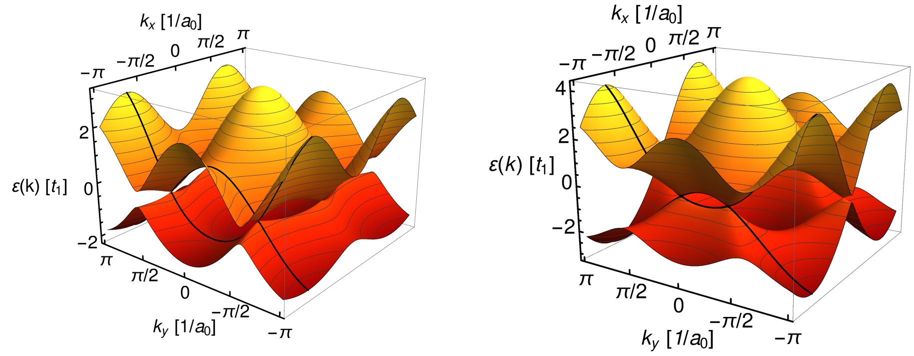

(b) Stretching, $\beta < 1$.

(c) Subcritical compression, $1 < \beta < \beta_c$.

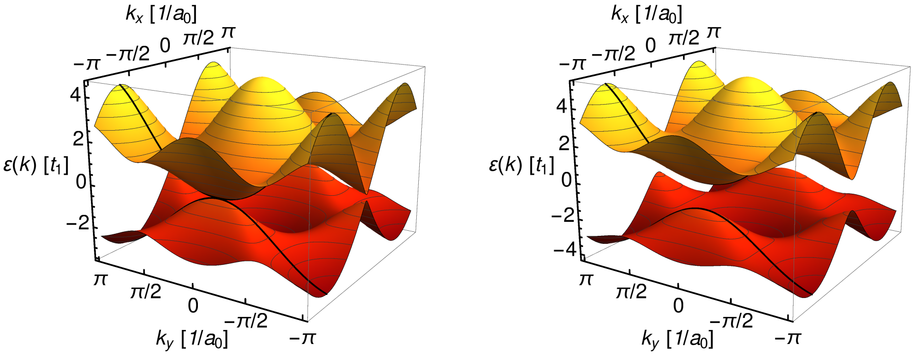

(d) Critical compression, $\beta = \beta_c$.

(e) Supercritical compression, $\beta > \beta_c$.

Figure 5.6: Dispersion relation resulting from the tight-binding model of the hexagonal lattice under uniaxial strain, $t_1' = \beta t_1$, in x-direction. The critical strain is $\beta_c = 2 - 3t_3/t_1$.

5.2.2 Uniaxial strain in “boron nitride”

The two sublattices, A and B, of the hexagonal lattice might be inequivalent, in contrast to graphene where they are occupied by equivalent carbon atoms. This is the case, *e.g.*, in the two-dimensional material hexagonal boron nitride [152, 161] and can also be easily realized in a photonic experiment [162].

In the tight-binding model, different atoms on the two sublattices can be represented by different on-site potentials for the sublattices, *i.e.* ε_A the on-site potential on sublattice A and ε_B the on-site potential on sublattice B with $\varepsilon_A \neq \varepsilon_B$. Then, the Hamiltonian of Eq. (5.3) becomes

$$H_{\text{tb}} = \begin{pmatrix} \varepsilon_A + f_2(\vec{k}) & f_1(\vec{k}) + f_3(\vec{k}) \\ f_1^*(\vec{k}) + f_3^*(\vec{k}) & \varepsilon_B + f_2(\vec{k}) \end{pmatrix}. \tag{5.11}$$

The resulting dispersion is

$$\varepsilon_\pm(\vec{k}) = \frac{\varepsilon_A + \varepsilon_B}{2} + f_2(\vec{k}) \pm \sqrt{\left(\frac{\varepsilon_A - \varepsilon_B}{2}\right)^2 + |f_1(\vec{k}) + f_3(\vec{k})|^2} \tag{5.12}$$

which is shown in Fig. 5.7. It can be seen that the two bands do not touch, rather, an energy gap $\Delta\varepsilon = |\varepsilon_A - \varepsilon_B|$ is found. Further, the low-energy expansion of the dispersion is no longer linear but parabolic. Hence, the dispersion of the material described by this model is that of a two-dimensional usual semiconductor.

We discuss now which effects the uniaxial strain has on the band structure of boron nitride like systems. It can be implemented in the same way as for the graphene-like system considered in the previous paragraph. The resulting dispersions for different strain are shown in Fig. 5.8. The effects are very similar, however, here it does not lead to a phase transition as the band structure

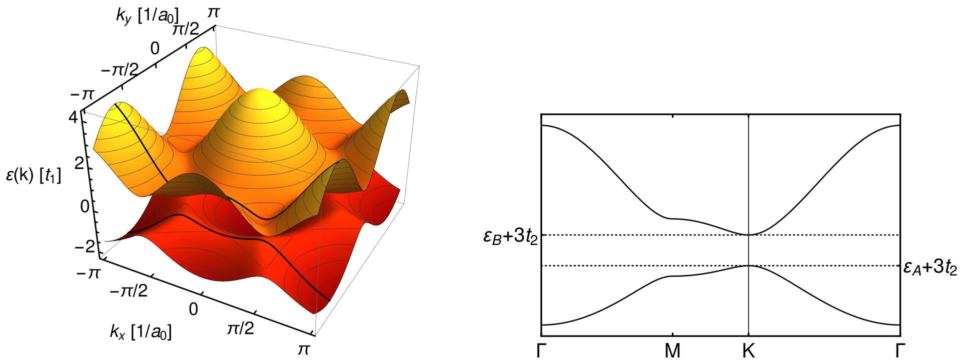

(a) Full dispersion.

(b) Dispersion along the high symmetry path in the Brillouin zone.

Figure 5.7: Dispersion relation given in Eq. (5.12) resulting from the tight-binding model of the hexagonal lattice with two different on-site potentials, the energy difference is chosen as $\Delta\varepsilon = |\varepsilon_A - \varepsilon_B| = t_1$.

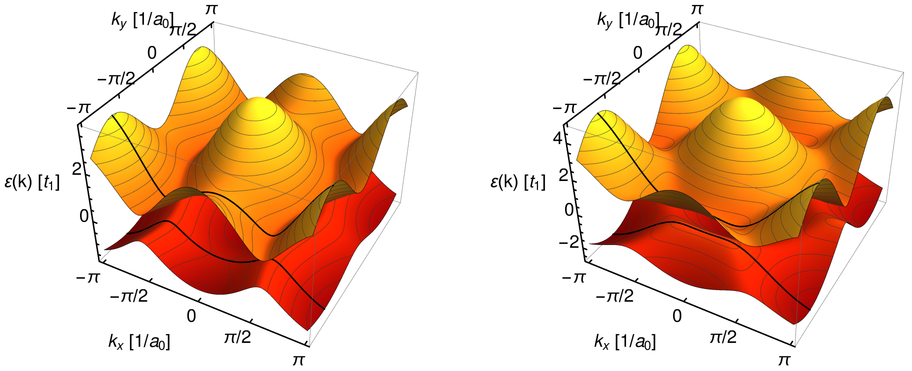

(a) Stretching, $\beta < 1$.

(b) Subcritical compression, $1 < \beta < \beta_c$.

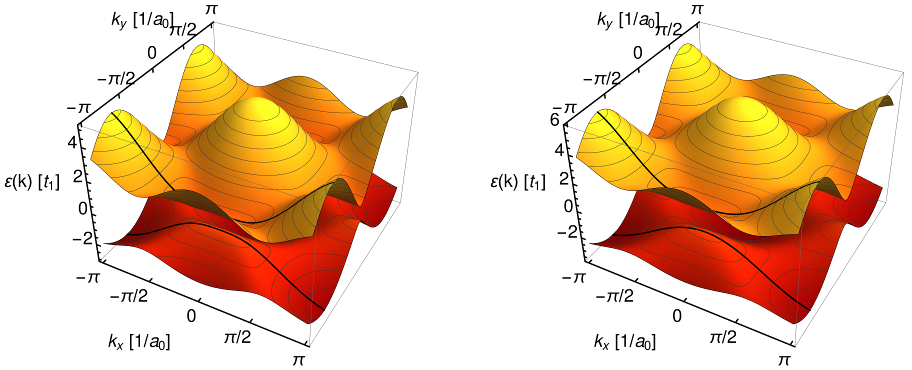

(c) Critical compression, $\beta = \beta_c$.

(d) Supercritical compression, $\beta > \beta_c$.

Figure 5.8: Dispersion relation resulting from the tight-binding model of the hexagonal lattice with two different on-site potentials under uniaxial strain, $t_1' = \beta t_1$, in x-direction. The critical strain is $\beta_c = 2 - 3t_3/t_1$, the difference between the on-site potentials is $\Delta\varepsilon = |\varepsilon_A - \varepsilon_B| = t_1$.

is already gapped. For strain in the x-direction, the parabolic extrema of the bands move along the k_y-direction. At the critical strain β_c the two neighboring extrema merge and, for even stronger strain, the band gap increases.

5.3 Finite honeycomb systems under strain

For all finite systems, it is important to understand the influence of the boundary. In graphene, especially, the possible existence of edge states is of great interest. Theoretically, the appearance of edge states in clean and freestanding graphene is well understood [39, 163]. However, they are difficult to measure in experiments with real graphene. On the one hand, it is hard to control the precise configuration of the boundaries, on the other hand, the dangling bonds at the lattice terminations have to be passivated [40, 41]. In suitably chosen artificial graphene, the predicted edge states can be easily observed and studied in detail. Due to the versatility of the artificial graphene realizations, edge phenomena can be examined that are not accessible in graphene.

Here, we study finite graphene-like and boron nitride-like systems under uniaxial strain with different boundary shapes. Under uniaxial strain, edge states at the boundaries perpendicular to the strain direction are found independent of the edge termination.

5.3.1 Tight-binding model on finite hexagonal lattice systems

For an efficient description of finite lattice systems in the tight-binding model, the second quantized notation is especially useful. The tight-binding Hamiltonian Eq. (5.3) for the hexagonal lattice can be alternatively expressed using creation and annihilation operators. The symmetrical and undistorted tight binding Hamiltonian on the hexagonal lattice with equal on-site potential on both sublattices then reads

$$\begin{aligned} H =& \varepsilon_0 \sum_i \left(\hat{a}_i^\dagger \hat{a}_i + \hat{b}_i^\dagger \hat{b}_i \right) - t_1 \sum_{\langle i,j \rangle} \left(\hat{a}_i^\dagger \hat{b}_j + \text{h.c.} \right) \\ & - t_2 \sum_{\langle\langle i,j \rangle\rangle} \left(\hat{a}_i^\dagger \hat{a}_j + \hat{b}_i^\dagger \hat{b}_j + \text{h.c.} \right) - t_3 \sum_{\langle\langle\langle i,j \rangle\rangle\rangle} \left(\hat{a}_i^\dagger \hat{b}_j + \text{h.c.} \right) \end{aligned} \tag{5.13}$$

where $\hat{a}_i^\dagger$ ($\hat{a}_i$) creates (annihilates) an electron on lattice site i on sublattice A with analogous definitions for sublattice B. The summations run over all lattice sites $i = 1, \ldots, N$, the nearest neighbors $\langle i, j \rangle$, next-nearest neighbors $\langle\langle i, j \rangle\rangle$ and third-nearest neighbors $\langle\langle\langle i, j \rangle\rangle\rangle$, respectively. Diagonalizing this Hamiltonian gives the eigenenergies ε_n and the eigenstates ψ_n of the system.

From the eigenstates and their energies further quantities can be obtained. The numerical density of states is the histogram of the energies of all eigenstates of the system. We define the local density of states as

$$g_{\delta\varepsilon}(\vec{r}, \varepsilon) = \sqrt{\frac{1}{N} \sum_n |\psi_n(\vec{r})|^2} \tag{5.14}$$

where the sum runs over all states n in a small energy interval $\varepsilon - \delta\varepsilon < \varepsilon_n < \varepsilon + \delta\varepsilon$ and N is the number of states over which is summed. This quantity is related to experiments on real graphene as in a scanning tunneling microscopy experiment, typically, a quantity proportional to the local density of states is measured instead of a single state.

The manipulations discussed in the previous section, uniaxial strain and different on-site potentials, can be easily included in this model of the finite system, too.

5.3.2 Hexagonal graphene flakes

Hexagonally shaped finite honeycomb lattice systems are especially suited to study edge states as they can be chosen to show only one of the two natural boundary configurations of the hexagonal lattice, either armchair or zigzag boundaries which are defined in Fig. 5.2. It has been shown that edge states in graphene occur at the zigzag edge, whereas no edge states are possible at an armchair edge [39, 163]. This is, however, only true for the undistorted system. For anisotropic nearest neighbor coupling, edge states can appear also on the armchair edges [164]. Under uniaxial strain, edge states at the boundary perpendicular to the strain direction are found independent of the edge termination. The appearance of edge states is unrelated to the phase transition discussed above and has been observed in photonic graphene, both, in a microwave realization [143] and in a realization with visible light [159].

The two hexagonally shaped systems, one with purely armchair boundaries and one with purely zigzag boundaries, which we will study here are shown in Fig. 5.9. The tight-binding model is solved for the finite systems to obtain the wave functions (eigenstates) and the corresponding energies.

As a reference, we examine the undistorted system first. The numerical density of states and the local density of states around the Dirac energy are shown in Fig. 5.10(a) for the armchair system and in Fig. 5.11(a) for the zigzag system. The energy interval around the Dirac energy used to obtain the local

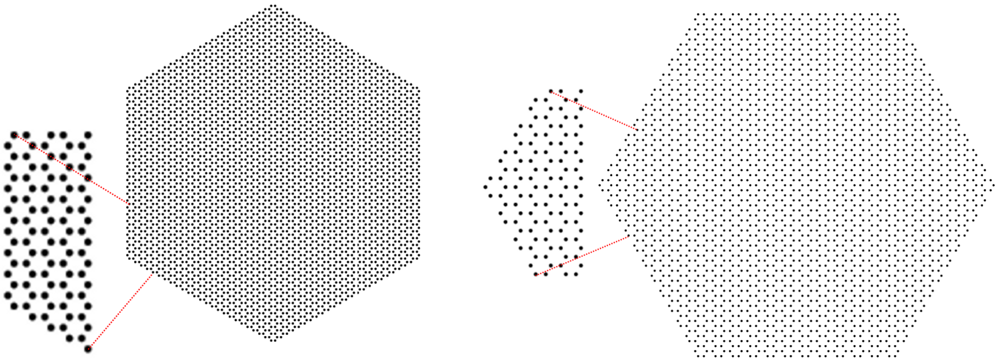

(a) Pure zigzag boundaries (3750 lattice sites).

(b) Pure armchair boundaries (2382 lattice sites).

Figure 5.9: Schematics of the terminated hexagonal lattice systems with pure zigzag and armchair boundaries.

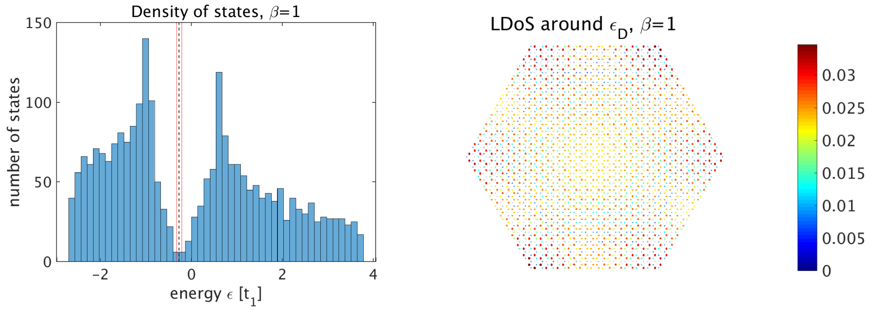

(a) Symmetric, $\beta = 1$.

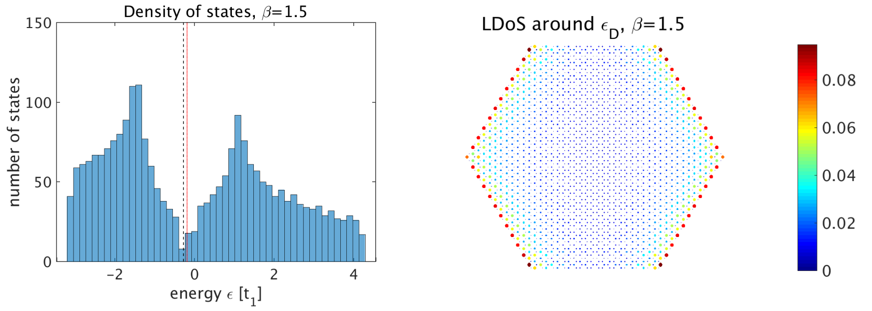

(b) Subcritical compression, $1 < \beta < \beta_c$.

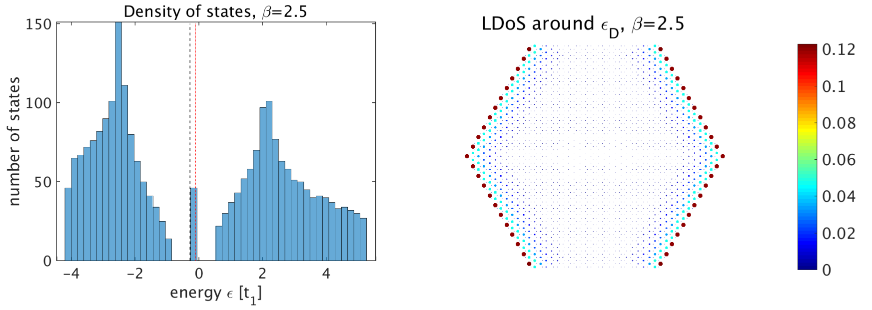

(c) Supercritical compression, $\beta > \beta_c$.

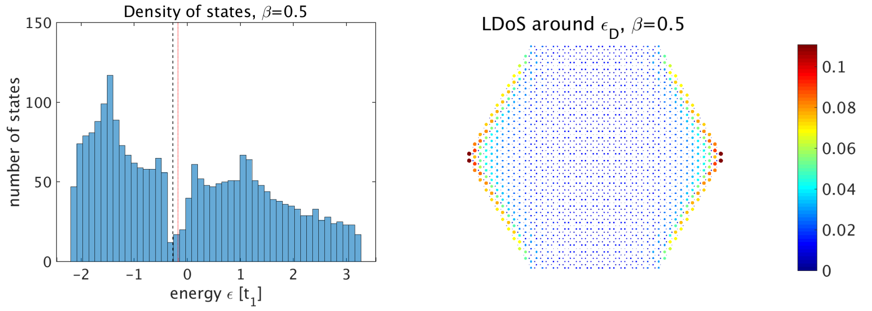

(d) Stretching, $\beta < 1$.

Figure 5.10: Density of states and local density of states around the Dirac energy for the armchair system shown in Fig. 5.9(b) calculated from the tight-binding model including uniaxial strain, $t_1' = \beta t_1$. The local density of states is calculated from states in the energy interval indicated in the numerical density of states.

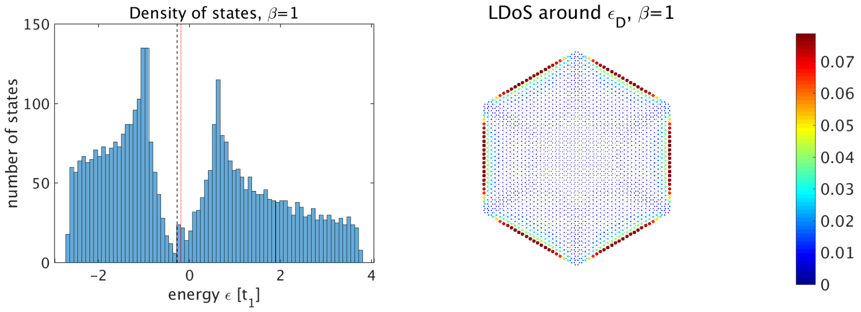

(a) Symmetric, $\beta = 1$.

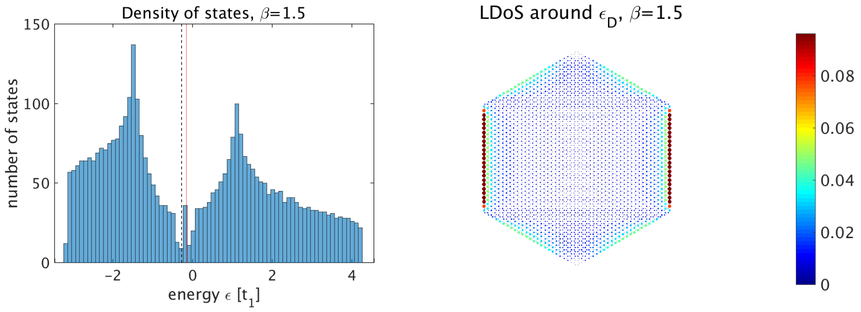

(b) Subcritical compression, $1 < \beta < \beta_c$.

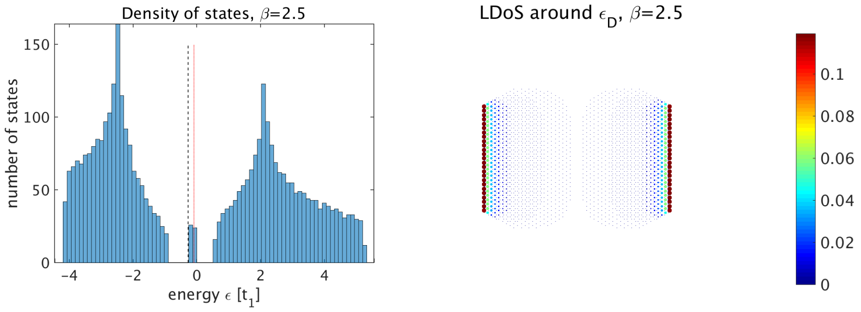

(c) Supercritical compression, $\beta > \beta_c$.

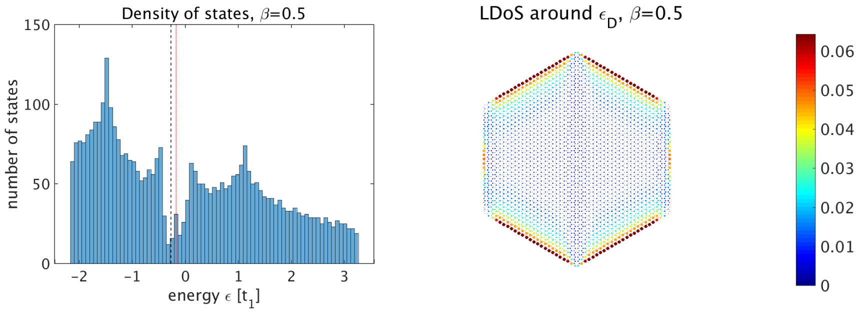

(d) Stretching, $\beta < 1$.

Figure 5.11: Density of states and local density of states around the Dirac energy for the zigzag system shown in Fig. 5.9(a) calculated from the tight-binding model including uniaxial strain, $t_1' = \beta t_1$. The local density of states is calculated from states in the energy interval indicated in the numerical density of states.

density of states is indicated in the plot of the numerical density of states. As the system is finite it has a discrete energy spectrum and no band structure, thus, the numerical density of states reproduces only approximately the full density of states of the infinite lattice shown in Fig. 5.3(b), the main features are in very good agreement. For the finite zigzag terminated system we find states at the Dirac energy, whereas, in the infinite system there is no state right at the Dirac energy. By looking at the local density of states it is clear that these states are localized at the edges, as expected. For the armchair terminated system, however, there is no state at the Dirac energy as in the infinite system and, clearly, there is also no edge state. The local density of states around the Dirac energy shows almost uniform intensity over the whole system.

If we apply compressive strain, $\beta > 1$, states occur at the Dirac energy in both systems, the zigzag and the armchair system (see panels (b) and (c) of Fig. 5.10 and 5.11). These states are localized at the edges perpendicular to the strain direction, *i.e.*, here at the edges in the y-direction. For the zigzag system, the edge states are no longer symmetrical on all edges, for the armchair system, the edge states show up only under strain. The edge states occur already for subcritical strain where the dispersion is still gapless. This means that the formation of edge states under strain is independent of the phase transition observed for uniaxial strain. The opening of the gap is also clearly seen in the numerical density of states. For stronger strain the number of states at the Dirac energy increases and the states are more strongly localized.

It is interesting to observe that the edge states have high intensity only on one sublattice for each edge. For the zigzag-terminated system this is not surprising as the outer atoms on each edge belong only to one sublattice (*cf.* Fig. 5.2). If one edge consists of A atoms the opposite edge is comprised of B atoms. An armchair edge, however, shows both sublattices equally. Nevertheless, the edge states select one sublattice on each edge. This is explained by the corners which are defects in the armchair termination. A corner consists of a single atom that breaks the symmetry between the two sublattices.

The results for the application of stretching strain, $\beta < 1$, are shown in panel (d) of Figs. 5.10 and 5.11. The numerical density of states shows the behavior expected from the dispersion shown in Fig. 5.6. The two maxima in each band are the remnants of the van-Hove singularities expected from the two different energies of the local extrema at the different M-points in the strain direction and perpendicular to it. The states around the Dirac energy show different behavior for the two edge terminations. For the zigzag termination the resulting states are states localized in the edges parallel to the strain direction. This can be interpreted as the edge states resulting from compressive strain in the perpendicular direction. In the system with armchair edges, in contrast, the states are localized on the same edges as for the compressive strain. However, this is realized in such a way that now the other sublattice shows high intensity. The state is not localized on the lattice sites of the sublattice corresponding to the lattice site directly on the corner as for compressive strain but on the sublattice defined by the lattice sites next to the corner. This change in sublattice is also observed for the zigzag system where two neighboring edges show different sublattices as their outer lattice sites.

In the microwave experiments [143], where the model of uniaxial strain has been implemented, a hexagonal system with armchair edges with 222 lattice sites has been studied. We find a very good agreement with the results found in the experiment, however, we study a much larger system here. Moreover, we find the effect to be independent of the edge termination.

5.3.3 Circular graphene flake

Now, we examine a circular honeycomb lattice system. The model system that we consider is shown in Fig. 5.12. Due to the discreteness of the lattice, the boundary is not a perfectly smooth circle. It rather shows some generic termination of the hexagonal lattice which is neither purely armchair nor purely zigzag terminated. Edge states are expected at every boundary of the graphene lattice which is not purely armchair terminated [165].

The calculated density of states and the eigenenergies of the states of the circular system under uniaxial strain are shown in Fig. 5.13. Here, we observe a similar behavior as for the purely zigzag terminated system discussed in the previous paragraph. In the unstrained system, see panel (a), we find several states at the Dirac energy, otherwise, the numerical density of states approximates very well the density of states of the infinite system (*cf.* Fig. 5.3(b)). The states around the Dirac energy are localized on the parts of the boundary which are predominantly zigzag terminated, on the predominantly armchair terminated parts no intensity is found.

If strain in x-direction is applied, the edge states are now found on the edges perpendicular to the strain direction for compressive strain, $\beta > 1$, and on the edges parallel to the strain direction for stretching, $\beta < 1$, as observed

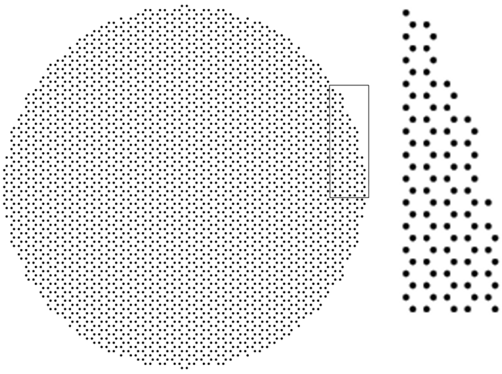

Figure 5.12: Schematics of the circular “graphene flake” with 3366 lattice sites. The right part shows a close-up of the lattice sites in the rectangle.

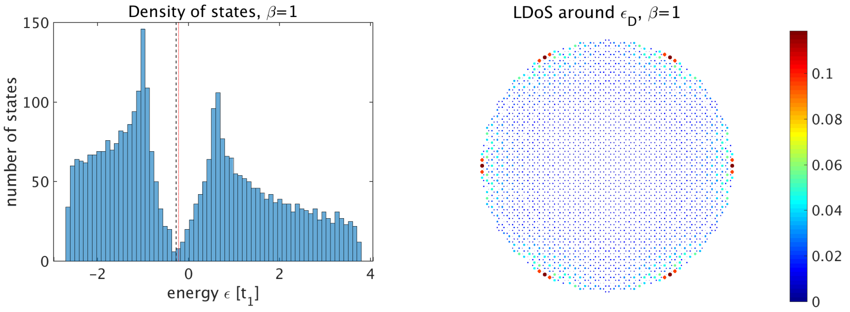

(a) Symmetric, $\beta = 1$.

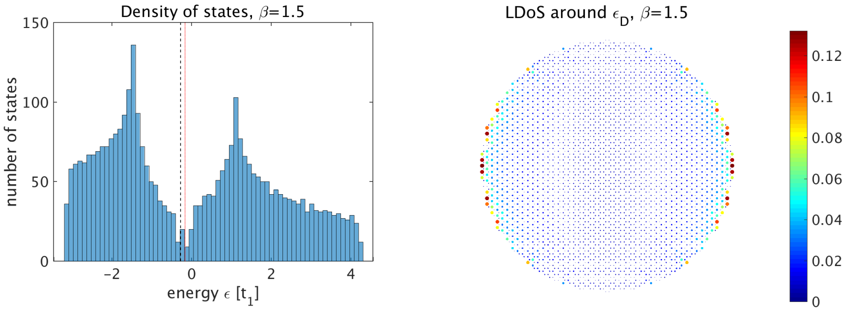

(b) Subcritical compression, $1 < \beta < \beta_c$.

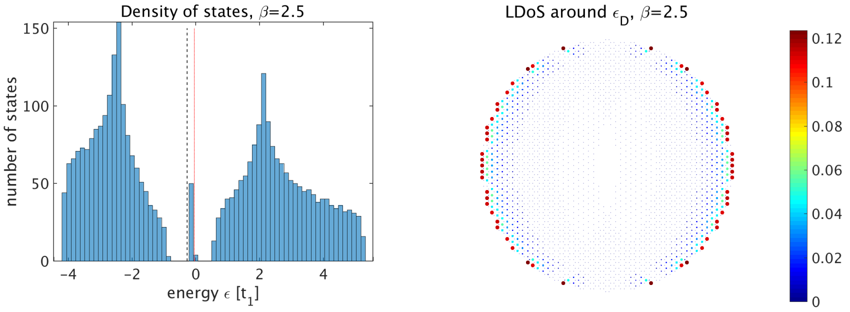

(c) Supercritical compression, $\beta > \beta_c$.

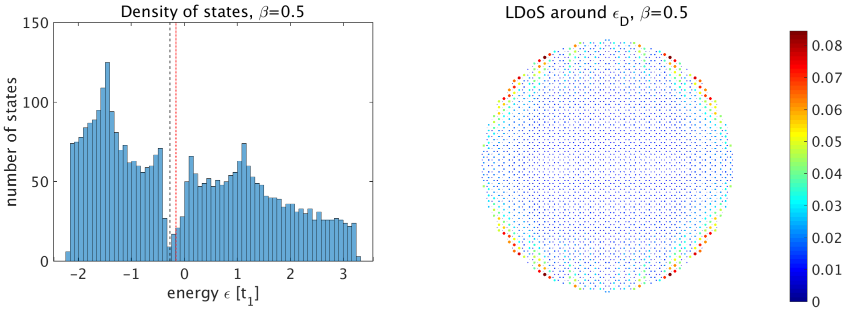

(d) Stretching, $\beta < 1$.

Figure 5.13: Density of states and local density of states around the Dirac energy for the circular hexagonal lattice systems shown in Fig. 5.12 calculated from the tight-binding model including uniaxial strain, $t_1' = \beta t_1$. The local density of states is calculated from states in the energy interval indicated in the numerical density of states.

for the zigzag system in the last paragraph. For supercritical strain, $\beta > \beta_c$, we also find the expected phase transition to the gapped phase.

We examine now the evolution of single states under uniaxial strain in the circular system. First, we look at two bulk states shown in Fig. 5.14, the state with number $1 + x = 7$ in the lower band and the corresponding state $N - x = 3360$ in the upper band, where $N = 3366$ is the number of lattice sites in the whole system. In the undistorted system (see panel (a)), the states show the typical structure of modes in a radially symmetric system with radial and azimuthal nodes. The states chosen here, show no radial node and three azimuthal nodal lines. The states can, however, not exhibit the radial symmetry arbitrarily, they also have to reflect the symmetry of the underlying lattice, the reflection symmetries and the discrete rotational symmetry.

Further, we see that the states in the lower and in the upper band exhibit different behavior concerning the sublattices. Whereas the sign of the eigenstate amplitudes in the lower band is the same on neighboring lattice sites, the sign of the amplitude changes from lattice site to lattice site for a state in the upper band. The corresponding states in the upper and the lower band are orthogonal, but the resulting intensities are the same for both states.

The uniaxial strain breaks the rotational symmetry of the lattice. The states have to reflect this new symmetry as well. The two different states, however, evolve differently under strain. Whereas, the hole-like state is oriented parallel to the strain direction for compression and perpendicular to it for stretching, the electron-like states behaves the other way around. Hence, the states are deformed differently and their intensities are no longer the same.

Finally, we examine two states near the Dirac energy, shown in Fig. 5.15. These states are strongly localized at the boundary and no longer reflect the circular symmetry as they probe the edges of the system which are not smoothly curved but rather irregular due to the lattice. Under strain, these states evolve as expected for edge states from the discussion above.

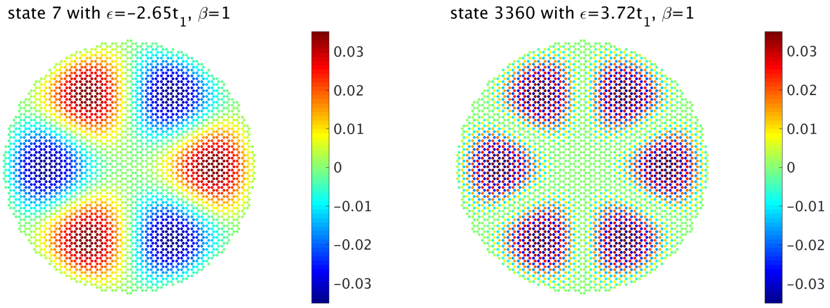

(a) Symmetric, $\beta = 1$.

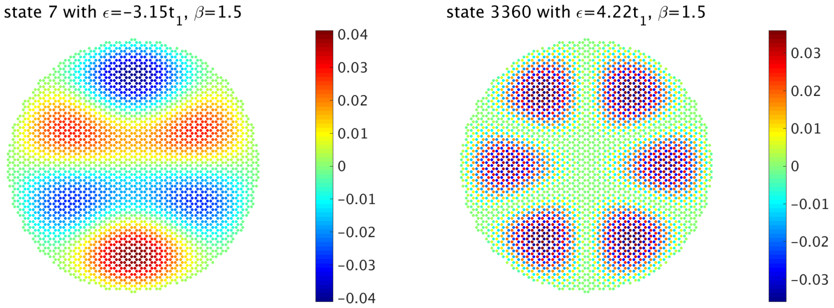

(b) Subcritical compression, $1 < \beta < \beta_c$.

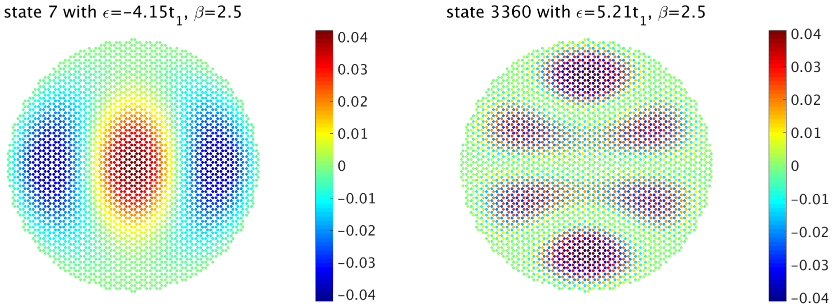

(c) Supercritical compression, $\beta > \beta_c$.

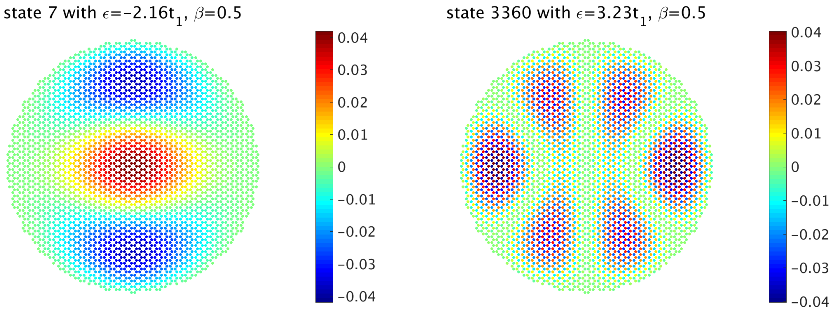

(d) Stretching, $\beta < 1$.

Figure 5.14: Evolution of bulk states under uniaxial strain in the circular system shown in Fig. 5.12. Left: State $1 + x$ with $x = 6$ in the lower band. Right: State $N - x$ with $x = 6$ in the upper band.

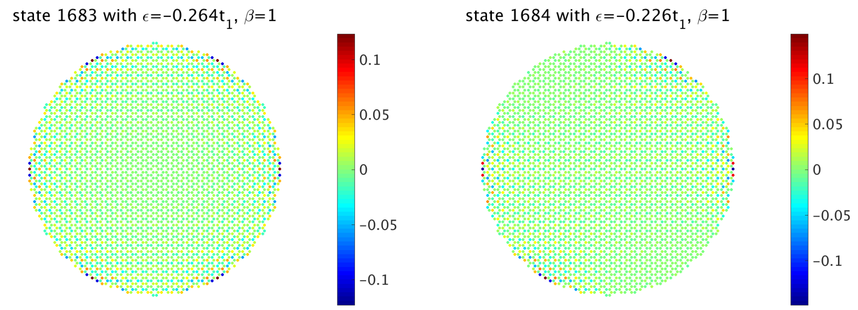

(a) Symmetric, $\beta = 1$.

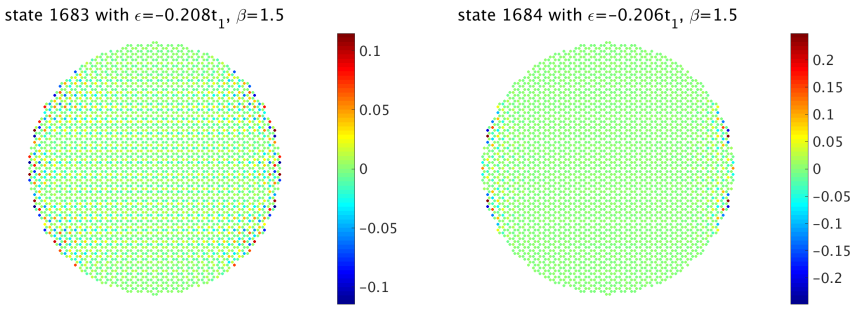

(b) Subcritical compression, $1 < \beta < \beta_c$.

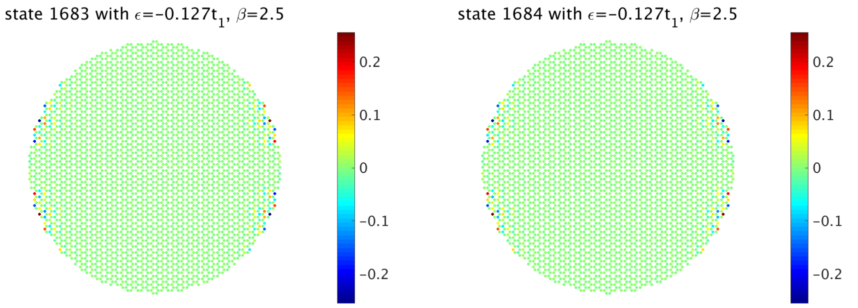

(c) Supercritical compression, $\beta > \beta_c$.

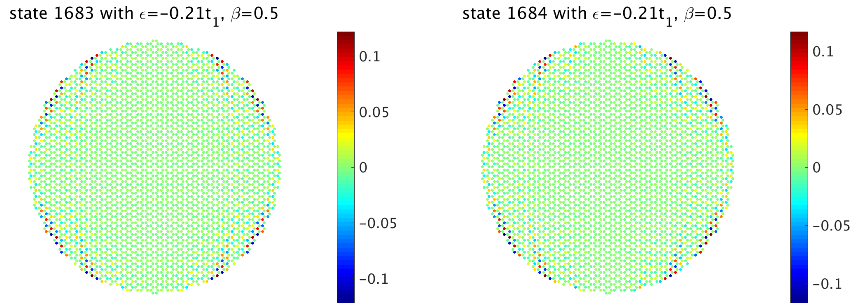

(d) Stretching, $\beta < 1$.

Figure 5.15: Evolution of edge states (left: state $N/2$, right: state $N/2+1$) under uniaxial strain in the circular system shown in Fig. 5.12.

5.3.4 Hexagonal “boron nitride” flakes

To conclude this section, we study finite boron-nitride-like systems under uniaxial strain. Here, we examine the two hexagonally shaped systems shown in Fig. 5.9 with purely armchair and purely zigzag boundaries, respectively. The results are shown in Fig. 5.16 for the armchair system and in Fig. 5.17 for the zigzag system. For the edge states, we observe a similar behavior as in the graphene-like systems. In the undistorted system, edge states are only found at zigzag edges. Under uniaxial strain, edge states occur also in the armchair system.

In the graphene-like systems, we have observed that the edge states have high intensity only on one sublattice for each edge. In the boron-nitride-like systems, there occur two kinds of edge states which are separated in energy as the two sublattices have different on-site energy. As the bulk bands are gapped, the edge state spectrum is also gapped. The edge states on the sublattice with lower energy occur, in consequence, for lower energies than the edge states which are localized on the other sublattice with higher energy.

As already mentioned above, a hexagonal boron-nitride-like system has also been realized in a microwave experiment [162]. In this setup, uniaxial strain could be studied in principle as in the microwave realization of graphene [143], however, only the undistorted system has been examined.

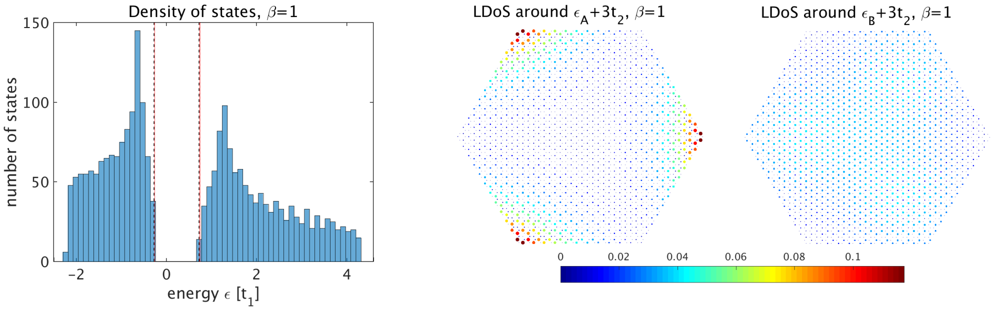

(a) Symmetric, $\beta = 1$.

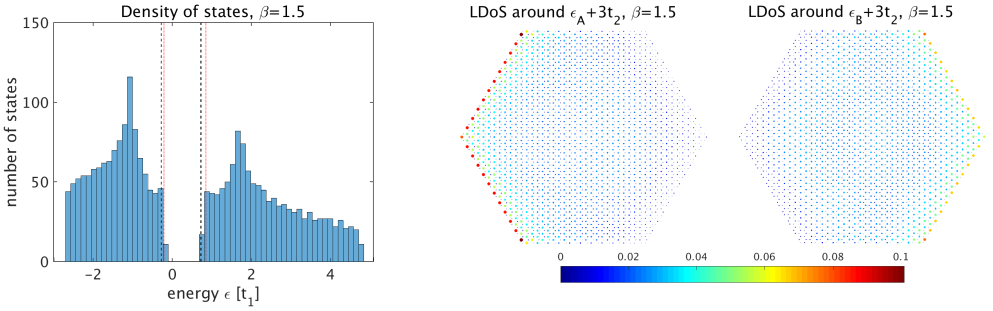

(b) Subcritical compression, $1 < \beta < \beta_c$.

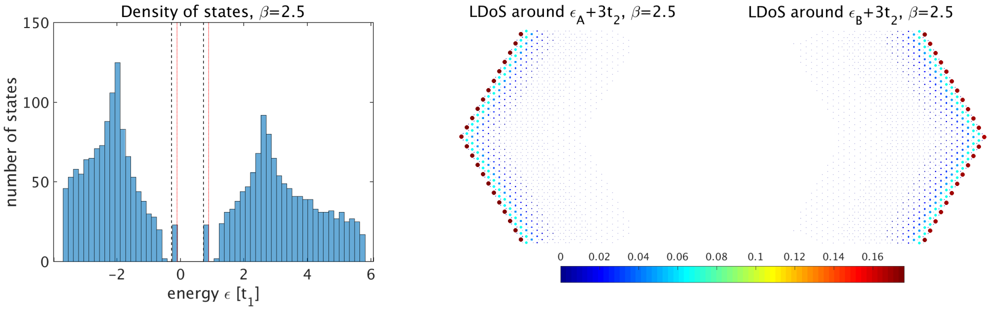

(c) Supercritical compression, $\beta > \beta_c$.

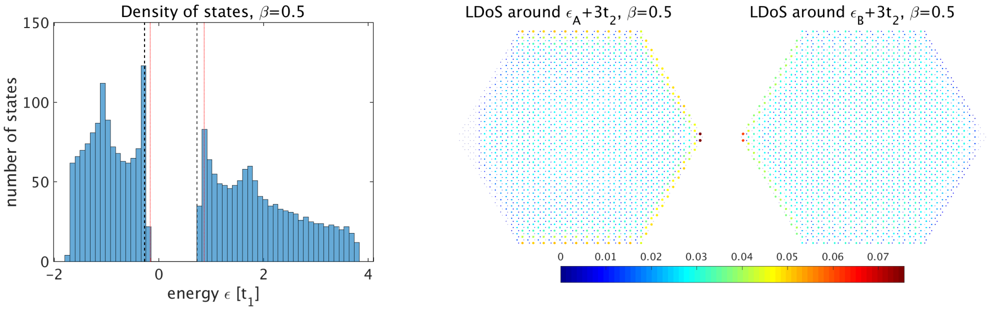

(d) Stretching, $\beta < 1$.

Figure 5.16: Density of states and local density of states around the band edges for the armchair system shown in Fig. 5.9(b) calculated from the tight-binding model with different on-site potentials on the two sublattices, $\Delta\varepsilon = |\varepsilon_A - \varepsilon_B| = t_1$, including uniaxial strain, $t_1' = \beta t_1$. The local density of states is calculated from states in the energy intervals indicated in the numerical density of states.

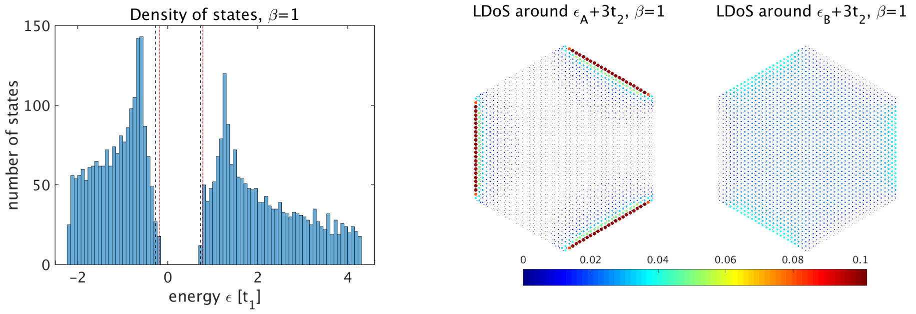

(a) Symmetric, $\beta = 1$.

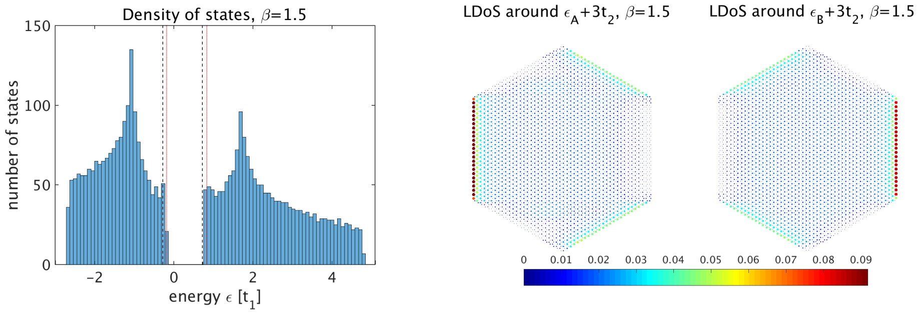

(b) Subcritical compression, $1 < \beta < \beta_c$.

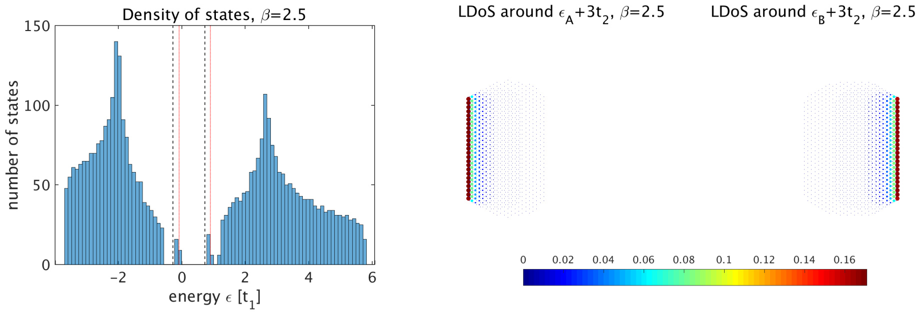

(c) Supercritical compression, $\beta > \beta_c$.

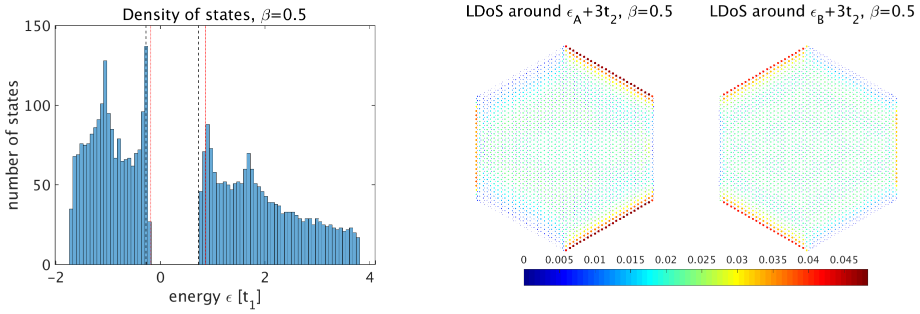

(d) Stretching, $\beta < 1$.

Figure 5.17: Density of states and local density of states around the band edges for the zigzag system shown in Fig. 5.9(a) calculated from the tight-binding model with different on-site potentials on the two sublattices, $\Delta\varepsilon = |\varepsilon_A - \varepsilon_B| = t_1$, including uniaxial strain, $t_1' = \beta t_1$. The local density of states is calculated from states in the energy intervals indicated in the numerical density of states.

5.4 Graphene cavities in an effective ray model

In analogy to the dielectric optical microcavities considered in the first part of this work which are resonant cavities for electromagnetic waves, finite graphene samples can be interpreted as resonant cavities for Dirac electrons [166]. A strong analogy between the electronic states in graphene quantum dots and electromagnetic modes in optical microcavities have been found in experiments [44, 47]. Therefore, a similar treatment of the two systems is plausible.

In experiments, it is often desired to study graphene and other hexagonal lattice systems that are not only structured by the finite size of the sample but have some additional internal structure, be it of their shape or their electronic properties. From a fundamental point of view, it is of interest, for example, to test if the predictions made for relativistic massless particles, *e.g.* the Klein tunneling (see below), hold in such graphene samples [150, 151, 166]. From a practical point of view, it is necessary to control the structure of graphene samples to build functional devices like transistors [42]. The desired internal structure can be imposed by mechanical manipulation (*e.g.* strain, see above), chemical doping, by the substrate, or by electrical gating [42–44].

Analogously to the ray description of optical microcavities, we also want to describe graphene devices in an effective ray model. To this end, we have to approximate the wave functions of the electrons in graphene by rays, instead of the electromagnetic waves in an optical device. As Fermat's principle applies universally, the laws of reflection and refraction are the same in both cases. The role of the refractive index contrast is taken by a potential step. The reflection and transmission coefficients have to be obtained in a similar way as for light. The wave functions on both sides of the potential step have to be matched according to the imposed boundary condition. A similar ray-based approach has been studied in Ref. [167, 168] for the scattering of an electron wave off a circular graphene *p*-*n*-junction. Here, however, we want to model the electronic wave inside and predict the emission out of the confinement with a ray description.

In the context of the optical devices in the previous chapters, we have always considered the wave nature of the light, and not the discrete nature of single photons. Analogously, the effective ray model considered here, does not apply to single electrons but rather to properties of a large ensemble of electrons. A single electron cannot be split into a reflected and a transmitted part, just as a single photon in the optical context. Thus, the reflection and transmission coefficients are probabilities of reflection or transmission for a single electron and apply to the intensity only in a statistical sense as an averaged quantity over a large ensemble of electrons.

The implementation of a ray description of graphene cavities is analogous to the optical case described in appendix A. The major difference is that appropriate reflection coefficients have to be used which will be given in the next section. Results for different systems are discussed in the subsequent sections.

5.4.1 Klein tunneling and graphene billiards

The transmission and reflection of electrons at a potential barrier in graphene is expected to be different than in other materials due to the unusual dispersion and the chirality of the charge carriers. The transmission coefficient for an electron incident on a potential barrier in graphene has been derived in [150].

In the following, the energy range is always restricted to the regime where the linear expansion of the dispersion around the Dirac point is valid. A rectangular potential barrier of width D and height V_0 is considered as shown in Fig. 5.18. This can be achieved by doping the graphene sample suitably, thus, shifting the Fermi level as schematically depicted in the upper part of Fig. 5.18. In the limit of high barriers $|V_0| \gg E$, the transmission probability through the barrier becomes [150]

$$T(\chi) = \frac{\cos^2(\chi)}{1 - \cos^2(q_x(\chi)D)\sin^2(\chi)} \tag{5.15}$$

where χ is the angle of incidence defined by the components of the wavevector, $k_x = k\cos(\chi)$ and $k_y = k\sin(\chi)$, perpendicular to and along the barrier, respectively. $q_x = \sqrt{(E - V_0)^2/v_0^2 - k^2\sin^2(\chi)}$ is the x-component of the wavevector inside the barrier with the velocity v_0 of the charge carriers described by the effective Dirac equation given in Eq. (5.8).

The transmission probability $T(\chi)$ and the resulting reflection probability $R(\chi) = 1 - T(\chi)$ are shown in Fig. 5.19 for two different barriers. The reflection vanishes, $R = 0$ or $T = 1$, at the resonances $q_x D = m\pi$ for all integers m. More remarkably, the reflection probability always vanishes for $\chi = 0$. Independent of the width, a high potential barrier in graphene is completely transparent for

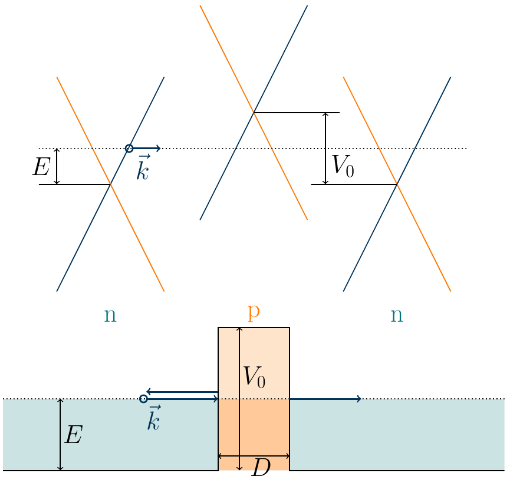

Figure 5.18: Reflection and transmission at a potential barrier in graphene obtained by doping. The incident electron is characterized by the wave-vector $\vec{k}$ and the energy E which is measured from the Dirac point. The width of the potential barrier is D, its height $V_0 > E$

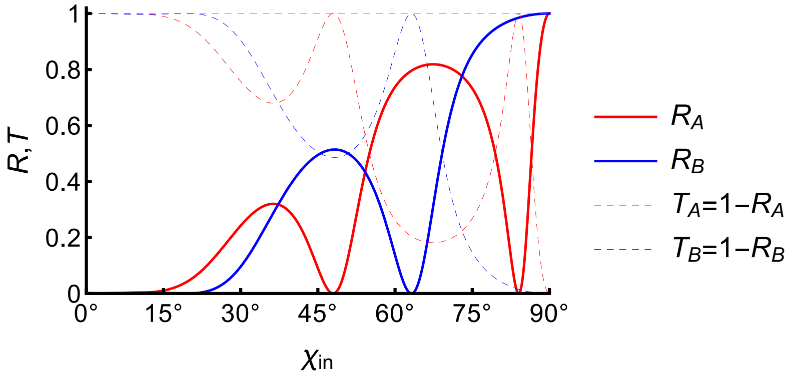

Figure 5.19: Reflection (solid) and transmission (dashed) coefficients at a potential barrier for an electron in graphene calculated from the formula given in [150] with $D = 100\,\mathrm{nm}$, $E = 80\,\mathrm{meV}$, $V_0 = 183\,\mathrm{meV}$ (A, red) and $V_0 = 207\,\mathrm{meV}$ (B, blue).

a normally incident electron. This is the manifestation of the so-called Klein paradox in graphene [150, 151]. The Klein paradox refers to the counterintuitive prediction that a relativistic particle described by the Dirac equation will be perfectly transmitted through an infinitely high potential barrier [149]. This is a direct consequence of the chirality of Dirac particles. Imagine a right moving electron with pseudospin "up" hitting the barrier under normal incidence (*cf.* Fig. 5.18). As the chirality, the projection of the pseudospin onto the direction of propagation, has to be conserved, it cannot be scattered back into a left moving electron state without flipping its pseudospin direction. It can only be scattered into a hole state inside the barrier which has the correct pseudospin. The prohibited backscattering at both ends of the barrier leads to perfect transmission through the potential barrier.

A cavity for electrons in graphene can be constructed with a ring-shaped

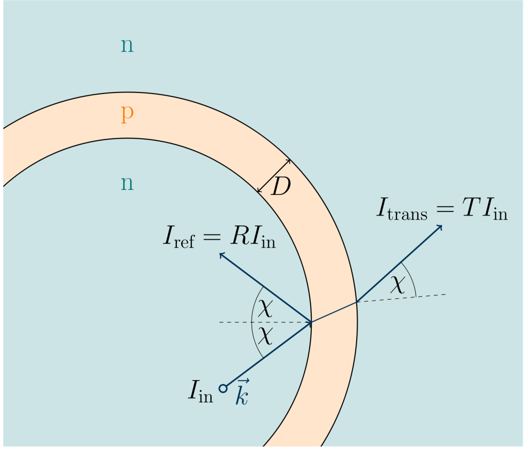

Figure 5.20: "Graphene billiards" formed by an annular n-p-n-junction.

potential barrier schematically depicted in Fig. 5.20. However, the electrons are poorly confined in such a cavity as the reflectivity is smaller than one for all incident angles but for grazing incidence parallel to the interface. An equivalent to total internal reflection at a dielectric interface in the optical case is not found at such a graphene barrier. This construction introduces a further difference to the usual dielectric optical cavities. The potential in the inner region enclosed by the barrier and the potential in the outer region are the same. Therefore, the optical microcavities studied in the previous chapters are actually not a good analogy to these graphene systems. A better analogy is a glass ring placed in air where one does not want to study the optical modes inside the glass but the light confined in the air region enclosed by the ring and its transmission through the glass ring into the air region outside.

In an effective ray description of such graphene cavities, we consider only the limit of thin barriers. This justifies the approximation that a ray incident on the barrier is partly specularly reflected and partly transmitted through the barrier without changing its direction. The shift of the transmitted ray along the boundary caused by the refraction into and out of the barrier can be neglected if the barrier is very small compared to the mean radius of the structure. The intensities of the reflected and transmitted rays are given by the reflection and transmission probabilities for a single electron.

5.4.2 Circular n-p-n-junction

As in the optical case, we consider first a circular cavity as a testbed for the model. Due to the radial symmetry, the angular momentum has to be conserved and isotropic emission is expected.

Some exemplary ray trajectories in the circular graphene cavity are shown in Fig. 5.21. The trajectories inside the circle are the same as in the usual geometrical optics system or in a closed billiard as the ray is still specularly reflected at the boundary. However, the transmission looks different than in a typical optical case. In the approximation of a vanishingly thin barrier, considered here, the direction of the transmitted ray does not change with respect to the incident ray. Further, there is no region of total internal reflection. Thus, a transmitted ray occurs for all incident angles. Consequently, the intensity in the reflected part of the ray is very low and soon there is almost no intensity left inside the cavity.

The far-field emission resulting from the ray calculations for the two different reflection coefficients shown in Fig. 5.19 is given in Fig. 5.22. As expected, the emission pattern is isotropic independent of the applied reflection coefficient. The emission is calculated for different transition times and scaled such that the maxima of each curve are equal. Time is measured in units of l/v_0 with the path length l that the ray has traversed in the cavity and the velocity v_0 of the charge carriers described by the effective Dirac equation given in Eq. (5.8). The length is measured in multiples of the radius of the cavity. The necessary scaling factors illustrate the decay of the intensity inside the cavity and the difference between the two reflection coefficients.

In the case of the "red" reflection coefficient (given by the red curve in Fig. 5.19, resulting far-field in Fig. 5.22(a)) the intensity decay is very fast, whereas, it is slower in the case of the "blue" reflection coefficient (given by the blue curve in Fig. 5.19, resulting far-field in Fig. 5.22(b)). This is clear from the behavior of the reflection coefficients. The red reflection coefficient is always much smaller than one but for parallel incidence, whereas, the blue reflection

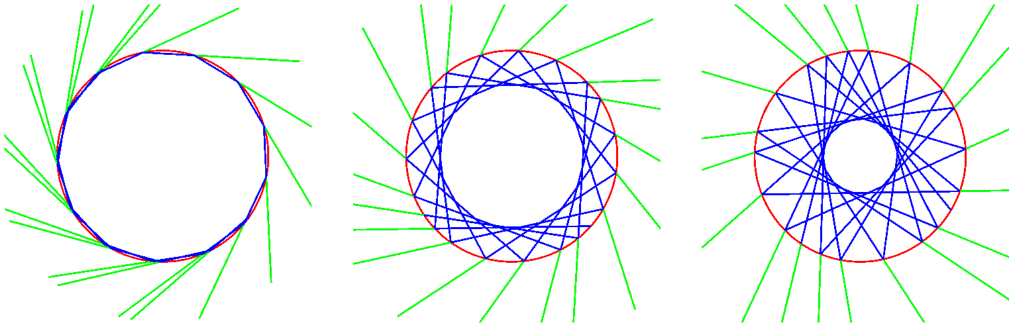

Figure 5.21: Exemplary trajectories with different initial conditions in a circular graphene cavity. The ray trajectory inside the cavity is drawn in blue, the transmitted rays in green, the cavity boundary in red.

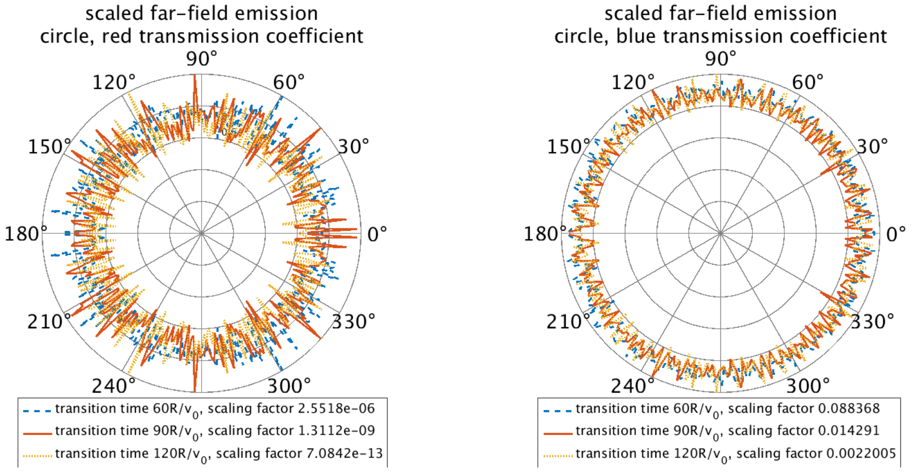

(a) $V_0 = 183\,\mathrm{meV}$ (red in Fig. 5.19).

(b) $V_0 = 207\,\mathrm{meV}$ (blue in Fig. 5.19).

Figure 5.22: Far-field emission of the circular graphene cavity of radius R with the reflection and transmission probabilities resulting from electrons with energy $E = 80\,\mathrm{meV}$ incident on a barrier of width $D = 100\,\mathrm{nm}$ and two different heights V_0 (see Fig. 5.19).

coefficient is close to one at least for a small interval of large incident angles. Thus, there exist some rays in the case of the blue reflection coefficients that are better confined inside the cavity. Further, the fast decay of the intensity leads to strong fluctuations in the calculated far-field pattern.

5.4.3 Limaçon-shaped n-p-n-junction

As Limaçon-shaped cavities have proven useful in optics (see section 3.3), we discuss cavities of this shape as another example of graphene billiards. To be able to make direct comparisons, the Limaçon curve (Eq. (3.1)) with deformation parameter $\epsilon = 0.43$ is considered as the boundary of the system as in the optical case.

The far-field emission resulting from the ray calculations in the Limaçon-shaped graphene cavity for the two different reflection coefficients shown in Fig. 5.19 is given in Fig. 5.23 for different transition times. The transition times after which the emission patterns are obtained are twice as large in the case of the blue reflection coefficients as the transition times in the case of the red reflection coefficients. First, it is noted that the emission patterns reflect the mirror symmetry of the cavity. Second, some directionality is found for

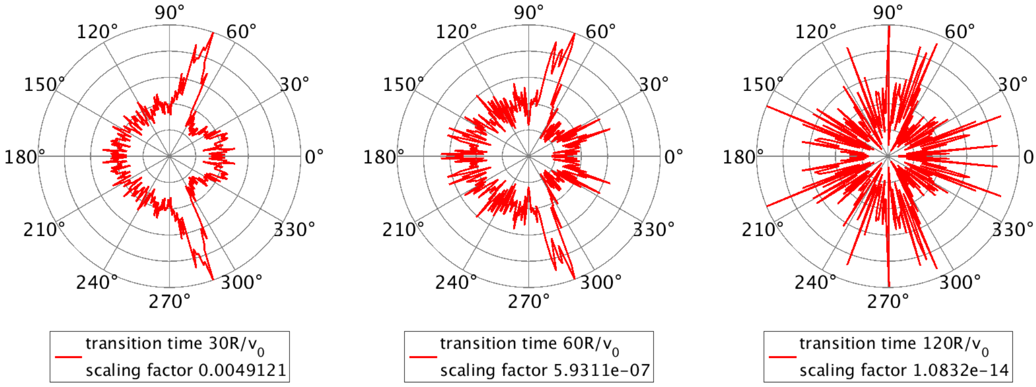

(a) $V_0 = 183\,\text{meV}$ (red in Fig. 5.19), transition times $30R/v_0$, $60R/v_0$, $120R/v_0$.

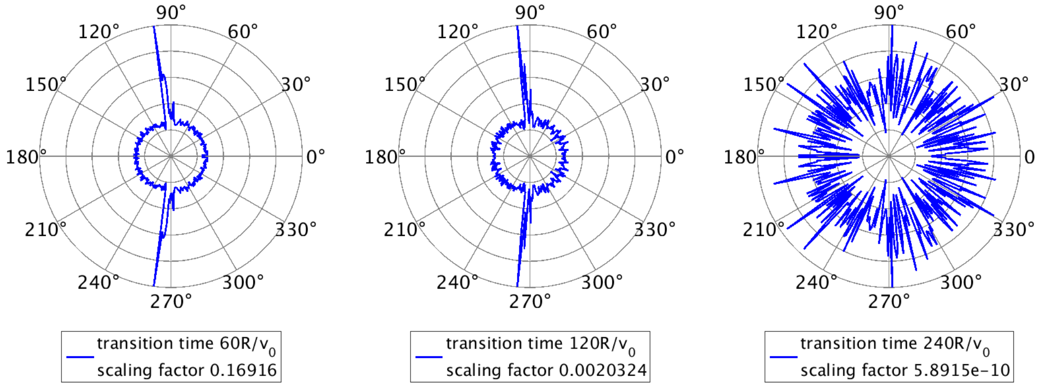

(b) $V_0 = 207\,\text{meV}$ (blue in Fig. 5.19), transition times $60R/v_0$, $120R/v_0$, $240R/v_0$.

Figure 5.23: Far-field emission of the Limaçon-shaped graphene cavity of mean radius R, deformation parameter $\epsilon = 0.43$ with the reflection and transmission probabilities resulting from electrons with energy $E = 80\,\text{meV}$ incident on a barrier of width $D = 100\,\text{nm}$ and two different heights V_0 (see Fig. 5.19). Note the different transition times in the two cases.

both reflection coefficients. Although a non-negligible amount of intensity is transmitted in all directions two distinct directions show enhanced intensity if the emission is obtained after short transition times. Due to the fast intensity decay, however, the directionality is lost if the emission pattern is obtained after a longer transition time. As discussed in the case of the circular graphene cavity, the intensity inside the cavity decays much faster for the red reflection coefficient than for the blue one.

5.4.4 Comment on the Goos-Hänchen shift in graphene

As mentioned already in chapter 2, the wave corrections to geometrical optics, the Goos-Hänchen shift and the Fresnel filtering effect, are not restricted to optics, rather they occur for every wave phenomena. The Goos-Hänchen shift has also been studied for electronic waves in graphene [70, 71]. This is an interesting topic by itself. The shift is found to be different for the two different pseudospin polarizations (sublattices) and, depending on the chosen setup, it can take on positive and negative values [70, 71, 169]. Further, it is predicted that the lateral shift can be tailored by mechanical strain [170]. Beyond that, the Goos-Hänchen shift can have measurable consequences on the conductance through a graphene p-n-p-device [71].

For a full ray description of graphene devices, the Goos-Hänchen shift should be appropriately included. However, this is beyond the scope of this work. In the exemplary setup studied here, the Goos-Hänchen shift probably does not play a role as no total reflection is reached. For the optical case in chapter 2, it has been discussed that the Goos-Hänchen effect only appears if total internal reflection is present. Furthermore, in the approximation of a very thin barrier that has been applied above, the lateral shift of the transmitted ray through the barrier has been neglected. This purely classical, geometrical effect should be included correctly before any wave-based corrections are considered.

5.5 Conclusions

In the first part of this chapter, we have studied the effect of uniaxial strain in a tight-binding model on the honeycomb lattice. The model has been applied to graphene-like and boron-nitride like systems where the two inequivalent sublattices of the honeycomb lattice are occupied by the same or two different species, respectively.

Uniaxial strain is an easy method to tune the band structure, where existence and size of the band gap depend on the strength of the strain. Further, the strain induces robust edge states that are independent of the precise boundary termination what we illustrate in several examples. Whereas, this model has been implemented in several experiments with artificial graphene [143, 159, 160], it remains an open question if it can be realized in real graphene.

In the last part, we have introduced an effective ray model as a possible method for an efficient description of graphene devices in the same spirit as the ray-optical description of dielectric optical microcavities. To illustrate this model we have applied it to systems with a circular and a Limaçon-shaped structure, respectively, two structures that we studied also in the optical case in chapter 3. Based on the concept of ray-wave correspondence, the ray description of dielectric optical microcavities is a well-established method. In the case of graphene-devices, however, more work is needed to check the validity and applicability of this model.

Appendix A

Implementation of the ray model

Here, the implementation of the ray dynamics is described. First, a general description is given that is valid for all the cases considered in this work. Then, the specific details are explained for systems with boundaries in polar coordinates and for polygonal systems. Finally, the differences between "optical billiards" and "graphene billiards" are discussed shortly.

A.1 The ray model in optical and similar billiards

To implement the ray dynamics in a computer program that follows the trajectory of a ray started at an arbitrary point on the boundary in an arbitrary direction pointing inside the cavity for a given number of "collisions" with the boundary and gives the far-field distribution of the emitted light, the following steps are necessary

1. Start a ray with given direction, starting point and intensity.
2. Find the point where it hits the boundary next.
3. Find the angle of incidence at the intersection point.
4. Determine the reflected and transmitted intensities from the angle of incidence, given by the appropriate reflection coefficients.
5. Determine the direction and position of the reflected and, if possible, transmitted ray from the angle of incidence.
6. If there is a transmitted ray, calculate the global far-field angle from the local angle of transmission.

The reflection point, the angle of reflection and the reflected intensity define the new ray to start the steps again.

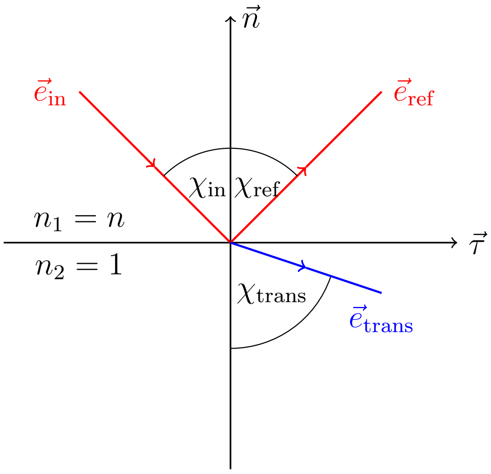

Figure A.1: Reflection and transmission of a ray at a dielectric (or similar) interface with relative refractive index $n = n_1/n_2$. The local tangent $\vec{\tau}$ and normal $\vec{n}$ to the boundary at the point of incidence are shown in black. The directions of the incident and reflected ray, $\vec{e}_{\rm in}$ and $\vec{e}_{\rm ref}$, are depicted as red arrows, the direction of the transmitted ray $\vec{e}_{\rm trans}$ as blue arrow. The angles of incidence $\chi_{\rm in}$, reflection $\chi_{\rm ref}$, and transmission $\chi_{\rm trans}$ are defined with respect to the local normal.

The normalized directions of the incoming, reflected, and transmitted rays are then given in the following way (see Fig. A.1 for notation):

$$\begin{aligned}\vec{e}_{\rm in} &= -\cos(\chi_{\rm in})\vec{n}_{\rm in} + \sin(\chi_{\rm in})\vec{\tau}_{\rm in} \\ \vec{e}_{\rm ref} &= \cos(\chi_{\rm ref})\vec{n}_{\rm ref} + \sin(\chi_{\rm ref})\vec{\tau}_{\rm ref} \\ \vec{e}_{\rm trans} &= -\cos(\chi_{\rm trans})\vec{n}_{\rm trans} + \sin(\chi_{\rm trans})\vec{\tau}_{\rm trans}\end{aligned} \tag{A.1}$$

The convention is to use positive angles $\chi \geq 0$ when the ray points in the same direction as the local tangent, the situation shown in Fig. A.1, and negative angles $\chi < 0$ when it points in the opposite direction. The subscripts “in”, “ref”, and “trans” at the tangent- and normal- vectors, $\vec{\tau}$ and $\vec{n}$, denote that the local tangent and normal at the respective points have to be used which do not need to be the same for incident reflected and transmitted ray due to the beam shift corrections.

The ray $\vec{r}$, starting with angle χ at point $\vec{p}$ on the boundary, is given by

$$\vec{r}(\alpha) = \vec{p} + \vec{e}_{\rm ref}\,(\chi)\ \alpha \tag{A.2}$$

with $\alpha \geq 0$. The intersection of the ray with the boundary (different from the starting point) gives the new point of incidence $\vec{p}_{\rm in}$. The angle between the ray and the local boundary normal at $\vec{p}_{\rm in}$ defines the angle of incidence. The explicit calculation of these two quantities is explained in detail in the next sections for systems with boundaries in polar coordinates and for polygonal systems.

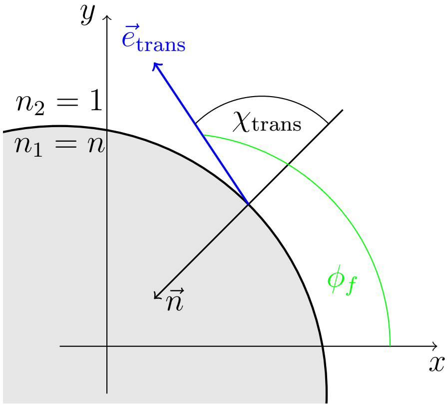

Figure A.2: Definition of the far-field angle ϕ_f.

If conventional ray optics, *i.e.* no beam shifts, is applied the points on the boundary $\vec{p}_{\mathrm{ref}}$ and $\vec{p}_{\mathrm{trans}}$, where the reflected and the transmitted rays start, coincide with the point of incidence, $\vec{p}_{\mathrm{in}} = \vec{p}_{\mathrm{ref}} = \vec{p}_{\mathrm{trans}}$. The angle of reflection equals the angle of incidence $\chi_{\mathrm{ref}} = \chi_{\mathrm{in}}$ and the angle of transmission is determined by Snell's law $\sin(\chi_{\mathrm{trans}}) = n \sin(\chi_{\mathrm{in}})$ where n is the relative refractive index. The relative refractive index is defined here and throughout this work such that the first medium where the incident ray propagates has $n_1 = n$ and the second medium outside has $n_2 = 1$. If $n > 1$ (corresponding to the transition from an optically thicker medium to an optically thinner medium) there is a transmitted ray only for $\sin(\chi_{\mathrm{in}}) < 1/n$, otherwise, total internal reflection occurs.

If beam shift corrections in terms of the Goos-Hänchen shift and/or the Fresnel filtering effect are included things become a bit more complicated. The points of reflection and transmission are shifted according to the corresponding Goos-Hänchen shift terms, $\vec{p}_{\mathrm{ref}} = \vec{p}_{\mathrm{in}} + \Delta\vec{r}_{\mathrm{GH}}{}^{\mathrm{ref}}(\chi_{\mathrm{in}})$ and $\vec{p}_{\mathrm{trans}} = \vec{p}_{\mathrm{in}} + \Delta\vec{r}_{\mathrm{GH}}{}^{\mathrm{trans}}(\chi_{\mathrm{in}})$. The angles of reflection and transmission have to be corrected by the angular shift due to the Fresnel filtering effect, $\chi_{\mathrm{ref}} = \chi_{\mathrm{in}} + \Delta\chi_{\mathrm{FF}}^{\mathrm{ref}}(\chi_{\mathrm{in}})$ and $\chi_{\mathrm{trans}} = \arcsin(n \sin(\chi_{\mathrm{in}})) + \Delta\chi_{\mathrm{FF}}^{\mathrm{trans}}(\chi_{\mathrm{in}})$ where the angles have to be measured with respect to the local normals at the corrected points of reflection and transmission.

To calculate the far-field emission pattern, not only the local transmission angle χ_{trans} but also the angle ϕ_f between the transmitted ray and the x-axis of the global coordinate frame need to be determined (see Fig. A.2). Given the direction $\vec{e}_{\mathrm{trans}}$, the far-field angle is defined by

$$\tan(\phi_f) = \frac{e_{\mathrm{trans},y}}{e_{\mathrm{trans},x}}. \tag{A.3}$$

Further, the intensities of the reflected and transmitted rays have to be calculated. Every ray is initialized with unit intensity, $I_0 = 1$. At each reflection at the boundary, the reflected intensity is $I_{\mathrm{ref}} = R(\chi_{\mathrm{in}}) I_{\mathrm{in}}$ and the transmitted intensity is $I_{\mathrm{trans}} = T(\chi_{\mathrm{in}})I_{\mathrm{in}}$ with the appropriate intensity reflection coefficient $R(\chi)$ and the corresponding transmission coefficient $T(\chi) = 1 - R(\chi)$.

A.2 Billiards with boundaries in polar coordinates

If the boundary of the system is defined by a curve $\rho(\phi)$ in polar coordinates, a point on the boundary is given by

$$\vec{p}(\phi) = \begin{pmatrix} \rho(\phi)\cos(\phi) \\ \rho(\phi)\sin(\phi) \end{pmatrix}.$$

The local tangent $\vec{\tau}$ and normal $\vec{n}$ to the boundary at point $\vec{p}(\phi)$ are

$$\vec{\tau}(\phi) = \frac{1}{|\vec{p}\,'(\phi)|}\vec{p}\,'(\phi) = \frac{1}{\sqrt{\rho^2(\phi) + \rho'^2(\phi)}} \begin{pmatrix} -\rho(\phi)\sin(\phi) + \rho'(\phi)\cos(\phi) \\ \rho(\phi)\cos(\phi) + \rho'(\phi)\sin(\phi) \end{pmatrix}$$
$$\vec{n}(\phi) = \begin{pmatrix} \tau_y(\phi) \\ -\tau_x(\phi) \end{pmatrix}$$

where the prime denotes the derivative with respect to the polar angle ϕ.

To find the intersection of the ray $\vec{r}$ (see Eq. (A.2)) with the boundary, the equation

$$\sqrt{r_x^2(\alpha) + r_y^2(\alpha)} \overset{!}{=} \rho\left(\arctan\left(\frac{r_y(\alpha)}{r_x(\alpha)}\right)\right) \tag{A.4}$$

has to be solved for α. The new intersection point is then $\vec{p}_{\mathrm{in}} = \vec{r}(\alpha)$, the new incident angle is given by $\sin(\chi_{\mathrm{in}}) = \vec{\tau}(\arctan(r_y(\alpha)/r_x(\alpha))) \cdot \vec{e}_{\mathrm{ref}}(\chi_{\mathrm{ref}})$. With the new point and angle of incidence, the next steps can be performed as explained in the general description.

A.3 Polygonal billiards

The ray calculations in a polygonal optical cavity follows the same principles as in the case of cavities with curved boundaries. However, the boundary is now given by straight lines between the corner points instead of a curve in polar coordinates. This leads to some differences in the actual implementation. Here, the implementation will be discussed at the example of a triangular system.

The boundary of the triangle is defined by its three corner points P_1, P_2, P_3 in the two dimensional plane. Without loss of generality the coordinate system can be chosen such that P_1 lies in the origin, $P_1 = (0, 0)$, and P_2 lies on the x-axis, $P_2 = (P_{2,x}, 0)$. The third point P_3 can then be chosen freely allowing for all possible triangles. If the area (or the circumference) of the triangle was normalized to 1 the degrees of freedom would be reduced to 2. However, this is not considered here. From the three points we can deduce the normalized tangent $\vec{\tau}_\sigma$ and the normalized inwards pointing normal $\vec{n}_\sigma$ to each side σ of the triangle:

$$\vec{\tau}_\sigma = \frac{\vec{P}_{\sigma+1} - \vec{P}_\sigma}{|\vec{P}_{\sigma+1} - \vec{P}_\sigma|} \qquad \vec{n}_\sigma = (-\tau_{\sigma,y}, \tau_{\sigma,x}) \tag{A.5}$$

where $\sigma = 1, 2, 3$ and $\sigma + 1 = 4$ corresponds to 1 cyclically.

The boundaries can be parameterized as

$$\vec{s}_\sigma(\beta) = \vec{P}_\sigma + \left(\vec{P}_{\sigma+1} - \vec{P}_\sigma\right) \beta \tag{A.6}$$

with $0 \le \beta < 1$. The point of intersection of the ray $\vec{r}$ (see Eq. (A.2)) with the boundary of the triangle is the solution of the equation

$$\vec{r}(\alpha) = \vec{s}_\sigma(\beta) \tag{A.7}$$

under the constraints $\alpha > 0$ (to ensure that not the starting point is hit) and $0 \le \beta < 1$ (to ensure that the point lies on the triangle and not somewhere outside). In consequence, the following linear equation has to be solved

$$\begin{pmatrix} e_{\mathrm{ref},x}(\chi_{\mathrm{ref}}) & P_{\sigma,x} - P_{\sigma+1,x} \\ e_{\mathrm{ref},y}(\chi_{\mathrm{ref}}) & P_{\sigma,y} - P_{\sigma+1,y} \end{pmatrix} \begin{pmatrix} \alpha \\ \beta \end{pmatrix} = \begin{pmatrix} P_{\sigma,x} - p_x \\ P_{\sigma,y} - p_y \end{pmatrix} \tag{A.8}$$

The new intersection point is then $\vec{p}_{\mathrm{in}} \equiv \vec{r}(\alpha) = \vec{s}_\sigma(\beta)$, the new incident angle is given by $\sin(\chi_{\mathrm{in}}) = \vec{\tau}_\sigma \cdot \vec{e}_{\mathrm{ref}}(\chi_{\mathrm{ref}})$. With the new point and angle of incidence, the next steps can be performed as explained in the general description.

A.4 Differences between optical and graphene billiards

An effective ray description of "graphene billiards" as discussed in section 5.4 is, in principle, analogous to the optical case. However, there are two important differences between the optical and the electronic system.

On the one hand, the appropriate reflection coefficients have to be used. Instead of the Fresnel coefficients or corrected Fresnel coefficients which result from the boundary conditions imposed on an electromagnetic wave at a dielectric interface, the reflection probabilities have to be used that result from the boundary conditions of the quantum mechanical wave function at the potential step or barrier. These reflection and transmission probabilities are derived in [150].

On the other hand, the effective refractive index, needed to determine the direction of the transmitted ray, has to be defined appropriately. It is determined by the potential difference between the different regions of the structure.

The reflection and transmission coefficients and the effective refractive indices suitable for the examples studied in this work are discussed in section 5.4.

Appendix B

Additional figures for the beam shifts

Here we show some additional figures which are different presentations of the data shown as three-dimensional plots in chapter 2.

Figure B.1 here is an alternative to Fig. 2.7.

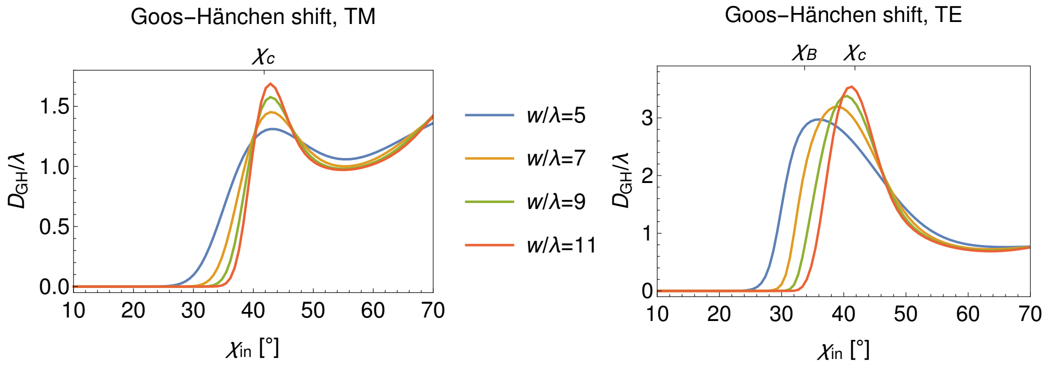

(a) Goos-Hänchen shift, TM polarization.

(b) Goos-Hänchen shift, TE polarization.

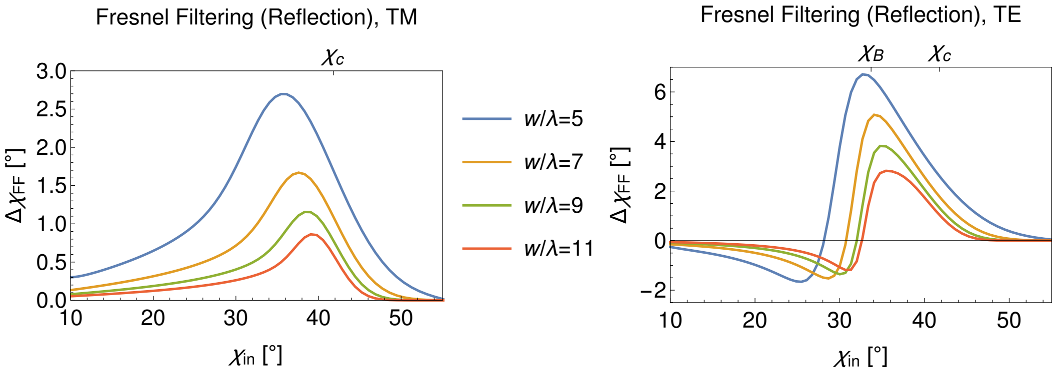

(c) Fresnel filtering, TM polarization.

(d) Fresnel filtering, TE polarization.

Figure B.1: Influence of the beam width on the Goos-Hänchen shift D_{GH} and on the Fresnel filtering effect $\Delta\chi_{\mathrm{FF}}$ at a planar interface according to Eq. (2.8) and Eq. (2.10), respectively. The wavenumber k is fixed while the beam waist w/λ is varied. The relative refractive index is $n = 1.5$, $\chi_c \approx 41.8°$, $\chi_B \approx 33.7°$. Alternative presentation of the data shown in Fig. 2.7.

Figure B.2 here is an alternative to Fig. 2.24.

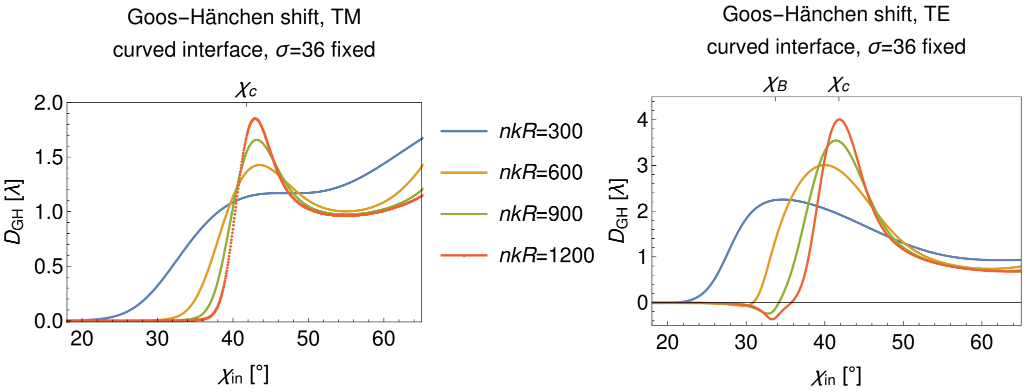

(a) Goos-Hänchen shift, TM polarization.

(b) Goos-Hänchen shift, TE polarization.

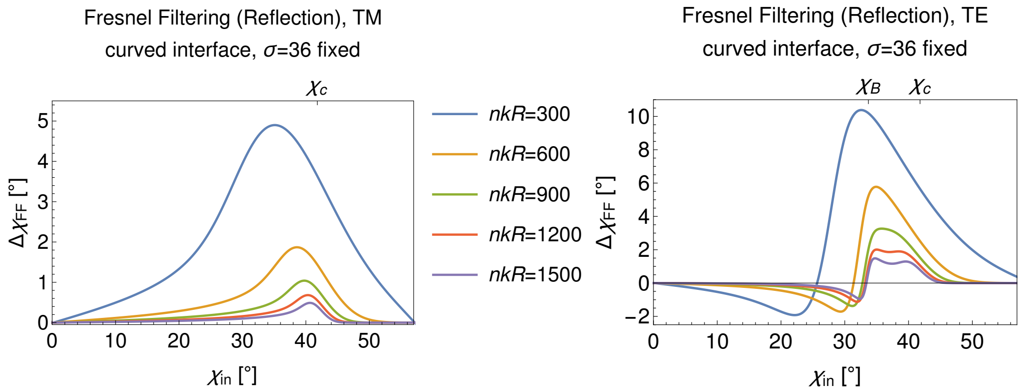

(c) Fresnel filtering, TM polarization.

(d) Fresnel filtering, TE polarization.

Figure B.2: Influence of angular spread on the Goos-Hänchen shift and the Fresnel filtering effect at convexly curved interfaces according to Eq. (2.27) and Eq. (2.30), respectively. Wavenumber k and angular spread $\sigma = 36$ are fixed while the curvature $\kappa = 1/R$ is varied. The relative refractive index is $n = 1.5$, $\chi_c \approx 41.8°$, $\chi_B \approx 33.7°$. Alternative presentation of the data shown in Fig. 2.24.

Figure B.3 here is an alternative to Fig. 2.25.

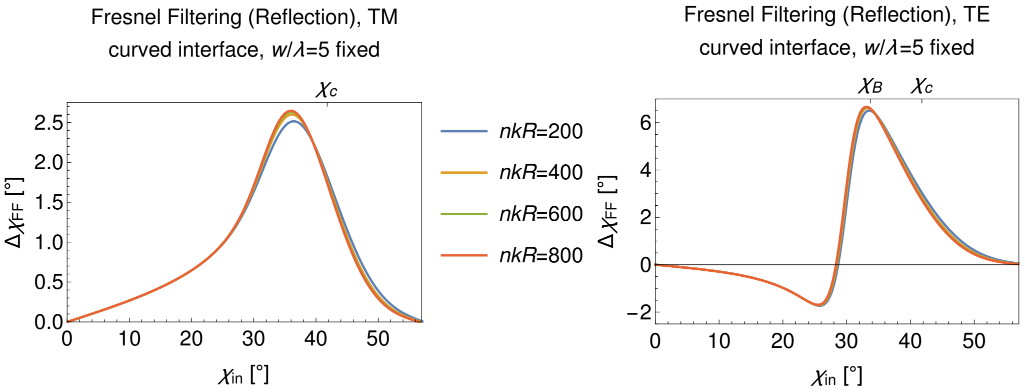

(a) Goos-Hänchen shift, TM polarization.

(b) Goos-Hänchen shift, TE polarization.

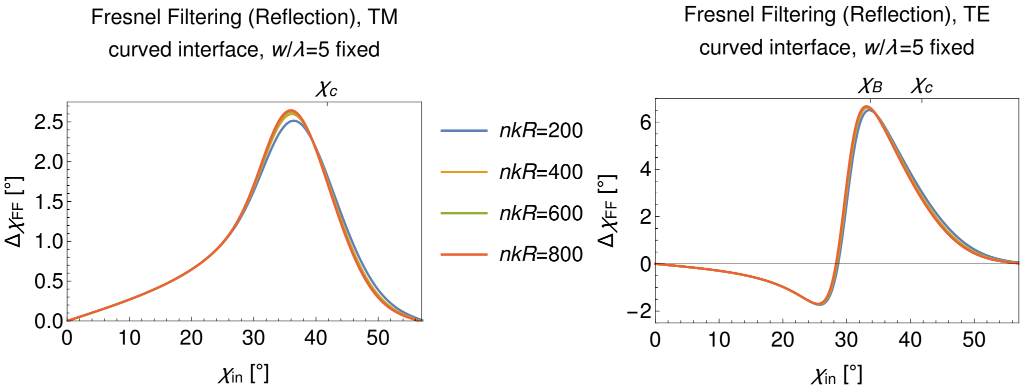

(c) Fresnel filtering, TM polarization.

(d) Fresnel filtering, TE polarization.

Figure B.3: Influence of the beam width on the Goos-Hänchen shift and the Fresnel filtering effect at convexly curved interfaces according to Eq. (2.27) and Eq. (2.30), respectively. Wavenumber k and width $w/\lambda = 5$ are fixed while the curvature $\kappa = 1/R$ is varied. The relative refractive index is $n = 1.5$, $\chi_c \approx 41.8°$, $\chi_B \approx 33.7°$. Alternative presentation of the data shown in Fig. 2.25.

Bibliography

[1] R. K. Chang and A. J. Campillo, eds., *Optical processes in microcavities*, Advanced series in applied physics, Vol. 3 (World Scientific, Singapore, 1996).

[2] K. Vahala, *Optical Microcavities* (World Scientific, Singapore, 2004).

[3] H. Cao and J. Wiersig, "Dielectric microcavities: Model systems for wave chaos and non-Hermitian physics," Rev. Mod. Phys. **87**, 61–111 (2015).

[4] K. Iga, F. Koyama, and S. Kinoshita, "Surface emitting semiconductor lasers," IEEE J. Quant. Electron. **24**, 1845–1855 (1988).

[5] J. D. Joannopoulos, S. G. Johnson, J. N. Winn, and R. D. Meade, *Photonic Crystals: Molding the Flow of Light*, 2nd ed. (Princeton University Press, Princeton and Oxford, 2008).

[6] C. G. B. Garrett, W. Kaiser, and W. L. Bond, "Stimulated emission into optical whispering modes of spheres," Phys. Rev. **124**, 1807–1809 (1961).

[7] L. Collot, V. Lefèvre-Seguin, M. Brune, J. M. Raimond, and S. Haroche, "Very high-Q whispering-gallery mode resonances observed on fused silica microspheres," EPL **23**, 327 (1993).

[8] V. S. Ilchenko, M. L. Gorodetsky, X. S. Yao, and L. Maleki, "Microtorus: a high-finesse microcavity with whispering-gallery modes," Opt. Lett. **26**, 256–258 (2001).

[9] S. L. McCall, A. F. J. Levi, R. E. Slusher, S. J. Pearton, and R. A. Logan, "Whispering-gallery mode microdisk lasers," Appl. Phys. Lett. **60**, 289–291 (1992).

[10] H. G. L. Schwefel, N. B. Rex, H. E. Tureci, R. K. Chang, A. D. Stone, T. Ben-Messaoud, and J. Zyss, "Dramatic shape sensitivity of directional emission patterns from similarly deformed cylindrical polymer lasers," J. Opt. Soc. Am. B **21**, 923–934 (2004).

[11] M. Lebental, N. Djellali, C. Arnaud, J.-S. Lauret, J. Zyss, R. Dubertrand, C. Schmit, and E. Bogomolny, "Inferring periodic orbits from spectra of simply shaped microlasers," Phys. Rev. A **76**, 023830 (2007).

[12] A. Chiasera, Y. Dumeige, P. Féron, M. Ferrari, Y. Jestin, G. Nunzi Conti, S. Pelli, S. Soria, and G. Righini, "Spherical whispering-gallery-mode microresonators," Laser & Photon. Rev. **4**, 457–482 (2010).

[13] Y.-F. Xiao, C.-L. Zou, Y. Li, C.-H. Dong, Z.-F. Han, and Q. Gong, "Asymmetric resonant cavities and their applications in optics and photonics: a review," Front. Optoelectron. China **3**, 109–124 (2010).

[14] L. He, Ş. K. Özdemir, and L. Yang, "Whispering gallery microcavity lasers," Laser & Photon. Rev. **7**, 60–82 (2013).

[15] J. U. Nöckel and A. D. Stone, "Chaotic light: A theory of asymmetric resonant cavities," in *Optical Processes in Microcavities*, Advanced series in applied physics, Vol. 3, edited by R. K. Chang and A. J. Campillo (World Scientific, Singapore, 1996) Chap. 11, pp. 389–426.

[16] J. Wiersig, J. Unterhinninghofen, Q. Song, H. Cao, M. Hentschel, and S. Shinohara, "Review on unidirectional light emission from ultralow-loss modes in deformed microdisks," in *Trends in Nano- and Micro-Cavities*, edited by O. Kwon, B. Lee, and K. An (Bentham Science Publishers, 2011) pp. 109–152.

[17] V. S. Ilchenko and A. B. Matsko, "Optical resonators with whispering-gallery modes-part II: applications," IEEE J. Sel. Top. Quantum Electron. **12**, 15–32 (2006).

[18] D. Dragoman, *Quantum-classical analogies*, The frontiers collection (Springer, Berlin, Heidelberg, 2004).

[19] H.-J. Stöckmann, *Quantum chaos: an introduction* (Cambridge University Press, Cambridge, 1999).

[20] J. D. Jackson, *Classical electrodynamics*, 3rd ed. (Wiley, New York, NY, 1999).

[21] U. S. Inan and R. A. Marshall, *Numerical Electromagnetics: The FDTD Method* (Cambridge University Press, Cambridge, 2011).

[22] A. Taflove and S. C. Hagness, *Advances in Computational Electrodynamics: The Finite-difference Time-domain Method*, 3rd ed. (Artech House, Boston, MA, 2005).

[23] B. Min, E. Ostby, V. Sorger, E. Ulin-Avila, L. Yang, X. Zhang, and K. Vahala, "High-Q surface-plasmon-polariton whispering-gallery microcavity," Nature **457**, 455–458 (2009).

[24] M. Oxborrow, “Traceable 2-d finite-element simulation of the whispering-gallery modes of axisymmetric electromagnetic resonators,” IEEE Trans. Microw. Theory Tech. **55**, 1209–1218 (2007).

[25] J. Wiersig, “Boundary element method for resonances in dielectric microcavities,” J. Opt. A: Pure Appl. Opt. **5**, 53 (2003).

[26] T. Harayama and S. Shinohara, “Ray-wave correspondence in chaotic dielectric billiards,” Phys. Rev. E **92**, 042916 (2015).

[27] J. Wiersig and M. Hentschel, “Combining directional light output and ultralow loss in deformed microdisks,” Phys. Rev. Lett. **100**, 033901 (2008).

[28] M. Hentschel and K. Richter, “Quantum chaos in optical systems: The annular billiard,” Phys. Rev. E **66**, 056207 (2002).

[29] T. Tanaka, M. Hentschel, T. Fukushima, and T. Harayama, “Classical phase space revealed by coherent light,” Phys. Rev. Lett. **98**, 033902 (2007).

[30] Y. Imry, *Introduction to mesoscopic physics*, 2nd ed., Mesoscopic physics and nanotechnology (Oxford University Press, Oxford, 2001).

[31] T. Ando, A. B. Fowler, and F. Stern, “Electronic properties of two-dimensional systems,” Rev. Mod. Phys. **54**, 437–672 (1982).

[32] H. Sakaki, “Scattering suppression and high-mobility effect of size-quantized electrons in ultrafine semiconductor wire structures,” Jpn. J. Appl. Phys. **19**, L735 (1980).

[33] R. G. Wheeler, K. K. Choi, A. Goel, R. Wisnieff, and D. E. Prober, “Localization and electron-electron interaction effects in submicron-width inversion layers,” Phys. Rev. Lett. **49**, 1674–1677 (1982).

[34] Y. Alhassid, “The statistical theory of quantum dots,” Rev. Mod. Phys. **72**, 895–968 (2000).

[35] S. M. Reimann and M. Manninen, “Electronic structure of quantum dots,” Rev. Mod. Phys. **74**, 1283–1342 (2002).

[36] L. Esaki, “A bird’s-eye view on the evolution of semiconductor superlattices and quantum wells,” IEEE J. Quant. Electron. **22**, 1611–1624 (1986).

[37] A. H. Castro Neto, F. Guinea, N. M. R. Peres, K. S. Novoselov, and A. K. Geim, “The electronic properties of graphene,” Rev. Mod. Phys. **81**, 109–162 (2009).

[38] V. Meunier, A. G. Souza Filho, E. B. Barros, and M. S. Dresselhaus, “Physical properties of low-dimensional sp^2-based carbon nanostructures,” Rev. Mod. Phys. **88**, 025005 (2016).

[39] K. Nakada, M. Fujita, G. Dresselhaus, and M. S. Dresselhaus, “Edge state in graphene ribbons: Nanometer size effect and edge shape dependence,” Phys. Rev. B **54**, 17954–17961 (1996).

[40] M. Y. Han, J. C. Brant, and P. Kim, “Electron transport in disordered graphene nanoribbons,” Phys. Rev. Lett. **104**, 056801 (2010).

[41] S. Das Sarma, S. Adam, E. H. Hwang, and E. Rossi, “Electronic transport in two-dimensional graphene,” Rev. Mod. Phys. **83**, 407–470 (2011).

[42] A. D. Güçlü, *Graphene Quantum Dots*, NanoScience and Technology (Springer, Berlin, Heidelberg, 2014).

[43] P. G. Silvestrov and K. B. Efetov, “Quantum dots in graphene,” Phys. Rev. Lett. **98**, 016802 (2007).

[44] Y. Zhao, J. Wyrick, F. D. Natterer, J. F. Rodriguez-Nieva, C. Lewandowski, K. Watanabe, T. Taniguchi, L. S. Levitov, N. B. Zhitenev, and J. A. Stroscio, “Creating and probing electron whispering-gallery modes in graphene,” Science **348**, 672–675 (2015).

[45] K. Todd, H.-T. Chou, S. Amasha, and D. Goldhaber-Gordon, “Quantum dot behavior in graphene nanoconstrictions,” Nano Lett. **9**, 416–421 (2009).

[46] S. Schnez, F. Molitor, C. Stampfer, J. Güttinger, I. Shorubalko, T. Ihn, and K. Ensslin, “Observation of excited states in a graphene quantum dot,” Appl. Phys. Lett. **94** (2009), 10.1063/1.3064128.

[47] A. Pieper, R. L. Heinisch, and H. Fehske, “Electron dynamics in graphene with gate-defined quantum dots,” EPL **104**, 47010 (2013).

[48] P. Stockschläder, J. Kreismann, and M. Hentschel, “Curvature dependence of semiclassical corrections to ray optics: How Goos-Hänchen shift and Fresnel filtering deviate from the planar case result,” EPL **107**, 64001 (2014).

[49] P. Stockschläder, J. Kreismann, and M. Hentschel, “Wave-inspired corrections for an efficient ray-optical description of micro-optics devices,” in *PIERS Prague 2015 Proceedings* (The Electromagnetics Academy, Cambridge, Massachusetts, 2015) pp. 1647–1651.

[50] P. Stockschläder, J. Kreismann, and M. Hentschel, “Ray picture and ray-wave correspondence in triangular microlasers,” to be published in J. Opt. (2016), preprint, arXiv:1512.06622 [physics.optics] .

[51] S. Tabachnikov, *Geometry and billiards*, 2nd ed. (American Mathematical Society, Providence, RI, 2009).

[52] A. Richter, "Playing billiards with microwaves — quantum manifestations of classical chaos," in *Emerging Applications of Number Theory*, edited by D. A. Hejhal, J. Friedman, M. C. Gutzwiller, and A. M. Odlyzko (Springer, New York, 1999) pp. 479–523.

[53] B. Dietz and A. Richter, "Quantum and wave dynamical chaos in superconducting microwave billiards," Chaos **25**, 097601 (2015).

[54] E. G. Altmann, J. S. E. Portela, and T. Tél, "Leaking chaotic systems," Rev. Mod. Phys. **85**, 869–918 (2013).

[55] S.-Y. Lee, S. Rim, J.-W. Ryu, T.-Y. Kwon, M. Choi, and C.-M. Kim, "Quasiscarred resonances in a spiral-shaped microcavity," Phys. Rev. Lett. **93**, 164102 (2004).

[56] S. Shinohara, T. Harayama, and T. Fukushima, "Fresnel filtering of Gaussian beams in microcavities," Opt. Lett. **36**, 1023–1025 (2011).

[57] E. G. Altmann, G. Del Magno, and M. Hentschel, "Non-Hamiltonian dynamics in optical microcavities resulting from wave-inspired corrections to geometric optics," EPL **84**, 10008 (2008).

[58] Q. H. Song, L. Ge, A. D. Stone, H. Cao, J. Wiersig, J.-B. Shim, J. Unterhinninghofen, W. Fang, and G. S. Solomon, "Directional laser emission from a wavelength-scale chaotic microcavity," Phys. Rev. Lett. **105**, 103902 (2010).

[59] B. Redding, L. Ge, Q. Song, J. Wiersig, G. S. Solomon, and H. Cao, "Local chirality of optical resonances in ultrasmall resonators," Phys. Rev. Lett. **108**, 253902 (2012).

[60] F. Goos and H. Hänchen, "Ein neuer und fundamentaler Versuch zur Totalreflexion," Ann. Phys. (Berlin) **436**, 333–346 (1947).

[61] K. Artmann, "Berechnung der Seitenversetzung des totalreflektierten Strahles," Ann. Phys. (Berlin) **437**, 87–102 (1948).

[62] H. M. Lai, F. C. Cheng, and W. K. Tang, "Goos-Hänchen effect around and off the critical angle," J. Opt. Soc. Am. A **3**, 550–557 (1986).

[63] H. E. Tureci and A. D. Stone, "Deviation from Snell's law for beams transmitted near the critical angle: application to microcavity lasers," Opt. Lett. **27**, 7–9 (2002).

[64] H. Schomerus and M. Hentschel, "Correcting ray optics at curved dielectric microresonator interfaces: Phase-space unification of Fresnel filtering and the Goos-Hänchen shift," Phys. Rev. Lett. **96**, 243903 (2006).

[65] M. Merano, A. Aiello, M. P. van Exter, and J. P. Woerdman, "Observing angular deviations in the specular reflection of a light beam," Nature Photon. **3**, 337–340 (2009).

[66] N. Fiedler-Ferrari, H. M. Nussenzveig, and W. J. Wiscombe, "Theory of near-critical-angle scattering from a curved interface," Phys. Rev. A **43**, 1005–1038 (1991).

[67] K. Y. Bliokh and A. Aiello, "Goos-Hänchen and Imbert-Fedorov beam shifts: an overview," J. Opt. **15**, 014001 (2013).

[68] J. B. Götte, S. Shinohara, and M. Hentschel, "Are Fresnel filtering and the angular Goos-Hänchen shift the same?" J. Opt. **15**, 014009 (2013).

[69] A. Schoch, "Seitliche Versetzung eines total reflektierten Strahls bei Ultraschallwellen," Acta Acust. united Ac. **2**, 18–19 (1952).

[70] X. Chen, X.-J. Lu, Y. Ban, and C.-F. Li, "Electronic analogy of the Goos-Hänchen effect: a review," J. Opt. **15**, 033001 (2013).

[71] C. W. J. Beenakker, R. A. Sepkhanov, A. R. Akhmerov, and J. Tworzydło, "Quantum Goos-Hänchen effect in graphene," Phys. Rev. Lett. **102**, 146804 (2009).

[72] S.-Y. Lee, J. Le Deunff, M. Choi, and R. Ketzmerick, "Quantum Goos-Hänchen shift and tunneling transmission at a curved step potential," Phys. Rev. A **89**, 022120 (2014).

[73] H. K. V. Lotsch, "Beam displacement at total reflection: The Goos-Hänchen effect I," OPTIK **32**, 116–137 (1970).

[74] F. Goos and H. Lindberg-Hänchen, "Neumessung des Strahlversetzungseffektes bei Totalreflexion," Ann. Phys. (Berlin) **440**, 251–252 (1949).

[75] B. R. Horowitz and T. Tamir, "Lateral displacement of a light beam at a dielectric interface," J. Opt. Soc. Am. **61**, 586–594 (1971).

[76] M. A. Porras, "Moment-method evaluation of the angular and lateral shifts of reflected light beams," Opt. Commun. **131**, 13 – 20 (1996).

[77] J. Kreismann, *Eine numerische Untersuchung zu Goos-Hänchen-Verschiebung und Fresnel-Filtern an gekrümmten Grenzflächen*, Bachelor's thesis, Technische Universität Ilmenau (2014).

[78] Ioffe Physico-Technical Institute, "New semiconductor materials. Characteristics and properties," `www.ioffe.ru/SVA/NSM/`.

[79] J. Unterhinninghofen and J. Wiersig, "Interplay of Goos-Hänchen shift and boundary curvature in deformed microdisks," Phys. Rev. E **82**, 026202 (2010).

[80] L.-M. Zhou, C.-L. Zou, Z.-F. Han, G.-C. Guo, and F.-W. Sun, "Negative Goos-Hänchen shift on a concave dielectric interface," Opt. Lett. **36**, 624–626 (2011).

[81] N. H. Tran, L. Dutriaux, P. Balcou, A. Le Floch, and F. Bretenaker, "Angular Goos-Hänchen effect in curved dielectric microstructures," Opt. Lett. **20**, 1233–1235 (1995).

[82] D. Kotik and M. Hentschel, "How curvature affects the far-field emission from deformed optical microcavities," J. Opt. **15**, 014010 (2013).

[83] M. Hentschel and H. Schomerus, "Fresnel laws at curved dielectric interfaces of microresonators," Phys. Rev. E **65**, 045603 (2002).

[84] H. M. Lai, C. W. Kwok, Y. W. Loo, and B. Y. Xu, "Energy-flux pattern in the Goos-Hänchen effect," Phys. Rev. E **62**, 7330–7339 (2000).

[85] Q. Song, W. Fang, B. Liu, S.-T. Ho, G. S. Solomon, and H. Cao, "Chaotic microcavity laser with high quality factor and unidirectional output," Phys. Rev. A **80**, 041807 (2009).

[86] C. Yan, Q. J. Wang, L. Diehl, M. Hentschel, J. Wiersig, N. Yu, C. Pflügl, F. Capasso, M. A. Belkin, T. Edamura, M. Yamanishi, and H. Kan, "Directional emission and universal far-field behavior from semiconductor lasers with Limaçon-shaped microcavity," Appl. Phys. Lett. **94**, 251101 (2009).

[87] S.-B. Lee, J. Yang, S. Moon, J.-H. Lee, K. An, J.-B. Shim, H.-W. Lee, and S. W. Kim, "Universal output directionality of single modes in a deformed microcavity," Phys. Rev. A **75**, 011802 (2007).

[88] G. D. Chern, H. E. Tureci, A. D. Stone, R. K. Chang, M. Kneissl, and N. M. Johnson, "Unidirectional lasing from InGaN multiple-quantum-well spiral-shaped micropillars," Appl. Phys. Lett. **83**, 1710–1712 (2003).

[89] S. Shinohara and T. Harayama, "Signature of ray chaos in quasibound wave functions for a stadium-shaped dielectric cavity," Phys. Rev. E **75**, 036216 (2007).

[90] T. Harayama, P. Davis, and K. S. Ikeda, "Stable oscillations of a spatially chaotic wave function in a microstadium laser," Phys. Rev. Lett. **90**, 063901 (2003).

[91] S. Shinohara, T. Fukushima, and T. Harayama, "Light emission patterns from stadium-shaped semiconductor microcavity lasers," Phys. Rev. A **77**, 033807 (2008).

[92] J. Unterhinninghofen, J. Wiersig, and M. Hentschel, "Goos-Hänchen shift and localization of optical modes in deformed microcavities," Phys. Rev. E **78**, 016201 (2008).

[93] S. Shinohara, M. Hentschel, J. Wiersig, T. Sasaki, and T. Harayama, "Ray-wave correspondence in Limaçon-shaped semiconductor microcavities," Phys. Rev. A **80**, 031801 (2009).

[94] I. N. Bronstein, K. A. Semendjajew, G. Musiol, and H. Mühlig, *Taschenbuch der Mathematik*, 6th ed. (Verlag Harri Deutsch, 2005).

[95] S.-Y. Lee, J.-W. Ryu, T.-Y. Kwon, S. Rim, and C.-M. Kim, "Scarred resonances and steady probability distribution in a chaotic microcavity," Phys. Rev. A **72**, 061801 (2005).

[96] M. Schermer, S. Bittner, G. Singh, C. Ulysse, M. Lebental, and J. Wiersig, "Unidirectional light emission from low-index polymer microlasers," Appl. Phys. Lett. **106**, 101107 (2015).

[97] E. G. Altmann, "Emission from dielectric cavities in terms of invariant sets of the chaotic ray dynamics," Phys. Rev. A **79**, 013830 (2009).

[98] C.-H. Yi, M.-W. Kim, and C.-M. Kim, "Lasing characteristics of a Limaçon-shaped microcavity laser," Appl. Phys. Lett. **95**, 141107 (2009).

[99] E. Ott, *Chaos in dynamical systems* (Cambridge Univ. Press, Cambridge, 1993).

[100] E. G. Altmann, J. S. E. Portela, and T. Tél, "Chaotic systems with absorption," Phys. Rev. Lett. **111**, 144101 (2013).

[101] E. G. Altmann, J. S. E. Portela, and T. Tél, "Chaotic explosions," EPL **109**, 30003 (2015).

[102] J. Wiersig and J. Main, "Fractal Weyl law for chaotic microcavities: Fresnel's laws imply multifractal scattering," Phys. Rev. E **77**, 036205 (2008).

[103] S. C. Creagh and M. M. White, "Differences between emission patterns and internal modes of optical resonators," Phys. Rev. E **85**, 015201 (2012).

[104] F. Albert, C. Hopfmann, A. Eberspächer, F. Arnold, M. Emmerling, C. Schneider, S. Höfling, A. Forchel, M. Kamp, J. Wiersig, and S. Reitzenstein, "Directional whispering gallery mode emission from Limaçon-shaped electrically pumped quantum dot micropillar lasers," Appl. Phys. Lett. **101**, 021116 (2012).

[105] E. Gutkin, "Billiards in polygons," Physica D: Nonlinear Phenomena **19**, 311–333 (1986).

[106] E. Gutkin, "Billiards in polygons: Survey of recent results," J. Stat. Phys. **83**, 7–26 (1996).

[107] M. Boshernitzan, G. Galperin, T. Krüger, and S. Troubetzkoy, "Periodic billiard orbits are dense in rational polygons," Trans. Amer. Math. Soc. **350**, 3523–3535 (1998).

[108] W. Veech, "Teichmüller curves in moduli space, Eisenstein series and an application to triangular billiards," Invent. Math. **97**, 553–583 (1989).

[109] R. Kenyon and J. Smillie, "Billiards on rational-angled triangles," Comment. Math. Helv. **75**, 65–108 (2000).

[110] A. M. Baxter and R. Umble, "Periodic orbits for billiards on an equilateral triangle," Am. Math. Monthly **115**, 479–491 (2008).

[111] B. Cipra, R. M. Hanson, and A. Kolan, "Periodic trajectories in right-triangle billiards," Phys. Rev. E **52**, 2066–2071 (1995).

[112] W. Hooper, "Periodic billiard paths in right triangles are unstable," Geometriae Dedicata **125**, 39–46 (2007).

[113] W. P. Hooper and R. E. Schwartz, "Billiards in nearly isosceles triangles," Journal of Modern Dynamics **3**, 159–231 (2009).

[114] P. Richens and M. Berry, "Pseudointegrable systems in classical and quantum mechanics," Physica D: Nonlinear Phenomena **2**, 495 – 512 (1981).

[115] J. S. Steven Kerckhoff, Howard Masur, "Ergodicity of billiard flows and quadratic differentials," Ann. Math. **124**, 293–311 (1986).

[116] J. Wiersig, "Quantum-classical correspondence in polygonal billiards," Phys. Rev. E **64**, 026212 (2001).

[117] J. Wiersig, "Hexagonal dielectric resonators and microcrystal lasers," Phys. Rev. A **67**, 023807 (2003).

[118] E. Bogomolny and C. Schmit, "Structure of wave functions of pseudointegrable billiards," Phys. Rev. Lett. **92**, 244102 (2004).

[119] E. Bogomolny, B. Dietz, T. Friedrich, M. Miski-Oglu, A. Richter, F. Schäfer, and C. Schmit, “First experimental observation of superscars in a pseudointegrable barrier billiard,” Phys. Rev. Lett. **97**, 254102 (2006).

[120] Q. Song, L. Ge, J. Wiersig, and H. Cao, “Formation of long-lived resonances in hexagonal cavities by strong coupling of superscar modes,” Phys. Rev. A **88**, 023834 (2013).

[121] C. C. Chen, K. W. Su, Y. F. Chen, and K. F. Huang, “Various high-order modes in vertical-cavity surface-emitting lasers with equilateral triangular lateral confinement,” Opt. Lett. **33**, 509–511 (2008).

[122] A. W. Snyder, *Optical waveguide theory*, reprinted ed., Science paperbacks (Chapman & Hall, London, 1983) reprinted by Kluwer Academic Publishers (2000).

[123] M. S. Kurdoglyan, S.-Y. Lee, S. Rim, and C.-M. Kim, “Unidirectional lasing from a microcavity with a rounded isosceles triangle shape,” Opt. Lett. **29**, 2758–2760 (2004).

[124] M. Hentschel, Q. J. Wang, C. Yan, F. Capasso, T. Edamura, and H. Kan, “Emission properties of electrically pumped triangular shaped microlasers,” Opt. Express **18**, 16437–16442 (2010).

[125] H. C. Chang, G. Kioseoglou, E. H. Lee, J. Haetty, M. H. Na, Y. Xuan, H. Luo, A. Petrou, and A. N. Cartwright, “Lasing modes in equilateral-triangular laser cavities,” Phys. Rev. A **62**, 013816 (2000).

[126] C. Lafargue, M. Lebental, A. Grigis, C. Ulysse, I. Gozhyk, N. Djellali, J. Zyss, and S. Bittner, “Localized lasing modes of triangular organic microlasers,” Phys. Rev. E **90**, 052922 (2014).

[127] H. E. Türeci, A. D. Stone, and B. Collier, “Self-consistent multimode lasing theory for complex or random lasing media,” Phys. Rev. A **74**, 043822 (2006).

[128] T. Harayama, S. Sunada, and K. S. Ikeda, “Theory of two-dimensional microcavity lasers,” Phys. Rev. A **72**, 013803 (2005).

[129] T.-Y. Kwon, S.-Y. Lee, J.-W. Ryu, and M. Hentschel, “Phase-space analysis of lasing modes in a chaotic microcavity,” Phys. Rev. A **88**, 023855 (2013).

[130] M. Hentschel, H. Schomerus, and R. Schubert, “Husimi functions at dielectric interfaces: Inside-outside duality for optical systems and beyond,” EPL **62**, 636 (2003).

[131] A. E. Siegman, *Lasers* (Univ. Science Books, Mill Valley, CA, 1986).

[132] I. Gozhyk, M. Boudreau, H. R. Haghighi, N. Djellali, S. Forget, S. Chénais, C. Ulysse, A. Brosseau, R. Pansu, J.-F. Audibert, S. Gauvin, J. Zyss, and M. Lebental, “Gain properties of dye-doped polymer thin films,” Phys. Rev. B **92**, 214202 (2015).

[133] I. Gozhyk, *Polarization and gain phenomena in dye-doped polymer micro-lasers*, Phd thesis, École normale supérieure de Cachan - ENS Cachan (2012).

[134] G. D. Chern, A. W. Poon, R. K. Chang, T. Ben-Messaoud, O. Alloschery, E. Toussaere, J. Zyss, and S.-Y. Kuo, “Direct evidence of open ray orbits in a square two-dimensional resonator of dye-doped polymers,” Opt. Lett. **29**, 1674–1676 (2004).

[135] S. Bittner, C. Lafargue, I. Gozhyk, N. Djellali, L. Milliet, D. T. Hickox-Young, C. Ulysse, D. Bouche, R. Dubertrand, E. Bogomolny, J. Zyss, and M. Lebental, “Origin of emission from square-shaped organic microlasers,” EPL **113**, 54002 (2016).

[136] K. S. Novoselov, A. K. Geim, S. V. Morozov, D. Jiang, Y. Zhang, S. V. Dubonos, I. V. Grigorieva, and A. A. Firsov, “Electric field effect in atomically thin carbon films,” Science **306**, 666–669 (2004).

[137] D. N. Basov, M. M. Fogler, A. Lanzara, F. Wang, and Y. Zhang, “*Colloquium*: Graphene spectroscopy,” Rev. Mod. Phys. **86**, 959–994 (2014).

[138] M. Polini, F. Guinea, M. Lewenstein, H. C. Manoharan, and V. Pellegrini, “Artificial honeycomb lattices for electrons, atoms and photons,” Nature Nanotech. **8**, 625–633 (2013).

[139] S. Reich, J. Maultzsch, C. Thomsen, and P. Ordejón, “Tight-binding description of graphene,” Phys. Rev. B **66**, 035412 (2002).

[140] G. Montambaux, F. Piéchon, J.-N. Fuchs, and M. O. Goerbig, “Merging of Dirac points in a two-dimensional crystal,” Phys. Rev. B **80**, 153412 (2009).

[141] G. Montambaux, F. Piéchon, J.-N. Fuchs, and M. O. Goerbig, “A universal hamiltonian for motion and merging of Dirac points in a two-dimensional crystal,” Eur. Phys. J. B **72**, 509–520 (2009).

[142] M. Bellec, U. Kuhl, G. Montambaux, and F. Mortessagne, “Tight-binding couplings in microwave artificial graphene,” Phys. Rev. B **88**, 115437 (2013).

[143] M. Bellec, U. Kuhl, G. Montambaux, and F. Mortessagne, “Topological transition of Dirac points in a microwave experiment,” Phys. Rev. Lett. **110**, 033902 (2013).

[144] C. Bena and L. Simon, “Dirac point metamorphosis from third-neighbor couplings in graphene and related materials,” Phys. Rev. B **83**, 115404 (2011).

[145] G. Montambaux, “An equivalence between monolayer and bilayer honeycomb lattices,” Eur. Phys. J. B **85**, 1–4 (2012).

[146] P. R. Wallace, “The band theory of graphite,” Phys. Rev. **71**, 622–634 (1947).

[147] J. C. Slonczewski and P. R. Weiss, “Band structure of graphite,” Phys. Rev. **109**, 272–279 (1958).

[148] T. Ando, T. Nakanishi, and R. Saito, “Berry’s phase and absence of back scattering in carbon nanotubes,” Journal of the Physical Society of Japan **67**, 2857–2862 (1998).

[149] O. Klein, “Die Reflexion von Elektronen an einem Potentialsprung nach der relativistischen Dynamik von Dirac,” Zeitschrift für Physik **53**, 157–165 (1929).

[150] M. I. Katsnelson, K. S. Novoselov, and A. K. Geim, “Chiral tunnelling and the Klein paradox in graphene,” Nature Phys. **2**, 620–625 (2006).

[151] C. W. J. Beenakker, “*Colloquium*: Andreev reflection and Klein tunneling in graphene,” Rev. Mod. Phys. **80**, 1337–1354 (2008).

[152] K. S. Novoselov, D. Jiang, F. Schedin, T. J. Booth, V. V. Khotkevich, S. V. Morozov, and A. K. Geim, “Two-dimensional atomic crystals,” Proc. Natl. Acad. Sci. USA **102**, 10451–10453 (2005).

[153] O. Peleg, G. Bartal, B. Freedman, O. Manela, M. Segev, and D. N. Christodoulides, “Conical diffraction and gap solitons in honeycomb photonic lattices,” Phys. Rev. Lett. **98**, 103901 (2007).

[154] S. R. Zandbergen and M. J. A. de Dood, “Experimental observation of strong edge effects on the pseudodiffusive transport of light in photonic graphene,” Phys. Rev. Lett. **104**, 043903 (2010).

[155] Y. Plotnik, M. C. Rechtsman, D. Song, M. Heinrich, J. M. Zeuner, S. Nolte, Y. Lumer, N. Malkova, J. Xu, A. Szameit, Z. Chen, and M. Segev, “Observation of unconventional edge states in ‘photonic graphene’,” Nature Mater. **13**, 57–62 (2014).

[156] U. Kuhl, S. Barkhofen, T. Tudorovskiy, H.-J. Stöckmann, T. Hossain, L. de Forges de Parny, and F. Mortessagne, "Dirac point and edge states in a microwave realization of tight-binding graphene-like structures," Phys. Rev. B **82**, 094308 (2010).

[157] Y. Li, X. Jiang, Z. Liu, and Z. Liu, "Strain effects in graphene and graphene nanoribbons: The underlying mechanism," Nano Research **3**, 545–556 (2010).

[158] Y. Hasegawa, R. Konno, H. Nakano, and M. Kohmoto, "Zero modes of tight-binding electrons on the honeycomb lattice," Phys. Rev. B **74**, 033413 (2006).

[159] M. C. Rechtsman, Y. Plotnik, J. M. Zeuner, D. Song, Z. Chen, A. Szameit, and M. Segev, "Topological creation and destruction of edge states in photonic graphene," Phys. Rev. Lett. **111**, 103901 (2013).

[160] J. Feilhauer, W. Apel, and L. Schweitzer, "Merging of the Dirac points in electronic artificial graphene," Phys. Rev. B **92**, 245424 (2015).

[161] C. R. Dean, A. F. Young, I. Meric, C. Lee, L. Wang, S. Sorgenfrei, K. Watanabe, T. Taniguchi, P. Kim, K. L. Shepard, and J. Hone, "Boron nitride substrates for high-quality graphene electronics," Nature Nanotech. **5**, 722–726 (2010).

[162] S. Barkhofen, M. Bellec, U. Kuhl, and F. Mortessagne, "Disordered graphene and boron nitride in a microwave tight-binding analog," Phys. Rev. B **87**, 035101 (2013).

[163] A. R. Akhmerov and C. W. J. Beenakker, "Boundary conditions for Dirac fermions on a terminated honeycomb lattice," Phys. Rev. B **77**, 085423 (2008).

[164] M. Kohmoto and Y. Hasegawa, "Zero modes and edge states of the honeycomb lattice," Phys. Rev. B **76**, 205402 (2007).

[165] M. Wimmer, A. R. Akhmerov, and F. Guinea, "Robustness of edge states in graphene quantum dots," Phys. Rev. B **82**, 045409 (2010).

[166] L. A. Ponomarenko, F. Schedin, M. I. Katsnelson, R. Yang, E. W. Hill, K. S. Novoselov, and A. K. Geim, "Chaotic Dirac billiard in graphene quantum dots," Science **320**, 356–358 (2008).

[167] J. Cserti, A. Pályi, and C. Péterfalvi, "Caustics due to a negative refractive index in circular graphene *p*-*n* junctions," Phys. Rev. Lett. **99**, 246801 (2007).

[168] J.-S. Wu and M. M. Fogler, “Scattering of two-dimensional massless Dirac electrons by a circular potential barrier,” Phys. Rev. B **90**, 235402 (2014).

[169] X. Chen, J.-W. Tao, and Y. Ban, “Goos-Hänchen-like shifts for Dirac fermions in monolayer graphene barrier,” Eur. Phys. J. B **79**, 203–208 (2011).

[170] Z. Wu, F. Zhai, F. M. Peeters, H. Q. Xu, and K. Chang, “Valley-dependent Brewster angles and Goos-Hänchen effect in strained graphene,” Phys. Rev. Lett. **106**, 176802 (2011).

Acknowledgments

First of all, I would like to thank Prof. Dr. Martina Hentschel for supervising me during the last years. I am grateful for support and advice, for the answers on all my questions, many discussions about physics and various other topics, and for her patience with my doubts and concerns. Besides being a great teacher and supervisor, she is a role model for me and, certainly, also for many other young scientists.

Thanks are also due to Prof. Dr. Erich Runge for valuable insights into physics as well as into the world of academia during group meetings ("Theorietee") and many other occasions. Without the members of his group, especially David Leipold, Lars Winterfeld, and Felix Schwarz, my time in Ilmenau wouldn't have been as pleasant as it was. I have much appreciated sharing an office with David and Lars and many interesting discussions during lunch and coffee breaks. They also helped me to understand the university and the local culture.

It has been a pleasure to work with Jakob Kreismann during all stages of his university education, having been a Bachelor's and a Master's student in Martina's group and now as a PhD student. It has been an invaluable support of my work that he shared his results and data with me.

In particular, I acknowledge Prof. Dr. Henning Schomerus of Lancaster University. In the context of the DFG research group FOR760, "Scattering systems with Complex Dynamics", he invited me to Lancaster. During my stay in Lancaster and on all other occasions I have met him in Dresden or in Ilmenau, he was interested in my work and found the time to discuss with me.

Funding through various sources enabled not only my time in Lancaster but also the participation in many conferences and workshops and several visists to the Max Planck Institute for the Physics of Complex Systems in Dresden. Especially, the time in Dresden has been very valuable and productive in the early stages of my work.

Last but not least, I have to thank Mrs. Dagmar Böhme. She helped me with all the forms and contracts at the university, especially, with arranging the reimbursement of travel expenses. Sometimes she even made things possible that seemed to be impossible.

Selbstständigkeitserklärung

Ich versichere, dass ich die vorliegende Arbeit ohne unzulässige Hilfe Dritter und ohne Benutzung anderer als der angegebenen Hilfsmittel angefertigt habe. Die aus anderen Quellen direkt oder indirekt übernommenen Daten und Konzepte sind unter Angabe der Quelle gekennzeichnet.

Weitere Personen waren an der inhaltlich-materiellen Erstellung der vorliegenden Arbeit nicht beteiligt. Insbesondere habe ich hierfür nicht die entgeltliche Hilfe von Vermittlungs- bzw. Beratungsdiensten (Promotionsberater oder anderer Personen) in Anspruch genommen. Niemand hat von mir unmittelbar oder mittelbar geldwerte Leistungen für Arbeiten erhalten, die im Zusammenhang mit dem Inhalte der vorgelegten Dissertation stehen.

Die Arbeit wurde bisher weder im In- noch im Ausland in gleicher oder ähnlicher Form einer Prüfungsbehörde vorgelegt.

Ich bin darauf hingewiesen worden, dass die Unrichtigkeit der vorstehenden Erklärung als Täuschungsversuch bewertet wird und gemäß §7 Abs. 10 der Promotionsordnung den Abbruch des Promotionsverfahrens zur Folge hat.

Ilmenau, den 17. März 2017